

Unified Harmonic Power-Flow and Stability Analysis of Power Grids with Converter-Interfaced Distributed Energy Resources

Présentée le 26 janvier 2024

Faculté des sciences et techniques de l'ingénieur
Laboratoire des systèmes électriques distribués
Programme doctoral en énergie

pour l'obtention du grade de Docteur ès Sciences

par

Johanna Kristin Maria BECKER

Acceptée sur proposition du jury

Dr S.-R. Cherkaoui, président du jury
Prof. M. Paolone, Dr A. M. Kettner, directeurs de thèse
Prof. K. Strunz, rapporteur
Prof. G. De Carne, rapporteur
Prof. D. Dujic, rapporteur

You're only given a little spark of madness.
You mustn't lose it.
— Robin Williams

To my parents.

Acknowledgements

I would like to express my sincere thanks to both of my thesis supervisors. I am immensely grateful to Prof. Mario Paolone. Your unconditional guidance and invaluable support over the past four years have been indispensable, enriching my professional and personal growth. Equally, my heartfelt thanks to Dr. Andreas Kettner, whose consistent and readily available support was crucial in the realization of this thesis. Your dedication and enduring enthusiasm for research have greatly inspired me. Thank you for believing in me from the moment that I first joined DESL as a master's student.

I'm grateful to the kind souls in ELL, including Dr. Rachid Cherkaoui for his open-heartedness, Sophie Flynn for her exceptional administrative skills, and all the other wonderful people who make ELL unique and heartwarming.

I've been fortunate to have wonderful office mates and friends throughout this journey. Alex and Francesco, you've shared both the ups and downs with me, and I couldn't have asked for better companions. Yihui, your unwavering optimism and dedication have been a pleasure to work alongside. Toni, your unique sense of humour has reminded me not to take life too seriously. And to Rahul, Ji, Vlad, Yu, Alina, Anne, and everyone else I may have missed, you've all made the last four years truly unforgettable.

I owe a special thanks to my friends from Freiburg for maintaining our strong bonds despite the distance. Our remote Yoga sessions and shared passion for bike-packing adventures have been sources of continuous energy and renewal. Myriel, thank you for always being there. Your support means a lot to me. Special thanks to Joanna, who I started this journey with in my bachelor's days. Your determination to fully grasping the essence of things is something I deeply admire and will always cherish.

Finally, the heartfelt thanks to my parents, to my brothers, Bastian and Ruben, and to Greg. The greatest gift in life is knowing there's always someone to support you when you stumble.

Lausanne, January 15, 2024

Johanna Becker

Abstract

Modern power distribution systems are experiencing a large-scale integration of *Converter-Interfaced Distributed Energy Resources* (CIDERs). Their presence complicates the analysis and mitigation of harmonics, whose creation and propagation may be amplified beyond limits of international standards by the interactions of individual CIDERs through the grid. To this end, appropriate analysis tools are required in order to model and quantify harmonic levels as well as to assess the associated harmonic stability, identify causes of instability, and develop robust controllers. Frequency-domain analysis has been identified to be a computationally efficient approach for the study of harmonics. However, many of the existing frequency-domain models are only valid for specific devices, or neglect the coupling between harmonics.

In order to overcome these limitations, a modular and generic modelling framework for power grids with a high share of CIDERs is proposed in this thesis. The framework models a power system as a composition of a grid and a number of resources (including, but not limited to, CIDERs). The grid components are characterized by compound electrical parameters, which allow to represent both transposed or non-transposed lines. The CIDERs are represented by a generic structure that allows to treat both grid-forming and grid-following CIDERs. In particular, this structure is fully modular w.r.t. different reference frames (e.g., between the electrical components and the control of a CIDER) as well as circuit configurations (e.g., between grid and resources). All components of the system model are represented by *Linear Time-Periodic* (LTP) models or functions, that are transformed to frequency domain by means of Fourier transform and Toeplitz theory.

Building on this modelling framework, a *Harmonic Power-Flow* (HPF) method is proposed. The HPF problem is formulated through the mismatch equations of the nodal quantities between the hybrid parameters of the grid and the closed-loop responses of the CIDERs. The system of equations is solved numerically using a Newton-Raphson algorithm. The results are validated against time-domain simulations in Simulink. The HPF method has been shown to accurately capture the propagation of harmonics between AC and DC components of CIDERs, and through entire hybrid AC/DC power systems.

For the purpose of stability assessment, the system model is derived in harmonic domain as the closed-loop model between the grid and the resources. On the obtained system

Abstract

model, an eigenvalue analysis is performed using LTP system theory. The *Harmonic Stability Assessment* (HSA) is shown to be applicable to individual CIDER models as well as to an entire power system. Furthermore, it can be used for sensitivity analysis of the eigenvalue loci w.r.t. control parameter variations. Additionally, the HSA is confirmed to be effective in identifying a harmonic instability in a small yet realistic example system operating under standard conditions.

Keywords: Distributed energy resources, power electronic converters, harmonic power-flow study, harmonic stability assessment, coupling of harmonic frequencies, unbalanced power grids.

Zusammenfassung

In modernen Verteilernetzen findet zurzeit in grossem Massstab eine Integration sogenannter *Converter-Interfaced Distributed Energy Resources* (CIDERs) statt. Ihr Vorkommen erschwert die Analyse und Dämpfung von Harmonischen (= Oberschwingungen), deren Entstehung und Ausbreitung durch das Zusammenspiel einzelner CIDERs im Netz derart verstärkt werden kann, dass die durch internationale Standards vorgeschriebenen Grenzwerte verletzt werden. Aus diesem Grund werden geeignete Analysewerkzeuge benötigt, um Harmonische zu modellieren und zu quantifizieren, sowie die damit verbundene harmonische Stabilität zu bewerten, die Ursachen etwaiger Instabilität zu identifizieren und robuste Regler zu entwickeln. Die Analyse im Frequenzbereich hat sich als ein hinsichtlich des Rechenaufwands effizienter Ansatz für derartige Untersuchungen erwiesen. Viele der vorhandenen Frequenzbereichsmodelle sind jedoch nur für bestimmte Maschinen gültig oder vernachlässigen die Kopplung zwischen Harmonischen verschiedener Ordnung.

Um diese Einschränkungen zu überwinden, wird in dieser Arbeit ein modularer und generischer Modellierungsansatz für Stromnetze mit einem hohen Anteil an CIDERs vorgeschlagen. Der Ansatz modelliert ein Stromnetz als Kombination aus dem Netz und einer Reihe von Ressourcen (einschliesslich CIDERs, aber nicht beschränkt auf diese). Die Netzkomponenten werden durch sogenannte elektrische Verbundparameter charakterisiert, die es ermöglichen, sowohl transponierte als auch nicht transponierte Leitungen darzustellen. Die CIDERs werden durch einen generischen Aufbau beschrieben, der es ermöglicht, sowohl netzbildende als auch netzfolgende CIDERs zu behandeln. Insbesondere ist dieser Aufbau vollständig modular in Bezug auf verschiedene Referenzrahmen (z.B. zwischen den elektrischen Komponenten und der Regelung einer CIDER) sowie auf verschiedene Schaltkreiskonfigurationen (z.B. zwischen Netz und Ressourcen). Alle Komponenten des Systemmodells werden durch *lineare zeit-periodische* (LTP)-Modelle oder -Funktionen dargestellt, die mittels Fourier-Transformation und Toeplitz-Theorie im Frequenzbereich abgebildet werden.

Aufbauend auf diesem Modellierungsansatz wird eine Methode des *harmonischen Lastflusses* (HPF) hergeleitet. Das HPF-Problem wird durch die Fehlergleichungen der Knotengrössen zwischen den Hybridparametern des Netzes und den Antworten des geschlossenen Regelkreises der CIDERs formuliert. Das Gleichungssystem wird numerisch mit einem Newton-Raphson-Verfahren gelöst. Die Ergebnisse werden anhand von Zeit-

Zusammenfassung

bereichssimulationen in Simulink validiert. Es wird gezeigt, dass die HPF-Methode die Ausbreitung von Harmonischen zwischen AC- und DC-Komponenten der CIDERs und durch ganze hybride AC/DC-Stromnetze präzise erfassen kann.

Zum Zweck der Stabilitätsanalyse wird das Systemmodell im harmonischen Bereich als ein geschlossener Regelkreis bestehend aus dem Netz und den Ressourcen modelliert. Für dieses Modell wird eine Eigenwertanalyse unter Verwendung der LTP-Systemtheorie durchgeführt. Es wird gezeigt, dass die *harmonische Stabilitätsanalyse* (HSA) sowohl für einzelne CIDER-Modelle als auch für ein ganzes Stromnetz effektiv durchgeführt werden kann. Darüber hinaus kann das genannte Modell für die Sensitivitätsanalyse der Lage der Eigenwerte in Bezug auf Variationen der Regelparameter verwendet werden. Des Weiteren wird gezeigt, dass die HSA eine harmonische Instabilität in einem kleinen aber realistischen Beispielsystem, das unter Standardbedingungen betrieben wird, wirksam identifiziert.

Stichwörter: Verteilte Energiequellen, leistungselektronische Umrichter, harmonische Lastflussberechnung, Analyse der harmonischen Stabilität, Kopplung zwischen harmonischen Frequenzen, asymmetrische Stromnetze.

Résumé

Les systèmes modernes de distribution d'énergie connaissent une intégration à grande échelle de *Ressources Énergétiques Distribuées Interfacées par Convertisseur* (CIDERS). Leur présence complique l'analyse et l'atténuation des fréquences harmoniques, dont la création et la propagation peuvent être amplifiées au-delà des limites des normes internationales par les interactions des différents CIDERS à travers le réseau. À cet effet, des outils d'analyse appropriés sont nécessaires pour modéliser et quantifier les niveaux d'harmoniques, ainsi que pour évaluer la stabilité harmonique du réseau, identifier les causes d'instabilité et développer des contrôleurs robustes. L'analyse dans le domaine fréquentiel a été identifiée comme une approche efficace sur le plan computationnel pour l'étude des harmoniques. Cependant, de nombreux modèles existants ne sont valides que pour des cas spécifiques, ou négligent le couplage entre les harmoniques.

Afin de surmonter ces limitations, cette thèse propose un cadre de modélisation modulaire et générique pour les réseaux électriques avec une part élevée de CIDERS. Ce cadre modélise un système d'alimentation comme une composition d'un réseau et d'un nombre de ressources (y compris, mais sans s'y limiter, les CIDERS). Les composants du réseau sont caractérisés par des paramètres électriques composés, qui permettent de représenter à la fois les lignes torsadées et non torsadées. Les CIDERS sont représentés par une structure générique qui permet de les traiter soit comme source maître ou comme source suivant le réseau. En particulier, cette structure est entièrement modulaire par rapport aux différents cadres de référence (e.g., entre les composants électriques et le contrôle d'un CIDER), ainsi qu'aux configurations de circuit (e.g., entre le réseau et les ressources). Tous les composants du modèle sont représentés par des modèles ou des fonctions *Linéaires Temps-Périodiques* (LTP), qui sont transformés dans le domaine fréquentiel au moyen de la transformation de Fourier et de l'algèbre de Toeplitz.

Sur la base de ce cadre de modélisation, une méthode de *Flux de Puissance Harmonique* (HPF) est proposée. Le problème du HPF est formulé à travers les équations de déséquilibre des quantités nodales entre les paramètres hybrides du réseau et les réponses des CIDERS en boucle fermée. Le système d'équations est résolu numériquement en utilisant l'algorithme de Newton-Raphson. Les résultats sont validés grâce à des simulations en temps réel dans Simulink. La méthode HPF permet de capturer avec précision la propagation des harmoniques entre les composants AC et DC des CIDERS et à travers

Résumé

des systèmes d'alimentation hybrides AC/DC entiers.

Afin d'évaluer la stabilité du système entier, son modèle est dérivé dans le domaine harmonique comme étant le modèle en boucle fermée entre le réseau et les ressources. Ouis, sur le modèle obtenu, une analyse des valeurs propres est réalisée en utilisant la théorie des systèmes LTP. L'*Évaluation de la Stabilité Harmonique* (HSA) s'avère applicable à des modèles individuels des CIDERS, ainsi qu'au système d'alimentation entier. De plus, elle peut être utilisée pour une analyse de sensibilité des lieux des valeurs propres par rapport aux variations des paramètres de contrôle. Finalement, le HSA est efficace pour identifier une instabilité harmonique dans un système d'exemple réduit mais réaliste, opérant dans des conditions typiques.

Mots clé : Ressources énergétiques distribuées, convertisseurs de puissance électroniques, débit de puissance harmonique, évaluation de stabilité harmonique, couplage de fréquences harmoniques, réseaux électriques déséquilibrés.

Contents

Acknowledgements	i
Abstract (English/Français/Deutsch)	iii
List of Figures	xiii
List of Tables	xix
List of Abbreviations	xxi
1 Introduction	1
1.1 Context and Motivation	1
1.2 Problem Statement	2
1.3 Contributions of the Thesis	6
1.4 Document Outline	7
2 Modelling Framework for Power System Components	9
2.1 State of the Art	10
2.1.1 Time-Domain Models	11
2.1.2 Frequency-Domain Models	11
2.1.3 Hybrid Models	13
2.1.4 Motivation for the Proposed Modelling Framework	14
2.2 Hypotheses of the Modelling Framework	15
2.2.1 Hypotheses of the AC Power System	15
2.2.2 Hypotheses of the Hybrid AC/DC Power System	16
2.3 Model of the Electrical Grid	18
2.3.1 Lumped-Element Model	18
2.3.2 Three-Phase Incidence Matrix	19
2.4 Generic Model of the Converter-Interfaced Distributed Energy Resources	20
2.4.1 Primer on Time-Periodic Signals	20
2.4.2 Time-Domain Model	21
2.4.3 Harmonic-Domain Model	28
2.4.4 Grid Response of the CIDER in Harmonic Domain	31

Contents

2.4.5	Extension of the Modelling Framework for Treating Nonlinearities within the Internal Response of a CIDER	35
2.5	Generic Model of the Network-Interfacing Converters	37
3	Derivation of the Specific Models of the CIDERs	39
3.1	State of the Art	40
3.1.1	Representation of the DC Side of a CIDER	40
3.1.2	Representation of the Actuator	41
3.2	Library of Component Models	42
3.2.1	PWM Actuator	42
3.2.2	Filter Stages	44
3.2.3	Controller Stages	45
3.2.4	Circuit Configurations and Reference Frames	48
3.2.5	PQ Law – Reference Calculation	50
3.3	Library of Resource Models	53
3.3.1	Grid-Forming CIDER – Considering Only AC-Side Characteristics	53
3.3.2	Grid-Following CIDER – Considering Only AC-Side Characteristics	57
3.3.3	Grid-Following CIDER – Including DC-Side Characteristics . . .	59
3.3.4	Network-Interfacing Converters	65
3.4	Validation of the Proposed Models	66
3.4.1	Methodology and Key Performance Indicators	66
3.4.2	Results and Discussion	70
4	Harmonic Power-Flow Algorithm	77
4.1	State of the Art	78
4.1.1	Methods without Frequency-Coupling Representation	78
4.1.2	Methods with Frequency-Coupling Representation	79
4.1.3	Motivation for the Proposed Method	79
4.2	Representation of the Electrical Grid for the HPF Study	80
4.2.1	Compound Admittance Matrix	82
4.2.2	Compound Hybrid Matrix	82
4.3	Algorithm for Harmonic Power-Flow Studies	84
4.3.1	Mathematical Formulation of the Problem for AC Power Systems	84
4.3.2	Numerical Solution via the Newton-Raphson Method	85
4.3.3	Extension of the Algorithm for AC Power Systems to Treat Non-linearities within the Internal Response of the CIDER	87
4.3.4	Extension of the Algorithm for Hybrid AC/DC Power Systems .	89
4.4	Validation of the Proposed Method	93
4.4.1	Harmonic Power-Flow Study of AC Power Systems	93
4.4.2	Harmonic Power-Flow Study of AC Power Systems with Nonlinearities within the Internal Response of the CIDER	98
4.4.3	Harmonic Power-Flow Study of Hybrid AC/DC Systems	105

5	Harmonic Stability Assessment	111
5.1	State of the Art	112
5.1.1	Studies without Representation of Frequency Coupling	112
5.1.2	Studies with Representation of Frequency Coupling	113
5.1.3	Motivation for the Proposed Method	114
5.2	Harmonic State-Space Model of a Power System	114
5.2.1	Harmonic State-Space Model of the Resources	115
5.2.2	Harmonic State-Space Model of the Electrical Grid	115
5.2.3	Open-Loop Model of the Power System	119
5.2.4	Closed-Loop Model of the Power System	122
5.3	Operators for the Harmonic Stability Assessment	123
5.4	Harmonic Stability Assessment of the Resources	125
5.4.1	Classification of the LTP eigenvalues	126
5.4.2	Impact of the Maximum Harmonic Order	130
5.4.3	Sensitivity Analysis of the Eigenvalues w.r.t. to the Control Pa- rameters	134
5.5	Harmonic Stability Assessment of a Power System	137
5.5.1	Test System Setup	137
5.5.2	Classification of the System Eigenvalues	138
5.5.3	Detailed Analysis of the System Eigenvalues	141
5.5.4	Sensitivity Analysis and Harmonic Instability	144
6	Conclusion	149
A	Appendix	153
A.1	Measurement Accuracy of Instrument Transformers	153
A.2	Modelling of Sources of Harmonics other than CIDERS	153
A.3	Frequency-Dependent Line Parameters	154
A.3.1	Impact on the Branch Admittance of the Line Model	154
A.3.2	Impact on the Results of the Harmonic Power-Flow Study	155
A.4	Decoupled Harmonic Power Flow	155
Bibliography		166
Curriculum Vitae		167

List of Figures

1.1	Overview of the methods developed in this thesis.	6
2.1	Exemplary illustration of the frequency-coupling effect of a model. In- and output signals are represented by their Fourier coefficients (i.e., for the case of a maximum harmonic order equal to two), the model behaviour w.r.t. coupling of frequencies is represented by the rectangular blocks. The positive and negative image of the signal is considered.	11
2.2	Overview of the power system structure consisting of the grid and the resources. The resources are partitioned into grid-forming \mathcal{S} and -following \mathcal{R} type.	16
2.3	Simplified schematic of a CIDER, e.g., a single-port device (Fig. 2.3a), and a NIC, e.g., a two-port device (Fig. 2.3b).	17
2.4	Partition of the nodes for a generic subsystem j (Fig. 2.4a) and for a hybrid AC/DC grid with NICs connecting \mathcal{R}_2^{AC} and \mathcal{S}_2^{DC} (Fig. 2.4b).	18
2.5	The grid is represented by branch and shunt elements. $\mathbf{i}_\ell(t)$ and $\mathbf{i}_t(t)$ are the current flows through the elements associated with the branch $\ell \in \mathcal{L}$ and shunt $t \in \mathcal{T}$, respectively. $\mathbf{v}_n(t)$ and $\mathbf{i}_n(t)$ are the phase-to-ground voltages and injected currents at node $n \in \mathcal{N}$, respectively.	19
2.6	Schematic diagram of a generic CIDER. The power hardware π consists of the actuator α and a cascade of filter stages φ_i (for simplicity, one stage is shown only), the outermost of which is connected to the grid γ . The control software κ consists of the reference calculation ρ and cascaded controllers κ_i , which track the setpoint σ . The transformations τ represent changes of electrical connection or reference frame.	22
2.7	Block diagram of the proposed generic state-space model of CIDERs. Note the modularity: power hardware π , control software κ , and grid γ are represented by separate blocks, which are interfaced via coordinate transformations. The reference calculation $\mathbf{r}(\cdot, \cdot)$ may be either linear (i.e., for Vf control) or nonlinear (i.e., for PQ control). The other blocks of the model are exactly linear (i.e., LTP systems and LTP transformations).	27
2.8	Overview of the difference between the HDR (Fig. 2.8a) and HTF (Fig. 2.8b) representation of a CIDER with emphasis on the two different operating points.	37

List of Figures

3.1	Different levels of approximations of the power hardware of a CIDER. Detailed representation Fig. 3.1a, the current-source representation Fig. 3.1b and the voltage-source representation Fig. 3.1c.	41
3.2	Schematic diagram of a three-phase two-level power converter, which is commonly used for CIDERs. The fourth leg is optional: it is required only if the power converter has to be able to inject or absorb homopolar currents.	42
3.3	Representation of the actuator by an average model, consisting of a controlled current source on the DC side and a controlled voltage source on the AC side.	43
3.4	Equivalent circuits of a filter stage i constructed from inductors (3.4a) or capacitors (3.4b), respectively. Observe that voltages, currents, and electrical parameters are expressed in the reference frame of the power hardware π	44
3.5	Block diagrams of a controller stage i associated with an inductive (3.5a) and capacitive (3.5b) filter stage, respectively. In general, the control law includes <i>Feed-Back</i> (FB), <i>Feed-Forward</i> (FF), and <i>Feed-Through</i> (FT) terms. Observe that voltages and currents are expressed in the reference frame of the control software κ	45
3.6	Schematic diagram of a grid-forming CIDER with an LC filter.	54
3.7	Schematic diagram of a grid-following CIDER with an LCL filter.	57
3.8	Overview of the grid-following CIDER including DC-side dynamics. The power hardware is connected through measurements and coordinate transformations (i.e., in case of AC signals) to the control software.	60
3.9	Simplified representation of the power hardware of a NIC.	66
3.10	Test setup for the validation of the individual CIDER models. The resource is represented by a detailed state-space model (see Section 3.3), and the power system by a TE (see Tables 3.1 and 3.2).	67
3.11	Overview of the tests for the validation of the CIDERs: 3.11a shows the test for the accuracy of the HDR in the operating point, and 3.11b shows the test for the validity of the HDR and HSS in case of deviations from the operating point.	70
3.12	Results of the validation on the individual grid-forming CIDER. The plots on the left-hand side show the spectra (i.e., for phase A), and the ones on the right-hand side the error.	71
3.13	Results of the validation on the individual grid-following CIDER. The plots on the left-hand side show the spectra (i.e., for phase A), and the ones on the right-hand side the error.	72

3.14	Results of the validation on the individual grid-following CIDER including the DC-side modelling. The grid current (3.14a) and DC-side voltage (3.14b) are shown. The plots on the left-hand side show the spectra (i.e., for phase A in case of the grid current), and the ones on the right-hand side the error defined through the KPIs.	73
3.15	Impact of the order of Taylor expansion in the reference calculation on the accuracy of the HDR for the grid-following CIDER (3.15a) and the grid-following CIDER considering the DC-side characteristics (3.15b). The plots show the error in magnitude and phase on the top and bottom defined through the KPIs.	74
3.16	Accuracy of the HDR and HSS the grid-following CIDERs considering only AC-side (3.16a) and considering DC-side characteristics (3.16b) for random deviations from the operating point. The solution for no deviation from the operating point is included as the first sample (and additionally as the violet point centered between the two boxes at each harmonic). The box plots show 25 and 75 percentile, outliers exceed 1.5-times the interquartile range.	76
4.1	The grid is represented by branch elements with compound impedance \mathbf{Z}_ℓ and shunt elements with compound admittance \mathbf{Y}_t . \mathbf{I}_ℓ and \mathbf{I}_t are the current flows through the branch and shunt elements, respectively. \mathbf{V}_n and \mathbf{I}_n are the phase-to-ground voltages and injected currents, respectively.	81
4.2	Schematic diagram of the test system, which is based on the CIGRÉ low-voltage benchmark microgrid [1] (in black) and extended by unbalanced impedance loads (in grey). For the cable parameters see Table 4.3. The set of grid-following resources are composed of constant impedance loads (\mathbf{Z}) and constant power loads (P/Q), their parameters are given in Table 4.4.	94
4.3	Results of the validation on the benchmark system. The plots show the maximum absolute errors over all nodes and phases, for voltages (left column) and currents (right column), in magnitude (top row) and phase (bottom row).	98
4.4	Mean and distribution of the timing performance of HPF for maximum numbers of CIDERs and with varying h_{max} for $N = 50$ simulations. The box-and-whisker plot visualizes 25 and 75 percentile of the sample, the whisker length is 1.5-times the interquartile range.	99
4.5	Results of the validation on the benchmark system for the extension of the solution algorithm. The grid-following CIDERs (PQ) and the constant impedance loads (\mathbf{Z}) are analysed. The plots show the maximum absolute errors over all nodes and phases, for voltages (left column) and currents (right column), in magnitude (top row) and phase (bottom row).	101

List of Figures

4.6	Comparison of the HPF study including (i.e., HPF-DC) and excluding the DC side of the CIDERS at three nodes throughout the benchmark system. The voltages for Phase A of these nodes are given in (4.6a) and the currents in (4.6b).	103
4.7	Comparison of the HPF study with the decoupled HPF study at three nodes throughout the benchmark system. The voltages for Phase A of these nodes are given in 4.7a and the currents in 4.7b.	104
4.8	Schematic diagram of the test system, which is based on the CIGRÉ low-voltage benchmark microgrid [2] (blue box) and interfaced through NICs (green box) to the DC subsystem (red box), parameters given in Table 4.9. The resources are composed of constant impedance loads (Z), constant power loads (P/Q), and constant current sources (I), parameters given in Table 4.10.	106
4.9	Results of the validation of the AC (Fig. 4.9a) and DC subsystem (Fig. 4.9b). The grid-following CIDERS (\mathcal{R}_1^{AC}) and the AC side of the NICs (\mathcal{R}_2^{AC}), as well as the DC-side resources (\mathcal{R}_1^{DC}) and the DC side of the NICs (\mathcal{S}_2^{DC}) are shown. The plots show the maximum absolute errors over all nodes and phases, for voltages (left column) and currents (right column), in magnitude (top row) and phase (bottom row).	108
5.1	Lumped-element model of the grid shown at nodes with a grid-forming resource (5.1a) and a grid-following resource (5.1b). The electrical quantity controlled by the resource is highlighted in red.	117
5.2	Block diagram of the power system.	120
5.3	Classification of the eigenvalues of the grid-forming CIDER. Fig. 5.3a: Eigenvalues on the left-hand side and eigenvector matrix \mathbf{V} on the right-hand side. Fig. 5.3b: Representation of the entries of \mathbf{V} by triplets (ABC) and pairs (DQ) in the sequence domain. Fig. 5.3c: Mapping of the harmonic sequences for a transformation from ABC coordinates to DQZ components and vice versa.	128
5.4	Classification of the eigenvalues of the grid-following CIDER considering only AC-side characteristics (Fig. 5.4a) and the grid-following CIDER including the DC-side characteristics (Fig. 5.4b). The eigenvalues are shown on the left-hand side and the matrix of the eigenvectors \mathbf{V} on the right-hand side.	131
5.5	Analysis of the impact of the maximum harmonic order on the location of the LTP eigenvalues for the grid-forming CIDER (Fig. 5.5a), the grid-following CIDER (Fig. 5.5b) and the grid-following CIDER that models the DC side (Fig. 5.5c)	133

5.6	Analysis of the impact of h_{max} on the location of the LTP eigenvalues for the three CIDERs. The CIDERs being analysed are the grid-forming and grid-following CIDERs that only model the AC-side characteristics (i.e., Section 3.3.1 and Section 3.3.2, respectively), and the grid-following CIDER that includes the DC-side modelling (i.e., Section 3.3.3). The plot shows the maximum distance between the LTI and the LTP eigenvalues for increasing h_{max}	134
5.7	Sensitivity curves w.r.t. the feedback gain K_{FB} of the controller stage associated with the grid-side inductance (Fig. 5.7a), the controller stage associated with the capacitance (Fig. 5.7b) and the controller stage associated with the actuator-side inductance (Fig. 5.7c) of the grid-following CIDER, which models only the AC-side characteristics. The maximum harmonic order considered for this analysis is $h_{max} = 5$	136
5.8	Schematic diagram of the test system used for the HSA. Its line lengths and cable parameters are based on the CIGRÉ low-voltage benchmark microgrid [1]. All cables are of type UG1 - for their parameters see Table 4.3.	137
5.9	Results of the HPF for a system with harmonic distortion (HPF-h), the HPF for a system with zero harmonic distortion (HPF-0) and a conventional power-flow (PF) at the fundamental frequency. The figure shows the magnitudes of the nodal quantities for phase A, at the three nodes, where resources are connected.	138
5.10	Classification of the closed-loop system eigenvalues into DI, CDI and CDV (Fig. 5.10a), and visualization of the eigenvector matrix associated with the eigenvalues (Fig. 5.10b).	139
5.11	Division of the system eigenvalues into the two sets associated with the grid (Fig. 5.11a) and with the resources (Fig. 5.11b), respectively. The left-hand side of both figures show the entire region containing all eigenvalues, while the right-hand side figures show a zoom on the regions of interest. Additionally, the eigenvalues of the open-loop grid and resource models are shown in (Fig. 5.11a) and (Fig. 5.11b), respectively.	142
5.12	Detailed view of the system eigenvalues associated with the resources. Additionally, the eigenvalues of the open-loop resource models are shown (i.e., PQ1/2 and TE). Note the indication showing how this set of eigenvalues of PQ2 change their location for the system model.	143
5.13	Detailed view of the system eigenvalues associated with the resources. Comparison of the system eigenvalues obtained with the HSS model considering a system with zero harmonic distortion to one with harmonic distortion. Additionally, the eigenvalues of the LTI model are shown.	144

List of Figures

5.14	Sensitivity analysis of the system eigenvalues for the LTP and LTI models w.r.t. the controller gain $K_{\alpha,FB}$ of the grid-following CIDER at N05. Fig. 5.14a and Fig. 5.14b show the system eigenvalues associated with the grid and the resources, respectively. The maximum harmonic order of this analysis is $h_{max} = 25$	145
5.15	Validation of the observed instability through TDS in Simulink. Fig. 5.15a gives the stability boundary for the test system if harmonics are present in the system (i.e., a “harmonic instability” in line with the definition in Section 1.2), and Fig. 5.15b shows the case without harmonic injection at the substation (i.e., purely sinusoidal behaviour). Each figure shows the nodal voltage of phase A (i.e., $v_{\gamma,A}$) and the injected power P at node N05, in the first and second plot of the figure, respectively. The last plot in both figures depicts the decrease of the controller gain $K_{\alpha,FB}$ of the grid-following CIDER at N05 as the system becomes unstable.	147
A.1	Comparison of line branch admittances of the π -section equivalents with and without frequency-dependence of the cable parameters. For illustration, the element (1, 1) of the compound admittance matrices of the cable types (i.e., UG1 and UG3) is shown. The curves labelled with the suffix “fd” correspond to the cable models with frequency-dependent parameters.	154
A.2	Impact of the frequency-dependent parameters on the results of the HPF study. The results are compared at three nodes throughout the benchmark system. The voltages for Phase A are given in A.2a and the currents in A.2b. The results labelled with the suffix “fd” correspond to the line models with frequency-dependent parameters.	156

List of Tables

3.1	Short-Circuit Parameters of the Thévenin Equivalent for the Resource Validation	67
3.2	Harmonic Voltages of the Thévenin Equivalent (see [3]).	68
3.3	Parameters of the Grid-Forming Resource (Rated Power 40 kVA)	68
3.4	Parameters of the Grid-Following Resource (Rated Power 60 kVA)	69
3.5	Parameters of the Grid-Following Resource Including the DC Side (Rated Power 60 kVA)	69
3.6	Statistics of the applied grid disturbances for obtaining the results in Fig. 3.16 for $N = 100$ samples.	75
4.1	Acronyms used in the legends of the plots in the validation section.	93
4.2	Short-Circuit Parameters of the Thévenin Equivalent for the Benchmark Grid.	95
4.3	Sequence Parameters of the Lines in the Test System.	95
4.4	Parameters of the CIDERs and Loads in the Test System for the HPF proposed in Section 4.3.2.	96
4.5	Ratio of Sequence Voltages and Currents at the Nodes with Resources for the Spectra Obtained using the HPF Method.	96
4.6	Timing Performance (for $N = 50$ Simulations of the HPF)	98
4.7	Parameters of the CIDERs and Loads in the Test System for the HPF proposed in Section 4.3.3.	100
4.8	Maximum THD at nodes with resources for the HPF method including and excluding the DC side of CIDERs.	102
4.9	Parameters of the Network-Interfacing Converters.	105
4.10	Parameters of the Grid-Following Resources, with the constant-power (P/Q), the constant-impedance (Z), and the constant-current (I) behaviour.	107
4.11	Short-Circuit Parameters of the Thévenin Equivalent for the hybrid AC/DC Grid.	107
4.12	AC (+/ - /0) and DC Parameters of the Lines.	109
A.1	Accuracy requirements for instrument transformers for voltage measurements including harmonics [4, 5].	153

List of Abbreviations

ADC	Analog-to-Digital Converter
ADN	Active Distribution Network
CDI	Control-Design Invariant
CDV	Control-Design Variant
CIDER	Converter-Interfaced Distributed Energy Resource
FB	Feed-Back
FF	Feed-Forward
FT	Feed-Through
PID	Proportional-Integral-Derivative
PR	Proportional-Resonant
DAC	Digital-to-Analog Converter
DAE	Differential-Algebraic Equation
DFS	Double Fourier Series
DFT	Discrete Fourier Transform
DHA	Direct Harmonic Analysis
DI	Design Invariant
DP	Dynamic Phasor
EHD	Extended Harmonic Domain
EMP	Exponentially Modulated Time-Periodic
EMTP	Electromagnetic Transients Program
HA	Harmonic Analysis

List of Abbreviations

HDR	Harmonic Domain Response
HPF	Harmonic Power Flow
HSA	Harmonic Stability Assessment
HSS	Harmonic State-Space
HTF	Harmonic Transfer Function
IHA	Iterative Harmonic Analysis
KPI	Key Performance Indicator
LAP	Linear Assignment Problem
LPF	Low-Pass Filter
LTI	Linear Time-Invariant
LTP	Linear Time-Periodic
MANA	Modified Augmented Nodal Analysis
MIMO	Multi-Input Multi-Output
MNA	Modified Nodal Analysis
NE	Norton Equivalent
NIC	Network-Interfacing Converter
PLL	Phase-Locked Loop
PWM	Pulse-Width Modulator
RMS	Root-Mean-Square
SPICE	Simulation Program with Integrated Circuit Emphasis
TDS	Time-Domain Simulation
TE	Thévenin Equivalent
THD	Total Harmonic Distortion

1 Introduction

1.1 Context and Motivation

Power distribution systems are undergoing a large-scale integration of distributed energy resources, such as renewable generators, energy storage systems, and modern loads. Typically, these resources are interfaced with the grid via power electronic converters. The controllability of such *Converter-Interfaced Distributed Energy Resources* (CIDERs) is of crucial importance for power-system operation [6]. Moreover, thanks to recent advances in power-system instrumentation and state estimation (e.g., [7]), real-time situational awareness is nowadays available for power distributions systems. The deployment of such automation technology is contributing to the development of *Active Distribution Networks* (ADNs), whose power flows can be regulated, mainly by controlling the CIDERs [8]. However, the presence of large numbers of CIDERs can jeopardize the stability of the system. Therefore, it is vital to first understand the causes of instabilities, and then apply this knowledge to design robust controllers.

Recently, several standardization committees have worked on the classification, modelling, and analysis of stability issues in ADNs (e.g., [9, 10]). The instabilities observed in such systems are related to the transfer or balance of power in the grid, or interactions between the resources. Due to the prevalence of CIDERs, *converter* a.k.a *harmonic stability* is of particular importance [9]. In such systems, unstable oscillations at harmonic frequencies (e.g., [11]) may occur due to interactions between AC/DC converters and their components, as well as the collective interactions of various CIDERs through the electrical grid.

For over a century, power system analysis has concentrated on the fundamental frequency component [12]. However, power systems are inherently complex, nonlinear systems characterized by time-varying signals composed of a continuous spectrum of frequencies [13]. These characteristics, especially in power systems with a high share of CIDERs, lead to an interaction between frequencies that is utterly neglected in standard power system

analysis. More specifically, it has been shown that modern power systems reach a so-called *harmonic steady state*, as opposed to the *sinusoidal steady state* that is traditionally considered. Given the increasing complexity of modern power systems, the traditional concepts of power system stability are being reconsidered in recent research [9].

1.2 Problem Statement

A power system can be described by a system of nonlinear *Differential-Algebraic Equations* (DAEs) [14] of the following form:

$$\dot{\mathbf{x}}(t) = \mathbf{f}(t, \mathbf{x}(t), \mathbf{y}(t)) \quad (1.1)$$

$$0 = \mathbf{g}(t, \mathbf{x}(t), \mathbf{y}(t)) \quad (1.2)$$

where $\mathbf{x}(t)$ is the vector of state variables (i.e., described by differential equations), $\dot{\mathbf{x}}(t)$ is the derivative of $\mathbf{x}(t)$ w.r.t. time, and $\mathbf{y}(t)$ is the vector of algebraic variables (i.e., described by algebraic equations). The functions $\mathbf{f}(\cdot)$ and $\mathbf{g}(\cdot)$ represent the differential and algebraic equations, respectively. If the Jacobian of $\mathbf{g}(\cdot)$ w.r.t. \mathbf{y} is invertible along a solution trajectory, one can solve (1.2) for \mathbf{y} and substitute the result into (1.1), which yields an expression of the form [14]:

$$\dot{\mathbf{x}}(t) = \tilde{\mathbf{f}}(t, \mathbf{x}(t)) \quad (1.3)$$

In this case, it suffices to study the reduced system (1.3) in order to assess the stability of the original system (1.1)–(1.2).

Definition of Harmonic Stability

For the purposes of this thesis, it is necessary to establish a formal definition of harmonic stability. To this end, the power system is assumed to be described by a periodic steady state. That is, all signals are composed of a superposition of sinusoids at the fundamental frequency and its integer multiples. From the system theoretical point of view, harmonic stability can be described as the existence of a steady-state solution to the system equations in form of a harmonic spectrum. Following the derivation given in [15] for the conventional stability of power systems, the following definition of harmonic stability is proposed:

Definition 1. Consider a system represented by the a set of dynamic equations as introduced in (1.3):

$$\dot{\mathbf{x}}(t) = \tilde{\mathbf{f}}(t, \mathbf{x}(t)) \quad (1.4)$$

Such a system is harmonically stable if its steady-state behaviour is described by a periodic trajectory, i.e.:

$$\exists T \in \mathbb{R} \quad s.t. \quad \tilde{\mathbf{f}}(t + kT, \mathbf{x}(t + kT)) = \tilde{\mathbf{f}}(t, \mathbf{x}(t)), \quad |\tilde{\mathbf{f}}| < \infty, \quad k \in \mathbb{N} \quad (1.5)$$

In general, such a periodic trajectory involves multiple harmonics which may interact with each other. Therefore, in light of the above, models of power systems that accurately capture the coupling between harmonic frequencies are required. Such models are an essential foundation for methods that can perform accurate *Harmonic Analysis* (HA) of the power system.

Objectives of this Thesis

The objective of this thesis is to develop methods that are capable to accurately capture the creation and propagation of harmonics in power systems and, ultimately, for the assessment of harmonic stability as established in Def. 1. Such methods should be based on a generic and modular modelling framework, which is versatile w.r.t. power system components. The approach should enable the examination of generic power systems, expanding the scope of analysis beyond the often rather specific case studies that has characterized the field thus far.

The challenge in terms of modelling framework is to treat the nonlinearities within the power system with sufficient accuracy. In practice, the models of the individual power system components need to be suitably approximated, such that they effectively represent the harmonic coupling. Furthermore, the coupling between harmonics due to the interaction of the resources and the electrical grid needs to be taken into account. Therefore, a modelling framework that can account for the time-varying behaviour of a generic power system and its components is essential. Notably, such a modelling framework must be versatile enough to enable both the identification of the harmonic steady state as well as the assessment of the harmonic stability.

Identification of the Harmonic Steady State

In order to analyse the creation and propagation of harmonics in a power system, steady-state methods can be employed. The system is assumed to be in periodic steady state, which allows to decompose the system variables into so-called harmonic phasors by means of the Fourier analysis. More precisely, a harmonic phasor is described by:

$$\hat{\mathbf{X}} = \text{col}_{h \in \mathcal{H}}(\mathbf{X}_h) \quad (1.6)$$

where $\mathbf{X}_h \in \mathbb{C}$ is the complex Fourier coefficient of a time-periodic signal $\mathbf{x}(t)$ at the h -th harmonic of the fundamental frequency f_1 , with $h \in \mathcal{H} \subset \mathbb{Z}$.

Chapter 1. Introduction

In [12], it is proposed to separate the nonlinear elements of the system (e.g., power electronic devices) from the linear ones. In the particular case of CIDERs, nonlinearities are primarily due to their control schemes (e.g., coordinate transformations or power reference calculations) and their actuators (e.g., PWM-controlled IGBT bridges). Transforming the linear elements into the harmonic domain is straightforward. The nonlinear elements can be approximated directly in the harmonic domain providing representations that account for the coupling between harmonics of different orders. The result is a set of nonlinear equations, which can be solved iteratively using numerical methods (e.g., Newton-Raphson methods).

In Chapter 4 of this thesis, the *Harmonic Power-Flow* (HPF) study is proposed, which represents the power system as a combination of the resources (i.e., the CIDERs) on the one hand, and the electrical grid on the other. In the harmonic domain, the responses of the CIDERs are derived by approximating their nonlinear subcomponents by suitable (possibly nonlinear) functions of the harmonic phasors. Then, the response of the combination of all resources is expressed as:

$$\hat{\mathbf{Y}}_{\mathcal{Q}} = \hat{\mathbf{G}}_{\mathcal{Q}}(\hat{\mathbf{U}}_{\mathcal{Q}}) \quad (1.7)$$

where $\hat{\mathbf{U}}_{\mathcal{Q}}$ and $\hat{\mathbf{Y}}_{\mathcal{Q}}$ represent the harmonic phasors of the time-domain inputs and outputs of the resource models, respectively. By contrast, the grid behaviour is linear within the typical frequency range considered for HA, allowing it to be represented by a linear transfer function in the harmonic domain:

$$\hat{\mathbf{Y}}_{\mathcal{G}} = \hat{\mathbf{G}}_{\mathcal{G}}\hat{\mathbf{U}}_{\mathcal{G}} \quad (1.8)$$

where $\hat{\mathbf{U}}_{\mathcal{G}}$ and $\hat{\mathbf{Y}}_{\mathcal{G}}$ are the harmonic-domain representations (i.e., harmonic phasors) of the time-domain inputs and outputs of the grid, respectively. In periodic steady state - much like in sinusoidal steady state - the mismatch equations between the resources and the grid must equal zero:

$$\Delta\hat{\mathbf{Y}} = \hat{\mathbf{Y}}_{\mathcal{G}} - \hat{\mathbf{Y}}_{\mathcal{Q}} = 0 \quad (1.9)$$

This equation is fundamental to the HPF method and solved using the Newton-Raphson method.

Assessment of the Harmonic Stability

For the *Harmonic Stability Assessment* (HSA) of power systems, dynamic methods are employed. To this end, the system is represented by the original set of differential equations (recall the system description in Def. 1). In order to assess the system stability, one could try to find a Lyapunov function w.r.t. the nonlinear system equations [15]. In general, finding such a function is highly complicated. Instead, one can analyse the

small-signal stability of a system around a certain operating point via Nyquist plots or eigenvalue analysis [15].

For the HSA in Chapter 5 of this thesis, the system variables are assumed to be described by exponentially modulated time-periodic signals. Such signals are expressed as Fourier series of a time-periodic signal modulated by a complex exponential term:

$$\mathbf{x}(t) = \sum_{h \in \mathcal{H}} \mathbf{X}_h \exp((s + jh2\pi f_1)t) \quad (1.10)$$

where $s \in \mathbb{C}$ is the Laplace operator. Any nonlinear component of the resources is linearized in time domain around time-periodic operating trajectories, which results in *Linear Time-Periodic* (LTP) state-space models. Recall that the grid is an inherently linear system in the frequency range considered, and is therefore fully represented by a *Linear Time-Invariant* (LTI) state-space model. Without going into the details of the derivations, both time-domain models can be described in harmonic domain by so-called *Harmonic State-Space* (HSS) models:

$$\hat{\Sigma} : \begin{cases} (s \cdot \text{diag}(\mathbf{1}) + j\hat{\Omega}) \hat{\mathbf{X}} = \hat{\mathbf{A}}\hat{\mathbf{X}} + \hat{\mathbf{B}}\hat{\mathbf{U}} \\ \hat{\mathbf{Y}} = \hat{\mathbf{C}}\hat{\mathbf{X}} + \hat{\mathbf{D}}\hat{\mathbf{U}} \end{cases} \quad (1.11)$$

where $\hat{\Omega}$ is a diagonal matrix composed of the harmonic frequencies. The matrices in (1.11) have a Toeplitz structure, which represents the coupling between harmonic frequencies. Note the similarity of (1.11) with the Laplace transformation of an LTI system.

Through combination of the various components of the power system, the HSS models of the resources and the grid, $\hat{\Sigma}_{\mathcal{Q}}$ and $\hat{\Sigma}_{\mathcal{G}}$, respectively, are formulated. Subsequently, the closed-loop system formed by the resources and the grid is obtained, and the HSS model of the entire power system $\hat{\Sigma}_{\mathcal{P}}$ is derived from it. This model can be employed for the HSA through eigenvalue analysis of the system matrix of $\hat{\Sigma}_{\mathcal{P}}$:

$$(s \cdot \text{diag}(\mathbf{1}) + j\hat{\Omega} - \hat{\mathbf{A}}_{\mathcal{P}}) \mathbf{V} = \mathbf{0} \quad (1.12)$$

where \mathbf{V} is the matrix of eigenvectors associated to eigenvalues of $\hat{\mathbf{A}}_{\mathcal{P}}$. Note the similarity of (1.12) with the characteristic equation of the standard eigenvalue problem.

The modelling framework developed in this thesis accommodates both the HPF method and the HSA. In this respect, recall that the framework aims at representing power systems with a high share of CIDERS, particularly focusing on the precise representation of any nonlinear components. More precisely, such nonlinear components are treated in different ways for each of these two applications. For instance, while the HPF method is by design capable of handling nonlinear functions of the harmonic phasors, the HSA requires HSS models (i.e., linearized models) of all components. This differentiation

Chapter 1. Introduction

	Representation of the Resources	Representation of the Grid	Equations Describing the Method
HPF (Chapter 4)	$\hat{\mathbf{Y}}_{\mathcal{Q}} = \hat{\mathbf{G}}_{\mathcal{Q}}(\hat{\mathbf{U}}_{\mathcal{Q}})$	$\hat{\mathbf{Y}}_{\mathcal{G}} = \hat{\mathbf{G}}_{\mathcal{G}}\hat{\mathbf{U}}_{\mathcal{G}}$	$\Delta\hat{\mathbf{Y}} = \hat{\mathbf{Y}}_{\mathcal{G}} - \hat{\mathbf{Y}}_{\mathcal{Q}} = 0$ (Mismatch equations)
HSA (Chapter 5)	$\hat{\Sigma}_{\mathcal{Q}}$	$\hat{\Sigma}_{\mathcal{G}}$	$(s \cdot \text{diag}(\mathbf{1}) + j\hat{\mathbf{\Omega}} - \hat{\mathbf{A}}_{\mathcal{P}})\mathbf{V} = 0$ (Eigenvalue problem)

Figure 1.1: Overview of the methods developed in this thesis.

between the two methods is also illustrated in Fig. 1.1. In this respect, the separate treatment of the nonlinear elements in the modelling framework ensures that both HPF and HSA can effectively employ the model, each according to its requirements.

1.3 Contributions of the Thesis

The contributions of this thesis are as follows.

1. A modelling framework for the analysis of power system with a high share of CIDERS is proposed. Its modular design enables the representation of CIDERS with generic components and diverse control laws, effectively capturing their time-varying characteristics and the coupling of harmonic frequencies. The models are formulated in time domain and transformed into harmonic-domain equivalents by means of the Fourier transform and Toeplitz theory. The proposed framework is suitable for modelling both pure AC power systems and hybrid AC/DC systems. To this end, the generic CIDER model is extended to represent *Network-Interfacing Converters* (NICs). The framework is applicable for both HPF study and HSA, being a powerful foundation for the analysis of generic power systems with a large amount of CIDERS.
2. A comprehensive library of component models, which facilitates the derivation of various CIDER models, is developed. This includes a modular representation of filter and controller stages, as well as matrices accounting for changes in coordinate frames between different components of the CIDER. Based on this library, models of common types of CIDERS are derived. These models can be readily integrated into the previously introduced modelling framework. Their accuracy is validated through *Time-Domain Simulations* (TDS) in Simulink.
3. An HPF method is proposed based on the aforementioned modelling framework. The algorithm is confirmed to be accurate and efficient for the analysis of AC, as well as hybrid AC/DC power systems. More precisely, the HPF study is shown to have comparable accuracy as standard measurement devices (i.e., instrument transformers). The computational performance of the algorithm is assessed through

comparison of its execution time against the one of the TDS. Furthermore, the algorithm of the HPF method for AC power systems is shown to be more accurate than a decoupled HPF, which treats each harmonic separately.

4. A method for the HSA through eigenvalue analysis of the HSS of generic power systems is developed based on the proposed modelling framework. To this end, the HSS model of the grid is formulated using the lumped-element models of the electrical connections as well as the associated incidence matrix. The HSA is shown to be applicable to individual CIDER models as well as entire power systems. It can be used for sensitivity analysis of the location of eigenvalues w.r.t. control parameter variations. In this respect, a classification of the eigenvalues into control-design variant, control-design invariant and design invariant is proposed, which is based on the sensitivities of the eigenvalue loci w.r.t. parameter changes. Additionally, the HSA is demonstrated to be suitable for the analysis of harmonic stability as defined in Def. 1. By analysing a test system, a case of harmonic instability is identified through the system eigenvalues and validated with TDS in Simulink.

1.4 Document Outline

The remainder of this thesis is organized as follows.

Chapter 2 introduces the framework for the modelling of power system components which is both generic and modular. The underlying hypotheses for AC power systems are introduced and subsequently extended for the analysis of hybrid AC/DC power systems. The basic representation of the grid by the lumped-element models of the grid components (e.g., lines and transformers) and the associated incidence matrix is introduced. In the development of the modelling framework, special attention is given to the model of the CIDERs. The individual blocks of the CIDER are first described in time domain and then transformed to harmonic domain by means of the Fourier transform and Toeplitz theory. Particular focus is put on the reference calculation, which is identified as a possible source of nonlinearity, and therefore needs to be treated separately. A further extension of the generic CIDER model is proposed for treating nonlinearities within its internal structure. Finally, a discussion of the modelling of NICs, which interconnect the AC and DC subsystems of hybrid AC/DC power systems, is given.

Chapter 3 discusses the derivation of the CIDER models used in this thesis. A detailed library of components that are typically used in CIDERs is presented - including the filter and controller stages, transformation matrices accounting for circuit configurations and changes of reference frames. Subsequently, models of each a typical grid-forming and grid-following CIDER are derived. First, only the AC-side characteristics are considered. Subsequently, a more detailed grid-following CIDER that additionally models the DC-

Chapter 1. Introduction

side characteristics is proposed. The accuracy of all aforementioned models is validated through TDS with Simulink.

Chapter 4 derives the algorithm of the HPF study for AC and hybrid AC/DC power systems. First, the HPF problem is formulated for AC power systems using the previously introduced models of the grid and the resources, and an algorithm for its solution, which is based on a Newton-Raphson method, is proposed. Second, an extended version of the algorithm that incorporates the extended generic CIDER model (i.e., the one with nonlinearities in its internal structure) is introduced. Third, the HPF method is generalized for the analysis of hybrid AC/DC power systems. All three versions of the HPF method are thoroughly validated through TDS carried out in Simulink.

Chapter 5 provides the derivation of HSA based on eigenvalue analysis of a generic AC power system. The HSS model of the grid is derived from the differential equations of the equivalent branch and shunt elements as well as the associated incidence matrix. The HSS model of the entire power system is obtained from the closed-loop configuration of the HSS models of the grid and the resources. A detailed analysis of the eigenvalues of the proposed CIDER models is given, and followed by the analysis of the system eigenvalues. Specifically, a case of harmonic instability is identified through the eigenvalues and validated through TDS.

Finally, the thesis is concluded with a summary of the conducted research and an outlook on future work.

2 Modelling Framework for Power System Components

Summary: *This chapter describes the modelling framework which is employed in subsequent chapters of this thesis for the HPF study and the HSA of generic power systems. The power system is represented by the combination of resources (i.e., CIDERs) and the grid. The distinguishing features of the proposed modelling framework are the following: (i) it employs a representation of the power system components which is both generic and modular, and (ii) it explicitly accounts for the coupling between harmonics. The structure of the generic power system is first introduced, while distinguishing between pure AC and hybrid AC/DC power systems, and the hypotheses underlying the framework are then defined. The components of the electrical grid are represented by lumped-element models, characterised by compound electrical parameters, which allow to represent both transposed or non-transposed lines. The incidence matrix of the electrical connections is used to represent any generic configuration of an electrical grid. CIDERs are represented by LTP systems, which are modular w.r.t. the resource components (i.e., controller and filter stages as well as reference calculation) and generic w.r.t. the control laws (i.e., grid-forming or grid-following). The models of the CIDERs are formulated in time domain and transformed into harmonic-domain equivalents. The nonlinear elements of the CIDER (i.e., the reference calculation) are identified and treated separately in order to allow for a numerically efficient solution of the system equations. The reference calculation of the CIDER is represented in different ways for the derivation of the mismatch equations of the power system employed for the HPF and the HSS model of the power system employed in the HSA, respectively. Moreover, an extension to the generic CIDER model is proposed, which allows to consider nonlinear elements within the internal structure of the CIDER (e.g., due to AC/DC conversion). Finally, based on the generic model of CIDERs, a generic model of NICs is proposed for the purpose of analysing hybrid AC/DC power systems.*

Publications:

- [16] A.M. Kettner, L. Reyes-Chamorro, J.K.M. Becker, Z. Zou, M. Liserre, and M. Paolone, “Harmonic power-flow study of polyphase grids with converter-interfaced distributed energy resources—part i: Modeling framework and algorithm,” *IEEE Trans. Smart Grid*, vol. 13, no. 1, pp. 458–469, 2021.
- [17] J.K.M. Becker, A.M. Kettner, L. Reyes-Chamorro, Z. Zou, M. Liserre, and M. Paolone, “Harmonic power-flow study of polyphase grids with converter-interfaced distributed energy resources—part ii: Model library and validation,” *IEEE Trans. Smart Grid*, vol. 13, no. 1, pp. 470–481, 2021.
- [18] J.K.M. Becker, A. M. Kettner, Y. Zuo, F. Cecati, S. Pugliese, M. Liserre, and M. Paolone, “Modelling of ac/dc interactions of converter-interfaced resources for harmonic power-flow studies in microgrids,” *IEEE Trans. on Smart Grid*, vol. 14, no. 3, pp. 2096–2110, 2022.
- [19] J.K.M. Becker, Y. Zuo, M. Paolone, and A.M. Kettner, “Harmonic power-flow study of hybrid ac/dc grids with converter-interfaced distributed energy resources,” in *2023 IEEE Belgrade PowerTech*, 2023, pp. 1–6.

2.1 State of the Art

In the context of HA, a model that accurately captures the time-varying characteristics of the power system is required. The presence of harmonics and the inherent nonlinear behaviour of certain power-system components lead to a coupling between different frequencies. This phenomenon is not usually accounted for in traditional power system modelling. However, frequency coupling is important in modern power systems with high share of CIDERs. To this end, the nonlinear parts of the CIDERs (e.g., due to the actuator or the controller) need to be modelled with high fidelity.

Therefore, a critical factor to consider when categorizing power system modelling methods is whether they include the effect of frequency coupling. Fig. 2.1 illustrates of the coupling of frequencies in a model. A model that ignores frequency coupling simply translates an input of a given frequency to an output of the same frequency but potentially different magnitude and phase. In a model that does consider frequency coupling, an input at any given frequency can result in outputs across a band of frequencies - potentially the entire spectrum.

Models for HA can be classified into *time-domain*, *frequency-domain*, and *hybrid* (i.e., a combination of both) models.

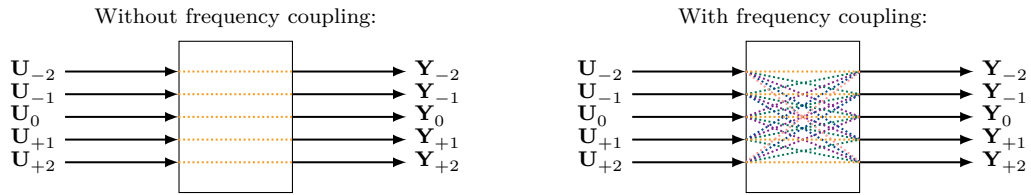


Figure 2.1: Exemplary illustration of the frequency-coupling effect of a model. In- and output signals are represented by their Fourier coefficients (i.e., for the case of a maximum harmonic order equal to two), the model behaviour w.r.t. coupling of frequencies is represented by the rectangular blocks. The positive and negative image of the signal is considered.

2.1.1 Time-Domain Models

In time domain, the grid and the connected resources (including their controllers) are described by a system of nonlinear DAEs, which is solved by numerical integration (e.g., using Runge-Kutta methods).

Electrical circuits can be studied via nodal analysis (i.e., using nodal equations given by Kirchhoff's current law) or mesh analysis (i.e., using branch equations given by Kirchhoff's voltage law) [20]. Classical nodal analysis is widely used in power-systems engineering. It relies on two fundamental hypotheses: i) all voltage and current sources are referenced w.r.t. the ground, and ii) the grid can be represented by a lumped-element model [21]. For instance, the *Electromagnetic Transient Program* (EMTP) [22] employs nodal analysis. If the circuit contains ungrounded voltage or current sources, the associated branch equations need to be considered, too. For example, the *Simulation Program with Integrated Circuit Emphasis* (SPICE) [23] utilizes this method, which is called *Modified Nodal Analysis* (MNA) [24]. Some electrical components (e.g., switches or controlled sources) cannot be described by nodal and branch equations alone, so additional equations have to be introduced. This universal approach, which is known as *Modified Augmented Nodal Analysis* (MANA), is notably implemented by the EMTP-RV [25].

Time-domain models can characterise the behaviour of many components without any further approximations, and can therefore yield extremely accurate results. In particular, the utilization of DAEs, facilitates the accurate representation of the nonlinear characteristics intrinsic to the system components, thereby allowing for a detailed representation of the frequency coupling. However, this accuracy comes at the cost of computational intensity, which hinders the analysis of large-scale power systems.

2.1.2 Frequency-Domain Models

Power system operation is often segmented into a sequence of quasi-steady states [12]. Traditionally, these steady states have been considered to be characterized solely by the

Chapter 2. Modelling Framework for Power System Components

fundamental frequency. However, in the context of HA, it is essential to consider generic periodic steady states, which include harmonic frequencies.

To decrease the computational complexity of the models, their signal content is limited to the so-called harmonic phasors. These harmonic phasors are the Fourier coefficients of the signals at the harmonic frequencies. Such a model is particularly suitable for analyses that focus on steady states.

Models without Frequency-Coupling Representation

In sinusoidal steady state, the grid and the resources (including their controllers) can be described using symmetrical components and the Park transform [26], respectively. More precisely, the resources' behaviour is transformed into a decoupled rotational reference frame, resulting in time-invariant transformed signals. This simplification allows for the model to be linearized around a constant operating point (i.e., the aforementioned time-invariant signals), transforming it into a LTI model. In principle, the LTI model can then be examined in the frequency domain to analyse the system behaviour at the harmonic frequencies. However, this model cannot capture coupling between frequencies, because it relies on linear transfer functions (recall Fig. 2.1). In both [27] and [28], the system components are described using impedance models, which are based on LTI models and are not correctly representing harmonic interactions. Furthermore, this approach is only capable of analysing symmetrical system components. Asymmetries (e.g., w.r.t. to the phase conductors) cannot be transformed into time-invariant behaviour by the Park transform.

Models with Frequency-Coupling Representation

On the other hand, a large variety of models that are capable of representing the frequency coupling effects have been proposed in the last decades.

Early works in the context of HA treat the system in harmonic steady state, which allows for the decomposition of the system variables into harmonic phasors. [12] proposes to separate the nonlinear elements of the system (e.g., power electronic devices) from the linear ones. Transforming the linear elements into the harmonic domain is straightforward. Representing the nonlinear elements requires deriving *Norton Equivalents* (NEs) within the harmonic domain. The result is a set of nonlinear equations, which can accurately represent the coupling of harmonics. These equations are then solved iteratively using numerical methods. This method of representing harmonic interactions was first proposed in [29] and has been widely adopted in subsequent studies. Works like [12, 30] and [31] further expand on this method, offering in-depth modelling of CIDERS and other power system components (e.g., transmission lines and synchronous machines) within the harmonic domain.

In the HSS approach, the LTP model of the system is derived via linearization around time-periodic trajectories. In contrast to the above approach, the system variables are represented by EMP signals as introduced in (1.10). An EMP signal is the combination of the Fourier series of a periodic signal modulated by a complex exponential (i.e., a term including both damped and oscillatory behaviour). Subsequently, the HSS model is constructed by converting the LTP model to the harmonic domain using Toeplitz theory. The result is the HSS model that effectively represents the coupling of harmonic frequencies. This approach was first introduced in [32]. The HSS approach has been a prominent research topic in the last decades, particularly in the context of modelling power systems with high share of CIDERs. Several studies have advanced the understanding of harmonic coupling within the individual CIDERs w.r.t. control interactions [33] and synchronization effects [34, 35]. Both [36] and [37] analyse grid-connected single-phase CIDERs, where the grid is approximated by a TE.

Traditionally, engineers and researchers work with models whose structure and parameters are completely known (i.e., white-box models). In this case, one can perform HA using analytical methods (e.g., [38]). However, modern power systems are so complex that both the structure and the parameters of the underlying models may only partially be known or even unknown (i.e., grey- or black-box models). Therefore, data-driven methods, which allow to cope with such lack of information, have recently gained attention. For instance, one can train an artificial neural network to learn the harmonic model of a CIDER, such as a photovoltaic generator [39] or an electric-vehicle charging station [40].

2.1.3 Hybrid Models

Hybrid models can be differentiated into two different categories. In case of the first category, the hybrid model is described partly in time domain and partly in frequency domain. In general, one can treat the strongly nonlinear resources in time domain (i.e., employing models with higher accuracy representing the coupling between frequencies in detail), and the weakly nonlinear ones in frequency domain (e.g., [41, 42]). The harmonic spectra of the strongly nonlinear elements are derived from time-domain simulations through Fourier analysis and then utilised in the frequency-domain model. These strongly nonlinear elements are usually a subset of the loads (e.g., CIDERs [41], as well as loads that include saturation effects [42]), while the network and some other loads are linear. Usually, only a handful of components are analysed in time domain in order to keep the computational intensity low.

The second category of hybrid model describes the system fully in time domain, but employs methods and concepts from the frequency domain. Although these models are formulated in time domain, they use the Fourier coefficients to separate the signals into harmonic phasors, which is why they are categorised as hybrid models in this context.

The so-called *Extended Harmonic Domain* (EHD) approach was developed to account for the dynamic behaviour of the power system [43]. In particular, the nonlinear equations are linearized around time-periodic trajectories, resulting in a small-signal LTP model. Additionally, the system variables are described by so-called dynamic harmonic phasors, whose Fourier coefficients may change over time. By applying the Toeplitz theory, the time-periodic system matrices are transformed into time-invariant equivalents in the EHD. This approach is suitable for TDS in the vicinity of the operating trajectory, while representing the coupling between frequencies. [44] validates the accuracy of EHD method for transient simulation scenarios. In a separate study, [45] investigates the phase-shifting characteristics of the EHD model of a power converter. In particular, the study reveals that a phase shift at the fundamental frequency affects only the phases of the harmonics and leaves their magnitudes unchanged.

The *Dynamic Phasor* (DP) method is another modelling technique designed for the dynamic analysis of the power system, which also addresses the effect of frequency coupling. Similar to the EHD, the DP decomposes the system variables into harmonic phasors with time-variant Fourier coefficients [46]. The nonlinear system equations can either be expressed in terms of these phasors, or - similarly to the EHD - an LTP model can be derived via small-signal analysis. The first option allows for large-signal TDS with reduced computational complexity compared to the traditional methods such as EMTP. DP models have been used for TDS of power systems, as shown in [47, 46] and [48]. In particular, [48] details the performance of a nonlinear DP model for a converter w.r.t. its computational complexity based on the number of harmonics considered in the analysis.

2.1.4 Motivation for the Proposed Modelling Framework

As discussed in detail in [9], distribution systems are particularly vulnerable to harmonic instability due to the prevalence of CIDERS. The thorough understanding of the generation and propagation of harmonics is a prerequisite for the design of controllers which are robust against harmonic instability. A suitable modelling framework that efficiently represents entire power systems including the inherent coupling between different frequencies is needed. Such a framework has to be computationally efficient and based on models that are *generic* (i.e., w.r.t. grid topology and control laws), *modular* (i.e., w.r.t. the components of resources and grid), and *accurate* (i.e., capture the creation and propagation of harmonics through the resources and the grid). In terms of computational burden, harmonic-domain methods seem to be promising as opposed to time-methods¹. As to generality and accuracy, the approaches based on LTP systems theory [43, 49]

¹Whether one uses time-domain or harmonic-domain methods for planning purposes depends on the application and its requirements. Notably, using time-domain methods one is restricted to deterministic analyses (i.e., a few known contingencies) due to the high simulation times. In contrast, harmonic-domain approaches can easily be used for stochastic analyses (e.g., Monte-Carlo simulations) due to their straight-forward parametrization and low simulation times.

2.2 Hypotheses of the Modelling Framework

appear promising. However, the existing approaches lack a certain level of modularity that would allow the analysis of generic power systems.

The goals of generality, modularity, and accuracy, are addressed by the proposed modelling framework as follows:

- *Generality*: The resources are represented by generic blocks (i.e., power hardware, control software, and reference calculation) as introduced in Section 2.4.2.
- *Modularity*: In addition, the cascaded structure of the power hardware (i.e., filter stages) and the control software (i.e., controller stages) is taken into account as depicted in Fig. 2.6.
- *Accuracy*: The framework is based on LTP systems theory (Section 2.4.1), which allows to consider the generation and propagation of harmonics (including the coupling between them).

2.2 Hypotheses of the Modelling Framework

2.2.1 Hypotheses of the AC Power System

First, a purely AC power system composed of the grid and resources is considered. The grid γ is composed of the nodes \mathcal{N} and the connections between them. Further details concerning the representation of the grid will be discussed in Section 2.3. For the nodes it is distinguished between the zero-injection nodes \mathcal{Z} and the nodes where resources are connected. The set of the latter is denoted by $\bar{\mathcal{Z}}$.

If there are zero-injection nodes in the grid, a reduction of the system state can be inferred by means of the Kron reduction [50]. As known, the Kron reduction enables to reconstruct the state of the original system from the reduced one. In this respect, in the remainder of this thesis it is assumed that a Kron reduction has been performed and thus the following relation holds:

$$\mathcal{Z} = \emptyset \implies \mathcal{N} = \bar{\mathcal{Z}} \quad (2.1)$$

Control Laws of CIDERs and Partition of the Resources

Depending on the operating mode, a CIDER is classified as either *grid-forming* or *grid-following* (e.g., [9]):

Definition 2. A grid-forming CIDER controls the magnitude and frequency of the grid voltage at its point of connection to the grid.

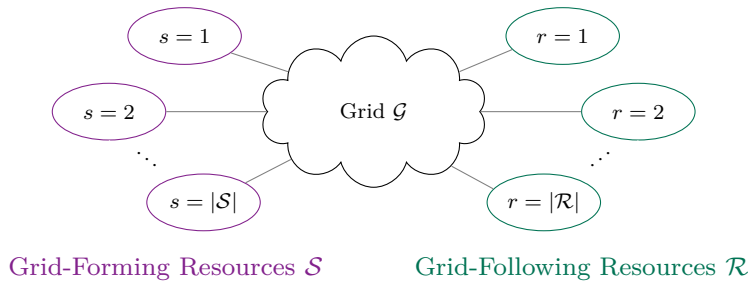


Figure 2.2: Overview of the power system structure consisting of the grid and the resources. The resources are partitioned into grid-forming \mathcal{S} and -following \mathcal{R} type.

Definition 3. A grid-following CIDER controls the injected current with a specific phase displacement w.r.t. the fundamental component of the grid voltage at its point of connection².

That is, a grid-forming CIDER behaves like a controlled voltage source with finite output impedance in series (i.e., it is possible to derive a *Thévenin Equivalent* (TE) circuit), and a grid-following CIDER like a controlled current source with a finite parallel impedance (i.e., it is possible to derive a NE circuit). As will be shown shortly, either behaviour can be represented by the so-called *grid response*, which characterizes the creation and propagation of harmonics by the respective resource. In line with these definitions, the nodes are classified depending on the behaviour of the resources which are connected to them. That is, the set of all nodes \mathcal{N} is partitioned into the disjoint sets \mathcal{S} and \mathcal{R} , where grid-forming resources $s \in \mathcal{S}$ ³ and grid-following resources $r \in \mathcal{R}$ are connected, respectively:

$$\mathcal{N} = \mathcal{S} \cup \mathcal{R}, \quad \mathcal{S} \cap \mathcal{R} = \emptyset \tag{2.2}$$

See also Fig. 2.2 for a graphical interpretation of the above.

For the sake of simplicity, it is assumed that only one resource is connected per node. Indeed, at one node multiple resources of the same type (i.e., belonging to either \mathcal{S} or \mathcal{R}) can be included in the analysis. In case of multiple grid-following resources connected to the same node, the injected currents can easily be superimposed. As to grid-forming resources, there is usually only one resource of this type per subnetwork.

2.2.2 Hypotheses of the Hybrid AC/DC Power System

The concepts outlined in Section 2.2.1 can be generalized from purely AC power systems to hybrid AC/DC power systems. Such hybrid AC/DC power systems are composed of

²This requires a grid-synchronization mechanism which provides knowledge of the fundamental-frequency phasor of the grid voltage (e.g., a *Phase-Locked Loop* (PLL)).

³Usually, in power systems there is one grid-forming node (i.e., the slack bus). However, in general the set of grid-forming resources can compromise several slack buses and/or CIDERs.

2.2 Hypotheses of the Modelling Framework

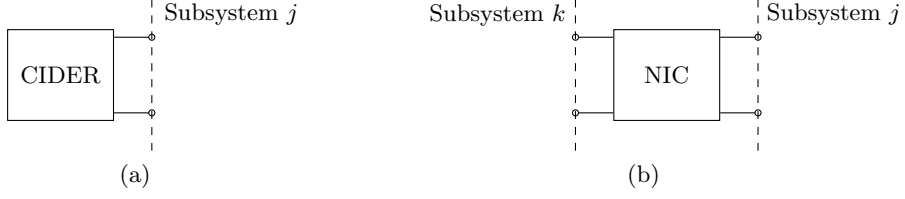


Figure 2.3: Simplified schematic of a CIDER, e.g., a single-port device (Fig. 2.3a), and a NIC, e.g., a two-port device (Fig. 2.3b).

multiple AC and DC subsystems connected with each other. The AC and DC subsystems are interconnected through NICs. Each subsystem j consists of the combination of the grid and resources, as described previously. Thus, it possesses two sets of resources:

$$\mathcal{N}^j = \mathcal{S}^j \cup \mathcal{R}^j, \quad \mathcal{S}^j \cap \mathcal{R}^j = \emptyset \quad (2.3)$$

In hybrid AC/DC power systems, which consist of multiple subsystems, devices can be of single- or two-port type. For instance, resources such as CIDERs are single-port devices, meaning they possess a single input/output terminal associated with one specific subsystem (see Fig. 2.3a). NICs in hybrid AC/DC power systems on the other hand are two-port devices, since they interconnect two different subsystems (see Fig. 2.3b). To this end, the following definition is introduced:

Definition 4. *A NIC is a device that interconnects two subsystems and, therefore, possesses one port per subsystem.*

As opposed to a CIDER, a NIC does not contain an energy source or sink. Depending on the implemented control law of the NIC, the ports exhibit either grid-forming or grid-following behaviour. More details on the internal structure of the NICs are given subsequently in Section 2.5.

Following the above reasoning, for each subsystem the sets \mathcal{R}^j and \mathcal{S}^j are further subdivided into two disjoint sets:

$$\mathcal{R}^j = \mathcal{R}_1^j \cup \mathcal{R}_2^j, \quad \mathcal{R}_1^j \cap \mathcal{R}_2^j = \emptyset \quad (2.4)$$

$$\mathcal{S}^j = \mathcal{S}_1^j \cup \mathcal{S}_2^j, \quad \mathcal{S}_1^j \cap \mathcal{S}_2^j = \emptyset \quad (2.5)$$

where \mathcal{R}_1^j and \mathcal{S}_1^j consist of all grid-forming and grid-following resources (e.g., CIDERs), respectively and \mathcal{R}_2^j and \mathcal{S}_2^j represent the nodes where the NICs are connected. The node partition of such a generic subsystem j is shown in Fig. 2.4a.

In Fig. 2.4b, the example of a hybrid AC/DC grid consisting of one AC and one DC subsystem is shown. In this example the control laws of the NICs are such that they connect \mathcal{R}_2^{AC} and \mathcal{S}_2^{DC} . Hence, the sets \mathcal{S}_2^{AC} and \mathcal{R}_2^{DC} are empty.

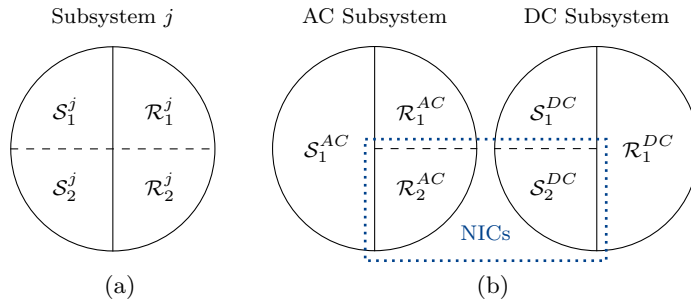


Figure 2.4: Partition of the nodes for a generic subsystem j (Fig. 2.4a) and for a hybrid AC/DC grid with NICs connecting \mathcal{R}_2^{AC} and S_2^{DC} (Fig. 2.4b).

Note that this extension of the modelling framework is generic. Meaning it can be applied to hybrid AC/DC grids with any combination and number of AC and DC subsystems.

Note further that this extension of the framework is only used for the formulation of the HPF study for hybrid AC/DC grids in Sections 4.3.4 and 4.4.3. In all other parts of this thesis, the notation introduced in the beginning of this section is employed. Namely, the nodes of a system solely consist of the two sets of grid-forming and -following nodes, and all connected resources are single-port devices.

2.3 Model of the Electrical Grid

In this section, the generic representation of the electrical grid is derived. To this end, one can derive the equivalent circuits of the branches and shunts as lumped-element models and the incidence matrix, both for three-phase grids. Note that the same theory can be applied to DC grids with minor modifications⁴.

2.3.1 Lumped-Element Model

Consider a generic three-phase grid: radial or meshed, including transposed or non-transposed lines⁵ with balanced or unbalanced nodal injections⁶ which is equipped with a neutral conductor. To this end, the following hypothesis is formulated:

⁴In the most generic of cases it can be necessary to represent power systems that are composed of combinations of three-, two- and one-phase subsystems. The theory introduced in this chapter can be applied in such cases with minor modifications.

⁵Notably, a line is *transposed* if the positions of its phase conductors are repeatedly swapped long the course of the line (i.e., a number of times that is an integer multiple of the number of phases), thus guaranteeing that its equivalent electrical parameters are circulant [51].

⁶The nodal injections or absorptions of a three-phase system are *balanced* if they consist of positive-sequence components only (i.e., the negative- and homopolar-sequence components are null) [52].

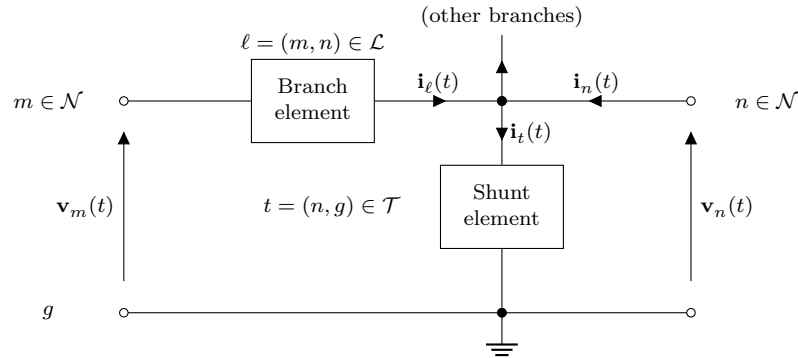


Figure 2.5: The grid is represented by branch and shunt elements. $\mathbf{i}_\ell(t)$ and $\mathbf{i}_t(t)$ are the current flows through the elements associated with the branch $\ell \in \mathcal{L}$ and shunt $t \in \mathcal{T}$, respectively. $\mathbf{v}_m(t)$ and $\mathbf{i}_n(t)$ are the phase-to-ground voltages and injected currents at node $n \in \mathcal{N}$, respectively.

Hypothesis 1. *The neutral conductor is grounded by an effective earthing system (i.e., which ensures that the neutral-to-ground voltages are negligible)[53, 54].*

Typically, effective earthing systems serve their purpose up to frequencies of a few kilohertz. Therefore, this hypothesis is reasonable in the context of HA, which typically considers harmonics up to order 20-25 (i.e., 1.0-1.5 kHz). That is, the phase-to-neutral voltages are equivalent to phase-to-ground voltages, and fully describe the grid state.

As mentioned before, the branch and shunt elements are represented by a set of lumped-element models that are linear and passive (i.e., they contain no active elements, such as voltage or current sources). Let g be the ground, which is common to all lumped elements and recall that $n \in \mathcal{N}$ is a node, which comprises the full set of phase terminals $p \in \mathcal{P} := \{\text{A, B, C}\}$. The lumped elements are divided into branch elements $\ell \in \mathcal{L} \subseteq \mathcal{N} \times \mathcal{N}$ and shunt elements $t \in \mathcal{T} = \mathcal{N} \times \{g\}$ as illustrated in Fig. 2.5.

This representation has two important advantages: i) it is valid irrespective of any asymmetries in the system w.r.t. the grid components (e.g., due to non-transposition of lines)⁷, and ii) it is valid irrespective of whether the nodal injections are balanced or unbalanced [55]. Therefore, the model is particularly suitable for power distribution systems (i.e., unlike sequence-domain equations), where such asymmetries are common.

2.3.2 Three-Phase Incidence Matrix

The grid topology is described by the *branch graph* $\mathfrak{B} := (\mathcal{N}, \mathcal{L})$. As will be shown shortly, its polyphase incidence matrix is used to obtain the model in combination with the branch and shunt parameters.

⁷The representation allows to describe the behaviour of the grid in phase coordinates rather than sequence components.

The *polyphase incidence matrix* $\mathcal{A}_{\mathcal{L}|\mathcal{N}}$ is defined as follows

$$\mathcal{A}_{\mathcal{L}|\mathcal{N}} : \left(\mathcal{A}_{\mathcal{L}|\mathcal{N}}\right)_{kn} := \begin{cases} +\text{diag}(\mathbf{1}_3) & \text{if } \ell_k = (n, \cdot) \\ -\text{diag}(\mathbf{1}_3) & \text{if } \ell_k = (\cdot, n) \\ \mathbf{0}_{3 \times 3} & \text{otherwise} \end{cases} \quad (2.6)$$

where $\text{diag}(\mathbf{1}_3)$ and $\mathbf{0}_{3 \times 3}$ are the identity and null matrix, respectively, of size 3×3 .

Note that, under the assumption that the nodes are ordered as $\mathcal{N} = [\mathcal{S}, \mathcal{R}]$, the incidence matrix can be expressed in terms of block matrices.

$$\mathcal{A}_{\mathcal{L}|\mathcal{N}} = [\mathcal{A}_{\mathcal{L}|\mathcal{S}} \mid \mathcal{A}_{\mathcal{L}|\mathcal{R}}] \quad (2.7)$$

This representation of the grid is employed both in the HPF study in Section 4.2 and the HSA in Section 5.2.2. For the HPF study, the hybrid parameters are derived directly in frequency domain based on the primitive branch and shunt admittance matrices in combination with the three-phase incidence matrix. For the HSA the LTP state-space model of the grid is derived from this generic representation employing the three-phase incidence matrix.

2.4 Generic Model of the Converter-Interfaced Distributed Energy Resources

This section introduces the generic model of the CIDERs. First, a brief summary of the theory employed in the context of time-periodic signals is given. In Section 2.4.2 the time-domain models of the individual components are given, then in Section 2.4.3 the harmonic-domain model is derived. For illustration purposes, the simplified model of the grid-forming and -following CIDERs, which considers the AC side only, is introduced first. Subsequently, it is shown how the derived generic model is extended for more sophisticated CIDER models that include nonlinearities within their internal structure.

2.4.1 Primer on Time-Periodic Signals

As discussed in Section 2.1.2, HA can be performed by means of LTP systems theory, which is a generalization of LTI systems theory [32]. Throughout this thesis, all quantities are assumed to be time-periodic and *Exponentially Modulated time-Periodic* (EMP) w.r.t. an underlying period T , which is the inverse of the fundamental frequency f_1 (i.e., $T = \frac{1}{f_1}$)⁸. Consider an exponentially modulated time-periodic vector $\mathbf{x}(t)$ and a

⁸Notably, the fundamental frequency does not need to be 50 Hz. In power systems, it is set by controllers that act on time-scales substantially longer than the controllers of the CIDERs. Thus, the fundamental frequency used for the HA can be fixed a priori in an independent analysis (i.e., using the

2.4 Generic Model of the Converter-Interfaced Distributed Energy Resources

time-periodic matrix $\mathbf{A}(t)$. As known from Fourier analysis, any time-periodic signal (i.e., real- or complex-valued) can be represented by a Fourier series as

$$\mathbf{x}(t) = \sum_{h \in \mathcal{H}} \mathbf{X}_h \exp((s + jh2\pi f_1)t) \quad (2.8)$$

$$\mathbf{A}(t) = \sum_{h \in \mathcal{H}} \mathbf{A}_h \exp(jh2\pi f_1 t) \quad (2.9)$$

where $s \in \mathbb{C}$ can be seen as the Laplace operator and $\mathbf{X}_h \in \mathbb{C}$ is the complex Fourier coefficient at the h -th harmonic of the fundamental frequency f_1 , with $h \in \mathcal{H} \subset \mathbb{Z}$ of $\mathbf{x}(t)$. Analogously, $\mathbf{A}_h \in \mathbb{C}$ is the complex Fourier coefficient at the h -th harmonic of $\mathbf{A}(t)$. In case the signal $\mathbf{x}(t)$ is real-valued, the positive and negative spectrum are complex conjugates of each other. By consequence:

$$\mathbf{X}_h = \text{conj}(\mathbf{X}_{-h}) \quad (2.10)$$

As known from Fourier analysis, the multiplication of two waveforms in time domain corresponds to the convolution of their spectra in frequency domain:

$$\mathbf{A}(t)\mathbf{x}(t) \leftrightarrow \mathbf{A}(f) * \mathbf{X}(f) = \hat{\mathbf{A}}\hat{\mathbf{X}} \quad (2.11)$$

where $\hat{\mathbf{A}}$ is the Toeplitz matrix of the Fourier coefficients \mathbf{A}_h , and $\hat{\mathbf{X}}$ the column vector of the Fourier coefficients \mathbf{X}_h [32]

$$\hat{\mathbf{A}} : \hat{\mathbf{A}}_{mk} = \mathbf{A}_h, \quad m, k \in \mathbb{N}, \quad h = m - k \in \mathcal{H} \quad (2.12)$$

$$\hat{\mathbf{X}} = \text{col}_{h \in \mathcal{H}}(\mathbf{X}_h) \quad (2.13)$$

Unless the associated signals are band-limited, such matrices and vectors are of infinite size. In practice, only the harmonics up to a certain maximum order h_{max} are considered⁹. Hence, the said Toeplitz matrices and column vectors are of finite size. It is worth noting that in a Toeplitz matrix, the diagonal elements depict the direct link between identical frequencies, while the off-diagonal elements account for the coupling between different harmonics (i.e., similar to the illustration in Fig. 2.1).

2.4.2 Time-Domain Model

Both, grid-forming and grid-following CIDERs have the same generic structure shown in Fig. 2.6: they consist of *power hardware* π and *control software* κ . The power hardware consists of an *actuator* α , for instance a full-wave or half-wave bridge, and a *filter* φ (e.g., an L, LC, LCL or higher-order filter). The filter consists of a cascade of filter stages φ_i ,

power balance equations of the system).

⁹Standards for voltage and power quality typically account for harmonics up to order 20-25 (i.e., 1.0-1.5 kHz) [3].

2.4 Generic Model of the Converter-Interfaced Distributed Energy Resources

and secondary controls). That is, they move the equilibrium by changing the setpoints, but have no impact on the harmonics (e.g., [57, 58]). Hence, the system-level controllers can be neglected for the purpose of steady-state analysis.

Observe that power hardware and control software are connected in a circular topology: one's outputs are the other's inputs. The power hardware subsystem is analog and continuous-time, whereas the control software subsystem is digital and discrete-time. These subsystems are interfaced via *Analog-to-Digital Converters* (ADCs) and *Digital-to-Analog Converters* (DACs), which are coupled with *Low-Pass Filters* (LPFs) for anti-aliasing¹¹ and anti-imaging¹², respectively.

In general, the models of the grid, power hardware and the control software can be formulated in different reference frames. This is represented by the transformations $\tau_{\kappa|\pi}$ and $\tau_{\pi|\kappa}$ in Fig. 2.6. Moreover, the electrical connections of grid and power hardware may be different (e.g., four-wire lines vs. three-leg or four-leg power converters). This is captured by the transformations $\tau_{\pi|\gamma}$ and $\tau_{\gamma|\pi}$ in Fig. 2.6.

For the purpose of HA, the system is assumed to be in periodic steady state. Hence, the following hypothesis is made:

Hypothesis 2. *There exists a steady state in which all time-variant quantities are periodic with period T . That is, the system behaviour is characterized by the fundamental frequency f_1 and the harmonic frequencies f_h of the harmonic orders $h \in \mathcal{H}$.*

The existence of a steady-state solution, as well as its location in the solution space, depend on the setpoints imposed by the system-level controllers. In the periodic state, the components of the CIDER as shown in Fig. 2.6 are described by LTP models.

Power Hardware

As previously mentioned, the power hardware is an analog continuous-time system. It is represented by the LTP model

$$\dot{\mathbf{x}}_{\pi}(t) = \mathbf{A}_{\pi}(t)\mathbf{x}_{\pi}(t) + \mathbf{B}_{\pi}(t)\mathbf{u}_{\pi}(t) + \mathbf{E}_{\pi}(t)\mathbf{w}_{\pi}(t) \quad (2.14)$$

$$\mathbf{y}_{\pi}(t) = \mathbf{C}_{\pi}(t)\mathbf{x}_{\pi}(t) + \mathbf{D}_{\pi}(t)\mathbf{u}_{\pi}(t) + \mathbf{F}_{\pi}(t)\mathbf{w}_{\pi}(t) \quad (2.15)$$

where $\mathbf{x}_{\pi}(t)$, $\mathbf{u}_{\pi}(t)$, $\mathbf{y}_{\pi}(t)$, and $\mathbf{w}_{\pi}(t)$ are the *state*, *input*, *output*, and *disturbance vector*, respectively, of the power hardware. Accordingly, $\mathbf{A}_{\pi}(t)$, $\mathbf{B}_{\pi}(t)$, $\mathbf{C}_{\pi}(t)$, $\mathbf{D}_{\pi}(t)$, $\mathbf{E}_{\pi}(t)$, and $\mathbf{F}_{\pi}(t)$ are the *system*, *input*, *output*, *feed-through*, *input disturbance*, and *output*

¹¹Aliasing is the effect of overlapping copies of the frequency spectrum, which are repeated at multiples of the sampling frequency. It occurs if the sampling frequency of the signal is not at least two times bigger than any frequency component of the signal (i.e., the Nyquist-Shannon Theorem is not satisfied).

¹²Imaging is the reverse effect. The sampled signal introduces high-frequency components in the analog signal, due to repeating spectrum copies of the digital signal at multiples of the sampling frequency.

Chapter 2. Modelling Framework for Power System Components

disturbance matrix, respectively. The sizes of these vectors and matrices depend on the reference frame in which the power hardware is modelled¹³.

This LTP description of the power hardware is generic: for instance, it allows to represent the behaviour of switching equipment (e.g., [59, 49]). If this is not required, the LTP equations may be simplified to LTI (i.e., a trivial case of periodic).

External Transform

The transformations linking the grid and the power hardware are described by

$$\tau_{\pi|\gamma} : \mathbf{w}_\pi(t) = \mathbf{T}_{\pi|\gamma}(t)\mathbf{w}_\gamma(t) \quad (2.16)$$

$$\tau_{\gamma|\pi} : \mathbf{y}_\gamma(t) = \mathbf{T}_{\gamma|\pi}^+(t)\mathbf{y}_\pi(t), [\mathbf{T}_{\gamma|\pi}^+(t)]_{1,I} = \mathbf{T}_{\gamma|\pi}(t) \quad (2.17)$$

where $\mathbf{T}_{\pi|\gamma}(t)$ and $\mathbf{T}_{\gamma|\pi}(t)$ are the associated transformation matrices. Only one column block of $\mathbf{T}_{\gamma|\pi}^+(t)$ is nonzero, since $\mathbf{y}_\gamma(t)$ includes only the block $\mathbf{y}_{\pi,I}(t)$ of $\mathbf{y}_\pi(t)$ (i.e., since the connection with the grid is at the outermost filter stage).

Control Software

The control software is a digital discrete-time system. In this respect, the following hypothesis is made:

Hypothesis 3. *The ADCs, DACs, and their LPFs (see Fig. 2.6) are designed such that an exact reconstruction of the signals is feasible in the frequency band of interest for HPF studies (i.e., in line with the Nyquist-Shannon sampling theorem).*

That is, the effects of sampling and quantization in the ADCs and reconstruction in the DACs can be neglected¹⁴. Therefore, the control software can be represented by an equivalent continuous-time model. Analogous to (2.14)–(2.15) of the power hardware, the control software is described by the LTP system

$$\dot{\mathbf{x}}_\kappa(t) = \mathbf{A}_\kappa(t)\mathbf{x}_\kappa(t) + \mathbf{B}_\kappa(t)\mathbf{u}_\kappa(t) + \mathbf{E}_\kappa(t)\mathbf{w}_\kappa(t) \quad (2.18)$$

$$\mathbf{y}_\kappa(t) = \mathbf{C}_\kappa(t)\mathbf{x}_\kappa(t) + \mathbf{D}_\kappa(t)\mathbf{u}_\kappa(t) + \mathbf{F}_\kappa(t)\mathbf{w}_\kappa(t) \quad (2.19)$$

The size of the matrices and vectors depends on the frame of reference in which the control software is modelled¹⁵.

¹³If phase coordinates are used, $\mathbf{x}_\pi, \mathbf{y}_\pi \in \mathbb{R}^{3I \times 1}$ and $\mathbf{u}_\pi \in \mathbb{R}^{3 \times 1}$. The sizes of the matrices follow from (2.14)–(2.15).

¹⁴If the sampling time of the controllers can not be chosen high enough to mitigate these effects, one needs to properly represent the corresponding blocks through their equivalent transfer functions.

¹⁵In case direct-quadrature components are used, $\mathbf{x}_\kappa, \mathbf{u}_\kappa \in \mathbb{R}^{2I \times 1}$ and $\mathbf{y}_\kappa \in \mathbb{R}^{2 \times 1}$. The sizes of the matrices follow from (2.18)–(2.19).

2.4 Generic Model of the Converter-Interfaced Distributed Energy Resources

As previously mentioned, in general, each filter stage can be coupled with a controller stage. Accordingly, each control loop i is associated with a corresponding block in $\mathbf{y}_\pi(t)$ and $\mathbf{u}_\kappa(t)$:

$$\mathbf{y}_\pi(t) = \text{col}_i(\mathbf{y}_{\pi,i}(t)) \quad (2.20)$$

$$\mathbf{u}_\kappa(t) = \text{col}_i(\mathbf{u}_{\kappa,i}(t)) \quad (2.21)$$

If some filter stages are not coupled with a controller stage, the associated blocks can simply be omitted.

Internal Transform

Recall from Fig. 2.6 that the outputs of the power hardware are connected to the inputs of the control software, and vice versa. Since the influence of the ADCs, DACs, and LPFs can be neglected according to Hyp. 3, only the transformations remain:

$$\mathbf{u}_\kappa(t) = \mathbf{T}_{\kappa|\pi}^+(t)\mathbf{y}_\pi(t), \quad \mathbf{T}_{\kappa|\pi}^+(t) = \text{diag}_i(\mathbf{T}_{\kappa|\pi}(t)) \quad (2.22)$$

$$\mathbf{u}_\pi(t) = \mathbf{T}_{\pi|\kappa}(t)\mathbf{y}_\kappa(t) \quad (2.23)$$

$$\mathbf{w}_\rho(t) = \mathbf{T}_{\kappa|\pi}(t)\mathbf{w}_\pi(t) \quad (2.24)$$

The Clarke [60] and Park [26] transform are notable examples, which are widely used. In general, the transformation matrices are rectangular. Notably, it is common to model the power hardware in phase (ABC) coordinates and the control software in *Direct-Quadrature* (DQ) components, respectively. In this case, $\mathbf{T}_{\kappa|\pi} = \mathbf{T}_{\text{DQ|ABC}} \in \mathbb{R}^{2 \times 3}$ and $\mathbf{T}_{\pi|\kappa} = \mathbf{T}_{\text{ABC|DQ}} \in \mathbb{R}^{3 \times 2}$. Usually, the reference calculation is defined in the same reference frame as the control software.

Reference Calculation

The reference calculation is described by the function $\mathbf{r}(\cdot, \cdot)$

$$\rho: \quad \mathbf{w}_\kappa(t) = \mathbf{r}(\mathbf{w}_\rho(t), \mathbf{w}_\sigma(t)) \quad (2.25)$$

It is important to note that $\mathbf{r}(\cdot, \cdot)$ need not be linear. However, for grid-following CIDERs (i.e., with PQ control), which compose the majority of resources in power grids, $\mathbf{r}(\cdot, \cdot)$ is usually nonlinear. For grid-forming CIDERs (i.e., with Vf control), which are the minority of resources (typically only one), $\mathbf{r}(\cdot, \cdot)$ is usually linear.

One can either treat this nonlinearity in harmonic domain or perform a linearization of the reference calculation already in time domain (i.e., a small-signal model). The first approach is introduced in Section 2.4.3, and then used for the derivation of the CIDER response for the HPF study in Chapter 4. The second approach is employed

Chapter 2. Modelling Framework for Power System Components

when deriving the harmonic domain state-space model of the CIDER for the HSA in Chapter 5. The derivations of the small-signal model is shown here below. To this end, assume the following:

Hypothesis 4. *The reference calculation $\mathbf{r}(\cdot, \cdot)$ is at least once differentiable w.r.t. both $\mathbf{w}_\rho(t)$ and $\mathbf{w}_\sigma(t)$ and can be represented by a small-signal model as:*

$$\begin{aligned} \mathbf{w}_\kappa(t) \approx & \bar{\mathbf{w}}_\kappa(t) + \delta_\rho \mathbf{r}(\bar{\mathbf{w}}_\rho(t), \bar{\mathbf{w}}_\sigma(t)) (\mathbf{w}_\rho(t) - \bar{\mathbf{w}}_\rho(t)) \\ & + \delta_\sigma \mathbf{r}(\bar{\mathbf{w}}_\rho(t), \bar{\mathbf{w}}_\sigma(t)) (\mathbf{w}_\sigma(t) - \bar{\mathbf{w}}_\sigma(t)) \end{aligned} \quad (2.26)$$

where $(\bar{\mathbf{w}}_\rho(t), \bar{\mathbf{w}}_\sigma(t))$ describes the operating point w.r.t. which the linearization is performed, $\bar{\mathbf{w}}_\kappa(t) = \mathbf{r}(\bar{\mathbf{w}}_\rho(t), \bar{\mathbf{w}}_\sigma(t))$ represents a shift of the origin, and

$$\delta_\rho = \frac{\delta}{\delta \mathbf{w}_\rho(t)} \quad (2.27)$$

$$\delta_\sigma = \frac{\delta}{\delta \mathbf{w}_\sigma(t)} \quad (2.28)$$

It is important to note that, as opposed to conventional linearization techniques in the context of LTI systems, the operating point $(\bar{\mathbf{w}}_\rho(t), \bar{\mathbf{w}}_\sigma(t))$ does not need to be constant, but can exhibit time-periodic behaviour.

Combining the Components

As specified in Fig. 2.6 and (2.14)–(2.15), the grid acts both as a disturbance and an output from the point of view of the power hardware. Whether the phase-to-ground voltage $\mathbf{v}(t)$ or the injected current $\mathbf{i}(t)$ at the point of connection is the disturbance or output, depends on the operating mode of the CIDER. According to Defs. 2 and 3:

$$\mathbf{w}_\gamma(t) \sim \begin{cases} \mathbf{i}(t) & \text{if CIDER is grid-forming} \\ \mathbf{v}(t) & \text{if CIDER is grid-following} \end{cases} \quad (2.29)$$

$$\mathbf{y}_\gamma(t) \sim \begin{cases} \mathbf{v}(t) & \text{if CIDER is grid-forming} \\ \mathbf{i}(t) & \text{if CIDER is grid-following} \end{cases} \quad (2.30)$$

Similarly, as specified in Fig. 2.6 and (2.18)–(2.19), the setpoint is a disturbance from the point of view of the control software. In view of Defs. 2 and 3:

$$\mathbf{w}_\sigma(t) \sim \begin{cases} V, f & \text{if CIDER is grid-forming} \\ P, Q & \text{if CIDER is grid-following} \end{cases} \quad (2.31)$$

The proposed generic state-space model is obtained by combining the models of the power hardware, the control software, the transformations, and the reference calculation. The corresponding block diagram is shown in Fig. 2.7. Note that the proposed model is fully modular thanks to the transformation linking its blocks. Therefore, each block

2.4 Generic Model of the Converter-Interfaced Distributed Energy Resources

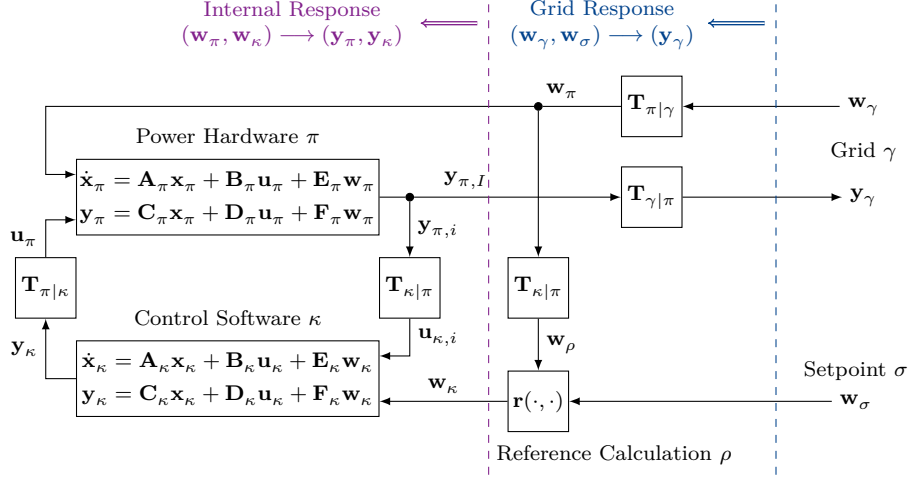


Figure 2.7: Block diagram of the proposed generic state-space model of CIDERs. Note the modularity: power hardware π , control software κ , and grid γ are represented by separate blocks, which are interfaced via coordinate transformations. The reference calculation $\mathbf{r}(\cdot, \cdot)$ may be either linear (i.e., for Vf control) or nonlinear (i.e., for PQ control). The other blocks of the model are exactly linear (i.e., LTP systems and LTP transformations).

can be modelled in a different frame of reference if desired. As previously mentioned, the grid is typically described in phase coordinates [55] or symmetrical components [52], and the control software in direct-quadrature-zero components [26] or alpha-beta-gamma components [60]. The power hardware can be described in any of these reference frames.

As shown in Fig. 2.7, the power hardware and control software form a closed-loop system via the transformation matrices $\mathbf{T}_{\pi|\kappa}(t)$ and $\mathbf{T}_{\kappa|\pi}(t)$. The internal response of the CIDER describes the behaviour of this closed-loop system:

Definition 5. *The internal response of the CIDER describes the relation from $\mathbf{w}_\pi(t)$ and $\mathbf{w}_\kappa(t)$ to $\mathbf{y}_\pi(t)$ and $\mathbf{y}_\kappa(t)$. It is derived as the closed-loop system between the power hardware, control software and the transformation matrices $\mathbf{T}_{\pi|\kappa}(t)$ and $\mathbf{T}_{\kappa|\pi}(t)$.*

The *grid response* additionally includes the reference calculation $\mathbf{r}(\cdot, \cdot)$ (i.e., grid-following or grid-forming control laws) as well as transformations $\mathbf{T}_{\kappa|\pi}(t)$ (i.e., a change of coordinates between power hardware and reference calculation) plus $\mathbf{T}_{\gamma|\pi}(t)$ and $\mathbf{T}_{\pi|\gamma}(t)$ (i.e., change of circuit configuration between grid and power hardware). Note that, as shown in Fig. 2.7, the grid-side quantities are the grid disturbance $\mathbf{w}_\gamma(t)$, the setpoint $\mathbf{w}_\sigma(t)$, and the grid output $\mathbf{y}_\gamma(t)$. Accordingly, the grid response is defined as follows.

Definition 6. *The grid response of the CIDER describes the relation from $\mathbf{w}_\gamma(t)$ and $\mathbf{w}_\sigma(t)$ to $\mathbf{y}_\gamma(t)$. It is derived through the combination of the internal response, the reference calculation $\mathbf{r}(\cdot, \cdot)$ and the grid-side transformations $\mathbf{T}_{\pi|\gamma}(t)$ and $\mathbf{T}_{\gamma|\pi}(t)$.*

2.4.3 Harmonic-Domain Model

In this section, the LTP systems and transformations from Section 2.4.2 are formulated in harmonic domain employing the theory on Toeplitz matrices introduced in Section 2.4.1. First, the models of the power hardware, control software and the internal transformation matrices are expressed in harmonic domain. Second, the internal response is derived as the closed-loop system between power hardware, control software and transformation matrices. Lastly, it is shown how the reference calculation and external transformations are represented in harmonic domain.

Open-Loop System

Consider the subsystem composed of the power hardware, control software, and the transformations that connect them (i.e., the parts related to the internal response as shown in Fig. 2.7). The time-domain state-space models (2.14)–(2.15) and (2.18)–(2.19) can be formulated in the harmonic domain.

$$\hat{\Psi}_\pi \hat{\mathbf{X}}_\pi = \hat{\mathbf{A}}_\pi \hat{\mathbf{X}}_\pi + \hat{\mathbf{B}}_\pi \hat{\mathbf{U}}_\pi + \hat{\mathbf{E}}_\pi \hat{\mathbf{W}}_\pi \quad (2.32)$$

$$\hat{\mathbf{Y}}_\pi = \hat{\mathbf{C}}_\pi \hat{\mathbf{X}}_\pi + \hat{\mathbf{D}}_\pi \hat{\mathbf{U}}_\pi + \hat{\mathbf{F}}_\pi \hat{\mathbf{W}}_\pi \quad (2.33)$$

$$\hat{\Psi}_\kappa \hat{\mathbf{X}}_\kappa = \hat{\mathbf{A}}_\kappa \hat{\mathbf{X}}_\kappa + \hat{\mathbf{B}}_\kappa \hat{\mathbf{U}}_\kappa + \hat{\mathbf{E}}_\kappa \hat{\mathbf{W}}_\kappa \quad (2.34)$$

$$\hat{\mathbf{Y}}_\kappa = \hat{\mathbf{C}}_\kappa \hat{\mathbf{X}}_\kappa + \hat{\mathbf{D}}_\kappa \hat{\mathbf{U}}_\kappa + \hat{\mathbf{F}}_\kappa \hat{\mathbf{W}}_\kappa \quad (2.35)$$

where the matrices $\hat{\Psi}_\pi$ and $\hat{\Psi}_\kappa$ are given by

$$\hat{\Psi}_\pi = s \cdot \text{diag}(\mathbf{1}_\pi) + j2\pi f_1 \text{diag}_{h \in \mathcal{H}}(h \cdot \mathbf{1}_\pi) = s \cdot \text{diag}(\mathbf{1}_\pi) + j\hat{\Omega}_\pi \quad (2.36)$$

$$\hat{\Psi}_\kappa = s \cdot \text{diag}(\mathbf{1}_\kappa) + j2\pi f_1 \text{diag}_{h \in \mathcal{H}}(h \cdot \mathbf{1}_\kappa) = s \cdot \text{diag}(\mathbf{1}_\kappa) + j\hat{\Omega}_\kappa \quad (2.37)$$

with $s \in \mathbb{C}$ analogous to the Laplace operator. Notably, this is due to the nature of the state-space variables. More precisely, as introduced in Section 2.4.1, these variables are assumed to be exponentially modulated complex signals.

The time-domain transformations (2.22)–(2.23) can analogously be formulated in the frequency domain as

$$\hat{\mathbf{U}}_\kappa = \hat{\mathbf{T}}_{\kappa|\pi}^+ \hat{\mathbf{Y}}_\pi \quad (2.38)$$

$$\hat{\mathbf{U}}_\pi = \hat{\mathbf{T}}_{\pi|\kappa} \hat{\mathbf{Y}}_\kappa \quad (2.39)$$

Equations (2.32)–(2.33) and (2.34)–(2.35) can be combined into

$$\hat{\Psi} \hat{\mathbf{X}} = \hat{\mathbf{A}} \hat{\mathbf{X}} + \hat{\mathbf{B}} \hat{\mathbf{U}} + \hat{\mathbf{E}} \hat{\mathbf{W}} \quad (2.40)$$

$$\hat{\mathbf{Y}} = \hat{\mathbf{C}} \hat{\mathbf{X}} + \hat{\mathbf{D}} \hat{\mathbf{U}} + \hat{\mathbf{F}} \hat{\mathbf{W}} \quad (2.41)$$

2.4 Generic Model of the Converter-Interfaced Distributed Energy Resources

where

$$\hat{\mathbf{X}} = \text{col}(\hat{\mathbf{X}}_\pi, \hat{\mathbf{X}}_\kappa) \quad (2.42)$$

$$\hat{\mathbf{A}} = \text{diag}(\hat{\mathbf{A}}_\pi, \hat{\mathbf{A}}_\kappa) \quad (2.43)$$

The remaining vectors (i.e., $\hat{\mathbf{Y}}$ etc.) and matrices (i.e., $\hat{\mathbf{B}}$ etc.) are defined analogously. Combining equations (2.38)–(2.39) yields

$$\hat{\mathbf{U}} = \hat{\mathbf{T}}\hat{\mathbf{Y}} \quad (2.44)$$

where

$$\hat{\mathbf{T}} = \begin{bmatrix} \mathbf{0} & \hat{\mathbf{T}}_{\pi|\kappa} \\ \hat{\mathbf{T}}_{\kappa|\pi}^+ & \mathbf{0} \end{bmatrix} \quad (2.45)$$

Internal Response (Closed-Loop System)

One can interpret (2.40)–(2.41) as the open-loop model of the subsystem composed of power hardware and control software excluding reference calculation, and (2.44) as the associated feedback control law. In order to obtain the closed-loop model, substitute (2.44) into (2.40)–(2.41) and solve for $\hat{\mathbf{X}}$ and $\hat{\mathbf{Y}}$:

$$\hat{\Psi}\hat{\mathbf{X}} = \tilde{\mathbf{A}}\hat{\mathbf{X}} + \tilde{\mathbf{E}}\hat{\mathbf{W}} \quad (2.46)$$

$$\hat{\mathbf{Y}} = \tilde{\mathbf{C}}\hat{\mathbf{X}} + \tilde{\mathbf{F}}\hat{\mathbf{W}} \quad (2.47)$$

where the matrices $\tilde{\mathbf{A}}$, $\tilde{\mathbf{C}}$, $\tilde{\mathbf{E}}$, and $\tilde{\mathbf{F}}$ are given by

$$\tilde{\mathbf{A}} = \hat{\mathbf{A}} + \hat{\mathbf{B}}(\text{diag}(\mathbf{1}) - \hat{\mathbf{T}}\hat{\mathbf{D}})^{-1}\hat{\mathbf{T}}\hat{\mathbf{C}} \quad (2.48)$$

$$\tilde{\mathbf{C}} = (\text{diag}(\mathbf{1}) - \hat{\mathbf{D}}\hat{\mathbf{T}})^{-1}\hat{\mathbf{C}} \quad (2.49)$$

$$\tilde{\mathbf{E}} = \hat{\mathbf{E}} + \hat{\mathbf{B}}(\text{diag}(\mathbf{1}) - \hat{\mathbf{T}}\hat{\mathbf{D}})^{-1}\hat{\mathbf{T}}\hat{\mathbf{F}} \quad (2.50)$$

$$\tilde{\mathbf{F}} = (\text{diag}(\mathbf{1}) - \hat{\mathbf{D}}\hat{\mathbf{T}})^{-1}\hat{\mathbf{F}} \quad (2.51)$$

and $\text{diag}(\mathbf{1})$ is an identity matrix of suitable size. Naturally, the matrices (2.48)–(2.51) can only be computed if the inverses of $\text{diag}(\mathbf{1}) - \hat{\mathbf{T}}\hat{\mathbf{D}}$ and $\text{diag}(\mathbf{1}) - \hat{\mathbf{D}}\hat{\mathbf{T}}$ exist. In this respect, the following hypothesis is made:

Hypothesis 5. *The closed-loop model (2.46)–(2.47) does exist, namely $\text{diag}(\mathbf{1}) - \hat{\mathbf{T}}\hat{\mathbf{D}}$ and $\text{diag}(\mathbf{1}) - \hat{\mathbf{D}}\hat{\mathbf{T}}$ are invertible.*

Note that, for state-space models that describe electrical circuits, it can be assumed that there are no short circuits (or bypass connection) between the individual components of the state-space model. Thus, the direct feed-through matrix \mathbf{D} between the input and output variable equals zero. For the power hardware in (2.35), it means that $\hat{\mathbf{D}}_\pi$ is zero.

Then, $\text{diag}(\mathbf{1}) - \hat{\mathbf{T}}\hat{\mathbf{D}}$ and $\text{diag}(\mathbf{1}) - \hat{\mathbf{D}}\hat{\mathbf{T}}$ simplify to

$$\text{diag}(\mathbf{1}) - \hat{\mathbf{T}}\hat{\mathbf{D}} = \begin{bmatrix} \text{diag}(\mathbf{1}_\pi) & -\hat{\mathbf{T}}_{\pi|\kappa}\hat{\mathbf{D}}_\kappa \\ \mathbf{0} & \text{diag}(\mathbf{1}_\kappa) \end{bmatrix} \quad (2.52)$$

$$\text{diag}(\mathbf{1}) - \hat{\mathbf{D}}\hat{\mathbf{T}} = \begin{bmatrix} \text{diag}(\mathbf{1}_\pi) & \mathbf{0} \\ -\hat{\mathbf{D}}_\kappa\hat{\mathbf{T}}_{\kappa|\pi} & \text{diag}(\mathbf{1}_\kappa) \end{bmatrix} \quad (2.53)$$

which are upper and lower block-triangular matrices, respectively. The inverse of upper and lower block-triangular matrices does exist if the matrices on the diagonal are square and non-singular [61]. Thus, one can deduce that the inverses of (2.52)–(2.53) do exist, and so does the closed-loop model of the CIDER.

External Transform

In order to obtain the grid response, the coordinate transformations between grid and power hardware need to be considered. From (2.16)–(2.17), one obtains:

$$\hat{\mathbf{W}}_\pi = \hat{\mathbf{T}}_{\pi|\gamma}\hat{\mathbf{W}}_\gamma \quad (2.54)$$

$$\hat{\mathbf{Y}}_\gamma = \hat{\mathbf{T}}_{\gamma|\pi}^+\hat{\mathbf{Y}}_\pi \quad (2.55)$$

Reference Calculation

In order to derive the grid response of the entire CIDER (i.e., from $\hat{\mathbf{W}}_\gamma$ to $\hat{\mathbf{Y}}_\gamma$), the reference calculation needs to be included via the term $\hat{\mathbf{W}}_\kappa$. Recall from (2.25), that the time-domain function $\mathbf{r}(\cdot, \cdot)$ is in general nonlinear. Hence, finding a corresponding relation in frequency domain may not be straightforward. However, one can assume the following:

Hypothesis 6. *There exists a differentiable function $\hat{\mathbf{R}}(\cdot, \cdot)$ that approximates $\mathbf{r}(\cdot, \cdot)$ in the harmonic domain:*

$$\hat{\mathbf{W}}_\kappa \approx \hat{\mathbf{R}}(\hat{\mathbf{W}}_\rho, \hat{\mathbf{W}}_\sigma) \quad (2.56)$$

It is worth noting that the harmonic-domain function for the reference calculation $\hat{\mathbf{R}}(\cdot, \cdot)$ can be nonlinear w.r.t. the Fourier coefficients of $\hat{\mathbf{W}}_\rho$ and $\hat{\mathbf{W}}_\sigma$. Differentiability of $\hat{\mathbf{R}}(\cdot, \cdot)$ is needed for the numerical solution of the HPF equations. More precisely, as will be explained in Section 3.2.5 and Section 4.3, the Newton-Raphson method requires the calculation of a Jacobian matrix in each iteration. Naturally, the Jacobian matrix exists only if the involved functions are differentiable.

For the derivation of the CIDER's harmonic-domain state-space model, the small-signal model of the reference calculation introduced in (2.26) needs to be transformed to harmonic domain, too. Recall that the matrices $\delta_\rho \mathbf{r}(\bar{\mathbf{w}}_\rho(t), \bar{\mathbf{w}}_\sigma(t))$ and $\delta_\sigma \mathbf{r}(\bar{\mathbf{w}}_\rho(t), \bar{\mathbf{w}}_\sigma(t))$

2.4 Generic Model of the Converter-Interfaced Distributed Energy Resources

are described by possibly nonlinear functions of the operating point and need to be approximated in the harmonic domain. To this end, the following hypothesis has to hold:

Hypothesis 7. *There exist matrices $\hat{\mathbf{R}}_\rho$ and $\hat{\mathbf{R}}_\sigma$ that approximate $\delta_\rho \mathbf{r}(\cdot, \cdot)$ and $\delta_\sigma \mathbf{r}(\cdot, \cdot)$ of (2.26) in the harmonic domain:*

$$\begin{aligned} \hat{\mathbf{W}}_\kappa \approx & \hat{\mathbf{W}}_\kappa + \hat{\mathbf{R}}_\rho(\hat{\mathbf{W}}_\rho, \hat{\mathbf{W}}_\sigma) [\hat{\mathbf{W}}_\rho - \hat{\mathbf{W}}_\rho] \\ & + \hat{\mathbf{R}}_\sigma(\hat{\mathbf{W}}_\rho, \hat{\mathbf{W}}_\sigma) [\hat{\mathbf{W}}_\sigma - \hat{\mathbf{W}}_\sigma] \end{aligned} \quad (2.57)$$

given the operating point composed of $\hat{\mathbf{W}}_\rho$ and $\hat{\mathbf{W}}_\sigma$. The Fourier coefficients of $\hat{\mathbf{W}}_\kappa$ can be computed using (2.56).

Keep in mind that the matrices $\hat{\mathbf{R}}_\rho$ and $\hat{\mathbf{R}}_\sigma$ are dependent on the operating point $\hat{\mathbf{W}}_\rho$, $\hat{\mathbf{W}}_\sigma$. For the sake of clarity, this dependency on the operating point is not explicitly stated for every instance of these matrices in the following derivations.

2.4.4 Grid Response of the CIDER in Harmonic Domain

The closed-loop model in (2.46)–(2.47) in combination with the appropriate representation of the reference calculation (i.e., (2.57) or (2.56)) and the external transformations in (2.54)–(2.55) form the grid response of the CIDER. Depending on the application (i.e., the HPF study or the HSA), the blocks will be combined to different formulations of the same model. This section aims at clarifying the differences between the two versions.

Grid Response Employed in the HPF Studies

For the HPF study, all signals (i.e., inputs and disturbances and therefore also outputs) are assumed to be in periodic steady state. As a consequence, in (2.36)–(2.37) s can be set to zero, and the closed-loop model in (2.46)–(2.47) simplifies to

$$j\hat{\Omega}\hat{\mathbf{X}} = \tilde{\mathbf{A}}\hat{\mathbf{X}} + \tilde{\mathbf{E}}\hat{\mathbf{W}} \quad (2.58)$$

$$\hat{\mathbf{Y}} = \tilde{\mathbf{C}}\hat{\mathbf{X}} + \tilde{\mathbf{F}}\hat{\mathbf{W}} \quad (2.59)$$

The grid response of the CIDER is derived as the combination of the internal response in (2.46)–(2.47) and the possibly nonlinear reference calculation in (2.56), as well as the external transformations.

To this end, solve (2.58) for $\hat{\mathbf{X}}$ and substitute the result into (2.59) in order to obtain the closed-loop transfer function from $\hat{\mathbf{W}}$ to $\hat{\mathbf{Y}}$:

$$\hat{\mathbf{Y}} = \hat{\mathbf{G}}\hat{\mathbf{W}}, \quad \hat{\mathbf{G}} = \tilde{\mathbf{C}}(j\hat{\Omega} - \tilde{\mathbf{A}})^{-1}\tilde{\mathbf{E}} + \tilde{\mathbf{F}} \quad (2.60)$$

Chapter 2. Modelling Framework for Power System Components

$\hat{\mathbf{G}}$ is the *closed-loop gain*. Note that the existence of the closed-loop model alone (i.e., Hyp. 5) does not guarantee the existence of the closed-loop gain. Indeed, in order for this to be true, the term $j\hat{\mathbf{\Omega}} - \tilde{\mathbf{A}}$ needs to be invertible. For the sake of rigour and clarity, this hypothesis is explicitly given.

Hypothesis 8. *The closed-loop transfer function (2.60) exists, i.e., the matrix $j\hat{\mathbf{\Omega}} - \tilde{\mathbf{A}}$ is assumed to be invertible.*

Recall (2.42)–(2.43) and write (2.60) in block form:

$$\begin{bmatrix} \hat{\mathbf{Y}}_{\pi} \\ \hat{\mathbf{Y}}_{\kappa} \end{bmatrix} = \begin{bmatrix} \hat{\mathbf{G}}_{\pi\pi} & \hat{\mathbf{G}}_{\pi\kappa} \\ \hat{\mathbf{G}}_{\kappa\pi} & \hat{\mathbf{G}}_{\kappa\kappa} \end{bmatrix} \begin{bmatrix} \hat{\mathbf{W}}_{\pi} \\ \hat{\mathbf{W}}_{\kappa} \end{bmatrix} \quad (2.61)$$

Recall from Hyp. 6 that the reference calculation can be approximated by a differentiable function $\hat{\mathbf{R}}(\cdot, \cdot)$. This representation of the reference calculation is restated here for the sake of clarity:

$$\hat{\mathbf{W}}_{\kappa} \approx \hat{\mathbf{R}}(\hat{\mathbf{W}}_{\rho}, \hat{\mathbf{W}}_{\sigma})$$

In line with (2.24), one finds that

$$\hat{\mathbf{W}}_{\rho} = \hat{\mathbf{T}}_{\kappa|\pi} \hat{\mathbf{W}}_{\pi} \quad (2.62)$$

Through substitution of (2.56) and (2.62) into (2.61), one obtains

$$\hat{\mathbf{Y}}_{\pi}(\hat{\mathbf{W}}_{\sigma}, \hat{\mathbf{W}}_{\pi}) = \hat{\mathbf{G}}_{\pi\pi} \hat{\mathbf{W}}_{\pi} + \hat{\mathbf{G}}_{\pi\kappa} \hat{\mathbf{R}}(\hat{\mathbf{W}}_{\sigma}, \hat{\mathbf{T}}_{\kappa|\pi} \hat{\mathbf{W}}_{\pi}) \quad (2.63)$$

In order to obtain the closed-loop transfer function w.r.t. the grid quantities $\hat{\mathbf{W}}_{\gamma}$ and $\hat{\mathbf{Y}}_{\gamma}$, the coordinate transformations between grid and power hardware need to be considered. Recall the formulation of the external transformations in harmonic domain from (2.54)–(2.55). For the sake of readability, they are restated here:

$$\begin{aligned} \hat{\mathbf{W}}_{\pi} &= \hat{\mathbf{T}}_{\pi|\gamma} \hat{\mathbf{W}}_{\gamma} \\ \hat{\mathbf{Y}}_{\gamma} &= \hat{\mathbf{T}}_{\gamma|\pi}^+ \hat{\mathbf{Y}}_{\pi} \end{aligned}$$

Combining (2.63)–(2.55) yields the desired function:

$$\hat{\mathbf{Y}}_{\gamma}(\hat{\mathbf{W}}_{\gamma}, \hat{\mathbf{W}}_{\sigma}) = \hat{\mathbf{T}}_{\gamma|\pi}^+ \hat{\mathbf{Y}}_{\pi}(\hat{\mathbf{T}}_{\pi|\gamma} \hat{\mathbf{W}}_{\gamma}, \hat{\mathbf{W}}_{\sigma}) \quad (2.64)$$

Recall from (2.29)–(2.31) that this generic function can represent a grid-forming or a grid-following CIDER (i.e., depending on which electrical quantities $\hat{\mathbf{Y}}_{\gamma}$, $\hat{\mathbf{W}}_{\gamma}$, and $\hat{\mathbf{W}}_{\sigma}$ actually represent).

Notably, this representation is purely describing the input/output relation of the CIDER response. In the rest of this thesis, it will be referred to this representation as the *Harmonic-Domain Response* (HDR). To this end, the following definition is proposed:

2.4 Generic Model of the Converter-Interfaced Distributed Energy Resources

Definition 7. The HDR of the grid response describes the relation between the grid disturbance and setpoints $\hat{\mathbf{W}}_\gamma$ and $\hat{\mathbf{W}}_\sigma$ and the grid output $\hat{\mathbf{Y}}_\gamma$ of a CIDER.

$$\hat{\mathbf{Y}}_\gamma = \hat{\mathbf{G}}(\hat{\mathbf{W}}_\gamma, \hat{\mathbf{W}}_\sigma) \quad (2.65)$$

Partial Derivatives of the Grid Response Employed in the HPF Method

As will be shown shortly, the partial derivative of $\hat{\mathbf{Y}}_\gamma$ w.r.t. $\hat{\mathbf{W}}_\gamma$ is needed for the numerical solution of the HPF problem. Note that $\hat{\mathbf{Y}}_\pi(\cdot, \cdot)$ in (2.64) and $\hat{\mathbf{R}}(\cdot, \cdot)$ in (2.63) are differentiable (the former is a linear function, the latter due to Hyp. 6). Hence, the chain rule can be applied, which yields

$$\partial_\gamma \hat{\mathbf{Y}}_\gamma(\hat{\mathbf{W}}_\gamma, \hat{\mathbf{W}}_\sigma) = \hat{\mathbf{T}}_{\gamma|\pi}^+ \partial_\pi \hat{\mathbf{Y}}_\pi(\hat{\mathbf{T}}_{\pi|\gamma} \hat{\mathbf{W}}_\gamma, \hat{\mathbf{W}}_\sigma) \hat{\mathbf{T}}_{\pi|\gamma} \quad (2.66)$$

$$\partial_\pi \hat{\mathbf{Y}}_\pi(\hat{\mathbf{W}}_\pi, \hat{\mathbf{W}}_\sigma) = \hat{\mathbf{G}}_{\pi\pi} + \hat{\mathbf{G}}_{\pi\kappa} \partial_\rho \hat{\mathbf{R}}(\hat{\mathbf{T}}_{\kappa|\pi} \hat{\mathbf{W}}_\pi, \hat{\mathbf{W}}_\sigma) \hat{\mathbf{T}}_{\kappa|\pi} \quad (2.67)$$

where ∂_γ , ∂_π , and ∂_ρ denote the partial derivatives w.r.t. $\hat{\mathbf{W}}_\gamma$, $\hat{\mathbf{W}}_\pi$, and $\hat{\mathbf{W}}_\rho$, respectively:

$$\partial_\gamma = \frac{\partial}{\partial \hat{\mathbf{W}}_\gamma}, \quad \partial_\pi = \frac{\partial}{\partial \hat{\mathbf{W}}_\pi}, \quad \partial_\rho = \frac{\partial}{\partial \hat{\mathbf{W}}_\rho} \quad (2.68)$$

Grid Response Employed in the HSA

For the HSA, the grid response of the CIDER is derived as the combination of the closed-loop model in (2.46)–(2.47) and the small-signal representation of the reference calculation in (2.57). In this way, the HSS model is capable of capturing also internal characteristics related to the states of the CIDERs.

To this end, recall the state-space model describing the internal response of the CIDER in (2.46)–(2.47). Keep in mind that the state, disturbance and output vectors are defined as the column vectors of the respective quantities from the power hardware and the control software. In line with these definitions, the model can be rewritten as follows:

$$\hat{\Psi} \hat{\mathbf{X}} = \tilde{\mathbf{A}} \hat{\mathbf{X}} + \tilde{\mathbf{E}}_\pi \hat{\mathbf{W}}_\pi + \tilde{\mathbf{E}}_\kappa \hat{\mathbf{W}}_\kappa \quad (2.69)$$

$$\hat{\mathbf{Y}} = \tilde{\mathbf{C}} \hat{\mathbf{X}} + \tilde{\mathbf{F}}_\pi \hat{\mathbf{W}}_\pi + \tilde{\mathbf{F}}_\kappa \hat{\mathbf{W}}_\kappa \quad (2.70)$$

where $\tilde{\mathbf{E}}_\pi$ and $\tilde{\mathbf{E}}_\kappa$ represent the columns of $\tilde{\mathbf{E}}$ associated with $\hat{\mathbf{W}}_\pi$ and $\hat{\mathbf{W}}_\kappa$, respectively, and $\tilde{\mathbf{F}}_\pi$ and $\tilde{\mathbf{F}}_\kappa$ are defined analogously.

Furthermore, recall the small-signal model of the reference calculation from (2.57) and rewrite it as:

$$\hat{\mathbf{W}}_\kappa = \hat{\mathbf{R}}_o \hat{\mathbf{W}}_o + \hat{\mathbf{R}}_\rho \hat{\mathbf{T}}_{\kappa|\pi} \hat{\mathbf{W}}_\pi + \hat{\mathbf{R}}_\sigma \hat{\mathbf{W}}_\sigma \quad (2.71)$$

where

$$\hat{\mathbf{R}}_o = \begin{bmatrix} \text{diag}(\mathbf{1}) & -\hat{\mathbf{R}}_\rho \hat{\mathbf{T}}_{\kappa|\pi} & -\hat{\mathbf{R}}_\sigma \end{bmatrix} \quad (2.72)$$

$$\hat{\mathbf{W}}_o = \text{col}(\hat{\mathbf{W}}_\kappa, \hat{\mathbf{W}}_\pi, \hat{\mathbf{W}}_\sigma) \quad (2.73)$$

where $\text{diag}(\mathbf{1})$ is an identity matrix of suitable size. As stated in Section 2.4.3, the coefficient matrices $\hat{\mathbf{R}}_o$, $\hat{\mathbf{R}}_\rho$ and $\hat{\mathbf{R}}_\sigma$ depend on the operating point $\hat{\mathbf{W}}_o$. For the sake of clarity, this dependency is not restated for every instance of these matrices in the subsequent derivations.

Finally, recall the external transformations in harmonic domain from (2.54)–(2.55). From this, one can extract the grid output $\hat{\mathbf{Y}}_\gamma$ from $\hat{\mathbf{Y}}$ as follows:

$$\hat{\mathbf{Y}}_\gamma = \hat{\mathbf{T}}_{\gamma|\pi}^+ \begin{bmatrix} \text{diag}(\mathbf{1}_\pi) & \mathbf{0}_\kappa \end{bmatrix} \hat{\mathbf{Y}} \quad (2.74)$$

where $\text{diag}(\mathbf{1}_\pi)$ is the identity matrix and $\mathbf{0}_\kappa$ the zero matrix whose sizes are compatible with $\hat{\mathbf{Y}}_\pi$ and $\hat{\mathbf{Y}}_\kappa$, respectively.

Combining (2.69)–(2.70) with (2.71) and adding the external transformations, leads to a state-space model describing the grid response of the CIDER.

Definition 8. *The HSS model describes the relation of the disturbances $\hat{\mathbf{W}}_\gamma$ and $\hat{\mathbf{W}}_\sigma$ w.r.t. the grid output $\hat{\mathbf{Y}}_\gamma$ with the equations:*

$$\hat{\Psi} \hat{\mathbf{X}} = \tilde{\mathbf{A}} \hat{\mathbf{X}} + \hat{\mathbf{E}}_\gamma \hat{\mathbf{W}}_\gamma + \hat{\mathbf{E}}_\sigma \hat{\mathbf{W}}_\sigma + \hat{\mathbf{E}}_o \hat{\mathbf{W}}_o \quad (2.75)$$

$$\hat{\mathbf{Y}}_\gamma = \hat{\mathbf{C}}_\gamma \hat{\mathbf{X}} + \hat{\mathbf{F}}_\gamma \hat{\mathbf{W}}_\gamma + \hat{\mathbf{F}}_\sigma \hat{\mathbf{W}}_\sigma + \hat{\mathbf{F}}_o \hat{\mathbf{W}}_o \quad (2.76)$$

with coefficient matrices

$$\hat{\mathbf{E}}_\gamma = \tilde{\mathbf{E}}_\pi \hat{\mathbf{T}}_{\pi|\gamma} + \tilde{\mathbf{E}}_\kappa \hat{\mathbf{R}}_\rho \hat{\mathbf{T}}_{\kappa|\pi} \hat{\mathbf{T}}_{\pi|\gamma} \quad (2.77)$$

$$\hat{\mathbf{E}}_\sigma = \tilde{\mathbf{E}}_\kappa \hat{\mathbf{R}}_\sigma \quad (2.78)$$

$$\hat{\mathbf{E}}_o = \tilde{\mathbf{E}}_\kappa \hat{\mathbf{R}}_o \quad (2.79)$$

$$\hat{\mathbf{F}}_\gamma = \hat{\mathbf{T}}_{\gamma|\pi}^+ \begin{bmatrix} \text{diag}(\mathbf{1}_\pi) & \mathbf{0}_\kappa \end{bmatrix} \left(\tilde{\mathbf{F}}_\pi \hat{\mathbf{T}}_{\pi|\gamma} + \tilde{\mathbf{F}}_\kappa \hat{\mathbf{R}}_\rho \hat{\mathbf{T}}_{\kappa|\pi} \hat{\mathbf{T}}_{\pi|\gamma} \right) \quad (2.80)$$

$$\hat{\mathbf{F}}_\sigma = \hat{\mathbf{T}}_{\gamma|\pi}^+ \begin{bmatrix} \text{diag}(\mathbf{1}_\pi) & \mathbf{0}_\kappa \end{bmatrix} \tilde{\mathbf{F}}_\kappa \hat{\mathbf{R}}_\sigma \quad (2.81)$$

$$\hat{\mathbf{F}}_o = \hat{\mathbf{T}}_{\gamma|\pi}^+ \begin{bmatrix} \text{diag}(\mathbf{1}_\pi) & \mathbf{0}_\kappa \end{bmatrix} \tilde{\mathbf{F}}_\kappa \hat{\mathbf{R}}_o \quad (2.82)$$

$$\hat{\mathbf{C}}_\gamma = \hat{\mathbf{T}}_{\gamma|\pi}^+ \begin{bmatrix} \text{diag}(\mathbf{1}_\pi) & \mathbf{0}_\kappa \end{bmatrix} \tilde{\mathbf{C}} \quad (2.83)$$

Recall that the matrices describing the small-signal model of the reference calculation are functions of the operating point $\hat{\mathbf{W}}_o$. By consequence, the aforesated matrices of the HSS model dependent on this operating point, too.

2.4 Generic Model of the Converter-Interfaced Distributed Energy Resources

The grid response of such a HSS model is described by the *Harmonic Transfer Function* (HTF) w.r.t. the disturbances.

$$\hat{\mathbf{Y}}_\gamma = \hat{\mathbf{G}}_\gamma(\hat{\mathbf{W}}_o)\hat{\mathbf{W}}_\gamma + \hat{\mathbf{G}}_\sigma(\hat{\mathbf{W}}_o)\hat{\mathbf{W}}_\sigma + \hat{\mathbf{G}}_o(\hat{\mathbf{W}}_o)\hat{\mathbf{W}}_o \quad (2.84)$$

where

$$\hat{\mathbf{G}}_\gamma(\hat{\mathbf{W}}_o) = \hat{\mathbf{C}}_\gamma(\hat{\Psi} - \tilde{\mathbf{A}})^{-1}\hat{\mathbf{E}}_\gamma(\hat{\mathbf{W}}_o) + \hat{\mathbf{F}}_\gamma(\hat{\mathbf{W}}_o) \quad (2.85)$$

$$\hat{\mathbf{G}}_\sigma(\hat{\mathbf{W}}_o) = \hat{\mathbf{C}}_\sigma(\hat{\Psi} - \tilde{\mathbf{A}})^{-1}\hat{\mathbf{E}}_\sigma(\hat{\mathbf{W}}_o) + \hat{\mathbf{F}}_\sigma(\hat{\mathbf{W}}_o) \quad (2.86)$$

$$\hat{\mathbf{G}}_o(\hat{\mathbf{W}}_o) = \hat{\mathbf{C}}_o(\hat{\Psi} - \tilde{\mathbf{A}})^{-1}\hat{\mathbf{E}}_o(\hat{\mathbf{W}}_o) + \hat{\mathbf{F}}_o(\hat{\mathbf{W}}_o) \quad (2.87)$$

Observe that the dependence of the gain matrices $\hat{\mathbf{G}}_\gamma$, $\hat{\mathbf{G}}_\sigma$ and $\hat{\mathbf{G}}_o$ on the operation point $\hat{\mathbf{W}}_o$ is explicitly stated in the above equation.

2.4.5 Extension of the Modelling Framework for Treating Nonlinearities within the Internal Response of a CIDER

The generic CIDER model introduced in Fig. 2.6 covers only the AC-side components. That is, the AC/DC converter and DC side are represented by a controlled AC voltage source. Since the parts of the model related to the internal response are all linear, they can be represented by LTP models without further approximations.

If other parts of the CIDER shall be analysed in detail, possibly nonlinear components need to be included into the CIDER model. Due to these nonlinearities, it is in general not possible to find an explicit analytical solution for the internal response, because the equations describing the closed-loop system cannot be solved analytically. However, one can locally approximate the internal response through linearization w.r.t. the operating point and apply the same methodology as before. To this end, the LTP models of the power hardware and control software are linearized in time domain around a time-periodic operating point. Thus, the operating point needs to be explicitly considered as a variable in the linearized version of the open-loop model (2.40)–(2.41).

Suppose that the nonlinearity is located in the power hardware and can be linearized around the time-periodic operating point $\mathbf{y}_{o,\pi}(t)$. Then, one obtains a model that is analogous to (2.14)–(2.15), in which $\mathbf{y}_{o,\pi}(t)$ appears as an additional variable:

$$\mathbf{A}_\pi : \mathbf{A}_\pi(t, \mathbf{y}_{o,\pi}(t)) \quad (2.88)$$

and \mathbf{B}_π etc. analogous. In order to facilitate the formulation of the CIDER model, a decomposition of the matrices w.r.t. to the dependency on the operating point is proposed. However, it is not generally guaranteed that such a separation can be achieved. Therefore, the following hypothesis is formulated:

Hypothesis 9. *The matrices of the extended CIDER model can be separated into a term $\tilde{\mathbf{A}}_\pi$ which is invariant w.r.t. the operating point, and another term $\bar{\mathbf{A}}_\pi$ which is a function of it:*

$$\mathbf{A}_\pi(t, \mathbf{y}_{o,\pi}(t)) = \tilde{\mathbf{A}}_\pi(t) + \bar{\mathbf{A}}_\pi(t, \mathbf{y}_{o,\pi}(t)) \quad (2.89)$$

and \mathbf{B}_π etc. analogous.

By consequence, in case the operating point changes, only the second term needs to be recalculated.

The same methodology can be employed in case nonlinearities exist in the control software. Therefore, the operating point that needs to be considered for the generic CIDER model is given by $\mathbf{y}_o(t) = \text{col}(\mathbf{y}_{o,\pi}(t), \mathbf{y}_{o,\kappa}(t))$.

Based on the linearized open-loop CIDER model in time domain, one can derive the open- and closed-loop model both in frequency domain. In doing so, keep in mind that the associated matrices in time and frequency domain are functions of $\mathbf{y}_o(t)$ and $\hat{\mathbf{Y}}_o$, respectively. The closed-loop model which characterizes the internal response is of the form (cf. (2.46)–(2.47))

$$\hat{\Psi}\hat{\mathbf{X}} = \tilde{\mathbf{A}}(\hat{\mathbf{Y}}_o)\hat{\mathbf{X}} + \tilde{\mathbf{E}}(\hat{\mathbf{Y}}_o)\hat{\mathbf{W}} \quad (2.90)$$

$$\hat{\mathbf{Y}} = \tilde{\mathbf{C}}(\hat{\mathbf{Y}}_o)\hat{\mathbf{X}} + \tilde{\mathbf{F}}(\hat{\mathbf{Y}}_o)\hat{\mathbf{W}} \quad (2.91)$$

Without loss of generality, it is assumed that this operating point is a subset of the output vector of the internal response (i.e., which includes the states that are typically associated with the operating point):

$$\mathbf{y}_o(t) \subset \mathbf{y}(t) \quad (2.92)$$

Note that, when defining the open-loop model of the CIDER, any block of the vectors \mathbf{x} , \mathbf{u} , and \mathbf{w} can be included in the output equation if needed. Accordingly, there exists a matrix \mathbf{T}_o such that the operating point is derived as

$$\mathbf{y}_o(t) = \mathbf{T}_o\mathbf{y}(t) \quad (2.93)$$

Respectively, in the harmonic domain

$$\hat{\mathbf{Y}}_o = \hat{\mathbf{T}}_o\hat{\mathbf{Y}} \quad (2.94)$$

These derivations will be used in Section 4.3.3 in the formulation of the Newton-Raphson method for solving the HPF problem and in Section 5.2.1 when deriving the system state-space model for the HSA.

2.5 Generic Model of the Network-Interfacing Converters

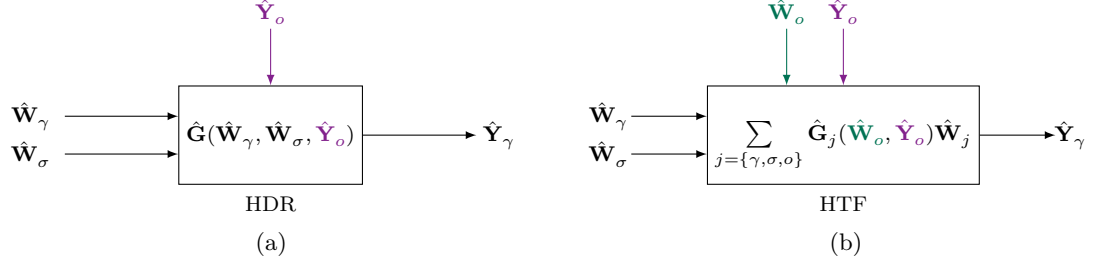


Figure 2.8: Overview of the difference between the HDR (Fig. 2.8a) and HTF (Fig. 2.8b) representation of a CIDER with emphasis on the two different operating points.

Impact of the Extension on the Grid Response

In case of the HDR, the extension of the modelling framework by the operating associated to the linearization of the internal response results in an additional argument:

$$\hat{\mathbf{Y}}_\gamma = \hat{\mathbf{G}}(\hat{\mathbf{W}}_\gamma, \hat{\mathbf{W}}_\sigma, \hat{\mathbf{Y}}_o) \quad (2.95)$$

The update of the HSS model for the extension of the modelling framework follows straightforward from the dependency of the matrices of the power hardware and control software on the operating point. Then, the HTF of the grid response, is given as:

$$\hat{\mathbf{Y}}_\gamma = \hat{\mathbf{G}}_\gamma(\hat{\mathbf{Y}}_o, \hat{\mathbf{W}}_o) \hat{\mathbf{W}}_\gamma + \hat{\mathbf{G}}_\sigma(\hat{\mathbf{Y}}_o, \hat{\mathbf{W}}_o) \hat{\mathbf{W}}_\sigma + \hat{\mathbf{G}}_o(\hat{\mathbf{Y}}_o, \hat{\mathbf{W}}_o) \hat{\mathbf{W}}_o \quad (2.96)$$

Recall that $\hat{\mathbf{W}}_o$ is the operating point that was used for the linearization of the reference calculation. Fig. 2.8 gives an illustration of the difference between HDR and HTF, as well as the different operating points.

2.5 Generic Model of the Network-Interfacing Converters

As mentioned in Section 2.2.2, the NICs are two-port devices interconnecting the AC and DC subsystems of a power system. Fundamentally, the structure of a NIC is similar to the one of a CIDER: i.e., it consists of power hardware and control software. However, as opposed to a CIDER, a NIC has two interfaces rather than one between AC and DC (i.e., due to the two-port nature of NICs). Hence, as compared to a CIDER, an additional pair of the grid disturbance and output needs to be considered. Except from that, the generic model of the NIC can be derived analogously to the procedure proposed in Section 2.4.

3 Derivation of the Specific Models of the CIDERs

Summary: *In this chapter, the applicability of the proposed modelling framework to common types of grid-forming and grid-following CIDERs is presented. More precisely, a library of component models that constitutes typical elements of the CIDERs is proposed. The representation of the PWM actuator, filter and controller stages, as well as circuit configurations and transformation matrices between different reference frames are introduced. The methods used to approximate the nonlinear PQ law, which is used as reference calculation, is discussed in detail. To this end, two distinct representations of the reference calculation, which are used for the HDR and for the HSS, respectively, are derived. Subsequently, the assembly of the specific CIDER models from the aforementioned components is detailed. More precisely, the models of grid-forming and grid-following CIDERs considering only the AC-side components, as well as a grid-following CIDER including the modelling of the DC-side components, are introduced. Incorporating the DC side and the AC/DC converter into the model introduces nonlinearities that can be represented by the extended CIDER model introduced in the previous chapter. For each specific CIDER model, the HDR and HSS model are derived and validated through TDS within Simulink. In this respect, Key Performance Indicators (KPIs) are introduced to assess the accuracy of the obtained spectra w.r.t. magnitude and phase discrepancies. First, the accuracy of the HDR at the operating point is assessed. Furthermore, the accuracy of the HDR for different approximations in the reference calculation is assessed for the grid-following CIDER. Finally, an evaluation of both representations (i.e., HDR and HSS) for deviations from the operating point is performed.*

Publications:

- [16] A.M. Kettner, L. Reyes-Chamorro, J.K.M. Becker, Z. Zou, M. Liserre, and M. Paolone, “Harmonic power-flow study of polyphase grids with converter-interfaced distributed energy resources—part i: Modeling framework and algorithm,” *IEEE Trans. Smart Grid*, vol. 13, no. 1, pp. 458–469, 2021.
- [17] J.K.M. Becker, A.M. Kettner, L. Reyes-Chamorro, Z. Zou, M. Liserre, and M. Paolone, “Harmonic power-flow study of polyphase grids with converter-interfaced distributed energy resources—part ii: Model library and validation,” *IEEE Trans. Smart Grid*, vol. 13, no. 1, pp. 470–481, 2021.
- [18] J.K.M. Becker, A. M. Kettner, Y. Zuo, F. Cecati, S. Pugliese, M. Liserre, and M. Paolone, “Modelling of ac/dc interactions of converter-interfaced resources for harmonic power-flow studies in microgrids,” *IEEE Trans. on Smart Grid*, vol. 14, no. 3, pp. 2096–2110, 2022.
- [19] J.K.M. Becker, Y. Zuo, M. Paolone, and A.M. Kettner, “Harmonic power-flow study of hybrid ac/dc grids with converter-interfaced distributed energy resources,” in *2023 IEEE Belgrade PowerTech*, 2023, pp. 1–6.

3.1 State of the Art

3.1.1 Representation of the DC Side of a CIDER

When it comes to the modelling of CIDERs a compromise between modelling depth (i.e., model accuracy compared to the real world) and computational complexity (i.e., execution speed and scalability of the model) has to be found. In the recent past, the modelling of CIDERs for frequency ranges beyond the power-system fundamental frequency component has been a prominent research topic [12, 62, 63]. To this end, different levels of abstraction can be applied w.r.t. the power hardware model [64]. In reality, CIDERs include both AC components (e.g., the filter stages) as well as DC components (e.g., the physical source or load). While the AC side is usually considered in full detail, different levels of abstraction can be applied to model the DC side.

The DC side is typically composed of the following components (see Fig. 3.1a): a DC source, a DC/DC converter (e.g., a boost converter), a DC-link capacitor connected to the AC/DC converter (e.g., [65, 66, 6]). However, this detailed model is unnecessarily complex for many studies. For most purposes, the dynamics of the DC source and the DC/DC converter can be neglected. In this case, as shown in Fig. 3.1b, the elements are approximated by a current source, which emulates their aggregated behaviour (e.g., active power-point tracking). This representation is commonly used for HA of CIDERs [67, 68]. If the DC-link capacitor is sufficiently large (i.e., the DC-link ripples are negligible), the

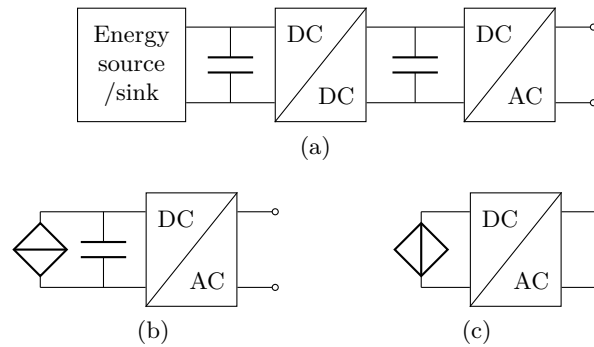


Figure 3.1: Different levels of approximations of the power hardware of a CIDER. Detailed representation Fig. 3.1a, the current-source representation Fig. 3.1b and the voltage-source representation Fig. 3.1c.

model can be simplified further. Namely, the entire DC side can be represented by a DC voltage source connected directly to the AC/DC converter (see Fig. 3.1c). This simple yet often effective model is frequently used for impedance modelling and stability analysis of CIDERs [69, 70] and power grids [71].

3.1.2 Representation of the Actuator

When modelling the PWM actuator of a CIDER, one can either consider or neglect the effects of the converter's switching. While switching frequencies are usually high for CIDERs in low-voltage distributions grids (i.e., as compared to the frequencies of interest for HA), they might be lower for medium-voltage applications in order to limit switching losses for higher power ratings. That is, for the modelling of CIDERs in low-voltage distribution grids, the effects of switching on the creation and propagation of harmonics can be neglected. For medium-voltage applications on the other hand, one might have to consider the switching as a possible source of harmonics (i.e., if the highest harmonic frequency considered is larger than half the switching frequency), which has to be reflected in the corresponding model.

Notably, the proposed modelling framework is sufficiently generic and modular to represent both cases. More precisely, the corresponding models would have to be developed using Toeplitz and Fourier theory. If the switching needs to be considered in the HA, a *Double Fourier Series* (DFS) results from the convolution of the spectra of the switching signals and the electrical quantities [72]. The calculation of the DFS involves Bessel functions, whose evaluation is non-trivial. In the recent literature, it has been proposed to use look-up tables in combination with HSS modelling for this purpose [73]. However, this approach incurs significant computational burden and compromises the scalability of the model. If the high-frequency contributions of the switching action (i.e., beyond the frequency range considered for the HA) can be neglected, average models are sufficient to represent the AC/DC converters [74, 75].

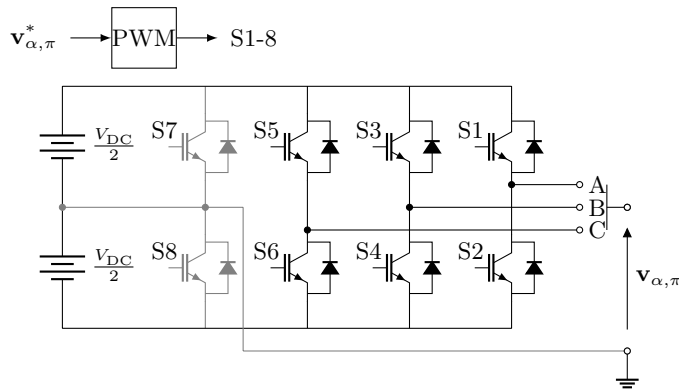


Figure 3.2: Schematic diagram of a three-phase two-level power converter, which is commonly used for CIDERs. The fourth leg is optional: it is required only if the power converter has to be able to inject or absorb homopolar currents.

3.2 Library of Component Models

In this section, the models of actuators, filters, and controllers are described. Note that, in order to obtain compact formulas, the time-dependency of the electrical quantities and signals is not explicitly stated each time.

3.2.1 PWM Actuator

The actuator is the power converter that interfaces the DC side of the CIDER (i.e., a source or load) with its AC side (i.e., the filter). It consists of an array of switches (i.e., power-transistor-type devices), which are controlled so that the output voltage of the actuator \mathbf{v}_α follows the reference \mathbf{v}_α^* (see Fig. 3.2). The switching signals are typically generated by a PWM. This modulation creates distortions in the output voltage of the power converter. Indeed, this is the reason why a filter is needed. In low-voltage distribution systems, these distortions occur at high frequencies (i.e., several kHz), which are far beyond the frequency range that is of interest for HA (i.e., up to 1-2 kHz) [3].

Assuming that the switching frequency of the PWM generator is high enough, these high-frequency components do not need to be considered [74]. Thus, the actuator can be represented by an *average model* [75].

Hypothesis 10. *In the frequency range of interest for the HPF study, the switching losses and high-frequency components due to the converter switching are negligible. Therefore, the converter can be represented by an average model based on the instantaneous power balance equation between the DC-side power P_δ and the AC-side power P_α .*

$$P_\delta(t) = P_\alpha(t) \quad (3.1)$$

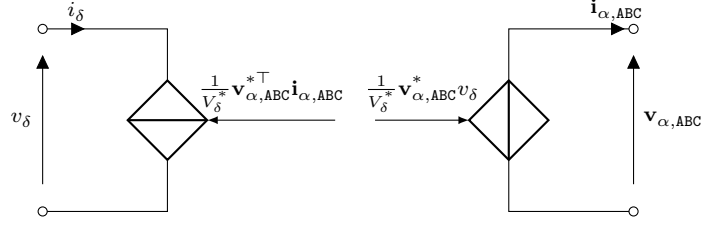


Figure 3.3: Representation of the actuator by an average model, consisting of a controlled current source on the DC side and a controlled voltage source on the AC side.

The average model consists of a controlled current source on the DC side and a controlled voltage source on the AC side [75] (see Fig. 3.3). The AC-side voltage is derived from the AC-side reference voltage $\mathbf{v}_{\alpha,ABC}^*$ and the DC-side voltage v_δ through:

$$\mathbf{v}_{\alpha,ABC}(t) = \frac{1}{V_\delta^*} \mathbf{v}_{\alpha,ABC}^*(t) v_\delta(t) \quad (3.2)$$

The DC-side current i_δ is derived from $\mathbf{v}_{\alpha,ABC}^*$ and the AC-side actuator current $\mathbf{i}_{\alpha,ABC}$:

$$i_\delta(t) = \frac{1}{V_\delta^*} \sum_{j=ABC} v_{\alpha,j}^*(t) i_{\alpha,j}(t) = \frac{1}{V_\delta^*} \mathbf{v}_{\alpha,ABC}^{*\top}(t) \mathbf{i}_{\alpha,ABC}(t) \quad (3.3)$$

These equations are nonlinear w.r.t. the state-space variables. Therefore, as previously outlined in Section 2.4.5, the actuator model is linearized around the operating point

$$\mathbf{y}_o(t) = \begin{bmatrix} \bar{\mathbf{v}}_{\alpha,ABC}^*(t) \\ \bar{\mathbf{i}}_{\alpha,ABC}(t) \\ \bar{v}_\delta(t) \end{bmatrix} \quad (3.4)$$

which leads to the following linear representation (i.e., a first-order Taylor expansion of (3.2) and (3.3) w.r.t. (3.4)):

$$\mathbf{v}_{\alpha,ABC}(t) \approx \frac{1}{V_\delta^*} \left(\bar{\mathbf{v}}_{\alpha,ABC}^*(t) v_\delta(t) + \bar{v}_\delta(t) \mathbf{v}_{\alpha,ABC}^*(t) - \bar{v}_\delta(t) \bar{\mathbf{v}}_{\alpha,ABC}^*(t) \right) \quad (3.5)$$

$$i_\delta(t) \approx \frac{1}{V_\delta^*} \left(\bar{\mathbf{v}}_{\alpha,ABC}^{*\top}(t) \mathbf{i}_{\alpha,ABC}(t) + \bar{\mathbf{i}}_{\alpha,ABC}^\top(t) \mathbf{v}_{\alpha,ABC}^*(t) - \bar{\mathbf{i}}_{\alpha,ABC}^\top(t) \bar{\mathbf{v}}_{\alpha,ABC}^*(t) \right) \quad (3.6)$$

For the most basic models of grid-forming and grid-following converters, it is common practice to model only the AC-side dynamics. That is, the DC side is represented by an ideal DC voltage source which is equal to the reference $v_\delta(t) = V_\delta^*$ and (3.2) reduces to

$$\mathbf{v}_{\alpha,ABC}(t) = \mathbf{v}_{\alpha,ABC}^*(t) \quad (3.7)$$

Notably, this equation corresponds to an ideal converter that precisely implements its voltage reference.

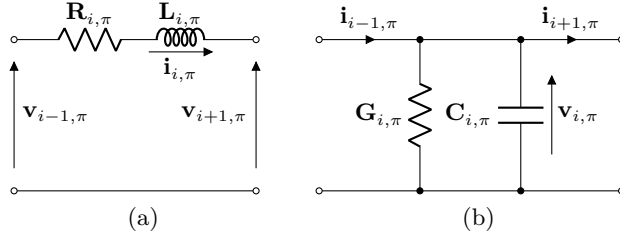


Figure 3.4: Equivalent circuits of a filter stage i constructed from inductors (3.4a) or capacitors (3.4b), respectively. Observe that voltages, currents, and electrical parameters are expressed in the reference frame of the power hardware π .

3.2.2 Filter Stages

In order to attenuate the high-frequency distortions resulting from the switching in the actuator, CIDERs are equipped with cascades of filter stages [6]. Each stage consists of inductors or capacitors (plus parasitic or damping resistors), which filter currents or voltages, respectively. Notably, the commonly used L-, LC-, and LCL-filters as well as higher-order filters are built in this way.

Consider any stage i in the cascade of filters. An inductive filter stage is represented by the equivalent circuit in Fig. 3.4a, which is described by the following differential equation:

$$\mathbf{v}_{i-1,\pi}(t) - \mathbf{v}_{i+1,\pi}(t) = \mathbf{R}_{i,\pi} \mathbf{i}_{i,\pi}(t) + \mathbf{L}_{i,\pi} \frac{d}{dt} \mathbf{i}_{i,\pi}(t) \quad (3.8)$$

$\mathbf{R}_{i,\pi}, \mathbf{L}_{i,\pi} \in \mathbb{R}^{\dim(\pi) \times \dim(\pi)}$ are the compound electrical parameters of the inductive filter stage, $\mathbf{i}_{i,\pi} \in \mathbb{R}^{\dim(\pi) \times 1}$ is the current flowing through it, and $\mathbf{v}_{i-1,\pi}, \mathbf{v}_{i+1,\pi} \in \mathbb{R}^{\dim(\pi) \times 1}$ are the voltages at the start and end node of the stage, respectively. Again, the sizes of these vectors and matrices depend on the reference frame in which the power hardware is modelled. A capacitive filter stage is represented by the equivalent circuit in Fig. 3.4b, which is described by

$$\mathbf{i}_{i-1,\pi}(t) - \mathbf{i}_{i+1,\pi}(t) = \mathbf{G}_{i,\pi} \mathbf{v}_{i,\pi}(t) + \mathbf{C}_{i,\pi} \frac{d}{dt} \mathbf{v}_{i,\pi}(t) \quad (3.9)$$

$\mathbf{G}_{i,\pi}, \mathbf{C}_{i,\pi} \in \mathbb{R}^{\dim(\pi) \times \dim(\pi)}$ are the compound electrical parameters of the capacitive filter stage, $\mathbf{v}_{i,\pi} \in \mathbb{R}^{\dim(\pi) \times 1}$ is the voltage across it, and $\mathbf{i}_{i-1,\pi}, \mathbf{i}_{i+1,\pi} \in \mathbb{R}^{\dim(\pi) \times 1}$ are the currents flowing into and out of the stage, respectively.

In practice, the filter stages are built from identical discrete elements (i.e., one element per phase). Accordingly, the following hypothesis can be made:

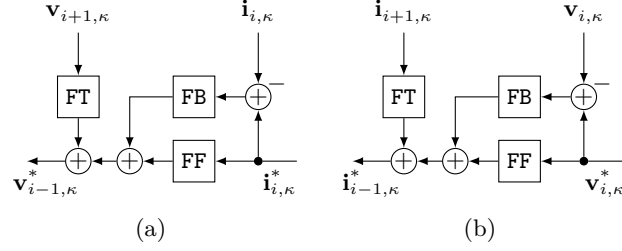


Figure 3.5: Block diagrams of a controller stage i associated with an inductive (3.5a) and capacitive (3.5b) filter stage, respectively. In general, the control law includes *Feed-Back* (FB), *Feed-Forward* (FF), and *Feed-Through* (FT) terms. Observe that voltages and currents are expressed in the reference frame of the control software κ .

Hypothesis 11. *The compound electrical parameters of the filter stages are diagonal matrices with equal nonzero entries. That is, an inductive filter stage is characterized by*

$$\mathbf{R}_{i,\pi} = R_i \text{diag}(\mathbf{1}_\pi), \quad \mathbf{L}_{i,\pi} = L_i \text{diag}(\mathbf{1}_\pi) \quad (3.10)$$

and a capacitive filter stage by

$$\mathbf{G}_{i,\pi} = G_i \text{diag}(\mathbf{1}_\pi), \quad \mathbf{C}_{i,\pi} = C_i \text{diag}(\mathbf{1}_\pi) \quad (3.11)$$

where $\text{diag}(\mathbf{1}_\pi)$ is the identity matrix w.r.t. reference frame of the power hardware. R_i , L_i and G_i , C_i are the parameters of the discrete elements.

3.2.3 Controller Stages

Each filter stage can be coupled with a corresponding controller, which regulates either the current through or the voltage across the filter element, depending on whether the filter stage is inductive or capacitive.¹ As illustrated in Fig. 3.5, such a controller generally performs *Feed-Back* (FB), *Feed-Forward* (FF), and *Feed-Through* (FT) control. More precisely, as shown in Figs. 3.5a and 3.5b, a stage i of the controller calculates the reference for the next-inner stage $i - 1$ from the deviation between its own state and the desired reference (i.e., via FB and FF control), as well as the state of the next-outer stage $i + 1$ (i.e., via FT control). In principle, each block of a controller stage could be composed of multiple subblocks connected in series or in parallel (e.g., for the mitigation of specific harmonics). In practice, simple *Proportional-Integral-Derivative* (PID) and *Proportional-Resonant* (PR) controllers are commonly used [76].

¹As already mentioned in Section 2.4, it is common practice for CIDERS with LCL filter to implement one instead of two current control loops. Notably, this can easily be represented in the proposed framework.

Example of Proportional-Integral Controllers

For the sake of illustration, PI-controllers are considered for FB control, and P-controllers for FF and FT control:

Hypothesis 12. *Each controller stage consists of a PI controller for FB control, and two P controllers for FF and FT controls.*

Let $\mathbf{K}_{\text{FB},i}, \mathbf{K}_{\text{FF},i}, \mathbf{K}_{\text{FT},i} \in \mathbb{R}^{\dim(\kappa) \times \dim(\kappa)}$ be the proportional gains and $T_{\text{FB},i}$ the integration time, respectively. The control law for an inductive filter stage is given by (see Fig. 3.5a)

$$\mathbf{v}_{i-1,\kappa}^*(t) = \begin{bmatrix} \mathbf{K}_{\text{FB},i} \left(\Delta \mathbf{i}_{i,\kappa}(t) + \frac{1}{T_{\text{FB},i}} \int \Delta \mathbf{i}_{i,\kappa}(t) dt \right) \\ + \mathbf{K}_{\text{FT},i} \mathbf{v}_{i+1,\kappa}(t) + \mathbf{K}_{\text{FF},i} \mathbf{i}_{i,\kappa}^*(t) \end{bmatrix} \quad (3.12)$$

$$\Delta \mathbf{i}_{i,\kappa}(t) := \mathbf{i}_{i,\kappa}^*(t) - \mathbf{i}_{i,\kappa}(t) \quad (3.13)$$

$\mathbf{v}_{i-1,\kappa}^*, \mathbf{i}_{i,\kappa}^* \in \mathbb{R}^{\dim(\kappa) \times 1}$ are the reference voltage at the input of the controller stage and the reference current at its output, respectively. $\mathbf{v}_{i+1,\kappa}, \mathbf{i}_{i,\kappa} \in \mathbb{R}^{\dim(\kappa) \times 1}$ are the voltage at the output of the filter stage and the current through it, respectively, expressed in the reference frame of the controller. The control law for a capacitive filter stage is analogous (see Fig. 3.5b):

$$\mathbf{i}_{i-1,\kappa}^*(t) = \begin{bmatrix} \mathbf{K}_{\text{FB},i} \left(\Delta \mathbf{v}_{i,\kappa}(t) + \frac{1}{T_{\text{FB},i}} \int \Delta \mathbf{v}_{i,\kappa}(t) dt \right) \\ + \mathbf{K}_{\text{FT},i} \mathbf{i}_{i+1,\kappa}(t) + \mathbf{K}_{\text{FF},i} \mathbf{v}_{i,\kappa}^*(t) \end{bmatrix} \quad (3.14)$$

$$\Delta \mathbf{v}_{i,\kappa}(t) := \mathbf{v}_{i,\kappa}^*(t) - \mathbf{v}_{i,\kappa}(t) \quad (3.15)$$

$\mathbf{i}_{i-1,\kappa}^*, \mathbf{v}_{i,\kappa}^* \in \mathbb{R}^{\dim(\kappa) \times 1}$ are the reference current at the input of the controller stage and the reference voltage at its output, respectively. $\mathbf{i}_{i+1,\kappa}, \mathbf{v}_{i,\kappa} \in \mathbb{R}^{\dim(\kappa) \times 1}$ are the current at the output of the filter stage and voltage across it, respectively, expressed in the reference frame of the controller.

Modelling Assumptions

Typically, the FB and FT controllers treat each coordinate in the reference frame independently, and apply equal gains to them. In line with this fact, the following hypothesis is made:

Hypothesis 13. *The FB and FT gains are diagonal matrices with equal nonzero entries. That is*

$$\mathbf{K}_{\text{FB},i} = K_{\text{FB},i} \text{diag}(\mathbf{1}_\kappa) \quad (3.16)$$

$$\mathbf{K}_{\text{FT},i} = K_{\text{FT},i} \text{diag}(\mathbf{1}_\kappa) \quad (3.17)$$

where $\text{diag}(\mathbf{1}_\kappa)$ is the identity matrix w.r.t. the reference frame of the control software.

The FF controllers, by contrast, are obtained by restating the dynamical models of the filter stages, which are given in the reference frame of the power hardware, in the reference frame of the control software [77]. To this end, the transformation matrices $\mathbf{T}_{\kappa|\pi} \in \mathbb{R}^{\dim(\kappa) \times \dim(\pi)}$ and $\mathbf{T}_{\pi|\kappa} \in \mathbb{R}^{\dim(\pi) \times \dim(\kappa)}$ are substituted into the filter equations (3.8)–(3.9). For the inductive filter stage, one obtains

$$\mathbf{v}_{i-1,\kappa}(t) - \mathbf{v}_{i+1,\kappa}(t) = \mathbf{R}_{i,\kappa} \mathbf{i}_{i,\kappa}(t) + \mathbf{L}_{i,\kappa} \frac{d}{dt} \mathbf{i}_{i,\kappa}(t) \quad (3.18)$$

where $\mathbf{R}_{i,\kappa}, \mathbf{L}_{i,\kappa} \in \mathbb{R}^{\dim(\kappa) \times \dim(\kappa)}$ are given by

$$\mathbf{R}_{i,\kappa} = \mathbf{T}_{\kappa|\pi}(t) \mathbf{R}_{i,\pi} \mathbf{T}_{\pi|\kappa}(t) + \mathbf{T}_{\kappa|\pi}(t) \mathbf{L}_{i,\pi} \frac{d}{dt} \mathbf{T}_{\pi|\kappa}(t) \quad (3.19)$$

$$\mathbf{L}_{i,\kappa} = \mathbf{T}_{\kappa|\pi}(t) \mathbf{L}_{i,\pi} \mathbf{T}_{\pi|\kappa}(t) \quad (3.20)$$

Analogously, for the capacitive filter stage, one finds

$$\mathbf{i}_{i-1,\kappa}(t) - \mathbf{i}_{i+1,\kappa}(t) = \mathbf{G}_{i,\kappa} \mathbf{v}_{i,\kappa}(t) + \mathbf{C}_{i,\kappa} \frac{d}{dt} \mathbf{v}_{i,\kappa}(t) \quad (3.21)$$

where $\mathbf{G}_{i,\kappa}, \mathbf{C}_{i,\kappa} \in \mathbb{R}^{\dim(\kappa) \times \dim(\kappa)}$ are given by

$$\mathbf{G}_{i,\kappa} = \mathbf{T}_{\kappa|\pi}(t) \mathbf{G}_{i,\pi} \mathbf{T}_{\pi|\kappa}(t) + \mathbf{T}_{\kappa|\pi}(t) \mathbf{C}_{i,\pi} \frac{d}{dt} \mathbf{T}_{\pi|\kappa}(t) \quad (3.22)$$

$$\mathbf{C}_{i,\kappa} = \mathbf{T}_{\kappa|\pi}(t) \mathbf{C}_{i,\pi} \mathbf{T}_{\pi|\kappa}(t) \quad (3.23)$$

Observe that the expressions for $\mathbf{R}_{i,\kappa}$ and $\mathbf{G}_{i,\kappa}$ include terms that result from the temporal derivatives of $\mathbf{i}_{i,\pi} = \mathbf{T}_{\pi|\kappa} \mathbf{i}_{i,\kappa}$ and $\mathbf{v}_{i,\pi} = \mathbf{T}_{\pi|\kappa} \mathbf{v}_{i,\kappa}$, respectively. These expressions often turn out to be time-invariant thanks to the diagonal nature of the matrices in Hyp. 11. For instance, as will be shown shortly, this is the case in the DQ frame.

Using (3.18) and (3.21), the FF gains can be set in order to achieve zero error in steady-state (e.g., [77]) via the following additional hypothesis.

Hypothesis 14. *The FF gains are set to*

$$\mathbf{K}_{\text{FF},i} = \begin{cases} \mathbf{R}_{i,\kappa} & \text{for inductive filter stages} \\ \mathbf{G}_{i,\kappa} & \text{for capacitive filter stages} \end{cases} \quad (3.24)$$

3.2.4 Circuit Configurations and Reference Frames

Circuit Configurations

Usually, the grid and the power hardware are both modelled in phase coordinates, but their circuit configuration may not be the same. Recall from Hyp. 1 that the grid is a four-wire system (i.e., three phase plus one neutral conductor), and the neutral conductor is effectively ground. In contrast, the power converters can be either four-leg or three-leg devices (i.e., with or without neutral conductor). If a CIDER with a four-leg power converter is connected to a four-wire grid, all sequence components (i.e., positive, negative, and homopolar sequences) of voltage and current can pass in both directions. This corresponds to

$$\mathbf{T}_{\pi|\gamma} = \mathbf{T}_{\gamma|\pi} = \text{diag}(\mathbf{1}_3) \quad (3.25)$$

By contrast, if a CIDER with a three-leg power converter is connected to a four-wire grid (as is often the case), homopolar sequences are blocked in both directions. This is represented by

$$\mathbf{T}_{\pi|\gamma} = \mathbf{T}_{\gamma|\pi} = \text{diag}(\mathbf{1}_3) - \frac{1}{3}\mathbf{1}_{3 \times 3} \quad (3.26)$$

Transformation Matrices

It is common practice to implement the control software in DQ components [76]. If the power hardware is modelled in phase (ABC) coordinates, as previously mentioned, one obtains

$$\mathbf{T}_{\kappa|\pi}(t) = \mathbf{T}_{\pi|\kappa}^T(t) \quad (3.27)$$

$$\mathbf{T}_{\pi|\kappa}(t) = \sqrt{\frac{2}{3}} \begin{bmatrix} \cos(\theta(t)) & -\sin(\theta(t)) \\ \cos\left(\theta(t) - \frac{2\pi}{3}\right) & -\sin\left(\theta(t) - \frac{2\pi}{3}\right) \\ \cos\left(\theta(t) + \frac{2\pi}{3}\right) & -\sin\left(\theta(t) + \frac{2\pi}{3}\right) \end{bmatrix} \quad (3.28)$$

where θ is a given reference angle². How the reference angle is obtained, depends on the type of CIDER. In case of a grid-forming CIDER, the reference angle is set (i.e., to zero for the slack node). For a grid-following CIDERs, the reference angle is determined by means of a synchronisation unit. In either case, it is assumed that θ is synchronized with the fundamental frequency tone.

Hypothesis 15. *Irrespective of the type of CIDER, the reference angle θ , w.r.t. which the DQ frame is defined, is given by*

$$\theta(t) = 2\pi f_1 t + \theta_0 \quad (3.29)$$

where θ_0 is a known offset.

²In this context, recall the earlier remark regarding the fact that the transformation matrices are generally rectangular not quadratic, because some coordinates may be omitted (here: the zero component).

If this hypothesis holds, the Fourier coefficients of the transformation matrices (3.27)–(3.28), which are needed for the harmonic-domain model, are described by the following matrices:

$$\mathbf{T}_{\pi|\kappa,+1} = \sqrt{\frac{2}{3}} \exp(j\theta_0) \begin{bmatrix} \frac{1}{2} & -\frac{1}{2j} \\ \frac{1}{2}\alpha^* & -\frac{1}{2j}\alpha^* \\ \frac{1}{2}\alpha & -\frac{1}{2j}\alpha \end{bmatrix} \quad (3.30)$$

$$\mathbf{T}_{\pi|\kappa,-1} = \mathbf{T}_{\pi|\kappa,+1}^* \quad (3.31)$$

where $\alpha = \exp\left(j\frac{2\pi}{3}\right)$. As explained in Section 2.4.1, the Fourier coefficients of time-periodic matrices appear on the diagonals of the associated Toeplitz matrices in the harmonic domain. For example, the coefficients of order $h = \pm 1$ appear on the first upper and lower diagonal, respectively. Accordingly, $\hat{\mathbf{T}}_{\kappa|\pi}$ and $\hat{\mathbf{T}}_{\pi|\kappa}$ have a block-band structure, which introduces coupling between the harmonics.

The impact of the transformation on the spectrum of the signal becomes more evident if the latter is expressed in sequence components. That is, the block-band structure of the transformation matrix shifts the harmonic orders as follows: The harmonic order of positive/negative sequences is decremented/incremented by 1, respectively, and the harmonic order of homopolar sequences remains unchanged [70]. Recall that for the purpose of HA, the spectrum must be truncated at a given maximum harmonic order. In view of the aforementioned frequency shift, the maximum harmonic orders for power hardware and control software should be chosen such that the loss of signal content is minimized. This goal can be achieved by setting:

$$h_{max,\kappa} = h_{max,\pi} + 1 \quad (3.32)$$

Feed-Forward Gain in the DQ Reference Frame

Having specified the reference frames, the FF gain $\mathbf{K}_{FF,i}$ as given in Hyp. 14 can be evaluated. By substitution of (3.27)–(3.28) and Hyp. 15 into (3.19) and (3.22), one can show that

$$\mathbf{R}_{i,DQ} = \begin{bmatrix} R_i & -2\pi f_1 L_i \\ 2\pi f_1 L_i & R_i \end{bmatrix} \quad (3.33)$$

$$\mathbf{G}_{i,DQ} = \begin{bmatrix} G_i & -2\pi f_1 C_i \\ 2\pi f_1 C_i & G_i \end{bmatrix} \quad (3.34)$$

The off-diagonal elements are a.k.a. decoupling terms [78]. Note that, the decoupling terms result from the temporal derivatives in (3.19) and (3.22). More precisely, due to the diagonal structure of $\mathbf{R}_{i,ABC}$ and $\mathbf{G}_{i,ABC}$, the transformed matrices in DQ-components $\mathbf{R}_{i,DQ}$ and $\mathbf{G}_{i,DQ}$ are time-invariant (as claimed).

3.2.5 PQ Law – Reference Calculation

In grid-following CIDERs, the reference angle θ needed for the DQ transform is provided by a synchronization unit, usually a *Phase-Locked Loop* (PLL). The reference current $\mathbf{i}_{\gamma,\text{DQ}}^*$ is computed in order to track the power setpoint $S_\sigma = P_\sigma + jQ_\sigma$ at the fundamental frequency. Without imposing any further conditions on θ , $\mathbf{i}_{\gamma,\text{DQ}}^*$ is given by [79]

$$\mathbf{i}_{\gamma,\text{DQ}}^*(t) = \frac{1}{v_{\gamma,\text{D}}^2(t) + v_{\gamma,\text{Q}}^2(t)} \begin{bmatrix} v_{\gamma,\text{D}}(t) & -v_{\gamma,\text{Q}}(t) \\ v_{\gamma,\text{Q}}(t) & v_{\gamma,\text{D}}(t) \end{bmatrix} \begin{bmatrix} P_\sigma \\ Q_\sigma \end{bmatrix} \quad (3.35)$$

In the vast majority of cases, synchronization units in general, and PLLs in particular, are designed to lock to the fundamental positive-sequence component of the grid voltage (e.g., [79]). This working principle leads to the following hypothesis.

Hypothesis 16. *The synchronization units of the grid-following CIDERs lock to the fundamental positive-sequence component of the grid voltage. Therefore, in steady state it holds that*

$$V_{\gamma,\text{Q},0} = \frac{1}{T} \int v_{\gamma,\text{Q}}(t) dt = 0 \quad (3.36)$$

For instance, this can be achieved by a closed-loop controller which adjusts θ in order to regulate $v_{\gamma,\text{Q}}$ to 0 [80].

As required by power quality standards (e.g., [3]), the grid voltages have to be maintained balanced and sinusoidal within specified limits³. Under these conditions, it is reasonable to assume the following.

Hypothesis 17. *The time-variant signal content of $v_{\gamma,\text{D}}(t)$ and $v_{\gamma,\text{Q}}(t)$, as given by $\xi_{\text{D}}(t)$ and $\xi_{\text{Q}}(t)$ below, is low:*

$$v_{\gamma,\text{D}}(t) = V_{\gamma,\text{D},0}(1 + \xi_{\text{D}}(t)), \quad |\xi_{\text{D}}(t)| \ll 1 \quad (3.37)$$

$$v_{\gamma,\text{Q}}(t) = V_{\gamma,\text{Q},0}(1 + \xi_{\text{Q}}(t)), \quad |\xi_{\text{Q}}(t)| \ll 1 \quad (3.38)$$

As a consequence of Hyps. 16 and 17, $v_{\gamma,\text{Q}}(t)$ can be neglected w.r.t. $v_{\gamma,\text{D}}(t)$ in (3.35):

$$\mathbf{i}_{\gamma,\text{DQ}}^*(t) \approx \begin{bmatrix} \frac{1}{v_{\gamma,\text{D}}(t)} & 0 \\ 0 & \frac{1}{v_{\gamma,\text{D}}(t)} \end{bmatrix} \begin{bmatrix} P_\sigma \\ Q_\sigma \end{bmatrix} \quad (3.39)$$

Nonlinear Approximation of the Reference Calculation

In order to calculate the HDR of the CIDER (i.e., the input/output expression of the grid response used for the HPF study), the Fourier coefficients of $\mathbf{i}_{\gamma,\text{DQ}}^*$ are needed.

³By contrast, the grid currents may be subject to unbalances and harmonics.

Unfortunately, the exact expressions that relate the Fourier coefficients of the reciprocal $v_{\gamma, \mathbf{D}}^{-1}$ and those of $v_{\gamma, \mathbf{D}}$ are complicated [81], and their evaluation is computationally intensive. However, taking advantage of Hyp. 17, a Taylor expansion can be employed. In this respect, the following approximations are made:

Hypothesis 18. *For the calculation of the reference current in the grid-following CIDERs, the reciprocal of the grid voltage can be approximated by a Taylor series of order n :*

$$\frac{1}{v_{\gamma, \mathbf{D}}(t)} \approx \frac{1}{V_{\gamma, \mathbf{D}, 0}} \sum_n (-1)^n \xi_{\mathbf{D}}^n(t) \quad (3.40)$$

where the Fourier series of $\xi_{\mathbf{D}}(t)$ is described by

$$\xi_{\mathbf{D}}(t) = \sum_{h \neq 0} \frac{V_{\gamma, \mathbf{D}, h}}{V_{\gamma, \mathbf{D}, 0}} \exp(jh2\pi f_1 t) \quad (3.41)$$

Employing this Taylor expansion, one can approximate the matrix in (3.39) by $\Psi^{(n)}(t)$

$$\Psi^{(n)}(t) = \frac{1}{V_{\gamma, \mathbf{D}, 0}} \sum_n (-1)^n \Xi_{\mathbf{D}}^n(t) \quad (3.42)$$

where

$$\Xi_{\mathbf{D}}(t) = \text{diag}(\mathbf{1}_2) \xi_{\mathbf{D}}(t) \quad (3.43)$$

Transforming (3.42) to the harmonic domain gives

$$\hat{\Psi}^{(n)} = \frac{1}{V_{\gamma, \mathbf{D}, 0}} \sum_n (-1)^n \hat{\Xi}_{\mathbf{D}}^n \quad (3.44)$$

where $\text{diag}(\mathbf{1})$ is a matrix of suitable size, composed of ones, and $\hat{\Xi}_{\mathbf{D}}$ describes the Toeplitz matrix built from the Fourier coefficients of $\Xi_{\mathbf{D}}(t)$.

For a first-order Taylor expansion one obtains

$$\hat{\Psi}^{(1)} = \frac{1}{V_{\gamma, \mathbf{D}, 0}} \left(\text{diag}(\mathbf{1}) - \hat{\Xi}_{\mathbf{D}} \right) \quad (3.45)$$

Analogously for the second-order expansion:

$$\hat{\Psi}^{(2)} = \frac{1}{V_{\gamma, \mathbf{D}, 0}} \left(\text{diag}(\mathbf{1}) - \hat{\Xi}_{\mathbf{D}} + \hat{\Xi}_{\mathbf{D}}^2 \right) \quad (3.46)$$

As stated in Section 2.4.3 the second order expansion of the reference calculation is employed when deriving the HDR of the resource. Expansions of higher order can easily be obtained using (3.44) with suitable n . For the sake of conciseness, the impact of the

Chapter 3. Derivation of the Specific Models of the CIDERs

order of the expansion on the CIDER's grid response is provided in the validation section of this chapter (see Section 3.4.2).

Note that the approximation of the PQ control law (3.39) is a nonlinear function of the Fourier coefficients of the grid voltage.

Partial Derivatives for the Numerical Solution of the HPF Problem

For the numerical solution of the HPF problem the derivative of the reference calculation w.r.t. the grid voltage is needed, to built the Jacobian matrix⁴. To this end, considering the first order expansion of the reference calculation suffices to obtain good convergence behaviour, as will be shown in Section 4.4.2. In order to derive the partial derivatives of the grid current reference the Fourier coefficients of $\hat{\Psi}^{(1)}$ are explicitly derived as a function of the grid voltage:

$$\hat{\Psi}_h^{(1)} = \text{diag}(\mathbf{1}_2) \begin{cases} \frac{1}{V_{\gamma,D,0}} & h = 0 \\ -\frac{V_{\gamma,D,h}}{V_{\gamma,D,0}^2} & \text{otherwise} \end{cases} \quad (3.47)$$

In this respect, the partial derivatives of $\hat{\Psi}^{(1)}$ w.r.t. $\hat{\mathbf{V}}_{\gamma,D}$ are obtained as

$$\frac{\delta \hat{\Psi}_0^{(1)}}{\delta \hat{\mathbf{V}}_{\gamma,D,h}} = \mathbf{1}_2 \begin{cases} -\frac{1}{V_{\gamma,D,0}^2} & h = 0 \\ 0 & \text{otherwise} \end{cases} \quad (3.48)$$

and

$$\frac{\delta \hat{\Psi}_k^{(1)}}{\delta \hat{\mathbf{V}}_{\gamma,D,h}} = \mathbf{1}_2 \begin{cases} 2\frac{V_{\gamma,D,h}}{V_{\gamma,D,0}^3} & h = 0 \\ -\frac{1}{V_{\gamma,D,0}^2} & \text{otherwise} \end{cases} \quad (3.49)$$

where $k \in \mathcal{H}, k \neq 0$. Thus,

$$\frac{\delta \hat{\mathbf{I}}_{\gamma,DQ}^*}{\delta \hat{\mathbf{V}}_{\gamma,D}} = \frac{\delta \hat{\Psi}^{(1)}}{\delta \hat{\mathbf{V}}_{\gamma,D}} \hat{\mathbf{S}} \quad (3.50)$$

$$\frac{\delta \hat{\mathbf{I}}_{\gamma,DQ}^*}{\delta \hat{\mathbf{V}}_{\gamma,ABC}} = \frac{\delta \hat{\mathbf{I}}_{\gamma,DQ}^*}{\delta \hat{\mathbf{V}}_{\gamma,D}} \hat{\mathbf{T}}_{\kappa|\pi} \hat{\mathbf{T}}_{\pi|\gamma} \quad (3.51)$$

where $\hat{\mathbf{S}}$ describes the column vector composed of the Fourier coefficients of the power setpoints.

⁴The Jacobian matrix is the matrix of the first-order derivatives of the system equations, that is used to update the solution estimate in each step of the Newton-Raphson algorithm.

Small-Signal Model of the Reference Calculation

For the representation of the reference calculation within the HSS model of the CIDER, the format introduced in (2.57) is employed. To this end, one needs to derive the coefficients $\hat{\mathbf{R}}_\rho$ and $\hat{\mathbf{R}}_\sigma$ originating from the Taylor expansion in time domain, as well as the shift of the origin $\hat{\mathbf{W}}_\kappa$. The coefficients for the small-signal model of (3.39) for the operating point $\bar{\mathbf{w}}_\rho(t)$ and a general power setpoint $\bar{\mathbf{w}}_\sigma(t)$ are given by

$$\bar{\mathbf{w}}_\kappa(t) = \frac{1}{\bar{\mathbf{w}}_\rho(t)} \bar{\mathbf{w}}_\sigma(t) \quad (3.52)$$

$$\mathbf{R}_\rho(t) = - \left(\frac{1}{\bar{\mathbf{w}}_\rho(t)} \right)^2 \bar{\mathbf{w}}_\sigma(t) \quad (3.53)$$

$$\mathbf{R}_\sigma(t) = \frac{1}{\bar{\mathbf{w}}_\rho(t)} \quad (3.54)$$

From this, the harmonic-domain quantities $\hat{\mathbf{W}}_\kappa$, $\hat{\mathbf{R}}_\rho$, and $\hat{\mathbf{R}}_\sigma$ are derived by means of the Teoplitz theory. It is worth noting that, as before, the reciprocal of $\bar{\mathbf{w}}_\rho(t)$ can be approximated by a n th-order Taylor expansion as stated in Hyp. 18.

In general, one would expect that the nonlinear approximation of the reference calculation performs better than the small-signal model. However, if both models are evaluated at the operating point (i.e., with zero deviation from it), they will yield the same results.

3.3 Library of Resource Models

In this section, the components introduced in Section 3.2 are combined to formulate the models of the different types of CIDERs. First, the simplified models of a grid-forming and -following CIDER is presented. The description “simplified” refers to the fact that they are represented by AC-side characteristics only. In these cases, the CIDERs can be modelled using the first version of the generic CIDER model in Section 2.4, where the nonlinearities of the model are limited to inside the reference calculation. Second, a grid-following CIDER that models the DC-side characteristics is introduced. To this end, the extension of the generic CIDER model proposed in Section 2.4.5 is employed.

3.3.1 Grid-Forming CIDER – Considering Only AC-Side Characteristics

Fig. 3.6 shows the schematic diagram of a typical grid-forming CIDER. Its power hardware consists of a PWM actuator, modelled by an ideal AC voltage source (see Section 3.2.1)

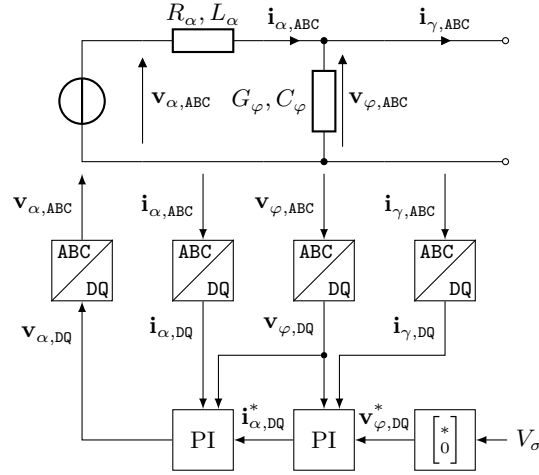


Figure 3.6: Schematic diagram of a grid-forming CIDER with an LC filter.

and an LC filter⁵, and its control software of a two-stage PI controller. The actuator is assumed to be a four-leg power converter which can inject or absorb homopolar currents⁶. This feature is of crucial importance for islanded operation, during which the grid-forming CIDER takes the role of the slack.

Power Hardware

The state of the power hardware is given by the inductor current $\mathbf{i}_{\alpha,ABC} \in \mathbb{R}^{3 \times 1}$ and the capacitor voltage $\mathbf{v}_{\varphi,ABC} \in \mathbb{R}^{3 \times 1}$. The input and disturbance are the actuator voltage $\mathbf{v}_{\alpha,ABC} \in \mathbb{R}^{3 \times 1}$ and grid current $\mathbf{i}_{\gamma,ABC} \in \mathbb{R}^{3 \times 1}$, respectively. The output includes both state and disturbance. That is

$$\mathbf{x}_{\pi}(t) = \begin{bmatrix} \mathbf{i}_{\alpha,ABC}(t) \\ \mathbf{v}_{\varphi,ABC}(t) \end{bmatrix} \in \mathbb{R}^{6 \times 1} \quad (3.55)$$

$$\mathbf{u}_{\pi}(t) = \mathbf{v}_{\alpha,ABC}(t) \in \mathbb{R}^{3 \times 1} \quad (3.56)$$

$$\mathbf{w}_{\pi}(t) = \mathbf{i}_{\gamma,ABC}(t) \in \mathbb{R}^{3 \times 1} \quad (3.57)$$

$$\mathbf{y}_{\pi}(t) = \begin{bmatrix} \mathbf{x}_{\pi}(t) \\ \mathbf{w}_{\pi}(t) \end{bmatrix} \in \mathbb{R}^{9 \times 1} \quad (3.58)$$

⁵If a grid-forming CIDER is equipped with an LCL filter, the output seen at the point of connection is the current through the grid-side inductor, and the disturbance is the nodal voltage (cf. (2.29) and (2.30)). As a consequence, such a CIDER would belong to the set \mathcal{R} .

⁶Note that, while four-leg power converters are not common, it does make sense to use them for grid-forming CIDERs (of which there are only a few in any case), because the power system has no ability to absorb homopolar sequences otherwise.

The time-domain state-space model of the power hardware is obtained by combining the differential equations (3.8) and (3.9) of the filter stages. This yields

$$\mathbf{A}_\pi(t) = \begin{bmatrix} -\mathbf{L}_\alpha^{-1} \mathbf{R}_\alpha & -\mathbf{L}_\alpha^{-1} \\ \mathbf{C}_\varphi^{-1} & -\mathbf{C}_\varphi^{-1} \mathbf{G}_\varphi \end{bmatrix} \quad (3.59)$$

$$\mathbf{B}_\pi(t) = \begin{bmatrix} \mathbf{L}_\alpha^{-1} \\ \mathbf{0}_{3 \times 3} \end{bmatrix} \quad (3.60)$$

$$\mathbf{E}_\pi(t) = \begin{bmatrix} \mathbf{0}_{3 \times 3} \\ -\mathbf{C}_\varphi^{-1} \end{bmatrix} \quad (3.61)$$

$$\mathbf{C}_\pi(t) = \begin{bmatrix} \text{diag}(\mathbf{1}_6) \\ \mathbf{0}_{3 \times 6} \end{bmatrix} \quad (3.62)$$

$$\mathbf{D}_\pi(t) = \mathbf{0}_{9 \times 3} \quad (3.63)$$

$$\mathbf{F}_\pi(t) = \begin{bmatrix} \mathbf{0}_{6 \times 3} \\ \text{diag}(\mathbf{1}_3) \end{bmatrix} \quad (3.64)$$

The sizes of these matrices follow directly from (3.55)–(3.58). Note that these matrices are time-invariant, which means that only the Fourier coefficient for $h = 0$ is nonzero. For instance:

$$\mathbf{A}_\pi(t) = \mathbf{A}_{\pi,0} \quad (3.65)$$

The same holds for the other matrices of the state-space model. Accordingly, the power hardware is an LTI system, which is a particular case of an LTP system.

Control Software

Recall from Hyp. 12 that each controller stage consists of one PI controller (i.e., for FB control) and two P controllers (i.e., for FF and FT control). Since the control software is composed of PI controllers, its state is given by the temporal integrals of the errors w.r.t. the inductor current $\Delta \mathbf{i}_{\alpha, \text{DQ}} \in \mathbb{R}^{2 \times 1}$ and the capacitor voltage $\Delta \mathbf{v}_{\varphi, \text{DQ}} \in \mathbb{R}^{2 \times 1}$. Its input and output are defined by the interconnection with the power hardware as shown in Fig. 3.6. The disturbance is the reference voltage $\mathbf{v}_{\varphi, \text{DQ}}^* \in \mathbb{R}^{2 \times 1}$ of the outer controller stage. Accordingly

$$\mathbf{x}_\kappa(t) = \int \begin{bmatrix} \Delta \mathbf{i}_{\alpha, \text{DQ}}(t) \\ \Delta \mathbf{v}_{\varphi, \text{DQ}}(t) \end{bmatrix} dt \in \mathbb{R}^{4 \times 1} \quad (3.66)$$

$$\mathbf{u}_\kappa(t) = \begin{bmatrix} \mathbf{i}_{\alpha, \text{DQ}}(t) \\ \mathbf{v}_{\varphi, \text{DQ}}(t) \\ \mathbf{i}_{\gamma, \text{DQ}}(t) \end{bmatrix} \in \mathbb{R}^{6 \times 1} \quad (3.67)$$

$$\mathbf{w}_\kappa(t) = \mathbf{v}_{\varphi, \text{DQ}}^*(t) \in \mathbb{R}^{2 \times 1} \quad (3.68)$$

$$\mathbf{y}_\kappa(t) = \mathbf{v}_{\alpha, \text{DQ}}(t) \in \mathbb{R}^{2 \times 1} \quad (3.69)$$

Chapter 3. Derivation of the Specific Models of the CIDERs

The time-domain state-space model of the control software is found by combining the differential equations (3.12) and (3.14) of the controller stages. This gives the following matrices. For the sake of readability the following substitution has been employed, $(\mathbf{K}_{\text{FF}} + \mathbf{K}_{\text{FB}}) = \mathbf{K}_{\text{FFB}}$.

$$\mathbf{A}_\kappa(t) = \begin{bmatrix} \mathbf{0}_{2 \times 2} & \frac{\mathbf{K}_{\text{FB},\varphi}}{T_{\text{FB},\varphi}} \\ \mathbf{0}_{2 \times 2} & \mathbf{0}_{2 \times 2} \end{bmatrix} \quad (3.70)$$

$$\mathbf{B}_\kappa(t) = \begin{bmatrix} -\text{diag}(\mathbf{1}_2) & -\mathbf{K}_{\text{FB},\varphi} & \mathbf{K}_{\text{FT},\varphi} \\ \mathbf{0}_{2 \times 2} & -\text{diag}(\mathbf{1}_2) & \mathbf{0}_{2 \times 2} \end{bmatrix} \quad (3.71)$$

$$\mathbf{E}_\kappa(t) = \begin{bmatrix} \mathbf{K}_{\text{FFB},\varphi} \\ \text{diag}(\mathbf{1}_2) \end{bmatrix} \quad (3.72)$$

$$\mathbf{C}_\kappa(t) = \begin{bmatrix} \frac{\mathbf{K}_{\text{FB},\alpha}}{T_{\text{FB},\alpha}} & \mathbf{K}_{\text{FFB},\alpha} \frac{\mathbf{K}_{\text{FB},\varphi}}{T_{\text{FB},\varphi}} \end{bmatrix} \quad (3.73)$$

$$\mathbf{D}_\kappa(t) = \begin{bmatrix} -\mathbf{K}_{\text{FB},\alpha} & \mathbf{K}_{\text{FT},\alpha} - \mathbf{K}_{\text{FFB},\alpha} \mathbf{K}_{\text{FB},\varphi} & \mathbf{K}_{\text{FFB},\alpha} \mathbf{K}_{\text{FT},\varphi} \end{bmatrix} \quad (3.74)$$

$$\mathbf{F}_\kappa(t) = \mathbf{K}_{\text{FFB},\alpha} \mathbf{K}_{\text{FFB},\varphi} \quad (3.75)$$

The sizes of these matrices follow directly from (3.66)–(3.69). Evidently, the control software is an LTI system, too. Indeed, this is one of the reasons for the popularity of the DQ frame since its invention almost a century ago [26].

Reference Calculation

In grid-forming CIDERs, the reference angle θ is computed from the frequency setpoint f_σ through integration over time

$$\theta(t) = 2\pi \int f_\sigma dt = 2\pi f_\sigma t \quad (3.76)$$

Hence, in line with Hyp. 15, the following hypothesis is made.

Hypothesis 19. *In steady state, the frequency setpoints of all grid-forming CIDERs are equal to the fundamental frequency:*

$$f_\sigma = f_1 \quad (3.77)$$

Indeed, if the grid-forming CIDERs attempted to impose incompatible frequencies on the power system, no steady-state equilibrium could exist. The reference voltage $\mathbf{v}_{\varphi,\text{DQ}}^*$ is calculated from the voltage setpoint V_σ as follows:

Hypothesis 20. *The reference voltage for the grid-forming CIDERs is calculated as*

$$\mathbf{v}_{\varphi,\text{DQ}}^*(t) = \sqrt{\frac{3}{2}} \begin{bmatrix} V_\sigma \\ 0 \end{bmatrix} \quad (3.78)$$

where V_σ is the setpoint for the peak voltage.

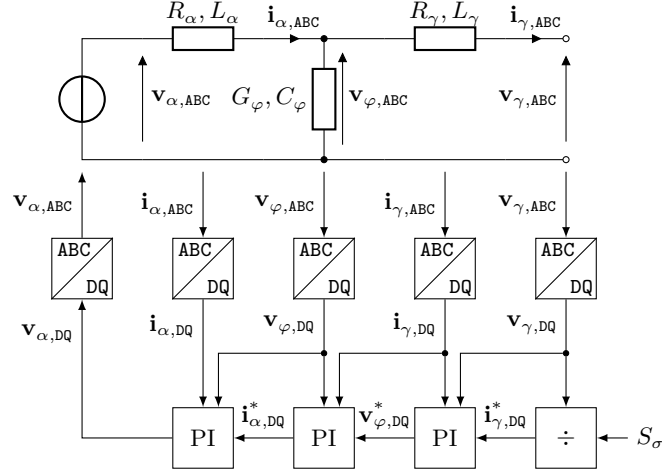


Figure 3.7: Schematic diagram of a grid-following CIDER with an LCL filter.

3.3.2 Grid-Following CIDER – Considering Only AC-Side Characteristics

Fig. 3.7 shows the schematic diagram of a typical grid-following CIDER. Its power hardware consists of a PWM actuator, modelled as an ideal AC voltage source (see Section 3.2.1) and an LCL filter, and its control software of a three-stage PI controller. The actuator is a three-leg power converter, which is commonly used for grid-following CIDERs.

Power Hardware

The state of the power hardware is described by the inductor currents $\mathbf{i}_{\alpha,ABC} \in \mathbb{R}^{3 \times 1}$ and $\mathbf{i}_{\gamma,ABC} \in \mathbb{R}^{3 \times 1}$ and the capacitor voltage $\mathbf{v}_{\varphi,ABC} \in \mathbb{R}^{3 \times 1}$. The input is the actuator voltage $\mathbf{v}_{\alpha,ABC} \in \mathbb{R}^{3 \times 1}$ and the disturbance is the grid voltage $\mathbf{v}_{\gamma,ABC} \in \mathbb{R}^{3 \times 1}$. The output consists of the state and the disturbance. Formally

$$\mathbf{x}_{\pi}(t) = \begin{bmatrix} \mathbf{i}_{\alpha,ABC}(t) \\ \mathbf{v}_{\varphi,ABC}(t) \\ \mathbf{i}_{\gamma,ABC}(t) \end{bmatrix} \in \mathbb{R}^{9 \times 1} \quad (3.79)$$

$$\mathbf{u}_{\pi}(t) = \mathbf{v}_{\alpha,ABC}(t) \in \mathbb{R}^{3 \times 1} \quad (3.80)$$

$$\mathbf{w}_{\pi}(t) = \mathbf{v}_{\gamma,ABC}(t) \in \mathbb{R}^{3 \times 1} \quad (3.81)$$

$$\mathbf{y}_{\pi}(t) = \begin{bmatrix} \mathbf{x}_{\pi}(t) \\ \mathbf{w}_{\pi}(t) \end{bmatrix} \in \mathbb{R}^{12 \times 1} \quad (3.82)$$

Chapter 3. Derivation of the Specific Models of the CIDERs

The matrices of the state-space model are obtained as

$$\mathbf{A}_\pi(t) = \begin{bmatrix} -\mathbf{L}_\alpha^{-1}\mathbf{R}_\alpha & -\mathbf{L}_\alpha^{-1} & \mathbf{0}_{3 \times 3} \\ \mathbf{C}_\varphi^{-1} & -\mathbf{C}_\varphi^{-1}\mathbf{G}_\varphi & -\mathbf{C}_\varphi^{-1} \\ \mathbf{0}_{3 \times 3} & \mathbf{L}_\gamma^{-1} & -\mathbf{L}_\gamma^{-1}\mathbf{R}_\gamma \end{bmatrix} \quad (3.83)$$

$$\mathbf{B}_\pi(t) = \begin{bmatrix} \mathbf{L}_\alpha^{-1} \\ \mathbf{0}_{6 \times 3} \end{bmatrix} \quad (3.84)$$

$$\mathbf{E}_\pi(t) = \begin{bmatrix} \mathbf{0}_{6 \times 3} \\ -\mathbf{L}_\varphi^{-1} \end{bmatrix} \quad (3.85)$$

$$\mathbf{C}_\pi(t) = \begin{bmatrix} \text{diag}(\mathbf{1}_9) \\ \mathbf{0}_{3 \times 9} \end{bmatrix} \quad (3.86)$$

$$\mathbf{D}_\pi(t) = \mathbf{0}_{12 \times 3} \quad (3.87)$$

$$\mathbf{F}_\pi(t) = \begin{bmatrix} \mathbf{0}_{9 \times 3} \\ \text{diag}(\mathbf{1}_3) \end{bmatrix} \quad (3.88)$$

Their sizes follow straightforward from (3.79)–(3.82). Note that these matrices are time-invariant as in the grid-forming case.

Control Software

Analogously, the state-space variables of the control software are given by

$$\mathbf{x}_\kappa(t) = \int \begin{bmatrix} \Delta \mathbf{i}_{\alpha, \text{DQ}}(t) \\ \Delta \mathbf{v}_{\varphi, \text{DQ}}(t) \\ \Delta \mathbf{i}_{\gamma, \text{DQ}}(t) \end{bmatrix} dt \in \mathbb{R}^{6 \times 1} \quad (3.89)$$

$$\mathbf{u}_\kappa(t) = \begin{bmatrix} \mathbf{i}_{\alpha, \text{DQ}}(t) \\ \mathbf{v}_{\varphi, \text{DQ}}(t) \\ \mathbf{i}_{\gamma, \text{DQ}}(t) \\ \mathbf{v}_{\gamma, \text{DQ}}(t) \end{bmatrix} \in \mathbb{R}^{8 \times 1} \quad (3.90)$$

$$\mathbf{w}_\kappa(t) = \mathbf{i}_{\gamma, \text{DQ}}^*(t) \in \mathbb{R}^{2 \times 1} \quad (3.91)$$

$$\mathbf{y}_\kappa(t) = \mathbf{v}_{\alpha, \text{DQ}}(t) \in \mathbb{R}^{2 \times 1} \quad (3.92)$$

The matrices of the state-space model are obtained as follows. As before, for the sake of readability the following substitution has been employed, $(\mathbf{K}_{\text{FF}} + \mathbf{K}_{\text{FB}}) = \mathbf{K}_{\text{FFB}}$.

$$\mathbf{A}_\kappa(t) = \begin{bmatrix} \mathbf{0}_{2 \times 2} & \frac{\mathbf{K}_{\text{FB}, \varphi}}{T_{\text{FB}, \varphi}} & \mathbf{K}_{\text{FFB}, \varphi} \frac{\mathbf{K}_{\text{FB}, \gamma}}{T_{\text{FB}, \gamma}} \\ \mathbf{0}_{2 \times 2} & \mathbf{0}_{2 \times 2} & \frac{\mathbf{K}_{\text{FB}, \gamma}}{T_{\text{FB}, \gamma}} \\ \mathbf{0}_{2 \times 2} & \mathbf{0}_{2 \times 2} & \mathbf{0}_{2 \times 2} \end{bmatrix} \quad (3.93)$$

$$\mathbf{B}_\kappa(t) = \begin{bmatrix} -\text{diag}(\mathbf{1}_2) & -\mathbf{K}_{\text{FB},\varphi} & \mathbf{K}_{\text{FT},\varphi} - \mathbf{K}_{\text{FFB},\varphi}\mathbf{K}_{\text{FB},\gamma} & \mathbf{K}_{\text{FFB},\varphi}\mathbf{K}_{\text{FT},\gamma} \\ \mathbf{0}_{2 \times 2} & -\text{diag}(\mathbf{1}_2) & -\mathbf{K}_{\text{FB},\gamma} & \mathbf{K}_{\text{FT},\gamma} \\ \mathbf{0}_{2 \times 2} & \mathbf{0}_{2 \times 2} & -\text{diag}(\mathbf{1}_2) & \mathbf{0}_{2 \times 2} \end{bmatrix} \quad (3.94)$$

$$\mathbf{E}_\kappa(t) = \begin{bmatrix} \mathbf{K}_{\text{FFB},\varphi}\mathbf{K}_{\text{FFB},\gamma} \\ \mathbf{K}_{\text{FFB},\gamma} \\ \text{diag}(\mathbf{1}_2) \end{bmatrix} \quad (3.95)$$

$$\mathbf{C}_\kappa(t) = \begin{bmatrix} \frac{\mathbf{K}_{\text{FB},\alpha}}{T_{\text{FB},\alpha}} & \mathbf{K}_{\text{FFB},\alpha} \frac{\mathbf{K}_{\text{FB},\varphi}}{T_{\text{FB},\varphi}} & \mathbf{K}_{\text{FFB},\alpha}\mathbf{K}_{\text{FFB},\varphi} \frac{\mathbf{K}_{\text{FB},\gamma}}{T_{\text{FB},\gamma}} \end{bmatrix} \quad (3.96)$$

$$\mathbf{D}_\kappa(t) = \begin{bmatrix} -\mathbf{K}_{\text{FB},\alpha} & \mathbf{K}_{\text{FT},\alpha} - \mathbf{K}_{\text{FFB},\alpha}\mathbf{K}_{\text{FB},\varphi} & (\mathbf{D}_\kappa)_3 & \mathbf{K}_{\text{FFB},\alpha}\mathbf{K}_{\text{FFB},\varphi}\mathbf{K}_{\text{FB},\gamma} \end{bmatrix} \quad (3.97)$$

$$(\mathbf{D}_\kappa)_3 = \mathbf{K}_{\text{FFB},\alpha} + \mathbf{K}_{\text{FT},\varphi} - \mathbf{K}_{\text{FFB},\varphi}\mathbf{K}_{\text{FB},\gamma} \quad (3.98)$$

$$\mathbf{F}_\kappa(t) = \prod_{i \in \{\alpha, \varphi, \gamma\}} \{\mathbf{K}_{\text{FFB},i}\} \quad (3.99)$$

Their sizes follow straightforward from (3.89)–(3.92). Note that these matrices are also time-invariant.

Reference Calculation

The reference calculation of this CIDER is a PQ law, which is in general a nonlinear function. Section 3.2.5 shows how this function can be approximated in order to fit into the modelling framework.

3.3.3 Grid-Following CIDER – Including DC-Side Characteristics

In this section, the detailed model of a grid-following CIDER including the DC-side dynamics is developed. Specifically, a CIDER with DC-voltage control is considered. To this end, the DC side is represented by the controlled current-source model as was introduced in Section 3.1. The precise structure of the CIDER is shown in Fig. 3.8. The power hardware consists of an LCL filter on the AC side, plus a current source and a link capacitor on the DC side. The control software is composed of a cascade of controllers. For the sake of illustration, PI controllers are considered. Note that the measurements and control signals, that are exchanged between the power hardware and control software, pass through coordinate transformations. In this particular case, the Park transform is employed. The reference calculation computes the current setpoint for the control software based on the power setpoint and the voltage at the point of connection.

Power Hardware

Assuming that the CIDER exhibits constant-power behaviour, the DC equivalent can be described by a controlled current source [82].

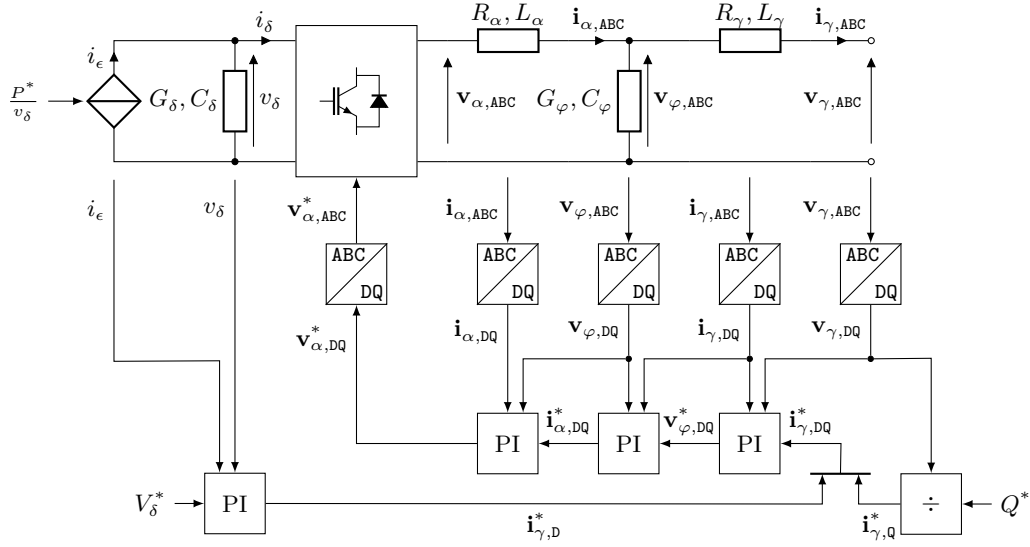


Figure 3.8: Overview of the grid-following CIDER including DC-side dynamics. The power hardware is connected through measurements and coordinate transformations (i.e., in case of AC signals) to the control software.

Hypothesis 21. *The DC equivalent current i_ϵ is computed in order to track the power setpoint P^* using the DC-side voltage v_δ :*

$$i_\epsilon(t) = \frac{P^*}{v_\delta(t)} \quad (3.100)$$

In general, it can be assumed that the DC-side voltage control loop of the CIDER is designed to track its reference with zero error (e.g., a well-tuned PI controller [83]). Namely, in steady-state its DC component $V_{\delta,0}$ follows the reference V_δ^* .

Hypothesis 22. *The DC-voltage control tracks the DC-voltage reference in the DC component without steady-state error. That is,:*

$$V_{\delta,0} = V_\delta^* \quad (3.101)$$

Typically, the DC-voltage harmonics are negligible when compared to the DC component [65]. The following assumption is made.

Hypothesis 23. *The time-variant signal content of $v_\delta(t)$, as given by $\xi(t)$ below, is low.*

$$v_\delta(t) = V_{\delta,0}(1 + \xi(t)), \quad |\xi(t)| \ll 1 \quad (3.102)$$

3.3 Library of Resource Models

As a consequence of Hyp. 22 and Hyp. 23, (3.100) can be approximated using a first order Taylor series around the DC voltage reference V_δ^* .

$$i_\epsilon(t) \approx \frac{P^*}{V_\delta^*} - \frac{P^*}{V_\delta^{*2}}(v_\delta(t) - V_\delta^*) \quad (3.103)$$

$$= 2\frac{P^*}{V_\delta^*} - \frac{P^*}{V_\delta^{*2}}v_\delta(t) \quad (3.104)$$

Note that this approximation of the DC equivalent current is in line with the theory developed in Section 2.4.2 and Section 2.4.3.

The AC/DC converter is represented by an average model, which was explained in detail in Section 3.2.1. The operating point considered in this context is given by

$$\mathbf{y}_o(t) = \begin{bmatrix} \bar{\mathbf{v}}_{\alpha,ABC}^*(t) \\ \bar{\mathbf{i}}_{\alpha,ABC}(t) \\ \bar{v}_\delta(t) \end{bmatrix} \quad (3.105)$$

The time-domain state-space model of the power hardware is obtained by combining the differential equations (3.8) and (3.9) of the filter stages. Notably, the filter equations for DC-link capacitor follow directly from (3.8) and (3.9) by setting the dimension of the vectors to 1 (i.e., a single wire rather than three phases).

To obtain the state-space model of the power hardware, the equations of the AC and the DC filter stages are combined with the linearized actuator model and the current of the DC equivalent. More precisely, one needs to insert (3.5) and (3.6) as well as (3.104) into the equations of the filter stages and, then, derive the corresponding state-space model.

Thus, the state of the combined power hardware is given by the inductor currents $\mathbf{i}_{\alpha,ABC}$ and $\mathbf{i}_{\gamma,ABC}$ and the capacitor voltage $\mathbf{v}_{\varphi,ABC}$ on the AC side and the capacitor voltage v_δ on the DC side. The input is the actuator voltage reference $\mathbf{v}_{\alpha,ABC}^*$. The disturbances are the grid voltage $\mathbf{v}_{\gamma,ABC}$, the average DC-side equivalent current described by $\frac{P^*}{V_\delta^*}$ and the operating point of the actuator voltage reference $\bar{\mathbf{v}}_{\alpha,ABC}^*$. The output includes the state and the grid voltage as well as the DC-side equivalent current i_ϵ . Namely,

$$\mathbf{x}_\pi(t) = \begin{bmatrix} \mathbf{i}_{\alpha,ABC}(t) \\ \mathbf{v}_{\varphi,ABC}(t) \\ \mathbf{i}_{\gamma,ABC}(t) \\ v_\delta(t) \end{bmatrix} \quad (3.106)$$

$$\mathbf{u}_\pi(t) = \mathbf{v}_{\alpha,ABC}^*(t) \quad (3.107)$$

$$\mathbf{w}_\pi(t) = \begin{bmatrix} \mathbf{v}_{\gamma,ABC}(t) \\ \frac{P^*}{V_\delta^*} \\ \bar{\mathbf{v}}_{\alpha,ABC}^*(t) \end{bmatrix} \quad (3.108)$$

Chapter 3. Derivation of the Specific Models of the CIDERs

$$\mathbf{y}_\pi(t) = \begin{bmatrix} \mathbf{x}_\pi(t) \\ \mathbf{v}_{\gamma,ABC}(t) \\ i_\epsilon(t) \end{bmatrix} \quad (3.109)$$

As one can see from (3.5) and (3.6) the third term is bilinear w.r.t. the components of the operating point (i.e., $\bar{v}_\delta \bar{\mathbf{v}}_{\alpha,ABC}^*$ and $\bar{\mathbf{i}}_{\alpha,ABC}^\top \bar{\mathbf{v}}_{\alpha,ABC}^*$). In order to put this in the form of an LTP system, one of the quantities (i.e., the voltage reference $\bar{\mathbf{v}}_{\alpha,ABC}^*$) is added to the disturbance vector, while \bar{v}_δ and $\bar{\mathbf{i}}_{\alpha,ABC}$ enter the matrices. Similarly, the first term of (3.104) (i.e., $\frac{P^*}{V_\delta^*}$) is defined as a disturbance to the state-space model.

Recall that the matrices can be separated in two terms: one which is invariant w.r.t. the operating point and one which depends on it.

$$\mathbf{A}_\pi(t) = \tilde{\mathbf{A}}_\pi(t) + \bar{\mathbf{A}}_\pi(t, \mathbf{y}_o(t)) \quad (3.110)$$

Each of these matrices can be described by its Fourier coefficients as in (2.9). The matrices that are invariant w.r.t. the operating point are given by

$$\tilde{\mathbf{A}}_{\pi,0} = \begin{bmatrix} -\mathbf{L}_\alpha^{-1} \mathbf{R}_\alpha & -\mathbf{L}_\alpha^{-1} & \mathbf{0}_{3 \times 3} & \mathbf{0}_{3 \times 1} \\ \mathbf{C}_\varphi^{-1} & -\mathbf{C}_\varphi^{-1} \mathbf{G}_\varphi & -\mathbf{C}_\varphi^{-1} & \mathbf{0}_{3 \times 1} \\ \mathbf{0}_{3 \times 3} & \mathbf{L}_\gamma^{-1} & -\mathbf{L}_\gamma^{-1} \mathbf{R}_\gamma & \mathbf{0}_{3 \times 1} \\ \mathbf{0}_{1 \times 3} & \mathbf{0}_{1 \times 3} & \mathbf{0}_{1 \times 3} & -C_\delta^{-1} G_\delta - C_\delta^{-1} \frac{P^*}{V_\delta^{*2}} \end{bmatrix} \quad (3.111)$$

$$\tilde{\mathbf{B}}_{\pi,0} = \mathbf{0}_{10 \times 3} \quad (3.112)$$

$$\tilde{\mathbf{E}}_{\pi,0} = \begin{bmatrix} \mathbf{0}_{6 \times 3} & \mathbf{0}_{6 \times 1} & \mathbf{0}_{6 \times 3} \\ -\mathbf{L}_\gamma^{-1} & \mathbf{0}_{3 \times 1} & \mathbf{0}_{3 \times 3} \\ \mathbf{0}_{1 \times 3} & -2C_\delta^{-1} & \mathbf{0}_{1 \times 3} \end{bmatrix} \quad (3.113)$$

$$\tilde{\mathbf{C}}_{\pi,0} = \begin{bmatrix} \text{diag}(\mathbf{1}_9) & \mathbf{0}_{9 \times 1} \\ \mathbf{0}_{1 \times 9} & 1 \\ \mathbf{0}_{3 \times 9} & \mathbf{0}_{3 \times 1} \\ \mathbf{0}_{1 \times 9} & -\frac{P^*}{V_\delta^{*2}} \end{bmatrix} \quad (3.114)$$

$$\tilde{\mathbf{D}}_{\pi,0} = \mathbf{0}_{14 \times 3} \quad (3.115)$$

$$\tilde{\mathbf{F}}_{\pi,0} = \begin{bmatrix} \mathbf{0}_{10 \times 3} & \mathbf{0}_{10 \times 1} & \mathbf{0}_{10 \times 3} \\ \text{diag}(\mathbf{1}_3) & \mathbf{0}_{3 \times 1} & \mathbf{0}_{3 \times 3} \\ \mathbf{0}_{1 \times 3} & 2 & \mathbf{0}_{1 \times 3} \end{bmatrix} \quad (3.116)$$

and all other Fourier coefficients equal to zero. The matrices that are a function of the operating point are given by

$$\bar{\mathbf{A}}_{\pi,h} = \begin{bmatrix} \mathbf{0}_{3 \times 3} & \mathbf{0}_{3 \times 6} & \frac{1}{V_\delta^*} \mathbf{L}_\alpha^{-1} \bar{\mathbf{V}}_{\alpha,ABC,h}^* \\ \mathbf{0}_{6 \times 3} & \mathbf{0}_{6 \times 6} & \mathbf{0}_{6 \times 1} \\ -\frac{1}{V_\delta^*} C_\delta^{-1} \bar{\mathbf{V}}_{\alpha,ABC,h}^{*\top} & \mathbf{0}_{1 \times 6} & 0 \end{bmatrix} \quad (3.117)$$

$$\bar{\mathbf{B}}_{\pi,h} = \begin{bmatrix} \frac{1}{V_\delta^*} \mathbf{L}_\alpha^{-1} \bar{V}_{\delta,h} \\ \mathbf{0}_{6 \times 3} \\ -\frac{1}{V_\delta^*} C_\delta^{-1} \bar{\mathbf{I}}_{\alpha,ABC,h}^\top \end{bmatrix} \quad (3.118)$$

$$\bar{\mathbf{E}}_{\pi,h} = \begin{bmatrix} \mathbf{0}_{3 \times 4} & -\frac{1}{V_\delta^*} \mathbf{L}_\alpha^{-1} \bar{V}_{\delta,h} \\ \mathbf{0}_{3 \times 4} & \mathbf{0}_{3 \times 3} \\ \mathbf{0}_{3 \times 4} & \mathbf{0}_{3 \times 3} \\ \mathbf{0}_{1 \times 4} & \frac{1}{V_\delta^*} C_\delta^{-1} \bar{\mathbf{I}}_{\alpha,ABC,h}^\top \end{bmatrix} \quad (3.119)$$

$$\bar{\mathbf{C}}_{\pi,h} = \mathbf{0}_{14 \times 10} \quad (3.120)$$

$$\bar{\mathbf{D}}_{\pi,h} = \mathbf{0}_{14 \times 3} \quad (3.121)$$

$$\bar{\mathbf{F}}_{\pi,h} = \mathbf{0}_{14 \times 7} \quad (3.122)$$

Note that, as opposed to the CIDER models which include only the AC-side components, the above-stated matrices possess Fourier coefficients at harmonic frequencies that are non-zero. This characteristic introduces additional coupling between harmonics.

Control Software

The state-space model of the control software is obtained employing the theory described in Section 3.3.2. The DC-side controller provides the reference for the DC current i_δ^* , which is used for the grid current reference in the D-component $i_{\gamma,D}^*$. Namely,

$$i_{\gamma,D}^*(t) = i_\delta^*(t) \quad (3.123)$$

This is a direct consequence of the assumed power conversion laws in Hyp. 10 (i.e., neglecting losses on the AC side).

The generic description of a controller stage that corresponds to a filter stage of the power hardware was given in Section 3.2.3. The description of the DC-side controller stage follows directly from this generic case by setting the dimension to 1.

Combining (3.123) with the equations of the controller stages from the AC and DC side leads to the state-space model of the control software. As can be seen from Fig. 3.8 the control software is composed of PI controllers. By consequence, its state is given by the temporal integrals of the errors w.r.t. the inductor currents $\Delta \mathbf{i}_{\alpha,DQ}$ and $\Delta \mathbf{i}_{\gamma,DQ}$, and the capacitor voltage $\Delta v_{\varphi,DQ}$. The input and output vectors are defined by the interconnection with the power hardware as shown in Fig. 3.8. The disturbance is the Q-component of the grid reference current $i_{\gamma,Q}^*$ and the DC-voltage reference V_δ^* . Accordingly

$$\mathbf{x}_\kappa(t) := \int \begin{bmatrix} \Delta \mathbf{i}_{\alpha,DQ}(t) \\ \Delta v_{\varphi,DQ}(t) \\ \Delta \mathbf{i}_{\gamma,DQ}(t) \\ \Delta v_\delta(t) \end{bmatrix} dt = \begin{bmatrix} \mathbf{x}_{\kappa,1}(t) \\ \mathbf{x}_{\kappa,2}(t) \\ \mathbf{x}_{\kappa,3}(t) \\ x_{\kappa,4}(t) \end{bmatrix} \quad (3.124)$$

$$\mathbf{u}_\kappa(t) := \begin{bmatrix} \mathbf{i}_{\alpha,\text{DQ}}(t) \\ \mathbf{v}_{\varphi,\text{DQ}}(t) \\ \mathbf{i}_{\gamma,\text{DQ}}(t) \\ v_\delta(t) \\ \mathbf{v}_{\gamma,\text{DQ}}(t) \\ i_\epsilon(t) \end{bmatrix} = \begin{bmatrix} \mathbf{u}_{\kappa,1}(t) \\ \mathbf{u}_{\kappa,2}(t) \\ \mathbf{u}_{\kappa,3}(t) \\ u_{\kappa,4}(t) \\ \mathbf{u}_{\kappa,5}(t) \\ u_{\kappa,6}(t) \end{bmatrix} \quad (3.125)$$

$$\mathbf{w}_\kappa(t) := \begin{bmatrix} i_{\gamma,\text{Q}}^*(t) \\ V_\delta^* \end{bmatrix} = \begin{bmatrix} w_{\kappa,1}(t) \\ w_{\kappa,2}(t) \end{bmatrix} \quad (3.126)$$

$$\mathbf{y}_\kappa(t) := \mathbf{v}_{\alpha,\text{DQ}}^*(t) \quad (3.127)$$

As opposed to the power hardware, the state-space model of the control software is described purely by constant parameters, since no linearization needs to be performed. Therefore, all matrices can be directly described by (3.128)–(3.141). For the sake of readability the following substitutions have been employed, $(K_{\text{FF}} + K_{\text{FB}}) = K_{\text{FFB}}$ and similarly $(\mathbf{K}_{\text{FF}} + \mathbf{K}_{\text{FB}}) = \mathbf{K}_{\text{FFB}}$.

$$\tilde{\mathbf{A}}_{\kappa,0} = \begin{bmatrix} \mathbf{0}_{2 \times 2} & \frac{\mathbf{K}_{\text{FB},\varphi}}{T_{\text{FB},\varphi}} & \mathbf{K}_{\text{FFB},\varphi} \frac{\mathbf{K}_{\text{FB},\gamma}}{T_{\text{FB},\gamma}} & \mathbf{K}_{\text{FFB},\varphi} \mathbf{K}_{\text{FFB},\gamma} \mathbf{e}_1 \frac{K_{\text{FB},\delta}}{T_{\text{FB},\delta}} \\ \mathbf{0}_{2 \times 2} & \mathbf{0}_{2 \times 2} & \frac{\mathbf{K}_{\text{FB},\gamma}}{T_{\text{FB},\gamma}} & \mathbf{K}_{\text{FFB},\gamma} \mathbf{e}_1 \frac{K_{\text{FB},\delta}}{T_{\text{FB},\delta}} \\ \mathbf{0}_{1 \times 2} & \mathbf{0}_{1 \times 2} & \mathbf{0}_{1 \times 2} & \frac{K_{\text{FB},\delta}}{T_{\text{FB},\delta}} \\ \mathbf{0}_{1 \times 2} & \mathbf{0}_{1 \times 2} & \mathbf{0}_{1 \times 2} & 0 \\ \mathbf{0}_{1 \times 2} & \mathbf{0}_{1 \times 2} & \mathbf{0}_{1 \times 2} & 0 \end{bmatrix} \quad (3.128)$$

$$\tilde{\mathbf{B}}_{\kappa,0} = \begin{bmatrix} -\text{diag}(\mathbf{1}_2) & -\mathbf{K}_{\text{FB},\varphi} & (\tilde{\mathbf{B}}_{\kappa,0})_{13} & (\tilde{\mathbf{B}}_{\kappa,0})_{14} & \mathbf{K}_{\text{FFB},\varphi} \mathbf{K}_{\text{FT},\gamma} & (\tilde{\mathbf{B}}_{\kappa,0})_{16} \\ \mathbf{0}_{2 \times 2} & -\text{diag}(\mathbf{1}_2) & -\mathbf{K}_{\text{FB},\gamma} & (\tilde{\mathbf{B}}_{\kappa,0})_{24} & \mathbf{K}_{\text{FT},\gamma} & \mathbf{K}_{\text{FFB},\gamma} \mathbf{e}_1 K_{\text{FT},\delta} \\ \mathbf{0}_{1 \times 2} & \mathbf{0}_{1 \times 2} & -\mathbf{e}_1^\top & -K_{\text{FB},\delta} & \mathbf{0}_{1 \times 2} & K_{\text{FT},\delta} \\ \mathbf{0}_{1 \times 2} & \mathbf{0}_{1 \times 2} & -\mathbf{e}_2^\top & 0 & \mathbf{0}_{1 \times 2} & 0 \\ \mathbf{0}_{1 \times 2} & \mathbf{0}_{1 \times 2} & \mathbf{0}_{1 \times 2} & -1 & \mathbf{0}_{1 \times 2} & 0 \end{bmatrix} \quad (3.129)$$

$$(\tilde{\mathbf{B}}_{\kappa,0})_{13} = \mathbf{K}_{\text{FT},\varphi} - \mathbf{K}_{\text{FFB},\varphi} \mathbf{K}_{\text{FB},\gamma} \quad (3.130)$$

$$(\tilde{\mathbf{B}}_{\kappa,0})_{14} = -\mathbf{K}_{\text{FFB},\varphi} \mathbf{K}_{\text{FFB},\gamma} \mathbf{e}_1 K_{\text{FB},\delta} \quad (3.131)$$

$$(\tilde{\mathbf{B}}_{\kappa,0})_{16} = \mathbf{K}_{\text{FFB},\varphi} \mathbf{K}_{\text{FFB},\gamma} \mathbf{e}_1 K_{\text{FT},\delta} \quad (3.132)$$

$$(\tilde{\mathbf{B}}_{\kappa,0})_{24} = -\mathbf{K}_{\text{FFB},\gamma} \mathbf{e}_1 K_{\text{FB},\delta} \quad (3.133)$$

$$\tilde{\mathbf{E}}_{\kappa,0} = \begin{bmatrix} \mathbf{K}_{\text{FFB},\varphi} \mathbf{K}_{\text{FFB},\gamma} \mathbf{e}_2 & \mathbf{K}_{\text{FFB},\varphi} \mathbf{K}_{\text{FFB},\gamma} \mathbf{e}_1 K_{\text{FFB},\delta} \\ \mathbf{K}_{\text{FFB},\gamma} \mathbf{e}_2 & \mathbf{K}_{\text{FFB},\gamma} \mathbf{e}_1 K_{\text{FFB},\delta} \\ 0 & K_{\text{FFB},\delta} \\ 1 & 0 \\ 0 & 1 \end{bmatrix} \quad (3.134)$$

$$\tilde{\mathbf{C}}_{\kappa,0} = \left[\frac{\mathbf{K}_{\text{FB},\alpha}}{T_{\text{FB},\alpha}} \quad \mathbf{K}_{\text{FFB},\alpha} \frac{\mathbf{K}_{\text{FB},\varphi}}{T_{\text{FB},\varphi}} \quad \mathbf{K}_{\text{FFB},\alpha} \mathbf{K}_{\text{FFB},\varphi} \frac{\mathbf{K}_{\text{FB},\gamma}}{T_{\text{FB},\gamma}} \quad \mathbf{K}_{\text{FFB},\alpha} \mathbf{K}_{\text{FFB},\varphi} \mathbf{K}_{\text{FFB},\gamma} \mathbf{e}_1 \frac{K_{\text{FB},\delta}}{T_{\text{FB},\delta}} \right] \quad (3.135)$$

$$\tilde{\mathbf{D}}_{\kappa,0} = \left[-\mathbf{K}_{\text{FB},\alpha} \quad (\tilde{\mathbf{D}}_{\kappa,0})_2 \quad (\tilde{\mathbf{D}}_{\kappa,0})_3 \quad (\tilde{\mathbf{D}}_{\kappa,0})_4 \quad \mathbf{K}_{\text{FFB},\alpha} \mathbf{K}_{\text{FFB},\varphi} \mathbf{K}_{\text{FT},\gamma} \quad (\tilde{\mathbf{D}}_{\kappa,0})_6 \right] \quad (3.136)$$

$$(\tilde{\mathbf{D}}_{\kappa,0})_2 = \mathbf{K}_{\text{FT},\alpha} - \mathbf{K}_{\text{FFB},\alpha} \mathbf{K}_{\text{FB},\varphi} \quad (3.137)$$

$$(\tilde{\mathbf{D}}_{\kappa,0})_3 = \mathbf{K}_{\text{FFB},\alpha} (\mathbf{K}_{\text{FT},\varphi} - \mathbf{K}_{\text{FFB},\varphi} \mathbf{K}_{\text{FB},\gamma}) \quad (3.138)$$

$$(\tilde{\mathbf{D}}_{\kappa,0})_4 = -\mathbf{K}_{\text{FFB},\alpha} \mathbf{K}_{\text{FFB},\varphi} \mathbf{K}_{\text{FFB},\gamma} \mathbf{e}_1 K_{\text{FB},\delta} \quad (3.139)$$

$$(\tilde{\mathbf{D}}_{\kappa,0})_6 = \mathbf{K}_{\text{FFB},\alpha} \mathbf{K}_{\text{FFB},\varphi} \mathbf{K}_{\text{FFB},\gamma} \mathbf{e}_1 K_{\text{FT},\delta} \quad (3.140)$$

$$\tilde{\mathbf{F}}_{\kappa,0} = \begin{bmatrix} \mathbf{K}_{\text{FFB},\alpha} \mathbf{K}_{\text{FFB},\varphi} \mathbf{K}_{\text{FFB},\gamma} \mathbf{e}_2 & \mathbf{K}_{\text{FFB},\alpha} \mathbf{K}_{\text{FFB},\varphi} \mathbf{K}_{\text{FFB},\gamma} \mathbf{e}_1 K_{\text{FFB},\delta} \end{bmatrix} \quad (3.141)$$

Reference Calculation

In Fig. 3.8, the calculation of the Q-component of the grid reference current $i_{\gamma,\text{Q}}^*(t)$ is performed using the reactive power setpoint Q^* and the D-component of the grid voltage.

$$i_{\gamma,\text{Q}}^*(t) = \frac{Q^*}{v_{\gamma,\text{D}}(t)} \quad (3.142)$$

In Section 3.2.5, it is described in detail how this reference calculation is approximated in order to be incorporated into the modelling framework.

3.3.4 Network-Interfacing Converters

For the analysis of hybrid AC/DC grids, the NICs that interconnect AC and DC subsystems need to be represented in detail. Recall the definition Def. 4 of NIC introduced in Section 2.2.2. As opposed to the CIDERs, that are single-port resources, a NIC is a two-port device, meaning it possesses one terminal on the AC and one on the DC side. The structure of a NIC is similar to the one of a CIDER introduced in Section 3.3.3. Like a CIDER, a NIC consists of power hardware and control software. As opposed to a CIDER, a NIC, being a two-port device, possesses two degrees of freedom w.r.t. its controlled quantities. Therefore, a NIC can regulate two electrical quantities at its ports, with the remaining two adjusting in response.

Power Hardware

The generic power hardware of a NIC is modelled by the structure in Fig. 3.9. It consists of an *LCL* filter on the AC side and a DC-link capacitor on the DC side. Note that, as compared to the CIDER in [18], a NIC has an additionally interface to the DC subsystem. Hence, the terminals of a NIC are characterized by the AC current i^{AC} and voltage v^{AC} , plus the DC current i^{DC} and voltage v^{DC} . The development of the time-domain state-space model of the power hardware including the DC-link capacitor is explained in detail in Section 3.3.3.

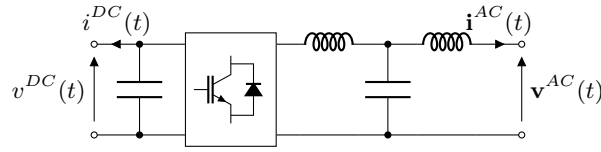


Figure 3.9: Simplified representation of the power hardware of a NIC.

Control Software and Reference Calculation

Two different types of control laws are considered for the NICs: regulation of either i) the DC-voltage and reactive power or ii) the active and reactive power injected on the AC side. In this thesis, these two types of resources are referred to as $V_{DC}Q$ -controlled NIC and PQ -controlled NIC, respectively. The time-domain state-space model of the control software and approximations of the reference calculation of a $V_{DC}Q$ -controlled NIC are shown in detail in Section 3.3.3. The control software and approximations of the reference calculation of a PQ -controlled NIC are analogous to the one of the grid-following CIDER proposed in Section 3.3.2. Further details on the derivations can be found in the respective sections.

Due to the similarity of the models of NICs and CIDERs, the individual grid responses of the NICs will not be validated in detail. Instead, in Section 4.4.3 it is shown, that the HPF algorithm employing these models has a good accuracy.

3.4 Validation of the Proposed Models

This section provides the validation of the grid responses of the proposed CIDERs, for both the HDR and HTF (i.e., the HSS used in the HSA). First, the methodology and KPIs, as well as the test setup are introduced. In order to assess the accuracy of the CIDER models, they are compared to TDS. The detailed models of the CIDERs are connected to a TE that injects the harmonics. Additionally, a detailed analysis of the needed order of the Taylor expansion in the context of the reference calculation is conducted.

3.4.1 Methodology and Key Performance Indicators

Test Setup

For the validation of the proposed CIDER models, the test setup shown in Fig. 3.10 is used. It consists of two parts: a TE that represents the grid, and a detailed model of the CIDER under investigation. The TE impedance is characterized by typical short-circuit parameters of a power distribution grid, which are given in Table 3.1. The TE voltage source injects harmonics, whose levels are given in Table 3.2. These levels are

3.4 Validation of the Proposed Models

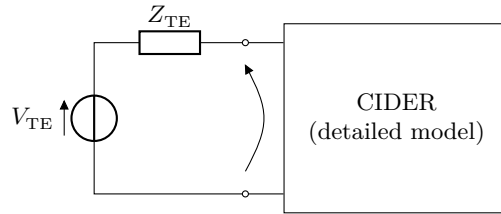


Figure 3.10: Test setup for the validation of the individual CIDER models. The resource is represented by a detailed state-space model (see Section 3.3), and the power system by a TE (see Tables 3.1 and 3.2).

Table 3.1: Short-Circuit Parameters of the Thévenin Equivalent for the Resource Validation

Parameter	Resource Validation	Description
V_n	230 V-RMS	Nominal voltage
S_{sc}	267 kW	Short-circuit power
$ Z_{sc} $	195 m Ω	Short-circuit impedance
R_{sc}/X_{sc}	6.207	Resistance-to-reactance ratio

set according to the limits specified in the standard BS-EN-50160:2000 [3]⁷. In line with this standard, harmonics up to order 25 (i.e., 1.25 kHz) are considered for HA. Note that, a TE voltage source with the maximum permissible distortion at each harmonic frequency corresponds to a stressed grid. This condition is deemed most suitable for the validation of the CIDER models, because it poses a challenge to the modelling framework. Moreover, it is crucial that the results are reliable when the system is under stress.

The exemplary parameters for the grid-forming and grid-following CIDER are listed in Tables 3.3 to 3.5, respectively. The filter parameters were derived following the design rules proposed in [84]. The setpoints are $V_\sigma = 253$ V-RMS and $f_\sigma = 50$ Hz for the grid-forming CIDER, and $P_\sigma = -50$ kW and $Q_\sigma = -16.4$ kVAR for the grid-following one. For the grid-following CIDER including the DC-side characteristics, the same PQ setpoints are chosen, and additionally the DC voltage reference is set to $V_\delta^* = 900$ V. The control parameters of the CIDERs are tuned by investigating the eigenvalue loci obtained through the HSA that will be introduced in Chapter 5⁸. In this particular case, the goal of the tuning was not to achieve optimal performance but to facilitate a meaningful case study.

The CIDER models discussed in Section 3.3 were implemented in Matlab, and compared against TDS with averaged models of the CIDERs in Simulink (recall Hyp. 10). The

⁷Note that the standard does not specify the angles of the harmonics.

⁸In practice, the PI controllers of CIDERs are tuned employing techniques like the symmetrical and/or magnitude optimum [85, 79], or pole placement [84].

Chapter 3. Derivation of the Specific Models of the CIDERs

Table 3.2: Harmonic Voltages of the Thévenin Equivalent (see [3]).

h	$ V_{TE,h} $	$\angle V_{TE,h}$
1	1.0 p.u.	0 rad
5	6.0 %	$\pi/8$ rad
7	5.0 %	$\pi/12$ rad
11	3.5 %	$\pi/16$ rad
13	3.0 %	$\pi/8$ rad
17	2.0 %	$\pi/12$ rad
19	1.5 %	$\pi/16$ rad
23	1.5 %	$\pi/16$ rad

Table 3.3: Parameters of the Grid-Forming Resource (Rated Power 40 kVA)

Filter stage	L/C	R/G	K_{FB}	T_{FB}	K_{FT}
Inductor (α)	0.49 mH	1.53 m Ω	4	8E-4	1
Capacitor (φ)	60.2 μ F	0 S	1.5	1E-3	0

solver used for the TDS is a fixed-step discrete solver with a sampling time of $T_s = 5\mu\text{s}$. The TDS are stopped once steady-state is reached, and the spectra are calculated using the *Discrete Fourier Transform* (DFT) on a time window composed by the last 5 periods of the fundamental frequency of the obtained signals. All analyses are performed in normalized units w.r.t. the base power $P_b = 50\text{ kW}$ and the base voltage $V_b = 230\text{ V-RMS}$.

Test Procedure

To assess the accuracy of the CIDER models, two different tests are performed based on the test setups in Fig. 3.10. The first aims at validating the HDR of the CIDERs for no deviations from the operating point, while the second compares the performance of the HDR and HSS for small deviations from the operating point.

For the first test setup, the HDR is computed by taking the grid disturbance $\hat{\mathbf{W}}_\gamma$ and the operating point $\hat{\mathbf{Y}}_o$ from the TDS. Then, the output of the HDR is compared to the corresponding measurement from the TDS. See Fig. 3.11a for an illustration of the test. As it was mentioned in Section 3.2.5, for no deviations from the operating point, one does not expect difference between the HDR and HSS. Therefore, the accuracy of the grid response in the operating point is assessed solely based on the HDR and TDS. In order to validate the chosen order in the Taylor expansion of the reference calculation for the grid-following CIDERs, a detailed analysis is performed. To this end, the errors between TDS and HDR for orders from $n = 1 \dots 6$ are assessed.

To test the accuracy of the HDR and HSS for deviations of the inputs from the operating point, the test shown in Fig. 3.11b is conducted. To this end, one simulation of the

3.4 Validation of the Proposed Models

Table 3.4: Parameters of the Grid-Following Resource (Rated Power 60 kVA)

Filter stage	L/C	R/G	K_{FB}	T_{FB}	K_{FT}
Actuator-side inductor (α)	325 μH	1.02 $\text{m}\Omega$	5	5E-4	1
Capacitor (φ)	90.3 μF	0 S	1	8E-4	0
Grid-side inductor (γ)	325 μH	1.02 $\text{m}\Omega$	1	1E-3	1

Table 3.5: Parameters of the Grid-Following Resource Including the DC Side (Rated Power 60 kVA)

Filter stage	L/C	R/G	K_{FB}	T_{FB}	K_{FT}
DC-Link Capacitor (δ)	310 μF	0 S	10	1E-2	0
Actuator-side inductor (α)	325 μH	1.02 $\text{m}\Omega$	2.5	5E-4	1
Capacitor (φ)	90.3 μF	0 S	0.8	1E-3	0
Grid-side inductor (γ)	325 μH	1.02 $\text{m}\Omega$	0.5	5E-3	1

TDS with an initial grid disturbance $\hat{\mathbf{W}}_\gamma^0$ is performed to determine the operating point. Subsequently, the grid disturbance is randomly perturbed for $N = 100$ separate instances. For each instance i , a perturbation $\Delta\hat{\mathbf{W}}_\gamma^i$ is added to the initial grid disturbance, while the operating points $\hat{\mathbf{W}}_o$ and $\hat{\mathbf{Y}}_o$ are kept constant (i.e., from the initial TDS). The perturbation $\Delta\hat{\mathbf{W}}_\gamma^i$ is derived as a combination of random positive, negative and homopolar sequences in each harmonic. More precisely, the magnitude of the positive sequence component is changed randomly between $\pm 10\%$ of the initial value, while the bound for the phase deviation is set to 20 mrad. The perturbation of the positive sequence harmonic components is set through their full range, namely they change from zero up to the percentages given in Table 3.2. Their phase perturbations are set to random values between 0 and 2π . For the negative and homopolar sequences the bounds are derived as 2% of the ones introduced above. In this case, all phase perturbations, also the ones of the fundamental component, are set to uniformly distributed random values between 0 and 2π . For each such perturbation i , the accuracy of the HDR and HSS is assessed by comparing their responses to the exact response from the TDS.

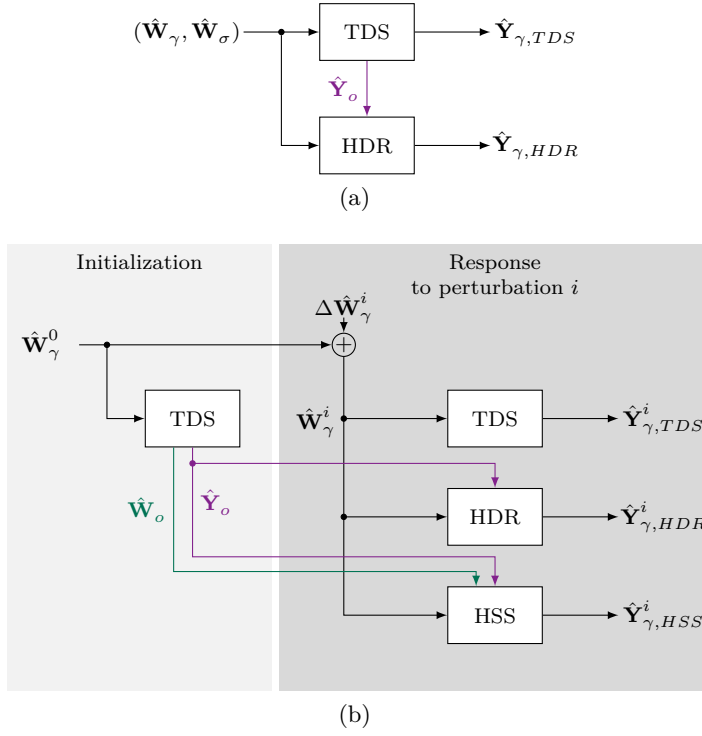


Figure 3.11: Overview of the tests for the validation of the CIDERs: 3.11a shows the test for the accuracy of the HDR in the operating point, and 3.11b shows the test for the validity of the HDR and HSS in case of deviations from the operating point.

Key Performance Indicators

In order to assess the accuracy and performance of the proposed models, suitable KPIs have to be defined. The accuracy is quantified by the errors of the harmonic phasors obtained using the CIDER models w.r.t. the DFT spectra of the time-domain signals. Let \mathbf{X}_h denote the Fourier coefficient of a polyphase electrical quantity (i.e., voltage or current). The KPIs are defined as follows:

$$e_{\text{abs}}(\mathbf{X}_h) := \max_p \left| |X_{h,p,HPF}| - |X_{h,p,TDS}| \right| \quad (3.143)$$

$$e_{\text{arg}}(\mathbf{X}_h) := \max_p \left| \angle X_{h,p,HPF} - \angle X_{h,p,TDS} \right| \quad (3.144)$$

So, $e_{\text{abs}}(\mathbf{X}_h)$ and $e_{\text{arg}}(\mathbf{X}_h)$ are the maximum absolute errors in magnitude and phase, respectively, over all phases $p \in \mathcal{P}$.

3.4.2 Results and Discussion

This section gives a discussion on the accuracy of the individual CIDER models. First, the HDR of the CIDERs introduced in Section 3.3 is validated against the TDS. Second,

3.4 Validation of the Proposed Models

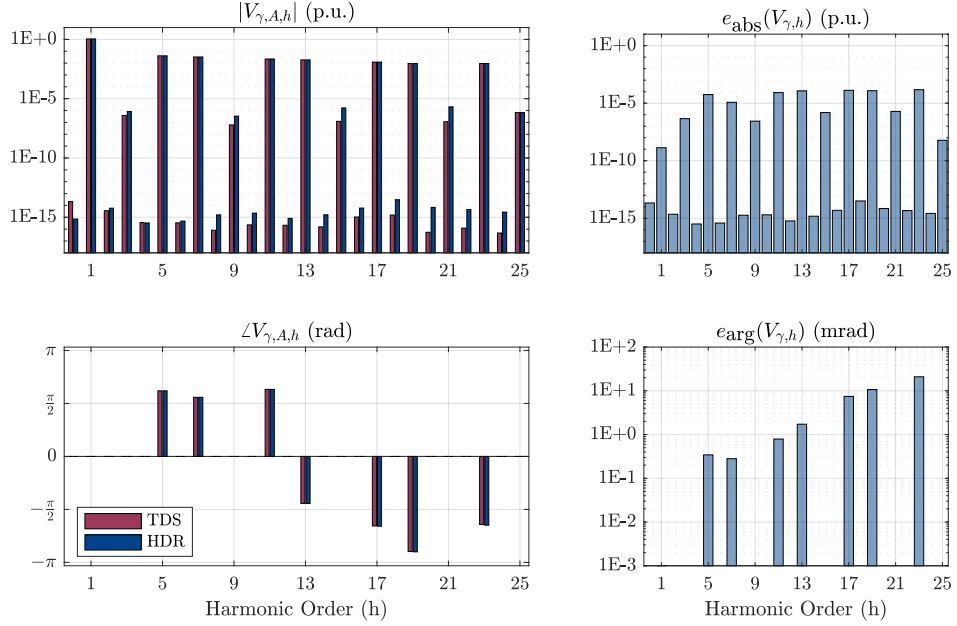


Figure 3.12: Results of the validation on the individual grid-forming CIDER. The plots on the left-hand side show the spectra (i.e., for phase A), and the ones on the right-hand side the error.

the accuracy of the HDR and HSS approach for deviations from the operating point is assessed by comparison with the results from the TDS.

Validation of the HDR

The result for the HDR of the previously proposed CIDER models are shown in Figs. 3.12 to 3.14, respectively. For the sake of simplicity, only the controlled quantities are shown. That is, the output voltage of the grid-forming CIDER, and the output current of the grid-following CIDER. For the CIDER that includes the DC-side characteristics, the output current and the DC voltage are shown.

The spectra on the left-hand sides of Figs. 3.12 to 3.14 show that the Fourier coefficients obtained using HDR and TDS are congruent both in magnitude and phase. This is confirmed by the error plots on the right-hand sides of the figures. The maximum errors are $e_{\text{abs}}(\mathbf{V}_{\gamma,23}) = 1.50\text{E-}4$ p.u. and $e_{\text{arg}}(\mathbf{V}_{\gamma,23}) = 20.93$ mrad for the grid-forming resource, and $e_{\text{abs}}(\mathbf{I}_{\gamma,7}) = 6.71\text{E-}4$ p.u. and $e_{\text{arg}}(\mathbf{I}_{\gamma,13}) = 11.86$ mrad for the grid-following one. The highest errors w.r.t. the CIDER including the DC-side characteristics are $e_{\text{abs}}(\mathbf{I}_{\gamma,1}) = 3.02\text{E-}4$ p.u. and $e_{\text{arg}}(\mathbf{I}_{\gamma,11}) = 6.42$ mrad for the grid current and $e_{\text{abs}}(\mathbf{V}_{\delta,18}) = 2.17\text{E-}6$ p.u. and $e_{\text{arg}}(\mathbf{V}_{\delta,24}) = 35.89$ mrad for the DC-link voltage. Notably, since the applied TE voltage does not include unbalances, the DC-link voltage in Fig. 3.14b exhibits only even harmonics. The observed errors are very low, i.e., lower than

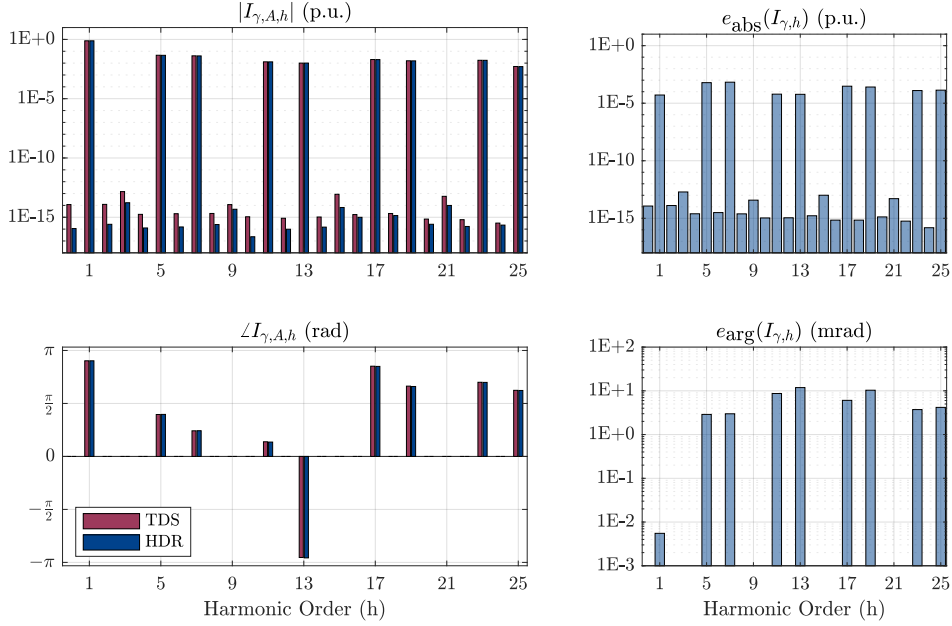


Figure 3.13: Results of the validation on the individual grid-following CIDER. The plots on the left-hand side show the spectra (i.e., for phase A), and the ones on the right-hand side the error.

the accuracy of standard measurement devices (i.e., compared to a 0.5 class instrument transformer, as defined in the standards [4, 86, 5], and shortly discussed in Appendix A.1). Therefore, they can be considered as negligible in practice.

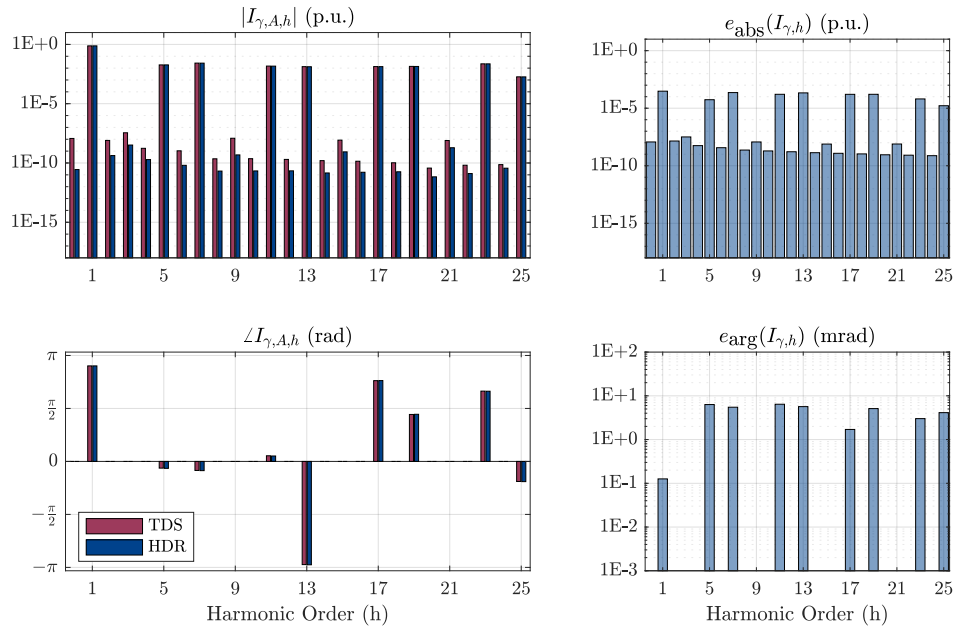
Fig. 3.15 shows the errors of the grid response of the two grid-following CIDERs employing different orders in the Taylor expansion of the reference calculation. The plots confirm the choice of $n = 2$, since the errors reduce significantly between the first and second order expansion, especially in the fundamental component. For higher orders no significant improvement is observed.

Accuracy of HDR and HSS for Deviations from the Operating Point

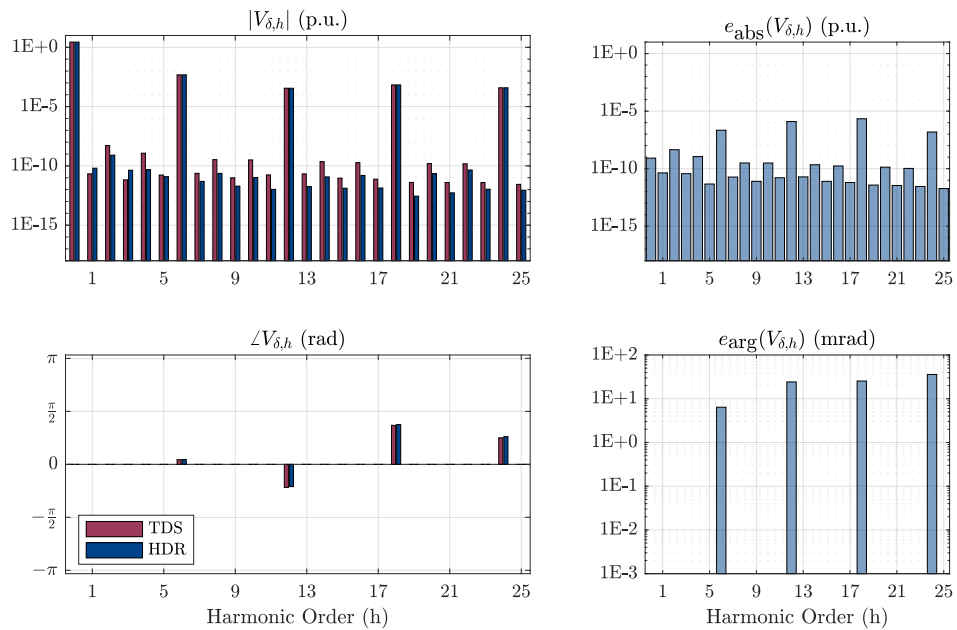
Fig. 3.16 shows the validation of the accuracy of the HDR and HSS for deviations from the operating point for the two grid-following CIDERs⁹. For both CIDERs and for both HDR and HSS, the errors are slightly higher for deviations from the operating point as opposed to the errors in Fig. 3.13 and Fig. 3.14. Notably, errors are now also present at the triplen harmonics. This is due to the fact that the perturbation of the grid disturbance includes all sequences at the specified harmonics.

⁹For the grid response of the grid-forming CIDER no linearizations were conducted, and hence, there is no need for this analysis in that case.

3.4 Validation of the Proposed Models

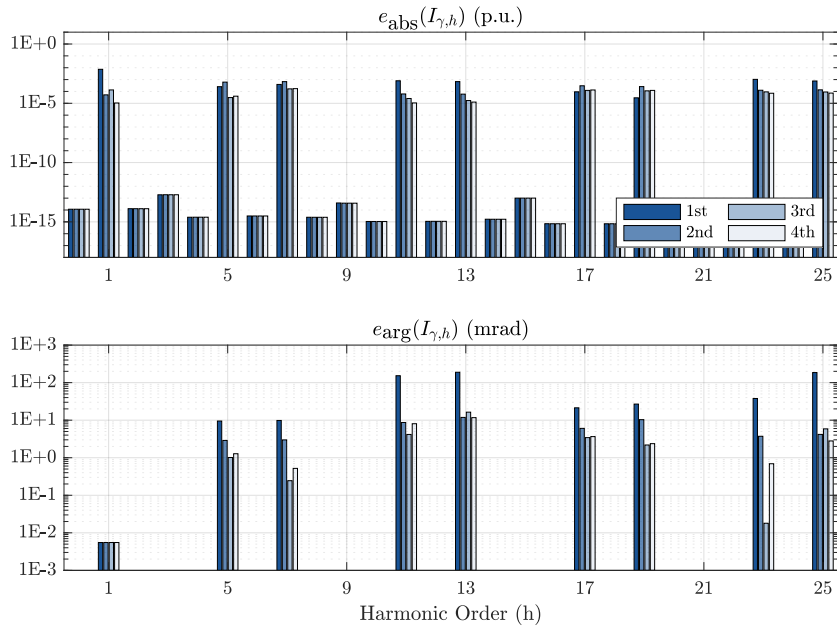


(a)

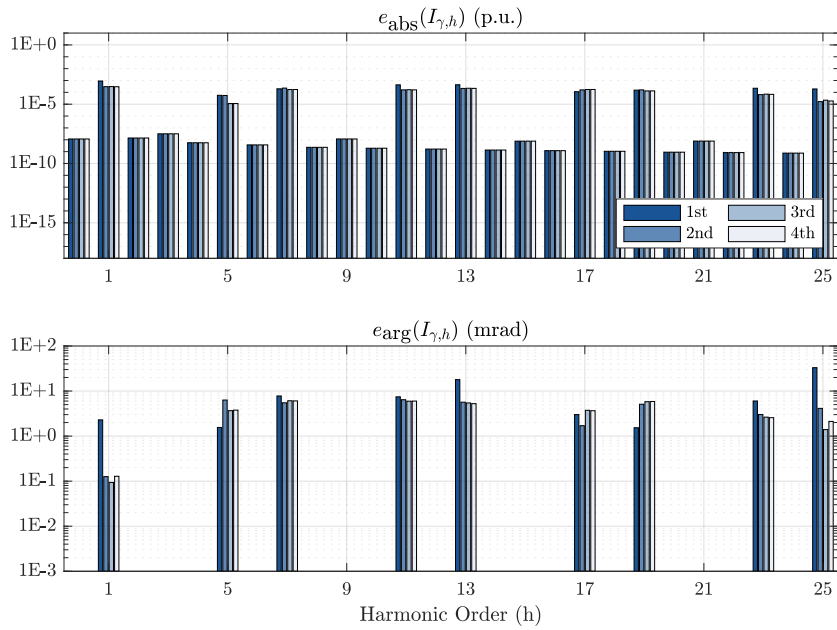


(b)

Figure 3.14: Results of the validation on the individual grid-following CIDER including the DC-side modelling. The grid current (3.14a) and DC-side voltage (3.14b) are shown. The plots on the left-hand side show the spectra (i.e., for phase A in case of the grid current), and the ones on the right-hand side the error defined through the KPIs.



(a)



(b)

Figure 3.15: Impact of the order of Taylor expansion in the reference calculation on the accuracy of the HDR for the grid-following CIDER (3.15a) and the grid-following CIDER considering the DC-side characteristics (3.15b). The plots show the error in magnitude and phase on the top and bottom defined through the KPIs.

3.4 Validation of the Proposed Models

Table 3.6: Statistics of the applied grid disturbances for obtaining the results in Fig. 3.16 for $N = 100$ samples.

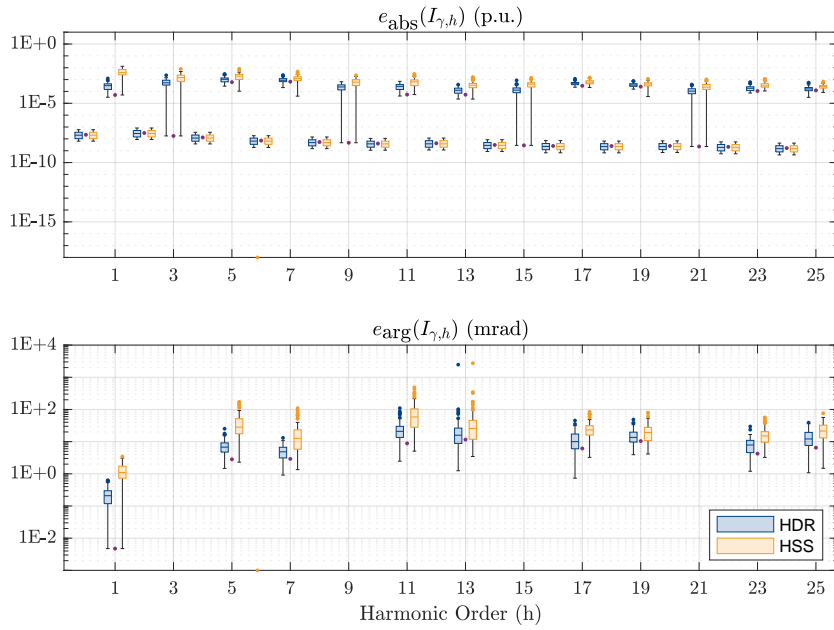
	THD(\mathbf{w}_γ^0)	min(THD)	max(THD)	μ (THD)
Case in Fig. 3.16a	11.33	7.88	17.16	12.82
Case in Fig. 3.16b	10.66	8.11	17.57	12.28

Fig. 3.16a shows the boxplot of the grid-following CIDER that models only the AC side. As expected, since the nonlinear approximation of the reference calculation performs better than the small-signal model, the errors of the HDR are smaller than the once of the HSS. Note that, as compared to the performance of the HDR in Fig. 3.13, the errors of the HDR shown here are bigger in some cases. Recall, the assumption behind the linearization of the reference calculation, namely, that the harmonics are small compared to the fundamental component (i.e., Hyp. 18). Thus, the more the grid disturbance is distorted, the more the linearization gets inaccurate.

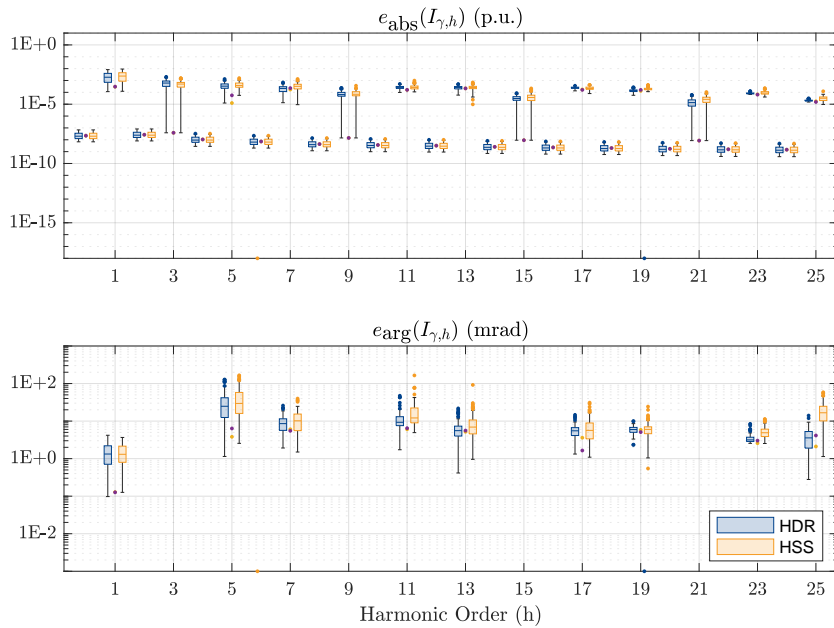
Table 3.6 gives the statistics of the *Total Harmonic Distortion* (THD) of the applied grid disturbances, where $\text{THD}(\mathbf{w}_\gamma^0)$ is the THD of the initially applied grid disturbance (i.e., the one that was used for the validation of the HDR in Fig. 3.13 and Fig. 3.14). As can be seen from Table 3.6, in average the applied disturbance for this validation exhibits a higher THD, than for the cases shown in Fig. 3.13 and Fig. 3.14¹⁰. Notably, despite the assumed THD being larger than what is usually permitted, the approximation is very accurate.

For the grid-following CIDER that models the DC side, the results are shown in Fig. 3.16b. Again, as expected, the HDR performs better than the HSS. Additionally, the same observations regarding the accuracy of the reference calculation can be made. In summary, the errors at all harmonics are below the accuracy of standard measurement devices, except from some outliers at the angles of the harmonics.

¹⁰The formally maximum allowable THD is set at 8% in [3].



(a)



(b)

Figure 3.16: Accuracy of the HDR and HSS the grid-following CIDERs considering only AC-side (3.16a) and considering DC-side characteristics (3.16b) for random deviations from the operating point. The solution for no deviation from the operating point is included as the first sample (and additionally as the violet point centered between the two boxes at each harmonic). The box plots show 25 and 75 percentile, outliers exceed 1.5-times the interquartile range.

4 Harmonic Power-Flow Algorithm

Summary: *In this chapter the HPF method for power systems with high share of CIDERs is introduced and validated. The HPF problem is formulated by combining the nodal equations of the grid with the HDR of the CIDERs, and solved using the Newton-Raphson method. The nodal equations of the grid are expressed using the hybrid parameters, which are derived from the admittance matrix. The HDRs of the CIDERs are derived from the generic models presented in the previous chapters (i.e., Chapters 2 and 3), which allows to treat both grid-forming and grid-following control laws. In order to address the extension of the generic CIDER model which can handle nonlinearities, an extension of the solution algorithm that explicitly accounts for the required operating point is proposed. First, the HPF methods for AC power systems are applied to a modified version of the CIGRÉ low-voltage benchmark microgrid. The method's accuracy and computational efficiency for both versions, i.e., the original formulation and the one that can handle the nonlinearities, are confirmed via TDS of the CIGRÉ low-voltage benchmark microgrid. Additionally, the HPF method is compared to a decoupled HPF study (i.e., one that solves the system equations independently at each harmonic frequency). A further extension to the solution algorithm for the HPF study of hybrid AC/DC power systems is proposed. To this end, the model of the NICs and the resulting coupling between the AC and DC subsystems is included in the mismatch equations and the associated Jacobian matrix. The extended HPF method is applied to a typical hybrid AC/DC grid, and its accuracy is validated through detailed TDS with Simulink.*

Publications:

- [16] A.M. Kettner, L. Reyes-Chamorro, J.K.M. Becker, Z. Zou, M. Liserre, and M. Paolone, “Harmonic power-flow study of polyphase grids with converter-interfaced distributed energy resources—part i: Modeling framework and algorithm,” *IEEE Trans. Smart Grid*, vol. 13, no. 1, pp. 458–469, 2021.
- [17] J.K.M. Becker, A.M. Kettner, L. Reyes-Chamorro, Z. Zou, M. Liserre, and M. Paolone, “Harmonic power-flow study of polyphase grids with converter-interfaced distributed energy resources—part ii: Model library and validation,” *IEEE Trans. Smart Grid*, vol. 13, no. 1, pp. 470–481, 2021.
- [18] J.K.M. Becker, A. M. Kettner, Y. Zuo, F. Cecati, S. Pugliese, M. Liserre, and M. Paolone, “Modelling of ac/dc interactions of converter-interfaced resources for harmonic power-flow studies in microgrids,” *IEEE Trans. on Smart Grid*, vol. 14, no. 3, pp. 2096–2110, 2022.
- [19] J.K.M. Becker, Y. Zuo, M. Paolone, and A.M. Kettner, “Harmonic power-flow study of hybrid ac/dc grids with converter-interfaced distributed energy resources,” in *2023 IEEE Belgrade PowerTech*, 2023, pp. 1–6.

4.1 State of the Art

HA that aims to obtain the harmonic steady state can be performed using different techniques. The most detailed and accurate analysis tools are the models used for TDS followed by a determination of the frequency spectrum. Recall from Section 2.1.1 that for time-domain analysis all components of the power system are described by a system of DAEs, and solved by numerical integration. The harmonic spectra are then calculated from the obtained waveforms via the DFT or similar techniques once they have reasonably settled to steady state. This approach is very accurate, yet also computational intensive.

Since for HPF analysis only the steady-state solutions (i.e., the periodic waveforms that remain after all transients have died out) are of interest, the analysis can be performed directly in the frequency domain. Namely, the DAEs from time domain can be restated as algebraic equations in the frequency domain using the Fourier transform. The unknowns of these so-called HPF equations are the harmonic phasors.

4.1.1 Methods without Frequency-Coupling Representation

In specific cases, the harmonic voltages and currents can be approximated by known linear functions of the respective fundamental tones alone (e.g., using a complex factor which expresses the harmonic distortion and phase shift of the harmonic w.r.t. the fundamental).

Under these circumstances, one can first calculate the fundamental voltages and currents in a standard power-flow study, and then infer the harmonic ones (i.e., via the said functions). This technique is called *Direct Harmonic Analysis* (DHA) [12]. In [87], such a decoupled HPF has been employed for the study of large power systems with multiple nonlinear loads.

4.1.2 Methods with Frequency-Coupling Representation

In general, the HPF equations are nonlinear, and hence have to be solved iteratively (e.g., using the Newton-Raphson method). This approach is called *Iterative Harmonic Analysis* (IHA) [12] or HPF study [88]. Moreover, this method can be generalized to include interharmonics [89].

Various works have studied how standard approaches for power-flow analysis can be extended to HPF study. In [90], the nodal equations are solved using the Newton-Raphson method. In [91], the branch equations are used instead. Other researchers use double-iterate methods for IHA. In [92], a standard power-flow study is performed at the master-level, and then refined through IHA at the slave-level. Notably, these subproblems are formulated in different reference frames, namely phase coordinates [55] and symmetrical components [52], respectively. In [93], the master instead performs a sophisticated AC/DC power-flow study. If the structure and parameters of the underlying models are only partially known or even unknown, one can employ data-driven methods. In [94], a recursive least-squares estimator is employed for data-driven HPF studies.

4.1.3 Motivation for the Proposed Method

Most existing HPF methods have an important shortcoming/disadvantage: they do not adequately represent the detailed resource and grid behaviour (e.g., in the case of CIDERS). In particular, they neglect the representation of the frequency coupling within the CIDERS. Moreover, although many studies have performed detailed HA of individual CIDERS (recall Section 2.1.2), they often ignore the propagation and interaction of harmonics through the electrical grid.

The HPF method proposed in this chapter employs the modelling framework presented in Chapter 2, incl. the detailed models of the CIDERS introduced in Chapter 3, in order to overcome the shortcomings of existing approaches. That is, the generality, modularity, and accuracy of the underlying models enable the HPF study of systems with arbitrary topology (i.e., radial or meshed), line configuration (i.e., transposed or untransposed), as well as CIDER architecture (i.e., cascaded filters and controllers, grid-following or -forming control).

4.2 Representation of the Electrical Grid for the HPF Study

This section introduces the representation of the grid used for the formulation of the HPF problem. More precisely, the derivation of the compound hybrid matrix of a three-phase grid based on its lumped-element model is presented. Notably, the same methodology applies (i.e., with the necessary modifications w.r.t. vector and matrix sizes) to DC subsystems in the context of the HPF method for hybrid AC/DC power systems as will be introduced Section 4.3.4.

Recall the lumped-element model of the grid introduced in Fig. 2.5. Based on this representation, the following hypotheses are made w.r.t. the properties of the grid model:

Hypothesis 24. *Since the lumped elements of the grid model are linear and passive, its circuit equations can be formulated independently at any given frequency f using compound electrical parameters (i.e., compound impedance matrices or compound admittance matrices). Each branch element ℓ is described by an impedance-type equation*

$$\mathbf{V}_m(f) - \mathbf{V}_n(f) = \mathbf{Z}_\ell(f)\mathbf{I}_\ell(f), \quad \forall \ell = (m, n) \in \mathcal{L} \quad (4.1)$$

where $\mathbf{Z}_\ell \in \mathbb{C}^{3 \times 3}$ is the compound impedance of the branch element, $\mathbf{I}_\ell \in \mathbb{C}^{3 \times 1}$ is the current flowing through it, and $\mathbf{V}_m, \mathbf{V}_n \in \mathbb{C}^{3 \times 1}$ are the phase-to-ground voltages at its start and end node, respectively. Each shunt element t is described by an admittance-type equation

$$\mathbf{I}_t(f) = \mathbf{Y}_t(f)\mathbf{V}_n(f), \quad \forall t = (n, g) \in \mathcal{T} \quad (4.2)$$

where $\mathbf{Y}_t \in \mathbb{C}^{3 \times 3}$ is the compound admittance of the shunt element, and $\mathbf{I}_t \in \mathbb{C}^{3 \times 1}$ the current flowing through it.

The advantage of formulating the grid equations in harmonic domain is that frequency-dependent phenomena can easily be incorporated into the model. The example of frequency-dependent line parameters is given in Appendix A.3.

In general, (4.1)–(4.2) do not correspond to an LTI system (i.e., linearity w.r.t. frequency does not guarantee time-invariance). More precisely, the grid model is LTI *if and only if* it consists of frequency-independent resistor, inductor, and capacitor elements¹ (e.g., [95]). Yet, the generic form of (4.1)–(4.2) does allow to treat frequency-dependent parameters if needed².

Moreover, note that (4.1)–(4.2) describe the behaviour of the grid in phase coordinates. It is important to note that these equations are valid irrespective of any asymmetries

¹For instance, the grid model is LTI if $\mathbf{Z}_\ell(f) = \mathbf{R}_\ell + j2\pi f\mathbf{L}_\ell$ ($\forall \ell \in \mathcal{L}$) and $\mathbf{Y}_t(f) = \mathbf{G}_t + j2\pi f\mathbf{C}_t$ ($\forall t \in \mathcal{T}$) for constant $\mathbf{R}_\ell, \mathbf{L}_\ell, \mathbf{G}_t,$ and \mathbf{C}_t .

²E.g., $\mathbf{Z}_\ell(f) = \mathbf{R}_\ell(f) + j2\pi f\mathbf{L}_\ell(f)$ and $\mathbf{Y}_t(f) = \mathbf{G}_t(f) + j2\pi f\mathbf{C}_t(f)$.

4.2 Representation of the Electrical Grid for the HPF Study

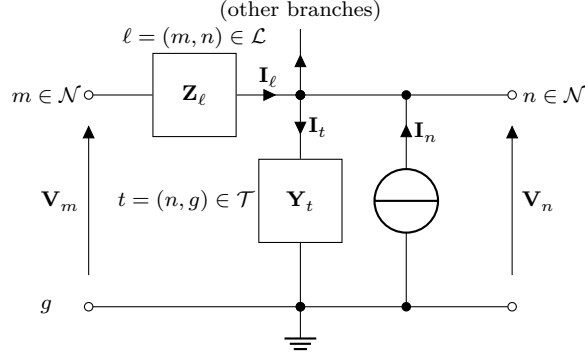


Figure 4.1: The grid is represented by branch elements with compound impedance \mathbf{Z}_ℓ and shunt elements with compound admittance \mathbf{Y}_t . \mathbf{I}_ℓ and \mathbf{I}_t are the current flows through the branch and shunt elements, respectively. \mathbf{V}_n and \mathbf{I}_n are the phase-to-ground voltages and injected currents, respectively.

in the system w.r.t. the grid components (e.g., due to non-transposition of lines) or the nodal injections/absorptions (e.g., due to unbalances of generation/load) [55]. Therefore, these phase-domain equations are particularly suitable for power distribution systems (i.e., unlike sequence-domain equations), where such asymmetries are common.

Note that the term “compound electrical parameters” refers to polyphase impedance or admittance matrices, which take into account the electromagnetic coupling between different phases (e.g., [51]). These compound electrical parameters are assumed to have the following properties:

Hypothesis 25. *The compound branch impedance matrices \mathbf{Z}_ℓ are symmetric, invertible, and lossy at all frequencies:*

$$\mathbf{Z}_\ell(f) : \begin{cases} \mathbf{Z}_\ell(f) = (\mathbf{Z}_\ell(f))^T \\ \exists \mathbf{Y}_\ell(f) = (\mathbf{Z}_\ell(f))^{-1} \\ \Re \{ \mathbf{Z}_\ell(f) \} \succeq 0 \end{cases} \quad (4.3)$$

The compound shunt admittance matrices \mathbf{Y}_t are symmetric, invertible, and lossy at all frequencies if they are nonzero:

$$\text{if } \mathbf{Y}_t(f) \neq \mathbf{0} : \begin{cases} \mathbf{Y}_t(f) = (\mathbf{Y}_t(f))^T \\ \exists \mathbf{Z}_t(f) = (\mathbf{Y}_t(f))^{-1} \\ \Re \{ \mathbf{Y}_t(f) \} \succeq 0 \end{cases} \quad (4.4)$$

These properties follow from fundamental laws of physics (e.g., Maxwell’s equations), and hold for a broad variety of grid components. For instance, the electrical parameters of lines, conventional transformers, and series or shunt compensators satisfy these properties [96].

Chapter 4. Harmonic Power-Flow Algorithm

Notably, the symmetry property holds for both transposed and non-transposed lines³. Only a few types of grid components, such as phase-shifting transformers, exhibit different characteristics (i.e., the symmetry property does not hold).

Observe that Hyp. 25 refers to the *exact* parameters of the grid components. In case the exact parameters are not known, they have to be inferred from measurements via system identification (e.g., least-squares regression). The obtained *estimated* parameters may violate the properties in Hyp. 25, unless corresponding constraints are imposed on the solution of the system-identification problem [97].

4.2.1 Compound Admittance Matrix

The *primitive compound admittance matrices* $\mathbf{Y}_{\mathcal{L}}$ and $\mathbf{Y}_{\mathcal{T}}$ associated with the branches and shunts, respectively, are defined as (e.g., see [98])

$$\mathbf{Y}_{\mathcal{L}}(f) := \text{diag}_{\ell \in \mathcal{L}}(\mathbf{Y}_{\ell}(f)) \in \mathbb{C}^{3|\mathcal{L}| \times 3|\mathcal{L}|} \quad (4.5)$$

$$\mathbf{Y}_{\mathcal{T}}(f) := \text{diag}_{t \in \mathcal{T}}(\mathbf{Y}_t(f)) \in \mathbb{C}^{3|\mathcal{N}| \times 3|\mathcal{N}|} \quad (4.6)$$

Let \mathbf{V} and \mathbf{I} be the vectors of all phase-to-ground voltages and nodal injected currents, respectively:

$$\mathbf{V}(f) := \text{col}_{n \in \mathcal{N}}(\mathbf{V}_n(f)) \in \mathbb{C}^{3|\mathcal{N}| \times 1} \quad (4.7)$$

$$\mathbf{I}(f) := \text{col}_{n \in \mathcal{N}}(\mathbf{I}_n(f)) \in \mathbb{C}^{3|\mathcal{N}| \times 1} \quad (4.8)$$

The *compound nodal admittance matrix* $\mathbf{Y} \in \mathbb{C}^{3|\mathcal{N}| \times 3|\mathcal{N}|}$, which links \mathbf{I} to \mathbf{V} , is calculated using the polyphase incidence matrix defined in Section 2.3.2 as follows:

$$\mathbf{I}(f) = \mathbf{Y}(f)\mathbf{V}(f), \quad \mathbf{Y}(f) = \mathcal{A}_{\mathcal{L}|\mathcal{N}}^T \mathbf{Y}_{\mathcal{L}}(f) \mathcal{A}_{\mathcal{L}|\mathcal{N}} + \mathbf{Y}_{\mathcal{T}}(f) \quad (4.9)$$

4.2.2 Compound Hybrid Matrix

Recall from Section 2.2.1, the partition of all nodes \mathcal{N} into \mathcal{S} and \mathcal{R} , i.e., with grid-forming and grid-following CIDERS, respectively. Note that this implies $|\mathcal{N}| = |\mathcal{S}| + |\mathcal{R}|$.

As proven in [96], the following Lemma holds:

Lemma 1. *Suppose that Hyps. 24 and 25 hold, the branch graph \mathfrak{B} is weakly connected, and the compound branch impedances $\mathbf{Z}_{\ell}(f)$ are strictly lossy (i.e., $\Re\{\mathbf{Z}_{\ell}(f)\} \succ 0 \forall \ell \in \mathcal{L}$).*

³The compound electrical parameters of a transposed line are *symmetric* and *circulant* (e.g., [51]). The symmetry property is given by physics, whereas the circulant property is enforced through construction (i.e., the transposition of the conductors). The compound electrical parameters of non-transposed lines are only symmetric.

4.2 Representation of the Electrical Grid for the HPF Study

Given the aforementioned partitioning of the nodes, the associated block form of the nodal admittance equations (4.9)

$$\begin{bmatrix} \mathbf{I}_S(f) \\ \mathbf{I}_R(f) \end{bmatrix} = \begin{bmatrix} \mathbf{Y}_{S \times S}(f) & \mathbf{Y}_{S \times R}(f) \\ \mathbf{Y}_{R \times S}(f) & \mathbf{Y}_{R \times R}(f) \end{bmatrix} \begin{bmatrix} \mathbf{V}_S(f) \\ \mathbf{V}_R(f) \end{bmatrix} \quad (4.10)$$

can be reformulated into the nodal hybrid equations

$$\begin{bmatrix} \mathbf{V}_S(f) \\ \mathbf{I}_R(f) \end{bmatrix} = \begin{bmatrix} \mathbf{H}_{S \times S}(f) & \mathbf{H}_{S \times R}(f) \\ \mathbf{H}_{R \times S}(f) & \mathbf{H}_{R \times R}(f) \end{bmatrix} \begin{bmatrix} \mathbf{I}_S(f) \\ \mathbf{V}_R(f) \end{bmatrix} \quad (4.11)$$

The blocks of the compound hybrid matrix \mathbf{H} are given by

$$\mathbf{H}_{S \times S}(f) = \mathbf{Y}_{S \times S}^{-1}(f) \in \mathbb{C}^{3|S| \times 3|S|} \quad (4.12)$$

$$\mathbf{H}_{S \times R}(f) = -\mathbf{Y}_{S \times S}^{-1}(f) \mathbf{Y}_{S \times R}(f) \in \mathbb{C}^{3|S| \times 3|R|} \quad (4.13)$$

$$\mathbf{H}_{R \times S}(f) = \mathbf{Y}_{R \times S}(f) \mathbf{Y}_{S \times S}^{-1}(f) \in \mathbb{C}^{3|R| \times 3|S|} \quad (4.14)$$

$$\mathbf{H}_{R \times R}(f) = \mathbf{Y}(f) / \mathbf{Y}_{R \times R}(f) \in \mathbb{C}^{3|R| \times 3|R|} \quad (4.15)$$

where $\mathbf{Y} / \mathbf{Y}_{R \times R}$ is the Schur complement of \mathbf{Y} w.r.t. $\mathbf{Y}_{R \times R}$.

Observe that (4.11) holds for any arbitrary frequency f (i.e., as stated in Hyp. 24 and 25). Now, consider the special case of *harmonic frequencies* f_h , which are defined by the *harmonic orders* $h \in \mathcal{H}$ w.r.t. a given *fundamental frequency* f_1 :

$$f_h := h \cdot f_1, \quad h \in \mathcal{H} \subset \mathbb{Z} \quad (4.16)$$

Due to the assumed linearity of the grid components (Hyp. 24), the hybrid nodal equations (4.11) can be formulated independently at each of the harmonic frequencies f_h . Combining the equations for the individual harmonic frequencies yields a system of equations for the entire harmonic spectrum

$$\begin{bmatrix} \hat{\mathbf{V}}_S \\ \hat{\mathbf{I}}_R \end{bmatrix} = \begin{bmatrix} \hat{\mathbf{H}}_{S \times S} & \hat{\mathbf{H}}_{S \times R} \\ \hat{\mathbf{H}}_{R \times S} & \hat{\mathbf{H}}_{R \times R} \end{bmatrix} \begin{bmatrix} \hat{\mathbf{I}}_S \\ \hat{\mathbf{V}}_R \end{bmatrix} \quad (4.17)$$

where

$$\hat{\mathbf{V}}_S := \text{col}_{h \in \mathcal{H}}(\mathbf{V}_S(f_h)) \in \mathbb{C}^{3|\mathcal{H}||S| \times 1} \quad (4.18)$$

$$\hat{\mathbf{H}}_{S \times S} := \text{diag}_{h \in \mathcal{H}}(\mathbf{H}_{S \times S}(f_h)) \in \mathbb{C}^{3|\mathcal{H}||S| \times 3|\mathcal{H}||S|} \quad (4.19)$$

The remaining blocks of $\hat{\mathbf{V}}$, $\hat{\mathbf{I}}$, and $\hat{\mathbf{H}}$ are defined analogously.

4.3 Algorithm for Harmonic Power-Flow Studies

This section introduces the HPF algorithm starting from the mathematical formulation of the problem, for the most simplified version of the modelling framework (i.e., no nonlinearities are modelled within the internal response of the CIDERS). First, the mismatch equations between the nodal quantities from point of view of the grid and the resources are stated and then solved via a Newton-Raphson method. To this end, the Jacobian matrix used in the numerical solution of the HPF problem is introduced. Subsequently, the algorithm is extended in order to account for the linearized CIDER models. Finally, an extension of the HPF method that is capable of analysing hybrid AC/DC grids is presented. To this end, the presence of NICs is included in the solution algorithm.

4.3.1 Mathematical Formulation of the Problem for AC Power Systems

In this subsection, pure AC power systems are considered. That is, the resources of the system consist - for now - only of CIDERS but not NICs. Recall from Section 2.2.1, the structure of an AC power system that is composed of the grid and the resources. The HPF problem is obtained by formulating the mismatch equations between the models of the CIDERS (i.e., the resources) and the grid. As stated in Section 2.2.1, the nodes are partitioned into the nodes \mathcal{S} and \mathcal{R} , which are the points of connection of grid-forming and grid-following CIDERS, respectively. If there are any zero-injection nodes (i.e., without resources), they can be eliminated via Kron reduction [96].

From point of view of the grid, the nodal equations are given by the hybrid parameters (4.17):

$$\hat{\mathbf{V}}_{\mathcal{S}}(\hat{\mathbf{I}}_{\mathcal{S}}, \hat{\mathbf{V}}_{\mathcal{R}}) = \hat{\mathbf{H}}_{\mathcal{S} \times \mathcal{S}} \hat{\mathbf{I}}_{\mathcal{S}} + \hat{\mathbf{H}}_{\mathcal{S} \times \mathcal{R}} \hat{\mathbf{V}}_{\mathcal{R}} \quad (4.20)$$

$$\hat{\mathbf{I}}_{\mathcal{R}}(\hat{\mathbf{I}}_{\mathcal{S}}, \hat{\mathbf{V}}_{\mathcal{R}}) = \hat{\mathbf{H}}_{\mathcal{R} \times \mathcal{S}} \hat{\mathbf{I}}_{\mathcal{S}} + \hat{\mathbf{H}}_{\mathcal{R} \times \mathcal{R}} \hat{\mathbf{V}}_{\mathcal{R}} \quad (4.21)$$

From point of view of the CIDERS, these nodal equations are established via their grid response (2.64). Recalling the definitions of the setpoint disturbance \mathbf{w}_{σ} (2.31), grid disturbance \mathbf{w}_{γ} (2.29), and grid output \mathbf{y}_{γ} (2.30), one finds

$$\forall s \in \mathcal{S} : \hat{\mathbf{V}}_s(\hat{\mathbf{I}}_s, V_{\sigma,s}, f_{\sigma,s}) = \hat{\mathbf{Y}}_{\gamma,s}(\hat{\mathbf{T}}_{\pi|\gamma} \hat{\mathbf{I}}_s, V_{\sigma,s}, f_{\sigma,s}) \quad (4.22)$$

$$\forall r \in \mathcal{R} : \hat{\mathbf{I}}_r(\hat{\mathbf{V}}_r, S_{\sigma,r}) = \hat{\mathbf{Y}}_{\gamma,r}(\hat{\mathbf{T}}_{\pi|\gamma} \hat{\mathbf{V}}_r, S_{\sigma,r}) \quad (4.23)$$

Note that (4.22) and (4.23) are in accordance with Defs. 2 and 3 (i.e., grid-forming and grid-following behaviour). Moreover, observe that functions of the form (4.22) or (4.23) can also be used to represent sources of harmonics other than CIDERS, such as conventional generators or loads. The sole difference is that the corresponding functions have to be derived from another suitable model or through system identification. Please see Appendix A.2 for further details on this matter.

4.3 Algorithm for Harmonic Power-Flow Studies

Algorithm 1 Newton-Raphson solution of the HPF problem.

```

1: procedure HPF( $\Delta\hat{\mathbf{V}}_{\mathcal{S}}(\cdot, \cdot, \cdot)$ ,  $\Delta\hat{\mathbf{I}}_{\mathcal{R}}(\cdot, \cdot, \cdot)$ ,  $\mathbf{V}_{\sigma}$ ,  $\mathbf{f}_{\sigma}$ ,  $\mathbf{S}_{\sigma}$ )
2:   # Initialization
3:    $\hat{\mathbf{I}}_{\mathcal{S}} \leftarrow \mathbf{0}$ 
4:    $\hat{\mathbf{V}}_{\mathcal{R}} \leftarrow \text{flat\_start}()$ 
5:   while  $\max(|\Delta\hat{\mathbf{V}}_{\mathcal{S}}|, |\Delta\hat{\mathbf{I}}_{\mathcal{R}}|) \geq \epsilon$  do
6:     # Residuals
7:      $\Delta\hat{\mathbf{V}}_{\mathcal{S}} \leftarrow \Delta\hat{\mathbf{V}}_{\mathcal{S}}(\hat{\mathbf{I}}_{\mathcal{S}}, \hat{\mathbf{V}}_{\mathcal{R}}, \mathbf{V}_{\sigma}, \mathbf{f}_{\sigma})$ 
8:      $\Delta\hat{\mathbf{I}}_{\mathcal{R}} \leftarrow \Delta\hat{\mathbf{I}}_{\mathcal{R}}(\hat{\mathbf{I}}_{\mathcal{S}}, \hat{\mathbf{V}}_{\mathcal{R}}, \mathbf{S}_{\sigma})$ 
9:     # Jacobian matrix
10:     $\hat{\mathbf{J}}_{\mathcal{S} \times \mathcal{S}} \leftarrow \partial_{\mathcal{S}} \Delta\hat{\mathbf{V}}_{\mathcal{S}}(\hat{\mathbf{I}}_{\mathcal{S}}, \hat{\mathbf{V}}_{\mathcal{R}}, \mathbf{V}_{\sigma}, \mathbf{f}_{\sigma})$ 
11:     $\hat{\mathbf{J}}_{\mathcal{S} \times \mathcal{R}} \leftarrow \partial_{\mathcal{R}} \Delta\hat{\mathbf{V}}_{\mathcal{S}}(\hat{\mathbf{I}}_{\mathcal{S}}, \hat{\mathbf{V}}_{\mathcal{R}}, \mathbf{V}_{\sigma}, \mathbf{f}_{\sigma})$ 
12:     $\hat{\mathbf{J}}_{\mathcal{R} \times \mathcal{S}} \leftarrow \partial_{\mathcal{S}} \Delta\hat{\mathbf{I}}_{\mathcal{R}}(\hat{\mathbf{I}}_{\mathcal{S}}, \hat{\mathbf{V}}_{\mathcal{R}}, \mathbf{S}_{\sigma})$ 
13:     $\hat{\mathbf{J}}_{\mathcal{R} \times \mathcal{R}} \leftarrow \partial_{\mathcal{R}} \Delta\hat{\mathbf{I}}_{\mathcal{R}}(\hat{\mathbf{I}}_{\mathcal{S}}, \hat{\mathbf{V}}_{\mathcal{R}}, \mathbf{S}_{\sigma})$ 
14:    # Newton-Raphson iteration
15:    
$$\begin{bmatrix} \Delta\hat{\mathbf{I}}_{\mathcal{S}} \\ \Delta\hat{\mathbf{V}}_{\mathcal{R}} \end{bmatrix} \leftarrow \begin{bmatrix} \hat{\mathbf{J}}_{\mathcal{S} \times \mathcal{S}} & \hat{\mathbf{J}}_{\mathcal{S} \times \mathcal{R}} \\ \hat{\mathbf{J}}_{\mathcal{R} \times \mathcal{S}} & \hat{\mathbf{J}}_{\mathcal{R} \times \mathcal{R}} \end{bmatrix}^{-1} \begin{bmatrix} \Delta\hat{\mathbf{V}}_{\mathcal{S}} \\ \Delta\hat{\mathbf{I}}_{\mathcal{R}} \end{bmatrix}$$

16:    
$$\begin{bmatrix} \hat{\mathbf{I}}_{\mathcal{S}} \\ \hat{\mathbf{V}}_{\mathcal{R}} \end{bmatrix} \leftarrow \begin{bmatrix} \hat{\mathbf{I}}_{\mathcal{S}} \\ \hat{\mathbf{V}}_{\mathcal{R}} \end{bmatrix} - \begin{bmatrix} \Delta\hat{\mathbf{I}}_{\mathcal{S}} \\ \Delta\hat{\mathbf{V}}_{\mathcal{R}} \end{bmatrix}$$

17:  end while
18: end procedure

```

The mismatches between (4.20)–(4.21) and (4.22)–(4.23) must be zero in equilibrium (by definition):

$$\Delta\hat{\mathbf{V}}_{\mathcal{S}}(\hat{\mathbf{I}}_{\mathcal{S}}, \hat{\mathbf{V}}_{\mathcal{R}}, \mathbf{V}_{\sigma}, \mathbf{f}_{\sigma}) = \mathbf{0} \quad (4.24)$$

$$\Delta\hat{\mathbf{I}}_{\mathcal{R}}(\hat{\mathbf{I}}_{\mathcal{S}}, \hat{\mathbf{V}}_{\mathcal{R}}, \mathbf{S}_{\sigma}) = \mathbf{0} \quad (4.25)$$

where \mathbf{V}_{σ} , \mathbf{f}_{σ} , and \mathbf{S}_{σ} are column vectors built of $V_{\sigma,s}$, $f_{\sigma,s}$ ($s \in \mathcal{S}$) and $S_{\sigma,r}$ ($r \in \mathcal{R}$), respectively. In contrast to existing formulations (e.g., [99, 88, 100]), the so-called *mismatch equations* (4.24)–(4.25) are in hybrid rather than admittance form. This reflects the grid-forming and grid-following behaviour.

4.3.2 Numerical Solution via the Newton-Raphson Method

The HPF problem is solved numerically via the Newton-Raphson method as described in Algorithm 1. For the solution of the Newton-Raphson algorithm, the Jacobian matrix $\hat{\mathbf{J}}$ is employed. In the context of the HPF algorithm, the Jacobian matrix describes the partial derivatives of the mismatch equations in (4.24)–(4.25) w.r.t. to the unknowns of

Chapter 4. Harmonic Power-Flow Algorithm

the HPF problem. This is described in block form as:

$$\hat{\mathbf{J}} = \begin{bmatrix} \partial_S \Delta \hat{\mathbf{V}}_S & \partial_{\mathcal{R}} \Delta \hat{\mathbf{V}}_S \\ \partial_S \Delta \hat{\mathbf{I}}_{\mathcal{R}} & \partial_{\mathcal{R}} \Delta \hat{\mathbf{I}}_{\mathcal{R}} \end{bmatrix} \quad (4.26)$$

where

$$\partial_S = \frac{\partial}{\partial \hat{\mathbf{I}}_S}, \quad \partial_{\mathcal{R}} = \frac{\partial}{\partial \hat{\mathbf{V}}_{\mathcal{R}}} \quad (4.27)$$

Since the mismatch equations in (4.24)–(4.25) are expressed as the difference of two terms, the same applies to the Jacobian matrix:

$$\hat{\mathbf{J}} = \hat{\mathbf{J}}^{RSC} - \hat{\mathbf{J}}^{GRD} \quad (4.28)$$

Note that, $\hat{\mathbf{J}}^{RSC}$ describes the partial derivatives of the resources' grid responses in (4.22)–(4.23) w.r.t. to the unknowns of the HPF problem. On the other hand, $\hat{\mathbf{J}}^{GRD}$ reflects the partial derivatives of the hybrid equations in (4.20)–(4.21) w.r.t. to the unknowns of the HPF problem.

The Jacobian matrix has to be recomputed in each iteration of the Newton-Raphson method (as usual). In the proposed formulation of the HPF problem, most terms in the Jacobian matrix are constant, which reduces the computational intensity. First, the partial derivatives of the grid model (4.20)–(4.21), which is linear, are the hybrid parameters. Consequently, the entries of $\hat{\mathbf{J}}^{GRD}$ are describes by:

$$\partial_S \hat{\mathbf{V}}_S(\hat{\mathbf{I}}_S, \hat{\mathbf{V}}_{\mathcal{R}}, \mathbf{V}_{\sigma}, \mathbf{f}_{\sigma}) = \hat{\mathbf{H}}_{S \times S} \quad (4.29)$$

$$\partial_{\mathcal{R}} \hat{\mathbf{V}}_S(\hat{\mathbf{I}}_S, \hat{\mathbf{V}}_{\mathcal{R}}, \mathbf{V}_{\sigma}, \mathbf{f}_{\sigma}) = \hat{\mathbf{H}}_{S \times \mathcal{R}} \quad (4.30)$$

$$\partial_S \hat{\mathbf{I}}_{\mathcal{R}}(\hat{\mathbf{I}}_S, \hat{\mathbf{V}}_{\mathcal{R}}, \mathbf{S}_{\sigma}) = \hat{\mathbf{H}}_{\mathcal{R} \times S} \quad (4.31)$$

$$\partial_{\mathcal{R}} \hat{\mathbf{I}}_{\mathcal{R}}(\hat{\mathbf{I}}_S, \hat{\mathbf{V}}_{\mathcal{R}}, \mathbf{S}_{\sigma}) = \hat{\mathbf{H}}_{\mathcal{R} \times \mathcal{R}} \quad (4.32)$$

which only need to be updated if the electrical parameters or the topology of the grid change. Second, $\hat{\mathbf{J}}^{RSC}$ is described by the partial derivatives of the CIDER models (4.22)–(4.23), which are given by

$$\partial_s \hat{\mathbf{V}}_s(\hat{\mathbf{I}}_s, V_{\sigma,s}, f_{\sigma,s}) = \partial_{\gamma} \hat{\mathbf{Y}}_{\gamma,s}(\hat{\mathbf{T}}_{\pi|\gamma} \hat{\mathbf{I}}_s, V_{\sigma,s}, f_{\sigma,s}) \quad (4.33)$$

$$\partial_r \hat{\mathbf{I}}_r(\hat{\mathbf{V}}_r, S_{\sigma,r}) = \partial_{\gamma} \hat{\mathbf{Y}}_{\gamma,r}(\hat{\mathbf{T}}_{\pi|\gamma} \hat{\mathbf{I}}_r, S_{\sigma,r}) \quad (4.34)$$

with

$$\partial_s = \frac{\partial}{\partial \hat{\mathbf{I}}_s}, \quad \partial_r = \frac{\partial}{\partial \hat{\mathbf{V}}_r} \quad (4.35)$$

4.3 Algorithm for Harmonic Power-Flow Studies

Recall from Section 2.4 that the reference calculation is the only block in the CIDER model which may be nonlinear. Hence, only the partial derivatives associated with resources for which the function $\hat{\mathbf{R}}(\cdot, \cdot)$ in (2.56) is actually nonlinear have to be updated in each iteration. The partial derivatives of the other resources need to be calculated only once.

It is important to note that, in contrast to many existing IHA methods (see Section 4.1), Algorithm 1 is *single-iterative* rather than *double-iterative* (i.e., the algorithm requires one single loop rather than two nested ones). This is thanks to the use of the closed-loop functions in (4.22)–(4.23), which allow to incorporate the CIDER behaviour directly into the nodal mismatch equations. As a result, a single-iterative calculation at the system level suffices to solve the HPF problem⁴.

In general, the HPF problem may have multiple equilibrium points – like any nonlinear problem. To which of these points the HPF method will converge depends on the initialization of the algorithm. Notably, one or several of such solutions may not be physically meaningful (i.e., analogous to solutions of the power-flow equations which lie on the lower portion of the well-known nose curve [101]). Hence, the choice of the initial point affects which solution the numerical solver converges to, and whether this solution is physically meaningful. Without any prior information (e.g., the solution of another HPF study for a similar operating point), the initial point can be chosen as follows:

- The injected currents of the nodes with grid-forming CIDERs are initialized with 0.
- The phase-to-ground voltages of the nodes with grid-following CIDERs are initialized with a “flat profile”, namely: (i) the fundamental voltage is set to a pure positive sequence with magnitude 1 p.u. and phase equal to 0 rad, and (ii) the harmonic voltages are set to 0.

As will be discussed shortly, the proposed method is robust w.r.t. the choice of the initial point (i.e., it converges reliably even if the initial point lies far from the final solution). The described procedure is preferred solely for its simplicity.

4.3.3 Extension of the Algorithm for AC Power Systems to Treat Nonlinearities within the Internal Response of the CIDER

When treating CIDERs that were subject to linearizations, as introduced in Section 2.4.5, the considered grid responses need to be updated. More specifically, from the point of view of the CIDERs, the nodal equations are now described by grid responses, that

⁴The standard approach is a double-iterative calculation with nested loops: one loop each at system and resource level, respectively.

Chapter 4. Harmonic Power-Flow Algorithm

include the dependency on the operating pint due to linearizations:

$$s \in \mathcal{S} : \hat{\mathbf{V}}_s(\hat{\mathbf{I}}_s, V_{\sigma,s}, f_{\sigma,s}, \hat{\mathbf{Y}}_{o,s}) = \hat{\mathbf{Y}}_{\gamma,s}(\hat{\mathbf{I}}_s, V_{\sigma,s}, f_{\sigma,s}, \hat{\mathbf{Y}}_{o,s}) \quad (4.36)$$

$$r \in \mathcal{R} : \hat{\mathbf{I}}_r(\hat{\mathbf{V}}_r, S_{\sigma,r}, \hat{\mathbf{Y}}_{o,r}) = \hat{\mathbf{Y}}_{\gamma,r}(\hat{\mathbf{V}}_r, S_{\sigma,r}, \hat{\mathbf{Y}}_{o,r}) \quad (4.37)$$

As before, grid-forming CIDERS take voltage and frequency as setpoints (i.e., $V_{\sigma,s}$ and $f_{\sigma,s}$), and grid-following CIDERS active and reactive power setpoints (i.e., $S_{\sigma,r} = P_{\sigma,r} + jQ_{\sigma,r}$). Note that (4.36) and (4.37) are in accordance with Defs. 2 and 3 (i.e., grid-forming and grid-following behaviour).

By consequence, the mismatch equations, which must be zero in equilibrium, are now formulated between (4.20)–(4.21) and (4.36)–(4.37). Hence, they are updated including the dependence on the operating point as:

$$\Delta \hat{\mathbf{V}}_{\mathcal{S}}(\hat{\mathbf{I}}_{\mathcal{S}}, \hat{\mathbf{V}}_{\mathcal{R}}, \mathbf{V}_{\sigma}, \mathbf{f}_{\sigma}, \hat{\mathbf{Y}}_{o,\mathcal{S}}) = \mathbf{0} \quad (4.38)$$

$$\Delta \hat{\mathbf{I}}_{\mathcal{R}}(\hat{\mathbf{I}}_{\mathcal{S}}, \hat{\mathbf{V}}_{\mathcal{R}}, \mathbf{S}_{\sigma}, \hat{\mathbf{Y}}_{o,\mathcal{R}}) = \mathbf{0} \quad (4.39)$$

where \mathbf{V}_{σ} , \mathbf{f}_{σ} , and \mathbf{S}_{σ} are column vectors built of the setpoints $V_{\sigma,s}$, $f_{\sigma,s}$ ($s \in \mathcal{S}$) and $S_{\sigma,r}$ ($r \in \mathcal{R}$), respectively. As for the first version of mismatch equations, it can be solved by means of a Newton-Raphson method.

As known from numerical analysis, the Newton-Raphson method requires the calculation (and inversion) of the Jacobian matrix $\hat{\mathbf{J}}$, which is computationally intensive. In the original HPF framework proposed in Section 4.3.2, most blocks of the Jacobian matrix are constant, because the grid equations (4.20)–(4.21) are exactly linear, and the CIDER responses (4.22)–(4.23) are linear except for the reference calculation. In the extended formulation (4.24)–(4.25) of the HPF problem, the operating points $\hat{\mathbf{Y}}_{o,\mathcal{S}}$ and $\hat{\mathbf{Y}}_{o,\mathcal{R}}$ of the CIDERS appear as additional unknowns. Therefore, the entire Jacobian matrix has to be recalculated in each iteration of the Newton-Raphson method. In doing so, the fact that the operating points are a subset of the internal responses – as postulated in (2.94) – needs to be taken into account. As a result, one obtains the extended Newton-Raphson algorithm which is shown in Algorithm 2. The differences w.r.t. to the original method are highlighted in blue.

Like the unknowns related to the grid (i.e., $\hat{\mathbf{V}}_{\mathcal{S}}$ and $\hat{\mathbf{I}}_{\mathcal{R}}$), the operating points of the CIDERS (i.e., $\hat{\mathbf{Y}}_{o,\mathcal{S}}$ and $\hat{\mathbf{Y}}_{o,\mathcal{R}}$) need to be initialized at the start (see Lines 3 and 4, and Lines 5 and 6 of Algorithm 2, respectively), and then updated during each iteration. For the initialization, one can make an “educated guess” based on the fact that the operating points are AC and DC quantities. In this respect, two different approaches are used:

- First, AC quantities are initialized assuming balanced, sinusoidal conditions (i.e., a positive sequence at the fundamental tone) and nominal values (e.g., magnitude 1 p.u. and angle 0 rad for voltages) or setpoints. This is known as “flat start”.

4.3 Algorithm for Harmonic Power-Flow Studies

Algorithm 2 Newton-Raphson solution of the Extended HPF problem.

```

1: procedure HPF( $\Delta\hat{\mathbf{V}}_S(\cdot, \cdot, \cdot)$ ,  $\Delta\hat{\mathbf{I}}_R(\cdot, \cdot, \cdot)$ ,  $\mathbf{V}_\sigma$ ,  $\mathbf{f}_\sigma$ ,  $\mathbf{S}_\sigma$  )
2:   # Initialization
3:    $\hat{\mathbf{I}}_S \leftarrow \mathbf{0}$ 
4:    $\hat{\mathbf{V}}_R \leftarrow \text{flat\_start}()$ 
5:    $\hat{\mathbf{Y}}_{o,S} \leftarrow \text{initialize\_operating\_point}()$ 
6:    $\hat{\mathbf{Y}}_{o,R} \leftarrow \text{initialize\_operating\_point}()$ 
7:   while  $\max(|\Delta\hat{\mathbf{V}}_S|, |\Delta\hat{\mathbf{I}}_R|) \geq \epsilon$  do
8:     # Residuals
9:      $\Delta\hat{\mathbf{V}}_S \leftarrow \Delta\hat{\mathbf{V}}_S(\hat{\mathbf{I}}_S, \hat{\mathbf{V}}_R, \mathbf{V}_\sigma, \mathbf{f}_\sigma, \hat{\mathbf{Y}}_{o,S})$ 
10:     $\Delta\hat{\mathbf{I}}_R \leftarrow \Delta\hat{\mathbf{I}}_R(\hat{\mathbf{I}}_S, \hat{\mathbf{V}}_R, \mathbf{S}_\sigma, \hat{\mathbf{Y}}_{o,R})$ 
11:    # Jacobian matrix
12:     $\hat{\mathbf{J}}_{S \times S} \leftarrow \partial_S \Delta\hat{\mathbf{V}}_S(\hat{\mathbf{I}}_S, \hat{\mathbf{V}}_R, \mathbf{V}_\sigma, \mathbf{f}_\sigma, \hat{\mathbf{Y}}_{o,S})$ 
13:     $\hat{\mathbf{J}}_{S \times R} \leftarrow \partial_R \Delta\hat{\mathbf{V}}_S(\hat{\mathbf{I}}_S, \hat{\mathbf{V}}_R, \mathbf{V}_\sigma, \mathbf{f}_\sigma, \hat{\mathbf{Y}}_{o,S})$ 
14:     $\hat{\mathbf{J}}_{R \times S} \leftarrow \partial_S \Delta\hat{\mathbf{I}}_R(\hat{\mathbf{I}}_S, \hat{\mathbf{V}}_R, \mathbf{S}_\sigma, \hat{\mathbf{Y}}_{o,R})$ 
15:     $\hat{\mathbf{J}}_{R \times R} \leftarrow \partial_R \Delta\hat{\mathbf{I}}_R(\hat{\mathbf{I}}_S, \hat{\mathbf{V}}_R, \mathbf{S}_\sigma, \hat{\mathbf{Y}}_{o,R})$ 
16:    # Newton-Raphson iteration
17:     $\begin{bmatrix} \Delta\hat{\mathbf{I}}_S \\ \Delta\hat{\mathbf{V}}_R \end{bmatrix} \leftarrow \begin{bmatrix} \hat{\mathbf{J}}_{S \times S} & \hat{\mathbf{J}}_{S \times R} \\ \hat{\mathbf{J}}_{R \times S} & \hat{\mathbf{J}}_{R \times R} \end{bmatrix}^{-1} \begin{bmatrix} \Delta\hat{\mathbf{V}}_S \\ \Delta\hat{\mathbf{I}}_R \end{bmatrix}$ 
18:     $\begin{bmatrix} \hat{\mathbf{I}}_S \\ \hat{\mathbf{V}}_R \end{bmatrix} \leftarrow \begin{bmatrix} \hat{\mathbf{I}}_S \\ \hat{\mathbf{V}}_R \end{bmatrix} - \begin{bmatrix} \Delta\hat{\mathbf{I}}_S \\ \Delta\hat{\mathbf{V}}_R \end{bmatrix}$ 
19:    # Update
20:     $\hat{\mathbf{Y}}_{o,s} \leftarrow \hat{\mathbf{T}}_{o,s} \hat{\mathbf{Y}}_s \quad \forall s \in \mathcal{S}$ 
21:     $\hat{\mathbf{Y}}_{o,r} \leftarrow \hat{\mathbf{T}}_{o,r} \hat{\mathbf{Y}}_r \quad \forall r \in \mathcal{R}$ 
22:  end while
23: end procedure

```

- Second, DC quantities are initialized assuming ideal steady-state conditions (i.e., constant values) and using nominal values or setpoints. For the update, (2.94) is used: that is, the operating points are retrieved via the output equations of the CIDER (see Lines 20 and 21 of Algorithm 2).

4.3.4 Extension of the Algorithm for Hybrid AC/DC Power Systems

The HPF method proposed in Section 4.3.3 describes AC power systems by two sets of nodal equations. Namely, the nodal quantities are expressed from the point of view of the grid and the CIDERs, respectively. When analysing hybrid AC/DC grids, the additional presence of NICs at the interface between the AC and DC subsystems has to be represented in the algorithm. To this end, recall from Section 2.2.2 the partition of the nodes of each subsystem into the sets \mathcal{S}^j and \mathcal{R}^j . The unknowns of the HPF

problem are the nodal injected currents at the nodes \mathcal{S}^j and the nodal phase-to-ground voltages at the nodes \mathcal{R}^j (i.e., the quantities that are not regulated by the respective type of resource). The nodal equations of a hybrid AC/DC grid are then obtained as the combination of the nodal equations of all subsystems.

Recall from Section 2.2.2 that in the context of the analysis of hybrid AC/DC grid, the resources are partitioned into CIDERs (i.e., single-port resources) and NICs (i.e., two-port resources). The grid responses of these two types of resources are introduced in the following.

Grid Response of the CIDERs

As stated in Section 2.4.2, the grid response of a CIDER (i.e., a single-port device) defines either the voltage in function of the current or vice versa, as was introduced in (4.36)–(4.37). For the sake of readability, it is stated explicitly for a specific subsystem j as follows:

$$s \in \mathcal{S}_1^j : \hat{\mathbf{V}}_s^j = \hat{\mathbf{Y}}_s(\hat{\mathbf{I}}_s^j, \hat{\mathbf{W}}_{\sigma,s}, \hat{\mathbf{Y}}_{o,s}) \quad (4.40)$$

$$r \in \mathcal{R}_1^j : \hat{\mathbf{I}}_r^j = \hat{\mathbf{Y}}_r(\hat{\mathbf{V}}_r^j, \hat{\mathbf{W}}_{\sigma,r}, \hat{\mathbf{Y}}_{o,r}) \quad (4.41)$$

where $\hat{\mathbf{V}}_s^j$ and $\hat{\mathbf{I}}_s^j$ are the column vectors of the Fourier coefficients of the terminal voltages $\mathbf{v}_s^j(t)$ and currents $\mathbf{i}_s^j(t)$, respectively, of the grid-forming resources. Similarly, $\hat{\mathbf{V}}_r^j$ and $\hat{\mathbf{I}}_r^j$ represent the column vectors of the terminal voltages and currents of the grid-following resources. The inputs $\hat{\mathbf{W}}_{\sigma,s}$ and $\hat{\mathbf{Y}}_{o,s}$ represent the setpoints and the operating points, respectively, of the CIDERs. The latter is needed in case a linearization was performed in the derivation of the CIDER model, as previously presented in Section 2.4.5 and Section 4.3.3. It is worth noting that this representation of the grid response is generic (e.g., it also applies to passive loads) and that it is valid irrespective of the type of grid it is connected to (i.e., AC or DC).

Grid Response of the Network-Interfacing Converters

The grid response of a NIC is described by two pairs of electrical quantities (i.e., voltages and currents at both ports). It is important to note that a NIC cannot exhibit grid-forming and grid-following behaviour arbitrarily at each port, as the corresponding circuit equations cannot be overdetermined. To be more precise, one cannot simultaneously control the voltages or currents at both ports. By consequence, if one port exhibits grid-forming behaviour, the other must exhibit grid-following behaviour.

Typically, NICs perform grid-forming control on the DC side and grid-following control on the AC side⁵. Thus, a NIC can be seen as a branch $m = (r, s)$ between two nodes $r \in \mathcal{R}_2^{AC}$

⁵In theory, it is possible to perform grid-forming control on the AC side and grid-following control on the DC side. In practice, this configuration is not employed to the best of the authors' knowledge.

4.3 Algorithm for Harmonic Power-Flow Studies

and $s \in \mathcal{S}_2^{DC}$ (i.e., $\mathcal{M} \subseteq \mathcal{R}_2^{AC} \times \mathcal{S}_2^{DC}$). The grid response of a NIC $m = (r, s) \in \mathcal{M}$ is described by

$$[\hat{\mathbf{I}}_r^{AC}, \hat{\mathbf{V}}_s^{DC}] = \hat{\mathbf{Y}}_m(\hat{\mathbf{V}}_r^{AC}, \hat{\mathbf{I}}_s^{DC}, \hat{\mathbf{W}}_{\sigma, m}, \hat{\mathbf{Y}}_{o, m}) \quad (4.42)$$

As for the case of CIDERS, $\hat{\mathbf{W}}_{\sigma, m}$ and $\hat{\mathbf{Y}}_{o, m}$ denote the setpoint and operating point, respectively.

Mismatch Equations

The nodal equations for each subsystem j seen from the grid are formulated using hybrid parameters as introduced in Section 4.2:

$$\hat{\mathbf{V}}_S^j = \hat{\mathbf{H}}_{S \times S}^j \hat{\mathbf{I}}_S^j + \hat{\mathbf{H}}_{S \times \mathcal{R}}^j \hat{\mathbf{V}}_{\mathcal{R}}^j \quad (4.43)$$

$$\hat{\mathbf{I}}_{\mathcal{R}}^j = \hat{\mathbf{H}}_{\mathcal{R} \times S}^j \hat{\mathbf{I}}_S^j + \hat{\mathbf{H}}_{\mathcal{R} \times \mathcal{R}}^j \hat{\mathbf{V}}_{\mathcal{R}}^j \quad (4.44)$$

where $\hat{\mathbf{H}}_{S \times S}^j$, $\hat{\mathbf{H}}_{S \times \mathcal{R}}^j$, $\hat{\mathbf{H}}_{\mathcal{R} \times S}^j$ and $\hat{\mathbf{H}}_{\mathcal{R} \times \mathcal{R}}^j$ are the blocks of the hybrid matrix $\hat{\mathbf{H}}^j$ associated with \mathcal{S}^j and \mathcal{R}^j . $\hat{\mathbf{I}}_S^j$ and $\hat{\mathbf{V}}_{\mathcal{R}}^j$ are the column vectors of all nodal injected currents at the nodes \mathcal{S}^j and all nodal phase-to-ground voltages at the nodes \mathcal{R}^j , respectively.

The HPF problem is given by the mismatch equations between the hybrid parameters in (4.43)–(4.44) and the grid responses of the CIDERS (4.40)–(4.41) and NICs (4.42). At the equilibrium, these mismatches must be zero. Thus, at the nodes where CIDERS are connected:

$$\Delta \hat{\mathbf{V}}_{S_1}^j(\hat{\mathbf{I}}_S^j, \hat{\mathbf{V}}_{\mathcal{R}}^j, \hat{\mathbf{W}}_{\sigma, S_1}^j, \hat{\mathbf{Y}}_{o, S_1}^j) = \mathbf{0} \quad (4.45)$$

$$\Delta \hat{\mathbf{I}}_{\mathcal{R}_1}^j(\hat{\mathbf{I}}_S^j, \hat{\mathbf{V}}_{\mathcal{R}}^j, \hat{\mathbf{W}}_{\sigma, \mathcal{R}_1}^j, \hat{\mathbf{Y}}_{o, \mathcal{R}_1}^j) = \mathbf{0} \quad (4.46)$$

Notably, this formulation corresponds to the one introduced in Section 4.3.3. At the nodes where NICs are connected, the argument of the mismatch equations has to be expanded to account for the quantity of the second terminal of the NICs. Thus,

$$\Delta \hat{\mathbf{V}}_{S_2}^{DC}(\hat{\mathbf{I}}_S^{DC}, \hat{\mathbf{V}}_{\mathcal{R}}^{DC}, \hat{\mathbf{V}}_{\mathcal{R}_2}^{AC}, \hat{\mathbf{W}}_{\sigma, S_2}^{DC}, \hat{\mathbf{Y}}_{o, S_2}^{DC}) = \mathbf{0} \quad (4.47)$$

$$\Delta \hat{\mathbf{I}}_{\mathcal{R}_2}^{AC}(\hat{\mathbf{I}}_S^{AC}, \hat{\mathbf{V}}_{\mathcal{R}}^{AC}, \hat{\mathbf{I}}_{S_2}^{DC}, \hat{\mathbf{W}}_{\sigma, \mathcal{R}_2}^{AC}, \hat{\mathbf{Y}}_{o, \mathcal{R}_2}^{AC}) = \mathbf{0} \quad (4.48)$$

where $\hat{\mathbf{V}}_{\mathcal{R}_2}^{AC}$ and $\hat{\mathbf{I}}_{S_2}^{DC}$ represent the coupling between the two subsystems. The combined system of these equations can be solved using the Newton-Raphson algorithm. To this end, the Jacobian matrix of the equations is required.

Jacobian Matrix

Recall from (4.28) the derivation of the Jacobian matrix $\hat{\mathbf{J}}$ as the difference between the Jacobian matrices of the nodal equations associated with the resources $\hat{\mathbf{J}}^{RSC}$ and the grid $\hat{\mathbf{J}}^{GRD}$, respectively.

For the hybrid AC/DC power system, $\hat{\mathbf{J}}^{GRD}$ is composed of the partial derivatives of the grid equations in (4.43)–(4.44) w.r.t. $\hat{\mathbf{I}}_S^j$ and $\hat{\mathbf{V}}_R^j$, respectively. More precisely, it is composed of the hybrid parameters of the AC and DC subsystem:

$$\hat{\mathbf{J}}^{GRD} = \left[\begin{array}{cc|cc} \hat{\mathbf{H}}_{S \times S}^{AC} & \hat{\mathbf{H}}_{S \times R}^{AC} & \mathbf{0} & \mathbf{0} \\ \hat{\mathbf{H}}_{R \times S}^{AC} & \hat{\mathbf{H}}_{R \times R}^{AC} & \mathbf{0} & \mathbf{0} \\ \hline \mathbf{0} & \mathbf{0} & \hat{\mathbf{H}}_{S \times S}^{DC} & \hat{\mathbf{H}}_{S \times R}^{DC} \\ \mathbf{0} & \mathbf{0} & \hat{\mathbf{H}}_{R \times S}^{DC} & \hat{\mathbf{H}}_{R \times R}^{DC} \end{array} \right] \quad (4.49)$$

Notably, this matrix has a block-diagonal structure, and exhibits no coupling between AC and DC quantities.

$\hat{\mathbf{J}}^{RSC}$ is composed of the partial derivatives of the grid responses in (4.40)–(4.41) and (4.42) w.r.t. $\hat{\mathbf{I}}_S^j$ and $\hat{\mathbf{V}}_R^j$, respectively. The following notation is introduced for the sake of conciseness:

$$\partial_{S_k}^j = \frac{\partial}{\partial \hat{\mathbf{I}}_{S_k}^j}, \quad \partial_{R_k}^j = \frac{\partial}{\partial \hat{\mathbf{V}}_{R_k}^j} \quad (4.50)$$

$\hat{\mathbf{J}}^{RSC}$ is described as follows:

$$\hat{\mathbf{J}}^{RSC} = \left[\begin{array}{ccc|cc} \underbrace{S^{AC}} & \underbrace{R^{AC}} & \underbrace{S^{DC}} & \underbrace{R^{DC}} \\ \hline \partial_{S_1}^{AC} \hat{\mathbf{V}}_{S_1}^{AC} & \mathbf{0} & \mathbf{0} & \mathbf{0} \\ \mathbf{0} & \partial_{R_1}^{AC} \hat{\mathbf{I}}_{R_1}^{AC} & \mathbf{0} & \mathbf{0} \\ \mathbf{0} & \mathbf{0} & \partial_{R_2}^{AC} \hat{\mathbf{I}}_{R_2}^{AC} & \partial_{S_2}^{DC} \hat{\mathbf{I}}_{R_2}^{AC} & \mathbf{0} \\ \hline \mathbf{0} & \mathbf{0} & \mathbf{0} & \partial_{S_1}^{DC} \hat{\mathbf{V}}_{S_1}^{DC} & \mathbf{0} & \mathbf{0} \\ \mathbf{0} & \mathbf{0} & \partial_{R_2}^{AC} \hat{\mathbf{V}}_{S_2}^{DC} & \mathbf{0} & \partial_{R_2}^{DC} \hat{\mathbf{V}}_{S_2}^{DC} & \mathbf{0} \\ \hline \mathbf{0} & \mathbf{0} & \mathbf{0} & \mathbf{0} & \mathbf{0} & \partial_{R_1}^{DC} \hat{\mathbf{I}}_{R_1}^{DC} \end{array} \right] \left. \begin{array}{l} \} S^{AC} \\ \} R^{AC} \\ \} S^{DC} \\ \} R^{DC} \end{array} \right\} \quad (4.51)$$

At the nodes where CIDERS are connected, the corresponding blocks of the Jacobian matrix exhibit a diagonal structure, since a resource influences only the quantity at its point of connection. These terms associated with the AC and DC single-port resources

4.4 Validation of the Proposed Method

Table 4.1: Acronyms used in the legends of the plots in the validation section.

Acronym	Full Name	Section/Algorithm
HPF	Harmonic Power-Flow	Section 4.3.2/Algorithm 1
HPF-DC	Harmonic Power-Flow including the DC characteristics of CIDERS	Section 4.3.3/Algorithm 2
Dec-HPF	Decoupled Harmonic Power-Flow	Appendix A.4

are highlighted in blue and orange, respectively, in (4.51). At nodes where NICs are connected, off-diagonal terms appear in the Jacobian matrix. They describe the coupling between the AC and DC port of the NICs, respectively, as well as between the AC and DC subsystems. These terms are highlighted in green in (4.51).

Details on the derivation of the partial derivatives in (4.49) and (4.51) can be found in Section 2.4.4.

Using the aforesaid expression for the mismatch equations and the Jacobian matrix, the HPF problem can be solved by means of the Newton-Raphson algorithm as described in Section 4.3.3.

4.4 Validation of the Proposed Method

In this section, the three different versions of the HPF algorithm are validated through TDS with Simulink⁶. Additionally, their accuracy w.r.t. other methods and their timing performance, as well as sensitivity to the initial point are assessed. To avoid confusions, the acronyms of the methods used in the legends of figures are summarized in Table 4.1.

4.4.1 Harmonic Power-Flow Study of AC Power Systems

This section validates the first version of the HPF algorithm that employs the simplified CIDER model and is introduced in Algorithm 1. First, the setup of the test system is characterized. Second, the methodology and KPIs are given. Finally, the results include a detailed analysis of the scalability and timing performance of the method, as well as its validation against TDS.

Test System Setup

The proposed HPF method is applied to the test system shown in Fig. 4.2, which is adapted from the CIGRÉ low-voltage benchmark microgrid [1]. That is, the HPF

⁶The implementation of the HPF method and its validation through the example systems discussed in this section are open source and can be found on [GitHub](#).

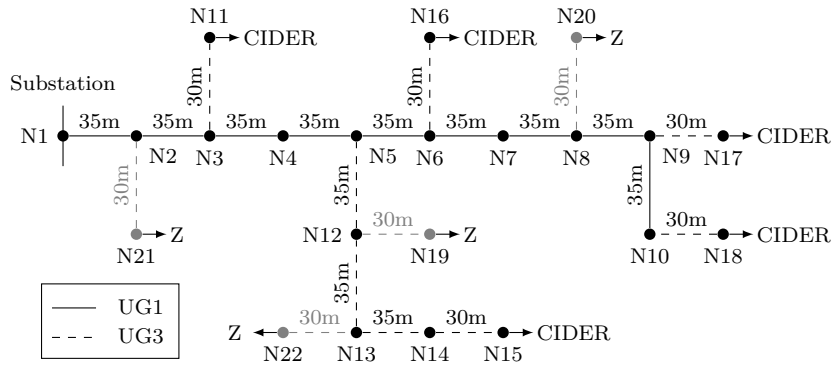


Figure 4.2: Schematic diagram of the test system, which is based on the CIGRÉ low-voltage benchmark microgrid [1] (in black) and extended by unbalanced impedance loads (in grey). For the cable parameters see Table 4.3. The set of grid-following resources are composed of constant impedance loads (Z) and constant power loads (P/Q), their parameters are given in Table 4.4.

problem is formulated for the complete system model, and solved numerically using the Newton-Raphson method.

The test system is characterized as follows. The substation is located in node N1. Its short-circuit parameters, which include both the substation transformer and the upstream grid, are listed in Table 3.1. The TE voltage source injects harmonics, whose levels are given in Table 3.2 and set according to the limits specified in the standard BS-EN-50160:2000 [3]⁷. The lines are built from underground cables, whose sequence parameters are given in Table 4.3. Note that, while the proposed HPF method can treat frequency-dependent cable parameters (see Section 4.2), the parameters of the benchmark microgrid are considered to be frequency-independent. A preliminary analysis was conducted with EMTP-RV in order to confirm that this approximation does hold well on the frequency range under consideration (i.e., ≤ 1.25 kHz). For further details, please see Appendix A.3. Five CIDERS are connected to the ends of the side feeders (i.e., in nodes N11 and N15-18): one grid-forming and four grid-following ones. Their parameters are the same as for the resource validation, see Tables 3.3 and 3.4. Additionally, unbalanced wye-connected constant-impedance loads, are connected at nodes N19-22. The unbalance of a load is expressed by phase weights, which indicate the distribution of the load among the phases. The setpoints and parameters of the CIDERS and loads are given in Table 4.4. Notably, the load unbalance is set such that the resulting voltage unbalance does not exceed the limits specified in [3] (i.e., $|V_{1,-}| \leq 2\% \cdot |V_{1,+}|$).

⁷Recall from Section 3.1.2 and Section 3.2.1 that the PWM actuator of the CIDERS is represented by average as opposed to switching models. Therefore, the CIDERS do only propagate but not create harmonics.

4.4 Validation of the Proposed Method

Table 4.2: Short-Circuit Parameters of the Thévenin Equivalent for the Benchmark Grid.

Parameter	System	Description
Validation		
V_n	230 V-RMS	Nominal voltage
S_{sc}	3.85 MW	Short-circuit power
$ Z_{sc} $	13.7 m Ω	Short-circuit impedance
R_{sc}/X_{sc}	0.271	Resistance-to-reactance ratio

Table 4.3: Sequence Parameters of the Lines in the Test System.

ID	R_+/R_-	R_0	L_+/L_-	L_0	C_+/C_-	C_0
UG1	0.162 Ω	0.529 Ω	0.262 mH	1.185 mH	637 nF	388 nF
UG3	0.822 Ω	1.794 Ω	0.270 mH	3.895 mH	637 nF	388 nF

Methodology

The validation of this first version of the HPF algorithm is three-fold: (i) the dependency of the algorithm’s convergence w.r.t. the initialization, (ii) the accuracy of the HPF method compared to the TDS, and (iii) the timing performance scalability properties of the algorithm are assessed.

As stated in Section 4.3.2, the solution of the HPF algorithm is dependent on the choice of the initial point. In order to assess the convergence behaviour of this first version of the proposed HPF method, the initial spectra of voltages and currents are varied. More precisely, the initial spectra are obtained as a superposition of random positive, negative, and homopolar sequences at each frequency (i.e., fundamental and harmonics), whose magnitudes and phases are uniformly distributed in the intervals $[0, 2]$ p.u. and $[0, 2\pi]$ rad, respectively.

The accuracy of the HPF method is assessed by means of the same KPIs used for the individual resources: the magnitude and phase errors of the HPF results w.r.t. DFT spectra of time-domain waveforms.

A detailed performance analysis of the HPF study is conducted. To this end, the method’s performance is quantified by the mean and standard deviation of the execution time of the HPF study through $N = 50$ simulations and compared to the execution time of the TDS (incl. the Fourier analysis). Moreover, a scalability analysis w.r.t. the numbers of CIDERS and w.r.t. the considered harmonic order in the HPF is performed. In the first case, the grid-following CIDERS at nodes N15-17 are consecutively replaced by wye-connected, balanced impedance loads, whose nominal power is equal to the setpoint of the associated CIDER. In the second case, the timing analysis for the HPF is repeated while increasing the considered maximum harmonic order h_{max} consecutively from 11 to 25. It is important to note that the TDS takes some time to reach the steady state.

Chapter 4. Harmonic Power-Flow Algorithm

Table 4.4: Parameters of the CIDERS and Loads in the Test System for the HPF proposed in Section 4.3.2.

Node	Load/Generator	S/ V	pf/f	Type	Phase weights
N11	Load	15.0 kVar	0.95	P/Q	[0.33 0.33 0.33]
N15	Load	52.0 kVar	0.95	P/Q	[0.33 0.33 0.33]
N16	Load	55.0 kVar	0.95	P/Q	[0.33 0.33 0.33]
N17	Load	35.0 kVar	0.95	P/Q	[0.33 0.33 0.33]
N18	-	230 V-RMS	50 Hz	V/f	-
N19	Load	51.2 kVar	0.95	Z	[0.31 0.50 0.19]
N20	Load	50.4 kVar	0.95	Z	[0.45 0.23 0.32]
N21	Load	61.5 kVar	0.95	Z	[0.24 0.39 0.37]
N22	Load	61.9 kVar	0.95	Z	[0.31 0.56 0.13]

Table 4.5: Ratio of Sequence Voltages and Currents at the Nodes with Resources for the Spectra Obtained using the HPF Method.

Node	$ V_{1,N} $	$ V_{1,H} $	$ I_{1,N} $	$ I_{1,H} $
	$ V_{1,P} $	$ V_{1,P} $	$ I_{1,P} $	$ I_{1,P} $
N01	0.26 %	0.19 %	12.45 %	9.25 %
N11	0.44 %	0.79 %	0.35 %	0.00 %
N15	1.64 %	3.79 %	1.08 %	0.00 %
N16	0.50 %	0.88 %	0.34 %	0.00 %
N17	0.43 %	0.68 %	0.30 %	0.00 %
N18	0.39 %	0.47 %	1.19 %	3.19 %
N19	1.36 %	3.19 %	26.22 %	24.44 %
N20	0.34 %	0.91 %	19.65 %	18.81 %
N21	0.47 %	0.61 %	13.17 %	13.40 %
N22	1.94 %	4.60 %	37.12 %	34.34 %

The settling time of this transient analysis strongly depends on the initialization of the simulation. In order to ensure a fair comparison between the HPF and the TDS, the execution time of the latter is measured only for 5 periods in steady state (i.e., the window length required for the DFT) plus the Fourier analysis (i.e., the DFT). Note well that this corresponds to the minimum amount of simulation time which would have to be done even if the initialization of the TDS were perfect.

Results and Discussion

Table 4.5 gives the voltage and current sequence components of the nodes where resources are connected. Indeed the passive impedance loads at N19-22 introduce significant unbalances in the nodal phase-to-ground voltages and injected currents.

4.4 Validation of the Proposed Method

The convergence of the method appears to be robust w.r.t. a random choice of the initial point (i.e., sequence components whose magnitudes and phases are uniformly distributed in the intervals $[0, 10]$ p.u. and $[0, 2\pi]$ rad, respectively). In fact, the method always converged to the same solution irrespective of its initial value. That is, neither divergence of the algorithm nor multiplicity of solutions have been observed. Naturally, this empirical evidence does not provide a general guarantee. Nevertheless, the fact that the convergence is not affected even by substantial variations of the initial point speaks for the robustness of the proposed method⁸.

Fig. 4.3 shows the maximum absolute errors over all nodes and phases, separately for grid-forming and grid-following CIDERs. The highest errors w.r.t. voltage magnitude and phase are $e_{\text{abs}}(\mathbf{V}_7) = 1.2\text{E-}4$ p.u. and $e_{\text{arg}}(\mathbf{V}_{25}) = 13.18$ mrad, respectively. The highest errors w.r.t. current magnitude and phase are $e_{\text{abs}}(\mathbf{I}_7) = 5.81\text{E-}4$ p.u. and $e_{\text{arg}}(\mathbf{I}_{13}) = 22.51$ mrad, respectively. Observe that the magnitude errors of the current harmonics are higher than those of the voltage harmonics, which is likely due to the Taylor approximation in the reference calculation of the grid-following CIDERs (i.e., Hyp. 18). Moreover, note that the phase error becomes slightly larger as the harmonic order increases. Nevertheless, the error levels are generally very low. Indeed, as it was the case in the resource validation, the magnitude and phase errors are lower than the accuracy of standard measurement equipment.

All simulations are run on the same laptop computer, namely a MacBook Pro 2019 with a 2.4 GHz Intel Core i9 CPU and 32 GB 2400 MHz DDR3 RAM. As shown in Table 4.6, the mean of the execution time of the HPF method lies between 1.75-6.52 sec with standard deviations from 0.03-0.1 sec depending on the number of CIDERs that are connected. By comparison, the execution time of the TDS excluding initial transients is around 28.33-33.39 sec, out of which ca. 0.6 sec are needed for the Fourier analysis (i.e., the DFT). Clearly, the HPF method is faster than the TDS, while yielding accurate results. The computational complexity of the HPF method in function of the maximum harmonic order is illustrated in the upper subplot of Fig. 4.4. Note that the execution time increases almost linearly, but a non-dominant higher-order component is clearly visible (i.e., as expected based on the involved matrix operations). The non-deterministic component of $T_{\text{exc},HPF}$ (i.e., the variation around the mean value) is illustrated in the lower subplot of Fig. 4.4. Observe that any deviation is small compared to the actual value of $T_{\text{exc},HPF}$.

⁸Ongoing research efforts are focusing on this particular characteristic to provide more detailed insights.

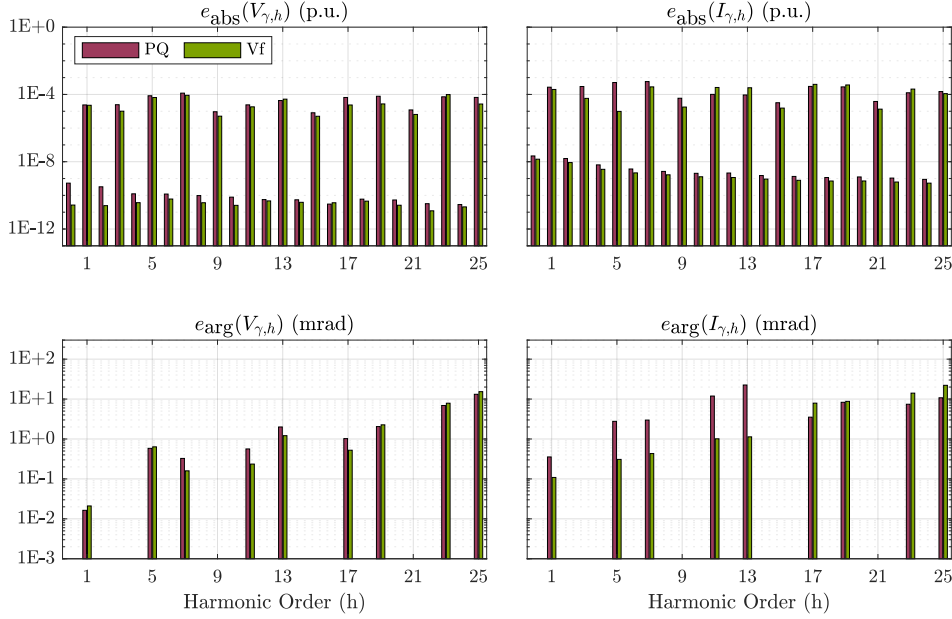


Figure 4.3: Results of the validation on the benchmark system. The plots show the maximum absolute errors over all nodes and phases, for voltages (left column) and currents (right column), in magnitude (top row) and phase (bottom row).

Table 4.6: Timing Performance (for $N = 50$ Simulations of the HPF)

No. of Following CIDERS	1	2	3	4
$T_{exc,TDS}$	28.33 sec	30.36 sec	31.28 sec	33.39 sec
$\mu(T_{exc,HPF})$	1.75 sec	3.97 sec	5.30 sec	6.52 sec
$\sigma(T_{exc,HPF})$	0.03 sec	0.07 sec	0.08 sec	0.10 sec

4.4.2 Harmonic Power-Flow Study of AC Power Systems with Nonlinearities within the Internal Response of the CIDER

This section validates the second version of the HPF algorithm that includes linearizations of the CIDER model, and is introduced in Algorithm 2. The same setup of the test system as in Section 4.4.1 is used. Thus, in the following only the changes as compared to the setup in Section 4.4.1 are pointed out. As before, the extended version of the HPF algorithm that includes the detailed characteristics of the CIDER’s DC sides is validated against TDS with Simulink. Additionally, it is compared to the previous version of the algorithm in Section 4.3.2 and to a classical decoupled HPF.

Test System Setup

The extension of the HPF algorithm that includes the DC side of the CIDERS is validated on the same test system as introduced in Section 4.4.1. The sole difference are the

4.4 Validation of the Proposed Method

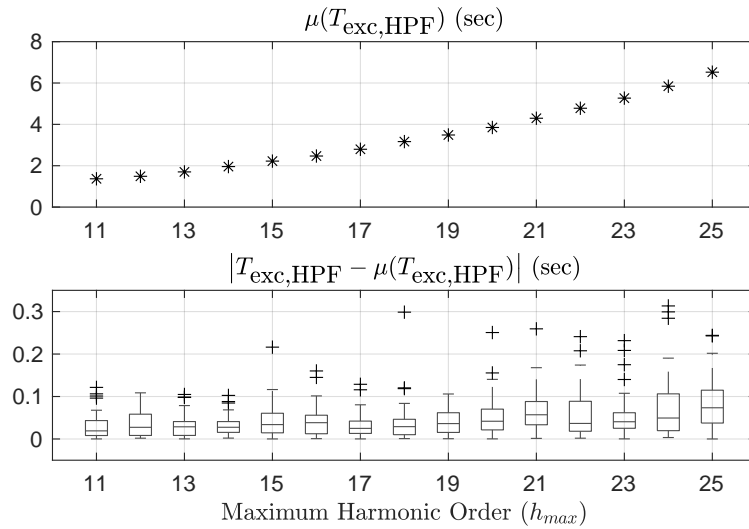


Figure 4.4: Mean and distribution of the timing performance of HPF for maximum numbers of CIDERs and with varying h_{max} for $N = 50$ simulations. The box-and-whisker plot visualizes 25 and 75 percentile of the sample, the whisker length is 1.5-times the interquartile range.

CIDERS that are connected. More specifically, five grid-following CIDERs, which include the modelling of the DC-side characteristics are connected at nodes N11, and N15-N18. The parameters of the grid-following CIDERs that take into account the DC-side characteristics are identical to the ones used in the individual resource validation (i.e., they are given in Table 3.5). Recall that in the test system, unbalances are introduced into the grid through the unbalanced wye-connected constant-impedance loads at nodes N19-N22. As before the amount of unbalance is expressed by phase weights, that describe the distribution of the load over the phases. All setpoints and phase weights of the CIDERs and loads for this case of the test system are given in Table 4.7.

Methodology

The validation of the HPF algorithm is three-fold: (i) the accuracy of the extended HPF method is validated against the results from Simulink (TDS), (ii) the extended HPF method that includes the DC side of the CIDERs, and the one that excludes it (i.e., using the models of the CIDERs introduced in Sections 3.3.1 and 3.3.2), are compared, (iii) the extended HPF method is compared with a classical decoupled HPF. For the decoupled HPF, the resources are represented by independent and superposed harmonic current sources and the system equations are solved independently at each harmonic frequency (see Appendix A.4 for more details).

In both cases the Newton-Raphson algorithm is initialized as described in Section 4.3.2. That is, initial values of AC and DC quantities are based on balanced, sinusoidal conditions

Chapter 4. Harmonic Power-Flow Algorithm

Table 4.7: Parameters of the CIDERs and Loads in the Test System for the HPF proposed in Section 4.3.3.

Node	Load/Generator	S	pf	Type	Phase weights
N11	Generator	15.8 kVar	0.95	P/Q	[0.33 0.33 0.33]
N15	Generator	52.0 kVar	0.95	P/Q	[0.33 0.33 0.33]
N16	Generator	55.0 kVar	0.95	P/Q	[0.33 0.33 0.33]
N17	Generator	35.0 kVar	0.95	P/Q	[0.33 0.33 0.33]
N18	Generator	47.0 kVar	0.95	P/Q	[0.33 0.33 0.33]
N19	Load	51.2 kVar	0.95	Z	[0.31 0.50 0.19]
N20	Load	50.4 kVar	0.95	Z	[0.45 0.23 0.32]
N21	Load	61.5 kVar	0.95	Z	[0.24 0.39 0.37]
N22	Load	61.9 kVar	0.95	Z	[0.31 0.56 0.13]

and nominal values or setpoints. In order to assess the robustness of the convergence, this initial point is distorted with random positive, negative and homopolar sequence components. The magnitudes and phases are chosen from uniform distributions within $\pm 20\%$ and $[0, 2\pi)$, respectively.

The accuracy of the result is assessed using the same KPIs as for the validation of the individual resource model. Additionally, the computation time of the HPF method is compared against the execution time of the TDS. Notably, the initial transients of the TDS are not taken into account in this context. Hence, it is computed as the sum of the simulation time for 5 periods of fundamental frequency and the time needed for the Fourier analysis. In order to compare the two versions of the HPF method (i.e., the one including and excluding the DC side of the CIDERs) the THD of the nodal voltages and injected currents are analysed. To reduce the amount of data to be displayed, the maximum THD over all phases is used.

Results and Discussion

The accuracy of the HPF method including the DC-side characteristics compared to the TDS is shown in Fig. 4.5. The highest errors at every harmonic frequency and over all nodes and phases are shown for the set of all grid-following CIDERs and the set of passive impedance loads. Notably, the errors for the third set (i.e., the zero-injection nodes) can be inferred directly from the hybrid parameters of the grid and the other nodal quantities (i.e., as a linear superposition). Accordingly, if high errors between HPF and TDS were to be observed at a zero-injection node, the origin of this issue would be at nodes with CIDERs, where these problems would be expected to be even more prominent. The maximum errors in Fig. 4.3 occur in the set of grid-following CIDERs. More precisely, the maximum errors regarding the voltage in magnitude and angle are $e_{\text{abs}}(\mathbf{V}_{19}) = 5.97\text{E-}4$ p.u. and $e_{\text{arg}}(\mathbf{V}_{25}) = 16.49$ mrad, respectively. In terms of errors

4.4 Validation of the Proposed Method

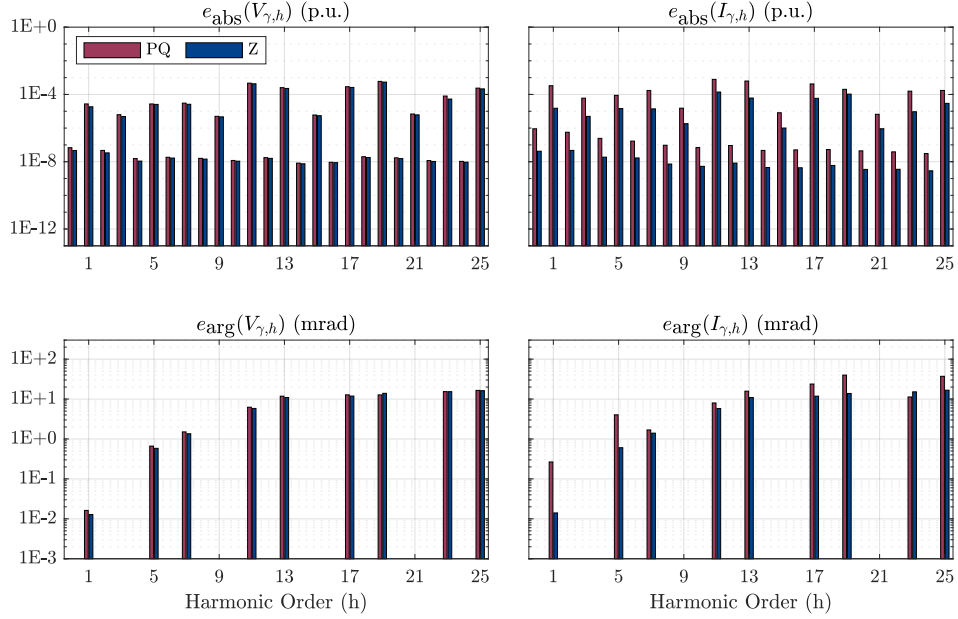


Figure 4.5: Results of the validation on the benchmark system for the extension of the solution algorithm. The grid-following CIDERS (PQ) and the constant impedance loads (Z) are analysed. The plots show the maximum absolute errors over all nodes and phases, for voltages (left column) and currents (right column), in magnitude (top row) and phase (bottom row).

w.r.t. current magnitude and angle the highest values are $e_{\text{abs}}(\mathbf{I}_{11}) = 7.88\text{E-}4$ p.u. and $e_{\text{arg}}(\mathbf{I}_{19}) = 39.89$ mrad, respectively. Notably, the observed errors are very low, i.e., lower than the accuracy of standard measurement devices (i.e., compared to a 0.5 class instrument transformer, as defined in the standards [4, 86, 5] (for a brief summary, see Appendix A.1). Therefore, the extended HPF method is regarded as precise and will be used as a benchmark in the subsequent analyses of this section.

All simulations are run on the same laptop computer as in Section 4.4.1, namely a MacBook Pro 2019 with a 2.4 GHz Intel Core i9 CPU and 32 GB 2400 MHz DDR4 RAM. The HPF method takes 9 iterations and 16.7 sec, while the TDS takes 52.3 sec, out of which 0.5 sec are used for the DFT. The TDS takes roughly three times as long as the HPF. Note that the implementation of the HPF was not done with a strong focus on numerical optimization.

In order to assess the impact of the DC-side modelling on the propagation of harmonics, analyses on the benchmark system were conducted using models of the CIDERS that either in- or exclude the DC side. The obtained results are shown in Fig. 4.6, where the comparison is done at three nodes throughout the system. The spectra differ significantly between the two versions, particular high differences are visible in the angles of the

Chapter 4. Harmonic Power-Flow Algorithm

Table 4.8: Maximum THD at nodes with resources for the HPF method including and excluding the DC side of CIDERS.

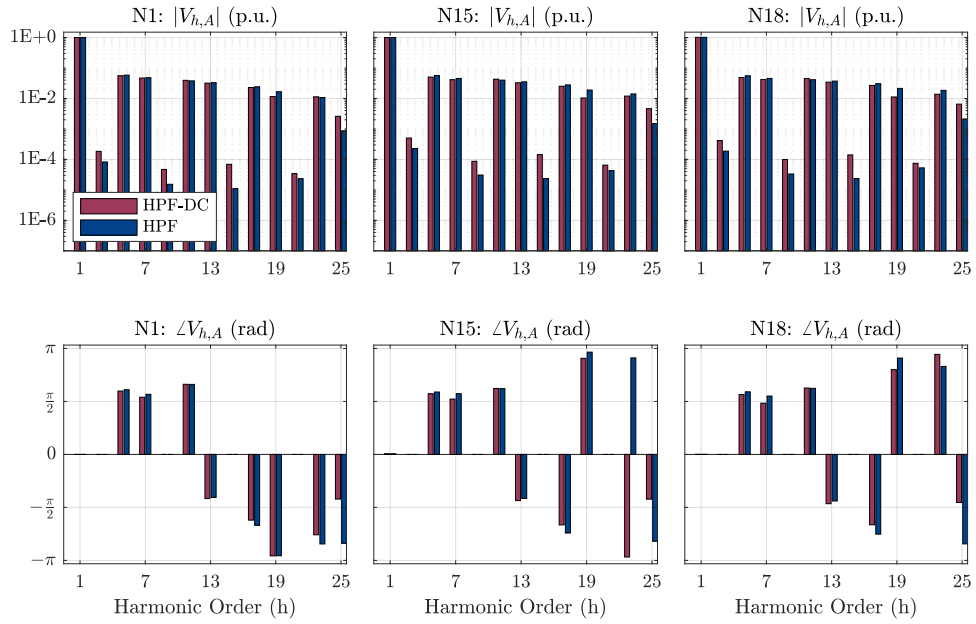
Node	$\text{THD}_{\max}(\mathbf{V}_\gamma)$		$\text{THD}_{\max}(\mathbf{I}_\gamma)$	
	HPF	HPF-DC	HPF	HPF-DC
N01	9.70	9.39	93.68	146.45
N11	9.83	9.31	17.19	20.62
N15	9.77	9.05	5.24	8.07
N16	9.92	9.20	5.21	7.99
N17	10.10	9.28	8.90	10.97
N18	10.11	9.26	6.65	8.95
N19	9.96	9.34	4.05	3.77
N20	10.12	9.36	5.11	4.70
N21	9.78	9.37	4.07	3.88
N22	9.96	9.30	4.06	3.75

currents. Similar observations can be drawn from Table 4.8, where the maximum THD in voltages and currents show significant differences between the two methods. One can conclude that the inclusion of the DC side into the CIDER modelling does have a strong impact on the harmonic propagation through the system.

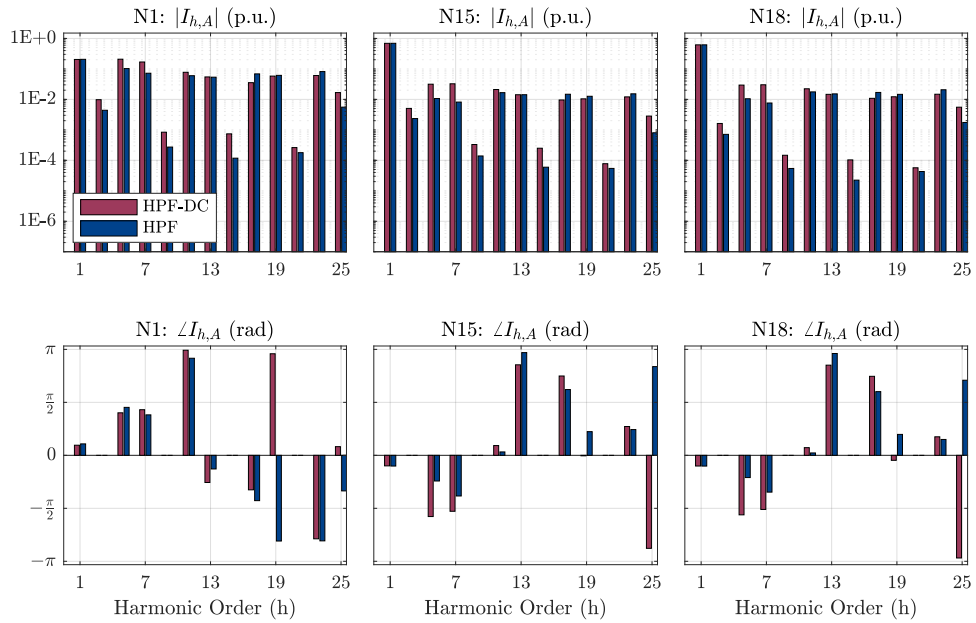
Lastly, the proposed extended HPF framework is benchmarked w.r.t. a classical decoupled HPF. In the classical decoupled HPF the CIDERS are represented by independent and superposed harmonic current sources. The complex ratios of the harmonic currents (see (A.3) in the Appendix A.4) are derived beforehand for a CIDER operating at rated power. For this purpose, the CIDER is connected directly to the TE of the system validation (similarly to the setup shown in Fig. 3.10). Fig. 4.7 shows the comparison between the proposed HPF method and the classical decoupled HPF method. More precisely, the spectra of voltages and currents for three nodes throughout the system are presented. The spectra show non-negligible differences in both magnitude and phase. One can conclude that the proposed HPF is more accurate than the classical decoupled version.

In conclusion, the HPF method that includes the DC side of the CIDERS clearly considers phenomena that the original HPF cannot capture (see Fig. 4.6). More precisely, the extended method provides improved accuracy in terms of the harmonic magnitudes and phase angles. However, the extended HPF method also demands more computational effort, as evidenced in terms of convergence time, i.e., 16.7 sec for the extended HPF and 6.5 sec for the original method for comparable problem size (the 22 bus system with five CIDERS). Therefore, one must make a choice between the benefit of increased accuracy and the drawback of additional computation time.

4.4 Validation of the Proposed Method

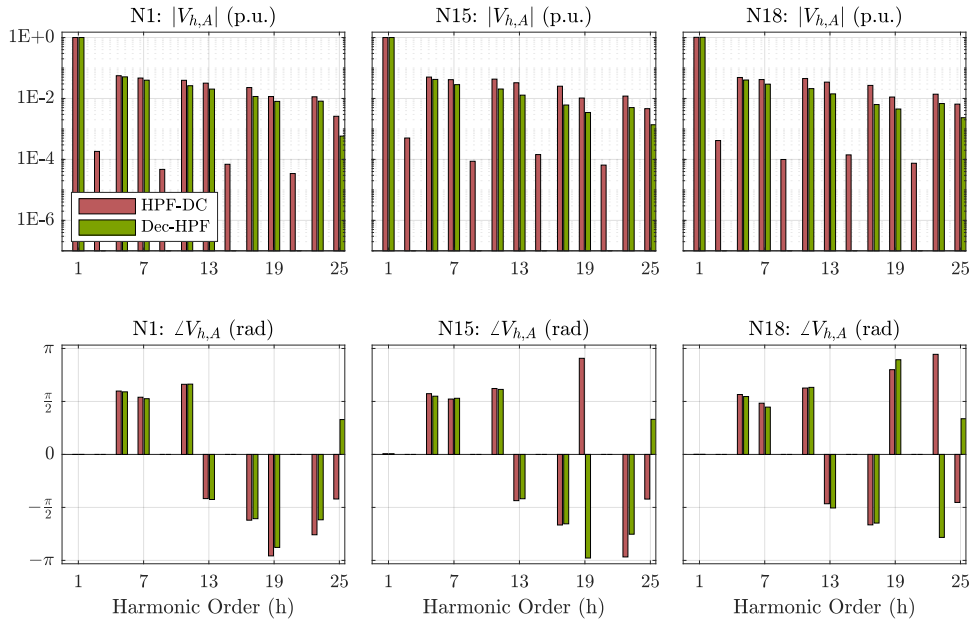


(a)

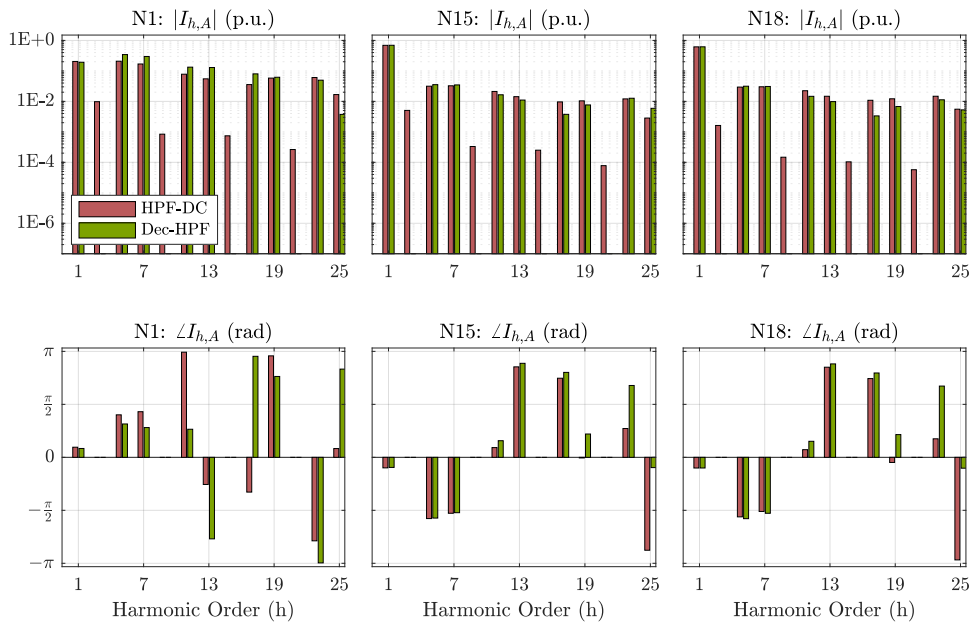


(b)

Figure 4.6: Comparison of the HPF study including (i.e., HPF-DC) and excluding the DC side of the CIDERS at three nodes throughout the benchmark system. The voltages for Phase A of these nodes are given in (4.6a) and the currents in (4.6b).



(a)



(b)

Figure 4.7: Comparison of the HPF study with the decoupled HPF study at three nodes throughout the benchmark system. The voltages for Phase A of these nodes are given in 4.7a and the currents in 4.7b.

4.4 Validation of the Proposed Method

Table 4.9: Parameters of the Network-Interfacing Converters.

AC Node	DC Node	P	Q	V_{DC}	Type
N15	N19	-	9.9 kVAr	900 V	V_{DC}/Q
N16	N20	30.0 kW	9.9 kVAr	-	P/Q
N17	N21	-25.0 kW	8.2 kVAr	-	P/Q
N18	N22	30.0 kW	9.9 kVAr	-	P/Q

4.4.3 Harmonic Power-Flow Study of Hybrid AC/DC Systems

This section presents the results of the HPF method for hybrid AC/DC grids proposed in Section 4.3.4. To this end, the setup of the hybrid AC/DC test system is introduced, and subsequently the spectrum of the AC and DC quantities are validated against the ones from Simulink (TDS),

Test System Setup

The HPF algorithm for hybrid AC/DC grids is validated on an extension of the benchmark AC microgrid proposed in [2]. More specifically, the benchmark system is extended by a DC grid following the example of [102]. As depicted in Fig. 4.8 the AC and DC subsystems are interfaced through NICs at the nodes N15-18 on the AC side and N19-22 on the DC side. Their specifications are given in Table 4.9. The AC subsystem is composed of a feeding substation at node N1, seven grid-following CIDERs at nodes N5, N9, N11 and N13 and two passive loads at nodes N3 and N14. The DC subsystem consists of three current sources at nodes N23 and N25-26, and a passive load at node N24. The references of the resources are given in Table 4.10. The feeding substation of the AC subsystem is modelled as a TE described by parameters depicted in Table 4.11. As for the other test systems, the TE injects harmonics with levels shown in Table 3.2 based on [3]. The line parameters of the AC and DC subsystems are given in Table 4.12.

Methodology

The validation of the HPF algorithm is performed through TDS in Simulink. To this end, the system in Fig. 4.2 is replicated using the models of the CIDERs in Section 3.3. The Matlab code of the HPF method is updated to account for hybrid AC/DC grids. For the TDS, a DFT over 5 periods of the fundamental frequency in steady state is performed. All signals are normalized w.r.t. the base power $P_b = 50$ kW and base voltage $V_b = 230$ V-RMS.

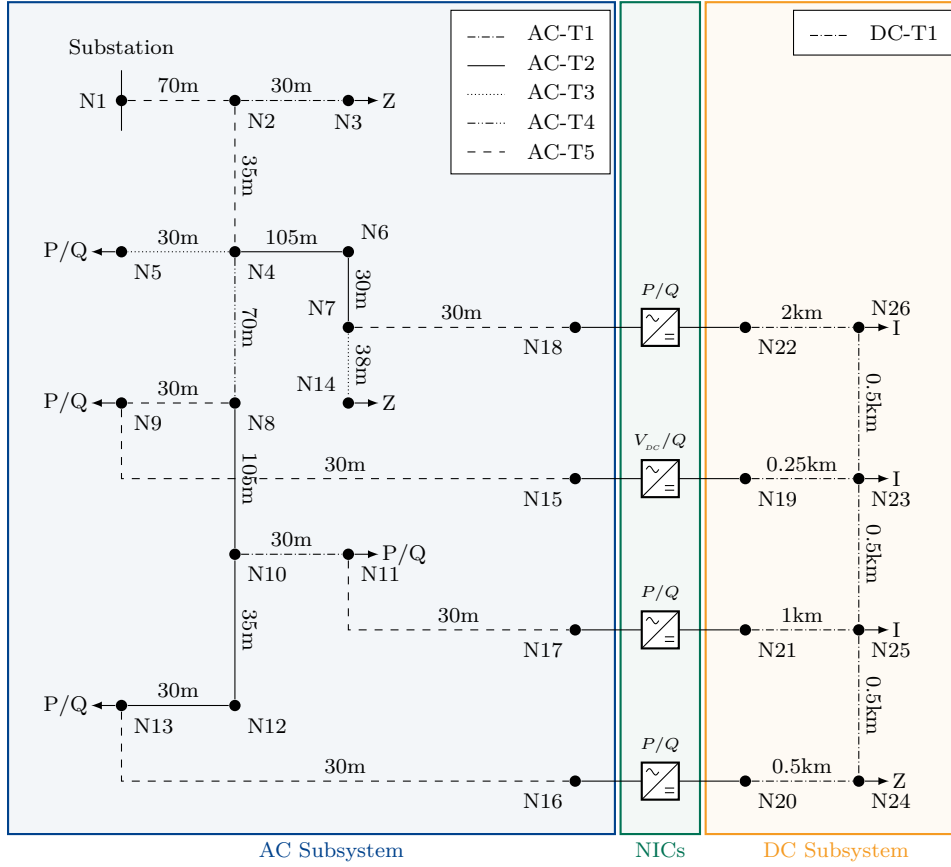


Figure 4.8: Schematic diagram of the test system, which is based on the CIGRÉ low-voltage benchmark microgrid [2] (blue box) and interfaced through NICs (green box) to the DC subsystem (red box), parameters given in Table 4.9. The resources are composed of constant impedance loads (Z), constant power loads (P/Q), and constant current sources (I), parameters given in Table 4.10.

Results and Discussion

In Fig. 4.9 the accuracy of the HPF algorithm for hybrid AC/DC grids is compared to the TDS in Simulink. The highest errors at every harmonic frequency and over all nodes and phases for nodal voltages and injected currents are shown for the two subsystems independently. In Fig. 4.9a the errors are shown for the set of all CIDERs and NICs, as well as the passive impedance loads. For the DC subsystem, the set of grid-forming (i.e., including the DC quantities of the NICs) and grid-following nodes is shown. The maximum errors regarding the voltages and currents occur in both subsystems in the nodes where the NICs are connected. More precisely, the maximum errors in magnitude and phase for the voltages are $e_{\text{abs}}(\mathbf{V}_{13}) = 1.34\text{E-}4$ p.u. and $e_{\text{arg}}(\mathbf{V}_{19}) = 12.23$ mrad in the AC subsystem and $e_{\text{abs}}(\mathbf{V}_6) = 1.03\text{E-}4$ p.u. and $e_{\text{arg}}(\mathbf{V}_6) = 11.26$ mrad in the DC subsystem, respectively. The maximum errors w.r.t. current magnitude and angle are $e_{\text{abs}}(\mathbf{I}_1) = 2.75\text{E-}4$ p.u. and $e_{\text{arg}}(\mathbf{I}_{25}) = 28.45$ mrad in the AC subsystem and

4.4 Validation of the Proposed Method

Table 4.10: Parameters of the Grid-Following Resources, with the constant-power (P/Q), the constant-impedance (Z), and the constant-current (I) behaviour.

Node	P	Q	Type
N05	-20.0 kW	-5.0 kVAr	P/Q
N09-1	4.7 kW	1.5 kVAr	P/Q
N09-2	2.0 kW	0.0 kVAr	P/Q
N11-1	10.7 kW	3.5 kVAr	P/Q
N11-2	8.7 kW	2.9 kVAr	P/Q
N13-1	10.0 kW	3.3 kVAr	P/Q
N13-2	-10.0 kW	0.1 kVAr	P/Q
N03	-20.0 kW	0.0 kVAr	Z
N14	-15.0 kW	-0.3 kVAr	Z
N23	5.0 kW	-	I
N25	10.0 kW	-	I
N26	5.0 kW	-	I
N24	-8.0 kW	-	Z

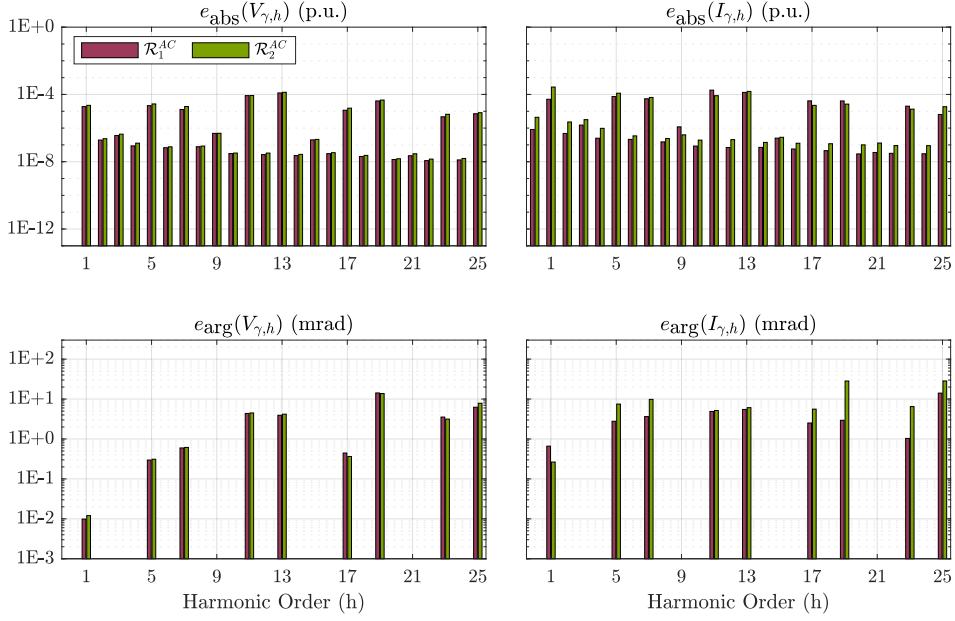
Table 4.11: Short-Circuit Parameters of the Thévenin Equivalent for the hybrid AC/DC Grid.

Parameter	Value	Description
V_n	230 V-RMS	Nominal voltage
S_{sc}	630 kW	Short-circuit power
$ Z_{sc} $	16.3 m Ω	Short-circuit impedance
R_{sc}/X_{sc}	0.125	Resistance-to-reactance ratio

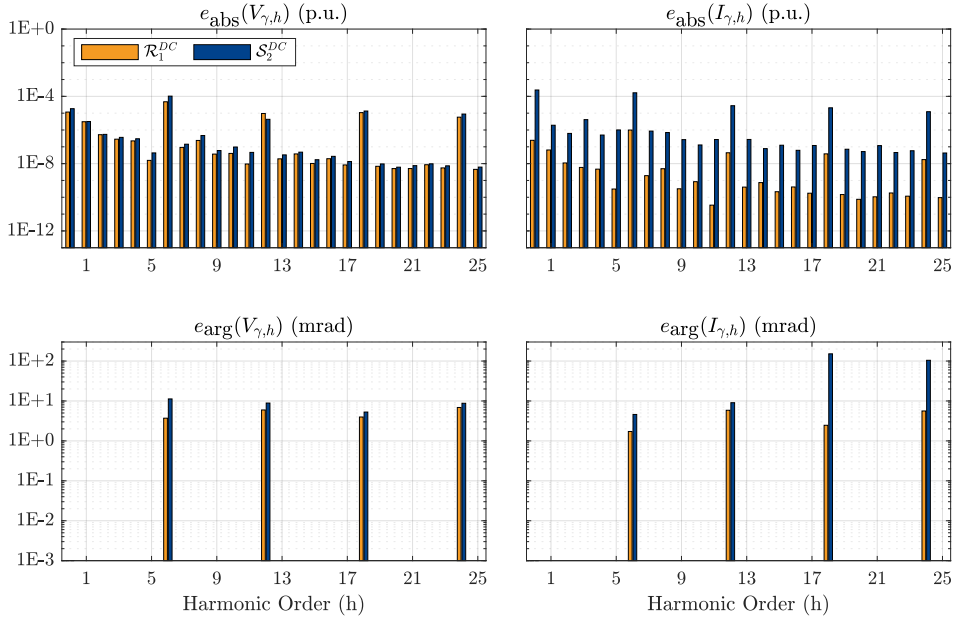
$e_{\text{abs}}(\mathbf{I}_0) = 2.39\text{E-}4$ p.u. and $e_{\text{arg}}(\mathbf{I}_{18}) = 151.63$ mrad in the DC subsystem, respectively. The obtained errors for both subsystems are lower than the accuracy of standard measurement equipment (i.e., they are unobservable in practice). Thus, the accuracy of the HPF method for hybrid AC/DC grids is validated.

A second extension of the HPF method for hybrid AC/DC power systems has been proposed above. Like the first extension, this version can account for elements that previous versions overlooked. However, the added elements also result in a higher complexity of the algorithm, and inherently longer convergence times.

Chapter 4. Harmonic Power-Flow Algorithm



(a)



(b)

Figure 4.9: Results of the validation of the AC (Fig. 4.9a) and DC subsystem (Fig. 4.9b). The grid-following CIDERS (\mathcal{R}_1^{AC}) and the AC side of the NICs (\mathcal{R}_2^{AC}), as well as the DC-side resources (\mathcal{R}_1^{DC}) and the DC side of the NICs (\mathcal{S}_2^{DC}) are shown. The plots show the maximum absolute errors over all nodes and phases, for voltages (left column) and currents (right column), in magnitude (top row) and phase (bottom row).

4.4 Validation of the Proposed Method

Table 4.12: AC (+/ - /0) and DC Parameters of the Lines.

ID	$R_{+/-/0}$ or R	$L_{+/-/0}$ or L	$C_{+/-/0}$ or C
AC-T1	3.30 Ω/km	0.45 mH/km	150 nF/km
AC-T2	1.21 Ω/km	0.42 mH/km	230 nF/km
AC-T3	0.78 Ω/km	0.40 mH/km	210 nF/km
AC-T4	0.55 Ω/km	0.39 mH/km	260 nF/km
AC-T5	0.27 Ω/km	0.38 mH/km	320 nF/km
DC-T1	0.08 Ω/km	0.28 mH/km	292 nF/km

5 Harmonic Stability Assessment

Summary: *In this chapter, the HSS model of a generic power system is proposed and employed it in the context of HSA through eigenvalue analysis. More precisely, the HSS model is formulated by combining the HSS models of the resources and the grid in closed-loop configuration. The HSS model of the resources is the combination of all HSS models of the individual resources as introduced in Chapter 2. The HSS model of the grid is derived from the dynamic equations of the individual branch and shunt elements in time domain and subsequently transformed to harmonic domain by means of Toeplitz theory. The system matrix of the HSS models on power system level or resource level can be further interpreted through eigenvalue analysis. Furthermore, one can perform a sensitivity analysis to determine how changes in model parameters affect the locations of eigenvalues. Based on this sensitivity analysis, a classification of eigenvalues into control-design variant, control-design invariant, and design invariant eigenvalues is proposed. First, the HSA of the open-loop CIDER models from Chapter 3 is performed. More precisely, an in-depth analysis of the classification of the eigenvalues into the aforementioned categories, the impact of the maximum harmonic order on the locations of the eigenvalues, and the sensitivity of the eigenvalues w.r.t. to specific control parameters is provided. Second, the HSA is performed for a small but representative example system. The analysis of the system eigenvalues w.r.t. classification of the eigenvalues and comparison to the open-loop components is performed. Finally, a harmonic instability is observed through the LTP system eigenvalues and validated through TDS in Simulink. It is also shown that this instability cannot be observed with a conventional stability criterion (i.e., the eigenvalues of the corresponding LTI system).*

5.1 State of the Art

Recently, the assessment of Harmonic Stability has seen a growing interest in the research community. The ability to evaluate this specific type of instability, arising from the presence of harmonics as well as the interaction between them (i.e., coupling between different frequencies), largely depends on the characteristics of the adopted models. Hence, the following literature review is separated into HSA based on approaches that either represent or do not represent the frequency coupling. Additionally, the same types of models as introduced in Section 2.1 will be explored in the following. Detailed discussions on this topic can be found in [49, 63].

Assuming that the system behaviour can be described by a linear or linearized model, the stability can be determined from the corresponding matrices either via eigenvalue analysis or using Nyquist techniques. In the case of LTI models, the required matrices are readily available for the corresponding techniques. Regarding the DP approaches, both linear or nonlinear models may be formulated. The linear models can directly be employed for the HSA, whereas for the nonlinear ones, a linearized model must first be derived (e.g., through small-signal analysis). Lastly, the system matrix of the HSS model can directly be employed for the HSA. Notably, EHD models are in general derived for dynamic power system simulations and usually not used for HSA.

5.1.1 Studies without Representation of Frequency Coupling

Some works studying harmonic instabilities employ impedance-based analysis methods, where the stability is determined through the Nyquist criterion from point of view of a specific resource. Therefore, these approaches may be referred to as point-of-connection-based methods. More precisely, the resources and the remainder of the system are represented by Norton and Thévenin Equivalents [103]. Naturally, these equivalents have to be recomputed upon any change in the parameters of the power system components or the topology of the power system itself.

In [28], an instability characterized by high harmonic distortion is identified using an impedance-based stability criterion. For this examination, a test system including five CIDERS connected in parallel is considered. The study shows that, if one of the five CIDERS is disconnected, the harmonic distortion in the system is significantly increased. This observation is further confirmed through the Nyquist plots of the system. In [27] the stability of a power system with several CIDERS is studied. The individual components (i.e., CIDERS and lines of the grid) are represented by impedances and employed to derive Nyquist plots.

However, these techniques cannot represent the coupling between distinct harmonics in the system (recall Fig. 2.1), since they rely on LTI system theory. Therefore, while these

stability criteria may be able to identify instabilities caused by an individual harmonic, they would fail to detect an instability arising from the interaction of multiple harmonics (i.e., coupling).

5.1.2 Studies with Representation of Frequency Coupling

In the HSA of models capturing frequency coupling, two modelling techniques are distinguished: DP and HSS models. Literature on the HSS approach frequently uses both Nyquist and eigenvalue techniques, whereas the DP approach predominantly utilizes eigenvalue analysis.

In [104] a nonlinear model derived through the DP methodology for the HSA of a power system is proposed. From the DP model, the small-signal model is obtained through linearization around a harmonic operating point, and an eigenvalue analysis is performed. A power system including three CIDERS is analysed in detail. More specifically, it is shown how, upon a parameter change, the harmonic components of the active power become unstable, while the fundamental component remains in steady state. The instability is also observed in the eigenvalues. In another study, the eigenvalues derived from an HSS model and a DP model for an individual three-phase CIDER are compared [48]. It is demonstrated that the eigenvalues from both methodologies coincide for the analysed CIDER, which suggests to that both approaches are equally effective in representing the coupling between harmonics and the corresponding stability margins.

The majority of HSA research employs LTP models to represent the components of power systems. In this case, the HSS model, generated using the Toeplitz matrices of the LTP system, serves as the foundation for the HSA.

In [105], a generalization of the Nyquist criterion to HSS models, which is similar to the generalized Nyquist criterion for LTI *Multi-Input Multi-Output* (MIMO) systems, was first proposed. In [106], the equivalent harmonic impedances of a single-phase system, comprising two CIDERS, are identified through small-signal current injections. The harmonic impedances are then used to derive the Nyquist plot of the system. In [107], the Nyquist plots for a single-phase grid-connected CIDER are derived. To this end, the equivalent impedance of the CIDER and the grid are obtained from the corresponding HSS models.

Many studies use the eigenvalues of the HSS model or poles of the corresponding HTF for stability assessment. The theory behind this is was first detailed in [32]. Current research often aims at understanding the causes of harmonic instability by investigating individual CIDERS. [34] provides an in-depth analysis of stability margins in grid-following CIDERS with different synchronization techniques and control approaches. The effects of parameter variations on the stability margin are identified through eigenvalue analysis and validated in power-hardware-in-the-loop experiments. In [35] a detailed

study of the HSA of a specific synchronization technique used in CIDERS, i.e., the so-called multiple second-order generalized integrator is proposed. Both [36] and [37] examine the stability of a single-phase CIDER connected to the grid, with the grid modelled as a TE. In [36], the instability is observed by means of the poles of the HTF, and validated through TDS and experiments. [37] examines the stability of the system through its eigenvalues and confirms the findings through TDS.

When conducting an eigenvalue analysis for the HSS system, additional insights can be gained from the associated eigenvectors. Specifically, each entry in an eigenvector is associated with a particular eigenvalue and quantifies its impact on the respective states. For LTI systems, this type of investigation is known as participation factor analysis or modal analysis [108]. In [109] a generalization of the participation factor analysis from LTI to LTP systems (i.e., to HSS models) is proposed. A detailed analysis in this respect is performed for the example of a grid-following CIDER.

5.1.3 Motivation for the Proposed Method

To summarize, DP and HSS methodologies appear to be most promising for HSA due to their capability of representing the frequency-coupling effects inherent to CIDERS. By contrast, other approaches fall short in capturing this phenomenon. However, under certain conditions, harmonic instabilities, which involve only a single harmonic (e.g., due to a resonance), might still be captured by such approaches.

W.r.t. modularity and ease of representation, HSS models appear to be particularly promising. However, a potential drawback of HSS models is its inherent large number of state variables, making it challenging to scale. A potential solution is mentioned by [62]: selecting only certain harmonic frequencies (through an appropriate method) in order to reduce the size of the model. The core idea is to prioritize and incorporate only a subset of harmonics which is dominant in the system.

Extensive research has been performed on the HSA of single CIDERS or on small systems as examples. Yet no approach has been proposed, that is capable of analysing generic power systems while taking into account the interactions of different CIDERS through the grid. Addressing this research gap, the modelling framework which has been proposed in Chapter 2, and further validated in Chapter 4, is adapted for the HSA in this chapter.

5.2 Harmonic State-Space Model of a Power System

In this section, the HSS model of the entire power system is derived. More specifically, the HSS models of the resources and the grid are combined into the HSS model of the power system. First, the HSS models of individual CIDERS is recalled. Second, it is shown how the lumped-element model of the grid, which was introduced in Section 2.3, can be

5.2 Harmonic State-Space Model of a Power System

described by a time-domain state-space model, which is then transformed to the HSS model of the grid. The HSS model of the individual CIDER is combined to form the HSS model of all resources, similar to the derivations in Section 2.4.3. Through combination of the HSS models of the resources and the grid, the open-loop HSS model of the power system is derived. Subsequently, the closed-loop model is calculated following the electrical interconnection between the resources and the grid. Note that the derivations of the HSS model of the system follows the same procedure as the derivations of the CIDERs closed-loop model in Section 2.4.3.

5.2.1 Harmonic State-Space Model of the Resources

Let $q \in \mathcal{Q}$ be an generic CIDER (i.e., irrespective of the governing control law). Recalling the general form of a CIDER's HSS as stated in (2.75)–(2.76), the CIDER q is modelled by the following equations:

$$\hat{\Psi}_q \hat{\mathbf{X}}_q = \hat{\mathbf{A}}_q \hat{\mathbf{X}}_q + \hat{\mathbf{E}}_{q,\gamma} \hat{\mathbf{W}}_{q,\gamma} + \hat{\mathbf{E}}_{q,\sigma} \hat{\mathbf{W}}_{q,\sigma} + \hat{\mathbf{E}}_{q,o} \hat{\mathbf{W}}_{q,o} \quad (5.1)$$

$$\hat{\mathbf{Y}}_{q,\gamma} = \hat{\mathbf{C}}_{q,\gamma} \hat{\mathbf{X}}_q + \hat{\mathbf{F}}_{q,\gamma} \hat{\mathbf{W}}_{q,\gamma} + \hat{\mathbf{F}}_{q,\sigma} \hat{\mathbf{W}}_{q,\sigma} + \hat{\mathbf{F}}_{q,o} \hat{\mathbf{W}}_{q,o} \quad (5.2)$$

Recall from Chapter 2 that the matrices of the HSS of an individual CIDER are a function of the operating points $\hat{\mathbf{W}}_{q,o}$ and $\hat{\mathbf{Y}}_{q,o}$. For the sake of clarity, this dependency is not specifically stated in the following.

5.2.2 Harmonic State-Space Model of the Electrical Grid

In this section, a state-space model of the grid is derived, based on the grid topology given by all nodes as well as the branches and shunts of the line connecting them. To this end, recall the definitions of the lumped-element model as well as the definitions of the nodes, branches and shunts introduced in Section 2.3. In general, the state-space variables of the grid are given by i) the three-phase currents of the branch inductors and ii) the three-phase voltages of the shunt capacitors¹.

Branches

The equation describing the dynamics of a branch $\ell \in \mathcal{L}$ connecting the nodes m and $n \in \mathcal{N}$ is given by

$$\mathbf{L}_\ell \frac{d}{dt} \mathbf{i}_\ell(t) = -\mathbf{R}_\ell \mathbf{i}_\ell(t) + \mathbf{v}_n(t) - \mathbf{v}_m(t) \quad (5.3)$$

¹Within typical frequency ranges used in HA (i.e., $f < 10$ kHz) the lumped-element models of lines and transformers are such that the branches are inductive and shunts capacitive.

Chapter 5. Harmonic Stability Assessment

Recall the polyphase incidence matrix $\mathcal{A}_{\mathcal{L}|\mathcal{N}}$ introduced in (2.6). With that, the system of equations for all branches in \mathcal{L} follows as

$$\frac{d}{dt}\mathbf{i}_{\mathcal{L}}(t) = -\mathbf{L}_{\mathcal{L}}^{-1}\mathbf{R}_{\mathcal{L}}\mathbf{i}_{\mathcal{L}}(t) + \mathbf{L}_{\mathcal{L}}^{-1}\mathcal{A}_{\mathcal{L}|\mathcal{N}}\mathbf{v}_{\mathcal{N}}(t) \quad (5.4)$$

with the branch currents and nodal voltages

$$\mathbf{i}_{\mathcal{L}}(t) = \text{col}_{\ell \in \mathcal{L}}(\mathbf{i}_{\ell}(t)) \quad (5.5)$$

$$\mathbf{v}_{\mathcal{N}}(t) = \text{col}_{n \in \mathcal{N}}(\mathbf{v}_n(t)) \quad (5.6)$$

and

$$\mathbf{L}_{\mathcal{L}} = \text{diag}_{\ell \in \mathcal{L}}(\mathbf{L}_{\ell}) \quad (5.7)$$

$$\mathbf{R}_{\mathcal{L}} = \text{diag}_{\ell \in \mathcal{L}}(\mathbf{R}_{\ell}) \quad (5.8)$$

Recall from (2.7), the separation of the incidence matrix into the grid-forming and grid-following quantities, $\mathcal{A}_{\mathcal{L}|\mathcal{S}}$ and $\mathcal{A}_{\mathcal{L}|\mathcal{R}}$, respectively. Applying this to (5.4) yields

$$\frac{d}{dt}\mathbf{i}_{\mathcal{L}}(t) = -\mathbf{L}_{\mathcal{L}}^{-1}\mathbf{R}_{\mathcal{L}}\mathbf{i}_{\mathcal{L}}(t) + \mathbf{L}_{\mathcal{L}}^{-1}\mathcal{A}_{\mathcal{L}|\mathcal{S}}\mathbf{v}_{\mathcal{S}}(t) + \mathbf{L}_{\mathcal{L}}^{-1}\mathcal{A}_{\mathcal{L}|\mathcal{R}}\mathbf{v}_{\mathcal{R}}(t) \quad (5.9)$$

with

$$\mathbf{v}_{\mathcal{S}}(t) = \text{col}_{n \in \mathcal{S}}(\mathbf{v}_n(t)) \quad (5.10)$$

$$\mathbf{v}_{\mathcal{R}}(t) = \text{col}_{n \in \mathcal{R}}(\mathbf{v}_n(t)) \quad (5.11)$$

Shunts

In general, the shunt capacitors define the state-space variables associated with the nodes (i.e., the capacitor voltages). The shunt capacitors to be considered can be i) due to the line parameters or ii) due to the filter elements of the connected resource (i.e. the capacitance of the grid-forming resource). In the latter case, the derivation of the dynamic equations differs slightly. To this end, the shunts are separated into two sets depending on which type of resource is connected at the corresponding node, i.e., grid-forming or grid-following resources.

At the nodes where grid-forming resources are connected, the resource controls the nodal voltage \mathbf{v}_s over its output capacitor \mathbf{C}_s ². A representation of this is shown in Fig. 5.1a. Since the shunt capacitor \mathbf{C}_{t_s} is usually small compared to \mathbf{C}_s it is neglected at grid-forming nodes. w.r.t. the latter, which allows for simplifications³. For the sake of

²Recall from Section 3.3.1 that a grid-forming converter with an LCL filter would belong to the set \mathcal{R} . This case is not considered here.

³This is usually true for low-voltage distribution grids. In case the shunt capacitors are not negligible compared to the output capacitor of the resource, the sum of all shunts can be combined in the resource's output capacitor.

5.2 Harmonic State-Space Model of a Power System

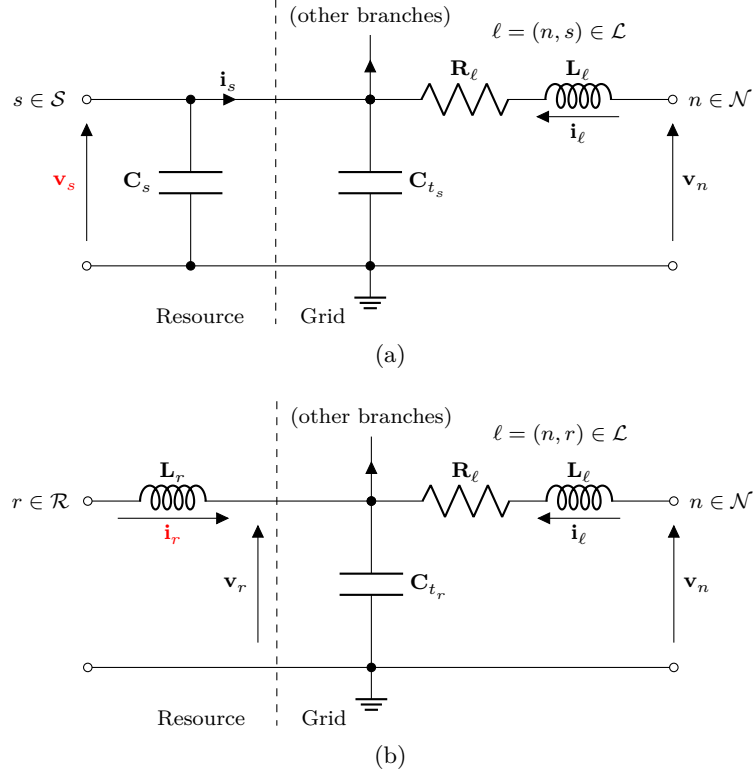


Figure 5.1: Lumped-element model of the grid shown at nodes with a grid-forming resource (5.1a) and a grid-following resource (5.1b). The electrical quantity controlled by the resource is highlighted in red.

conciseness, this hypothesis is specifically stated here:

Hypothesis 26. *The shunt capacitor C_{t_s} of a line connected to a grid-forming resource is small compared to C_s .*

The equation describing a node $s \in \mathcal{S} \subset \mathcal{N}$ connected to the branches \mathcal{L}_s , where \mathcal{L}_s describes the set of branches connected to node s , is given by

$$\mathbf{i}_s(t) = - \sum_{\ell \in \mathcal{L}_s} \mathbf{i}_\ell(t) \quad (5.12)$$

For all nodes $s \in \mathcal{S}$ the equation can be written compactly as

$$\mathbf{i}_\mathcal{S}(t) = \mathcal{A}_{\mathcal{S}|\mathcal{L}} \mathbf{i}_\mathcal{L}(t) \quad (5.13)$$

where $\mathcal{A}_{\mathcal{S}|\mathcal{L}} = \mathcal{A}_{\mathcal{L}|\mathcal{S}}^\top$.

At the nodes where grid-following resources are connected, the resource controls the current flowing through its grid-side filter inductance \mathbf{L}_r and being injected into the grid (Fig. 5.1b). The equations describing a node $r \in \mathcal{R} \subset \mathcal{N}$ connected to branches \mathcal{L}_r ,

Chapter 5. Harmonic Stability Assessment

where \mathcal{L}_r describes the set of branches connected to node r , is given by

$$\mathbf{C}_{t_r} \frac{d}{dt} \mathbf{v}_r(t) = -\mathbf{i}_r(t) + \sum_{\ell \in \mathcal{L}_r} \mathbf{i}_\ell(t) \quad (5.14)$$

which can be written for all nodes $r \in \mathcal{R}$ as

$$\frac{d}{dt} \mathbf{v}_{\mathcal{R}}(t) = \mathbf{C}_{\mathcal{T}}^{-1} \mathbf{A}_{\mathcal{R}|\mathcal{L}} \mathbf{i}_{\mathcal{L}}(t) - \mathbf{C}_{\mathcal{T}}^{-1} \mathbf{i}_{\mathcal{R}}(t) \quad (5.15)$$

where $\mathbf{A}_{\mathcal{R}|\mathcal{L}} = \mathbf{A}_{\mathcal{L}|\mathcal{R}}^\top$.

Combined State-Space Model of the Grid

In line with the previous explanations: i) the grid state is given by the branch currents and shunt voltages ii) the grid disturbances are the voltages and currents regulated by the grid-forming and grid-following resources, respectively iii) the grid outputs are the corresponding non-regulated quantities. Formally:

$$\mathbf{x}_{\mathcal{G}}(t) = \begin{bmatrix} \mathbf{i}_{\mathcal{L}}(t) \\ \mathbf{v}_{\mathcal{R}}(t) \end{bmatrix} \quad (5.16)$$

$$\mathbf{w}_{\mathcal{G}}(t) = \begin{bmatrix} \mathbf{v}_{\mathcal{S}}(t) \\ \mathbf{i}_{\mathcal{R}}(t) \end{bmatrix} \quad (5.17)$$

$$\mathbf{y}_{\mathcal{G}}(t) = \begin{bmatrix} \mathbf{i}_{\mathcal{S}}(t) \\ \mathbf{v}_{\mathcal{R}}(t) \end{bmatrix} \quad (5.18)$$

It follows

$$\dot{\mathbf{x}}_{\mathcal{G}}(t) = \mathbf{A}_{\mathcal{G}}(t) \mathbf{x}_{\mathcal{G}}(t) + \mathbf{E}_{\mathcal{G}}(t) \mathbf{w}_{\mathcal{G}}(t) \quad (5.19)$$

$$\mathbf{y}_{\mathcal{G}}(t) = \mathbf{C}_{\mathcal{G}}(t) \mathbf{x}_{\mathcal{G}}(t) + \mathbf{F}_{\mathcal{G}}(t) \mathbf{w}_{\mathcal{G}}(t) \quad (5.20)$$

with the matrices

$$\mathbf{A}_{\mathcal{G}}(t) = \mathbf{A}_{\mathcal{G},0} = \begin{bmatrix} -\mathbf{L}_{\mathcal{L}}^{-1} \mathbf{R}_{\mathcal{L}} & \mathbf{L}_{\mathcal{L}}^{-1} \mathbf{A}_{\mathcal{L}|\mathcal{R}} \\ -\mathbf{C}_{\mathcal{T}}^{-1} \mathbf{A}_{\mathcal{R}|\mathcal{L}} & \mathbf{0} \end{bmatrix} \quad (5.21)$$

$$\mathbf{E}_{\mathcal{G}}(t) = \mathbf{E}_{\mathcal{G},0} = \begin{bmatrix} \mathbf{L}_{\mathcal{L}}^{-1} \mathbf{A}_{\mathcal{L}|\mathcal{S}} & \mathbf{0} \\ \mathbf{0} & \mathbf{C}_{\mathcal{T}}^{-1} \end{bmatrix} \quad (5.22)$$

$$\mathbf{C}_{\mathcal{G}}(t) = \mathbf{C}_{\mathcal{G},0} = \begin{bmatrix} \mathbf{A}_{\mathcal{S}|\mathcal{L}} & \mathbf{0} \\ \mathbf{0} & \mathbf{I} \end{bmatrix} \quad (5.23)$$

$$\mathbf{F}_{\mathcal{G}}(t) = \mathbf{F}_{\mathcal{G},0} = \mathbf{0} \quad (5.24)$$

5.2.3 Open-Loop Model of the Power System

Combined Harmonic State-Space Model of all Resources

In order to derive the HSS of the entire system, one needs to combine the HSS of the individual CIDERs in (5.1)–(5.2) to the model of all resources.

$$\hat{\Psi}_{\mathcal{Q}} \hat{\mathbf{X}}_{\mathcal{Q}} = \hat{\mathbf{A}}_{\mathcal{Q}} \hat{\mathbf{X}}_{\mathcal{Q}} + \hat{\mathbf{E}}_{\mathcal{Q},\gamma} \hat{\mathbf{W}}_{\mathcal{Q},\gamma} + \hat{\mathbf{E}}_{\mathcal{Q},\sigma} \hat{\mathbf{W}}_{\mathcal{Q},\sigma} + \hat{\mathbf{E}}_{\mathcal{Q},o} \hat{\mathbf{W}}_{\mathcal{Q},o} \quad (5.25)$$

$$\hat{\mathbf{Y}}_{\mathcal{Q},\gamma} = \hat{\mathbf{C}}_{\mathcal{Q},\gamma} \hat{\mathbf{X}}_{\mathcal{Q}} + \hat{\mathbf{F}}_{\mathcal{Q},\gamma} \hat{\mathbf{W}}_{\mathcal{Q},\gamma} + \hat{\mathbf{F}}_{\mathcal{Q},\sigma} \hat{\mathbf{W}}_{\mathcal{Q},\sigma} + \hat{\mathbf{F}}_{\mathcal{Q},o} \hat{\mathbf{W}}_{\mathcal{Q},o} \quad (5.26)$$

where

$$\hat{\mathbf{X}}_{\mathcal{Q}} = \text{col}_{q \in \mathcal{Q}}(\hat{\mathbf{X}}_q) \quad (5.27)$$

$$\hat{\mathbf{A}}_{\mathcal{Q}} = \text{diag}_{q \in \mathcal{Q}}(\hat{\mathbf{A}}_q) \quad (5.28)$$

The remaining vectors (i.e., $\hat{\mathbf{Y}}_q$ etc.) and matrices (i.e., $\hat{\mathbf{E}}_q$ etc.) are defined analogously. Without loss of generality, one can assume that the resources \mathcal{Q} are ordered as $\mathcal{Q} = (\mathcal{S}, \mathcal{R})$. Such that,

$$\hat{\mathbf{W}}_{\mathcal{Q},\gamma} = \text{col}(\hat{\mathbf{I}}_{\mathcal{S}}, \hat{\mathbf{V}}_{\mathcal{R}}) \quad (5.29)$$

$$\hat{\mathbf{Y}}_{\mathcal{Q},\gamma} = \text{col}(\hat{\mathbf{V}}_{\mathcal{S}}, \hat{\mathbf{I}}_{\mathcal{R}}) \quad (5.30)$$

Harmonic State-Space Model of the Electrical Grid

Transforming (5.19)–(5.20) to harmonic domain employing the Toeplitz transform yields the HSS model of the grid:

$$\hat{\Psi}_{\mathcal{G}} \hat{\mathbf{X}}_{\mathcal{G}} = \hat{\mathbf{A}}_{\mathcal{G}} \hat{\mathbf{X}}_{\mathcal{G}} + \tilde{\mathbf{E}}_{\mathcal{G}} \tilde{\mathbf{W}}_{\mathcal{G}} \quad (5.31)$$

$$\tilde{\mathbf{Y}}_{\mathcal{G}} = \tilde{\mathbf{C}}_{\mathcal{G}} \hat{\mathbf{X}}_{\mathcal{G}} + \tilde{\mathbf{F}}_{\mathcal{G}} \tilde{\mathbf{W}}_{\mathcal{G}} \quad (5.32)$$

with

$$\tilde{\mathbf{W}}_{\mathcal{G}} = \text{col}_{h \in \mathcal{H}}(\mathbf{W}_{\mathcal{G},h}), \quad \text{and} \quad \mathbf{w}_{\mathcal{G}}(t) = \text{col}(\mathbf{i}_{\mathcal{S}}(t), \mathbf{v}_{\mathcal{R}}(t)) \quad (5.33)$$

$$\tilde{\mathbf{Y}}_{\mathcal{G}} = \text{col}_{h \in \mathcal{H}}(\mathbf{Y}_{\mathcal{G},h}), \quad \text{and} \quad \mathbf{y}_{\mathcal{G}}(t) = \text{col}(\mathbf{v}_{\mathcal{S}}(t), \mathbf{i}_{\mathcal{R}}(t)) \quad (5.34)$$

where $\mathbf{W}_{\mathcal{G},h}$ and $\mathbf{Y}_{\mathcal{G},h}$ describe the Fourier coefficients of $\mathbf{w}_{\mathcal{G}}(t)$ and $\mathbf{y}_{\mathcal{G}}(t)$ at the harmonic $h \in \mathcal{H}$, respectively.

Combination of the Grid and Resources

As will be shown shortly, the HSS model of the grid is combined with the HSS model of all resources (see Fig. 5.2). As can be seen in Fig. 5.2, the grid disturbance of the HSS model of all resources is the output of the HSS of the grid, and vice versa.

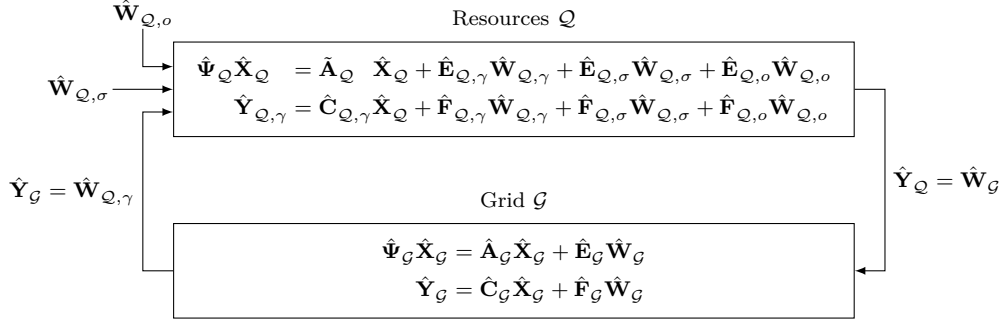


Figure 5.2: Block diagram of the power system.

Recall the structure of the disturbance and output of the HSS model of all resources from (5.29)–(5.30). The disturbance and output vectors are the combination of the harmonic-domain vector of all grid-forming currents or voltages and all grid-following voltages or currents, for the disturbance or output vectors, respectively. For the sake of illustration, this is specifically shown for $\hat{\mathbf{W}}_{\mathcal{Q},\gamma}$:

$$\hat{\mathbf{I}}_{\mathcal{S}} = \text{col}_{s \in \mathcal{S}}(\hat{\mathbf{I}}_s), \quad \text{where} \quad \hat{\mathbf{I}}_s = \text{col}_{h \in \mathcal{H}}(\mathbf{I}_{s,h}) \quad (5.35)$$

$$\hat{\mathbf{V}}_{\mathcal{R}} = \text{col}_{r \in \mathcal{R}}(\hat{\mathbf{V}}_r), \quad \text{where} \quad \hat{\mathbf{V}}_r = \text{col}_{h \in \mathcal{H}}(\mathbf{V}_{r,h}) \quad (5.36)$$

where $\mathbf{I}_{s,h}$ and $\mathbf{V}_{r,h}$ describe the Fourier coefficients of $\mathbf{i}_s(t)$ and $\mathbf{v}_r(t)$ at the harmonic $h \in \mathcal{H}$, respectively. Note that the Fourier coefficients which constitute $\hat{\mathbf{W}}_{\mathcal{Q},\gamma}$ and $\hat{\mathbf{Y}}_{\mathcal{Q},\gamma}$ are grouped per node (i.e., the different harmonics associated with a given node form a block). By contrast, $\tilde{\mathbf{W}}_{\mathcal{G}}$ and $\tilde{\mathbf{Y}}_{\mathcal{G}}$ are grouped per harmonic order (i.e., the different nodal phasors associated with a given harmonic order form a block). Notably, the quantities grouped w.r.t. the harmonic order are denoted by $\tilde{\mathbf{W}}$ and $\tilde{\mathbf{Y}}$, while quantities grouped w.r.t. the nodes are denoted by $\hat{\mathbf{W}}$ and $\hat{\mathbf{Y}}$.

In order to combine the two models, the ordering of the vectors w.r.t. nodes and harmonics must be compatible. In the formulations (5.25)–(5.26) and (5.42)–(5.43), this is not the case. That is, the former is composed of blocks grouped by node, and the latter of blocks grouped by harmonic. To this end, a permutation matrix, which performs a permutation from the grouping w.r.t. to the harmonics to the grouping w.r.t. the nodes, and vice versa, is introduced. Recall that the union of all nodes is defined by \mathcal{N} , and the harmonics are described by \mathcal{H} .

$$\hat{\mathbf{P}}_{\mathcal{N}|\mathcal{H}} : \left(\hat{\mathbf{P}}_{\mathcal{N}|\mathcal{H}} \right)_{ij} := \begin{cases} \text{diag}(\mathbf{1}_3) & \forall n \in \mathcal{N}, \forall h \in \mathcal{H} : \\ & i = (n-1)|\mathcal{H}| + h + (h_{max} + 1), \\ & j = (h + h_{max})|\mathcal{N}| + n, \\ \mathbf{0}_{3 \times 3} & \text{otherwise.} \end{cases} \quad (5.37)$$

5.2 Harmonic State-Space Model of a Power System

Then, the regrouped versions of the disturbance and output vector of the HSS model of the grid are given by:

$$\hat{\mathbf{W}}_G = \hat{\mathbf{P}}_{\mathcal{N}|\mathcal{H}} \tilde{\mathbf{W}}_G \quad (5.38)$$

$$\hat{\mathbf{Y}}_G = \hat{\mathbf{P}}_{\mathcal{N}|\mathcal{H}} \tilde{\mathbf{Y}}_G \quad (5.39)$$

as well as $\hat{\mathbf{P}}_{\mathcal{H}|\mathcal{N}} = \hat{\mathbf{P}}_{\mathcal{N}|\mathcal{H}}^\top$, which results in:

$$\hat{\mathbf{W}}_G = \text{col}(\hat{\mathbf{V}}_S, \hat{\mathbf{I}}_R) \quad (5.40)$$

$$\hat{\mathbf{Y}}_G = \text{col}(\hat{\mathbf{I}}_S, \hat{\mathbf{V}}_R) \quad (5.41)$$

With this, the HSS model of the grid is rewritten as:

$$\hat{\Psi}_G \hat{\mathbf{X}}_G = \hat{\mathbf{A}}_G \hat{\mathbf{X}}_G + \hat{\mathbf{E}}_G \hat{\mathbf{W}}_G \quad (5.42)$$

$$\hat{\mathbf{Y}}_G = \hat{\mathbf{C}}_G \hat{\mathbf{X}}_G + \hat{\mathbf{F}}_G \hat{\mathbf{W}}_G \quad (5.43)$$

with

$$\hat{\mathbf{E}}_G = \tilde{\mathbf{E}}_G \hat{\mathbf{P}}_{\mathcal{H}|\mathcal{N}} \quad (5.44)$$

$$\hat{\mathbf{C}}_G = \hat{\mathbf{P}}_{\mathcal{N}|\mathcal{H}} \tilde{\mathbf{C}}_G \quad (5.45)$$

$$\hat{\mathbf{F}}_G = \hat{\mathbf{P}}_{\mathcal{N}|\mathcal{H}} \tilde{\mathbf{F}}_G \hat{\mathbf{P}}_{\mathcal{H}|\mathcal{N}} \quad (5.46)$$

To calculate the open-loop model of the system, the HSS model of the resources (5.25)–(5.26) and the HSS model of the grid (5.42)–(5.43) are combined into

$$\hat{\Psi}_P \hat{\mathbf{X}}_P = \hat{\mathbf{A}}_P \hat{\mathbf{X}}_P + \hat{\mathbf{E}}_{P,\gamma} \hat{\mathbf{W}}_{P,\gamma} + \hat{\mathbf{E}}_{P,\sigma} \hat{\mathbf{W}}_{Q,\sigma} + \hat{\mathbf{E}}_{P,o} \hat{\mathbf{W}}_{Q,o} \quad (5.47)$$

$$\hat{\mathbf{Y}}_P = \hat{\mathbf{C}}_P \hat{\mathbf{X}}_P + \hat{\mathbf{F}}_{P,\gamma} \hat{\mathbf{W}}_{P,\gamma} + \hat{\mathbf{F}}_{P,\sigma} \hat{\mathbf{W}}_{Q,\sigma} + \hat{\mathbf{F}}_{P,o} \hat{\mathbf{W}}_{Q,o} \quad (5.48)$$

where

$$\hat{\mathbf{X}}_P = \text{col}(\hat{\mathbf{X}}_Q, \hat{\mathbf{X}}_G) \quad (5.49)$$

$$\hat{\mathbf{W}}_{P,\gamma} = \text{col}(\hat{\mathbf{W}}_{Q,\gamma}, \hat{\mathbf{W}}_G) \quad (5.50)$$

$$\hat{\mathbf{Y}}_P = \text{col}(\hat{\mathbf{Y}}_{Q,\gamma}, \hat{\mathbf{Y}}_G) \quad (5.51)$$

as well as for the matrices

$$\hat{\mathbf{A}}_P = \text{diag}(\hat{\mathbf{A}}_Q, \hat{\mathbf{A}}_G) \quad (5.52)$$

$$\hat{\mathbf{E}}_{P,\gamma} = \text{diag}(\hat{\mathbf{E}}_{Q,\gamma}, \hat{\mathbf{E}}_G) \quad (5.53)$$

and $\hat{\Psi}_P$, $\hat{\mathbf{C}}_P$, and $\hat{\mathbf{F}}_{P,\gamma}$ are built analogously.

The matrices, associated with $\hat{\mathbf{W}}_{\mathcal{Q},\sigma}$ and $\hat{\mathbf{W}}_{\mathcal{Q},o}$ are constructed as follows

$$\hat{\mathbf{E}}_{\mathcal{P},\sigma} = \text{col}(\hat{\mathbf{E}}_{\mathcal{Q},\sigma}, \mathbf{0}) \quad (5.54)$$

$$\hat{\mathbf{E}}_{\mathcal{P},o} = \text{col}(\hat{\mathbf{E}}_{\mathcal{Q},o}, \mathbf{0}) \quad (5.55)$$

and analogously for $\hat{\mathbf{F}}_{\mathcal{P},\sigma}$ and $\hat{\mathbf{F}}_{\mathcal{P},o}$.

5.2.4 Closed-Loop Model of the Power System

From (5.29)–(5.30) and (5.40)–(5.41), one can write the interconnection between the resources and the grid as:

$$\hat{\mathbf{W}}_{\mathcal{P},\gamma} = \hat{\mathbf{J}}_{\mathcal{P}} \hat{\mathbf{Y}}_{\mathcal{P}} \quad (5.56)$$

where

$$\hat{\mathbf{J}}_{\mathcal{P}} = \begin{bmatrix} \mathbf{0} & \text{diag}(\mathbf{1}) \\ \text{diag}(\mathbf{1}) & \mathbf{0} \end{bmatrix} \quad (5.57)$$

One can interpret (5.47)–(5.48) as the open-loop model of the power system, and (5.56) as the associated feedback control law. In order to obtain the closed-loop model, substitute (5.56) into (5.47)–(5.48) and solve for $\hat{\mathbf{X}}_{\mathcal{P}}$ and $\hat{\mathbf{Y}}_{\mathcal{P}}$:

$$\hat{\Psi}_{\mathcal{P}} \hat{\mathbf{X}}_{\mathcal{P}} = \tilde{\mathbf{A}}_{\mathcal{P}} \hat{\mathbf{X}}_{\mathcal{P}} + \tilde{\mathbf{E}}_{\mathcal{P},\sigma} \hat{\mathbf{W}}_{\mathcal{Q},\sigma} + \tilde{\mathbf{E}}_{\mathcal{P},o} \hat{\mathbf{W}}_{\mathcal{Q},o} \quad (5.58)$$

$$\hat{\mathbf{Y}}_{\mathcal{P}} = \tilde{\mathbf{C}}_{\mathcal{P}} \hat{\mathbf{X}}_{\mathcal{P}} + \tilde{\mathbf{F}}_{\mathcal{P},\sigma} \hat{\mathbf{W}}_{\mathcal{Q},\sigma} + \tilde{\mathbf{F}}_{\mathcal{P},o} \hat{\mathbf{W}}_{\mathcal{Q},o} \quad (5.59)$$

where the matrices $\tilde{\mathbf{A}}_{\mathcal{P}}$, $\tilde{\mathbf{E}}_{\mathcal{P},\sigma}$, $\tilde{\mathbf{E}}_{\mathcal{P},o}$, $\tilde{\mathbf{C}}_{\mathcal{P}}$, $\tilde{\mathbf{F}}_{\mathcal{P},\sigma}$, and $\tilde{\mathbf{F}}_{\mathcal{P},o}$ are given by

$$\tilde{\mathbf{A}}_{\mathcal{P}} = \hat{\mathbf{A}}_{\mathcal{P}} + \hat{\mathbf{E}}_{\mathcal{P},\gamma} (\text{diag}(\mathbf{1}) - \hat{\mathbf{J}}_{\mathcal{P}} \hat{\mathbf{F}}_{\mathcal{P},\gamma})^{-1} \hat{\mathbf{J}}_{\mathcal{P}} \hat{\mathbf{C}}_{\mathcal{P}} \quad (5.60)$$

$$\tilde{\mathbf{E}}_{\mathcal{P},\sigma} = \hat{\mathbf{E}}_{\mathcal{P},\sigma} + \hat{\mathbf{E}}_{\mathcal{P},\gamma} (\text{diag}(\mathbf{1}) - \hat{\mathbf{J}}_{\mathcal{P}} \hat{\mathbf{F}}_{\mathcal{P},\gamma})^{-1} \hat{\mathbf{J}}_{\mathcal{P}} \hat{\mathbf{F}}_{\mathcal{P},\sigma} \quad (5.61)$$

$$\tilde{\mathbf{E}}_{\mathcal{P},o} = \hat{\mathbf{E}}_{\mathcal{P},o} + \hat{\mathbf{E}}_{\mathcal{P},\gamma} (\text{diag}(\mathbf{1}) - \hat{\mathbf{J}}_{\mathcal{P}} \hat{\mathbf{F}}_{\mathcal{P},\gamma})^{-1} \hat{\mathbf{J}}_{\mathcal{P}} \hat{\mathbf{F}}_{\mathcal{P},o} \quad (5.62)$$

$$\tilde{\mathbf{C}}_{\mathcal{P}} = (\text{diag}(\mathbf{1}) - \hat{\mathbf{F}}_{\mathcal{P},\gamma} \hat{\mathbf{J}}_{\mathcal{P}})^{-1} \hat{\mathbf{C}}_{\mathcal{P}} \quad (5.63)$$

$$\tilde{\mathbf{F}}_{\mathcal{P},\sigma} = (\text{diag}(\mathbf{1}) - \hat{\mathbf{F}}_{\mathcal{P},\gamma} \hat{\mathbf{J}}_{\mathcal{P}})^{-1} \hat{\mathbf{F}}_{\mathcal{P},\sigma} \quad (5.64)$$

$$\tilde{\mathbf{F}}_{\mathcal{P},o} = (\text{diag}(\mathbf{1}) - \hat{\mathbf{F}}_{\mathcal{P},\gamma} \hat{\mathbf{J}}_{\mathcal{P}})^{-1} \hat{\mathbf{F}}_{\mathcal{P},o} \quad (5.65)$$

The matrices (5.60)–(5.65) can only be computed if the inverses of $\text{diag}(\mathbf{1}) - \hat{\mathbf{J}}_{\mathcal{P}} \hat{\mathbf{F}}_{\mathcal{P},\gamma}$ and $\text{diag}(\mathbf{1}) - \hat{\mathbf{F}}_{\mathcal{P},\gamma} \hat{\mathbf{J}}_{\mathcal{P}}$ exist. There is no general guarantee for this. However, recall from (5.24) that $\hat{\mathbf{F}}_{\mathcal{G}} = \mathbf{0}$. Thus, following the same argumentation as in Section 2.4.3, $\text{diag}(\mathbf{1}) - \hat{\mathbf{J}}_{\mathcal{P}} \hat{\mathbf{F}}_{\mathcal{P},\gamma}$ and $\text{diag}(\mathbf{1}) - \hat{\mathbf{F}}_{\mathcal{P},\gamma} \hat{\mathbf{J}}_{\mathcal{P}}$ are upper- and lower-blocktriangular matrices, and therefore their inverses exist.

5.3 Operators for the Harmonic Stability Assessment

Finally, by solving (5.58) for $\hat{\mathbf{X}}_{\mathcal{P}}$ and substituting the result into (5.59), the HTF of the system w.r.t. the disturbances is obtained as:

$$\hat{\mathbf{Y}}_{\mathcal{P}} = \hat{\mathbf{G}}_{\mathcal{P},\sigma} \hat{\mathbf{W}}_{\mathcal{Q},\sigma} + \hat{\mathbf{G}}_{\mathcal{P},o} \hat{\mathbf{W}}_{\mathcal{Q},o} \quad (5.66)$$

where

$$\hat{\mathbf{G}}_{\mathcal{P},\sigma} = \tilde{\mathbf{C}}_{\mathcal{P}}(\hat{\Psi}_{\mathcal{P}} - \tilde{\mathbf{A}}_{\mathcal{P}})^{-1} \tilde{\mathbf{E}}_{\mathcal{P},\sigma} + \tilde{\mathbf{F}}_{\mathcal{P},\sigma} \quad (5.67)$$

$$\hat{\mathbf{G}}_{\mathcal{P},o} = \tilde{\mathbf{C}}_{\mathcal{P}}(\hat{\Psi}_{\mathcal{P}} - \tilde{\mathbf{A}}_{\mathcal{P}})^{-1} \tilde{\mathbf{E}}_{\mathcal{P},o} + \tilde{\mathbf{F}}_{\mathcal{P},o} \quad (5.68)$$

Recall from Section 5.2.1 that the matrices of the HSS of an individual CIDER are a function of their operating point. Thus, the matrices of the HSS and the HTF of the system are also dependent on the operating point of all CIDERs, denoted by $\hat{\mathbf{W}}_{\mathcal{Q},o}$ and $\hat{\mathbf{Y}}_{\mathcal{Q},o}$. For the sake of clarity, this dependency is not stated explicitly.

5.3 Operators for the Harmonic Stability Assessment

This section gives a summary of the theory employed for the HSA of the individual resources in Section 5.4 and the entire power system in Section 5.5. First, the eigenvalue problem of a HSS model and the associated eigenvectors are introduced. Second, the concept of sensitivity analysis w.r.t. eigenvalue locations is given, as well as a discussion of different types of eigenvalues.

Eigenvalues and Eigenvectors

Consider a generic HSS model:

$$\hat{\Psi} \hat{\mathbf{X}} = \hat{\mathbf{A}} \hat{\mathbf{X}} + \hat{\mathbf{E}} \hat{\mathbf{W}} \quad (5.69)$$

$$\hat{\mathbf{Y}} = \hat{\mathbf{C}} \hat{\mathbf{X}} + \hat{\mathbf{F}} \hat{\mathbf{W}} \quad (5.70)$$

and its HTF w.r.t. the disturbance $\hat{\mathbf{W}}$.

$$\hat{\mathbf{G}} = \hat{\mathbf{C}}(\hat{\Psi} - \hat{\mathbf{A}})^{-1} \hat{\mathbf{E}} + \hat{\mathbf{F}} \quad (5.71)$$

The harmonic stability of this HSS model is determined through the poles of its HTF. More precisely, the poles of the system are the locations in the complex s-plane, where the HTF is not analytical, i.e., its value is infinite [32]. Recall the composition of the matrix $\hat{\Psi}$ of a HSS model (as it was introduced in (2.37)):

$$\hat{\Psi} = s \cdot \text{diag}(\mathbf{1}) + j\hat{\Omega} \quad (5.72)$$

As a consequence, the poles of the HTF are described by the eigenvalue problem associated with the matrix $\hat{\mathbf{A}} - j\hat{\mathbf{\Omega}}$:

$$\left(s \cdot \text{diag}(\mathbf{1}) - (\hat{\mathbf{A}} - j\hat{\mathbf{\Omega}}) \right) \mathbf{V} = \mathbf{0} \quad (5.73)$$

where \mathbf{V} is a matrix composed of the eigenvectors. More precisely, each eigenvalue of the system matrix has an associated eigenvector. One can analyse these vectors to understand the impact of a certain eigenvalue (also called mode) on a specific state variable, and vice versa. As already mentioned in Section 5.1, numerous tools exist for this kind of analyses in the context of LTI systems, i.e., participation factor analysis or modal analysis [108]. Generalizations of the theory concerning participation factors in the context of LTP systems are proposed in [109].

Sensitivity Analysis

It is common practice to assess the sensitivity of the location of the eigenvalues w.r.t. changes in the control parameters of the system. To this end, the control parameters are varied, and the resulting changes of the locations of the eigenvalues assessed. In this way, one can trace the so-called eigenvalue loci of the system. Naturally, not all eigenvalues of the system are affected by those changes of the control parameters. Some only change their location when the physical parameters of the system are varied, others do not change their location at all.

Eigenvalue Classification and Spurious Eigenvalues

In this thesis, three different types of eigenvalues are defined based on their impact on the system. To this end, the following naming is proposed: (i) the *Control-Design Invariant* (CDI), (ii) the *Control-Design Variant* (CDV) and (iii) the *Design Invariant* (DI) eigenvalues. To this end, the following definitions are introduced:

Definition 9. *A CDI eigenvalue is an eigenvalue whose location remains fixed upon changing the parameters of the controllers.*

Definition 10. *The location of a CDV eigenvalue can be changed by modifying one or several of the parameters of the control system.*

Definition 11. *A DI eigenvalue is an eigenvalue whose location remains fixed regardless of any parameter adjustments in the system.*

As will be explained shortly in Section 5.4.1, DI eigenvalues of the CIDER models occur due to the changes of the reference frame between power hardware (in this case: phase coordinates) and the control software (in this case: direct/quadrature components).

In a recent paper [106], which analyses eigenvalues of LTP systems, the concept of 'spurious' eigenvalues is mentioned. Recall that, when transforming LTP models into HSS models, Toeplitz matrices of infinite size would need to be used (i.e., in order to cover the entire, infinite spectrum). In practice, those infinite Toeplitz matrices need to be truncated at a given maximum harmonic order. Naturally, the truncation may introduce artefacts into the model, especially for the harmonics close to the boundaries of the model representation. Therefore, eigenvalues, representing effects close to the maximum harmonic order might not be representative of the real system behaviour. It is important to note that any tractable (i.e., finite) HSS model inherently suffers from this effect due to the applied truncation. For the case of the individual CIDERs, the DI eigenvalues are one kind of the spurious eigenvalues. The details of this analysis will be shown in Section 5.4.1. When combining several HSS models (i.e., through closed-loop analysis), it becomes increasingly complex to discern which eigenvalues are genuine and which are spurious. This challenge arises mainly because the mapping of the eigenvalues from an open-loop HSS model to its closed-loop version is not straightforward in general.

5.4 Harmonic Stability Assessment of the Resources

This section gives an overview on the HSA of the individual CIDERs. The CIDERs being studied are the same as the ones introduced and analysed in Chapter 3. These include both the grid-forming and grid-following CIDERs that only model the AC-side characteristics (i.e., Section 3.3.1 and Section 3.3.2, respectively), and the grid-following CIDER that includes also the DC-side modelling (i.e., Section 3.3.3). In the context of the HSA, several studies are conducted. First, the eigenvalues are classified into DI, CDI and CDV eigenvalues. Second, the impact of the maximum harmonic order on the eigenvalues of the CIDERs is analysed. Last, the sensitivity of the eigenvalue locations w.r.t. to the controller parameters (i.e., feedback gains) are assessed for a particular CIDER.

For the HSA of the individual CIDERs, the same parameters as given in Section 3.4 are used. Employing the HSS model of the CIDERs, the eigenvalues of system matrix $\tilde{\mathbf{A}}_q$ as defined in (5.1) are evaluated. Recall that the system matrix of the individual CIDERs is derived using the models introduced in Section 3.3, and possibly is a function of the operating point $\hat{\mathbf{Y}}_o$. For the HSA of the individual CIDER, if the derivation of the HSS model requires an operating point, it is taken from the spectra of the TDS conducted in Section 3.4. Note that the system matrix includes only the characteristics of the internal response of the CIDER, i.e., the matrices of the reference calculation do not enter the system matrix of the individual CIDERs.

5.4.1 Classification of the LTP eigenvalues

Methodology

As was introduced in Section 5.3, the eigenvalues of a resource, which consists of a plant and its associated controller, can be classified depending on their sensitivity w.r.t. the model parameters. Recall the definitions of the eigenvalues as DI, CDI and CDV. In order to determine these sets, the eigenvalues are first computed for an initial set of parameters. Subsequently, a subset of the parameters is varied and the eigenvalues are recomputed.

More precisely, for the determination of the DI eigenvalues, all parameters of the CIDER are varied, and the eigenvalues are recomputed. If an eigenvalue remains unchanged, it is classified as DI. Similarly, for the determination of the CDI and CDV eigenvalues, all parameters of the control software of a CIDER are varied and the locations of the new eigenvalues are compared to the initial set. In this case, the eigenvalues that remain unchanged are the CDI eigenvalues, and the ones that move are the CDV eigenvalues.

In order to perform such a comparison, the sets of eigenvalues calculated for each variation must be ordered identically. Unfortunately, state-of-the-art implementation, such as the `eig()` function of Matlab, do not ensure this. Therefore, the correct sorting must be found using a *Linear Assignment Problem* (LAP). The LAP, given two sample sets, assigns pairs of samples, such that the total cost of assignment is minimized. To this end, the cost of assignment is described by a cost function. In the context of sorting two sets of eigenvalues, the aim is to minimize the total distance between pairs of eigenvalues. Let Λ and $\tilde{\Lambda}$ be the two sets of eigenvalues to be sorted identically, and the cost function of assignment

$$\mathcal{C} : \Lambda \times \tilde{\Lambda} \rightarrow \mathbb{R} \quad (5.74)$$

Notably, the cost function \mathcal{C} can be described by a matrix \mathbf{C} :

$$\mathbf{C} : (\mathbf{C})_{ij} = |\lambda_i - \tilde{\lambda}_j| \quad (5.75)$$

Then, in order to solve the LAP, find a bijection $f : \Lambda \rightarrow \tilde{\Lambda}$, such that

$$\sum_{\lambda \in \Lambda} \mathbf{c}_{[\lambda, f(\lambda)]} \quad (5.76)$$

is minimized [110]. In general, there is no guarantee that minimizing this total distance will result in the correct sorting of the eigenvalues. In particular, if the trajectories of two sets of eigenvalues intersect each other, pairs of eigenvalues may be associated wrongly in the vicinity of the intersection point. In such situations, one can either include additional information about the characteristics of the eigenvalues (e.g., the eigenvectors) into the cost matrix or reduce the step size of the applied parameter change.

Results and Discussion

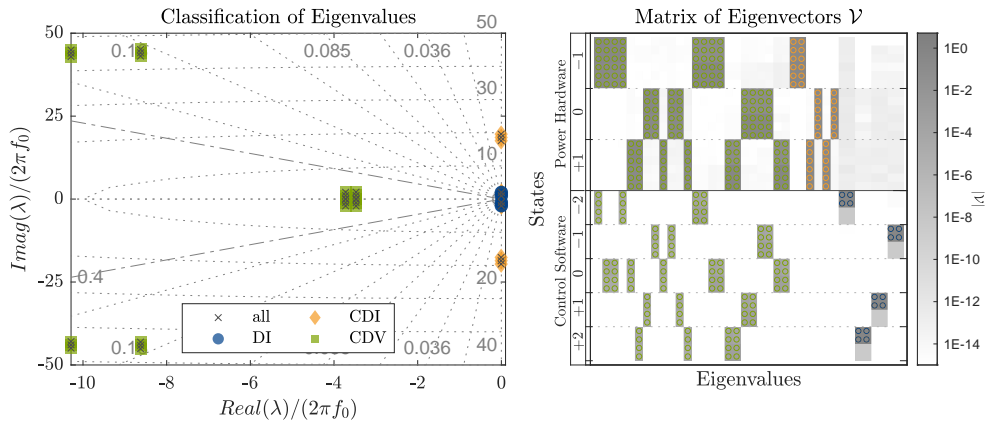
Fig. 5.3 shows the classification of the LTP eigenvalues for the grid-forming CIDER that was introduced in Section 3.3.1. For the sake of illustration, the analysis is performed for $h_{max} = 1$. Notably, the generalisation to higher orders of h_{max} is straightforward (i.e., the patterns of eigenvectors w.r.t. the eigenvalues are analogous).

The left-hand side subfigure of Fig. 5.3a shows the DI, CDI and CDV eigenvalues. In the plot, the grid consists of two distinct sets of lines, i) lines representing consistent damping factors across their length, and ii) lines indicating a constant natural frequency. Notably, the line that represents the critical damping factor of $\xi = 0.4$ is distinctly highlighted.

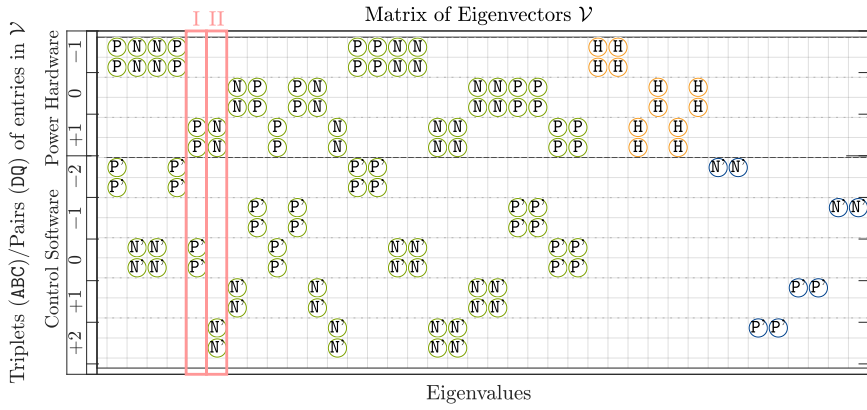
The right-hand side subfigure of Fig. 5.3a illustrates the magnitude of the entries of the eigenvector matrix \mathbf{V} in logarithmic scale. The entries that exceed a threshold value of $1\text{E-}8$ p.u. in magnitude are additionally highlighted in the same colour used for the classification of the eigenvalue. Note that rows (x-axis) and columns (y-axis) of the eigenvector matrix correspond to the states and eigenvalues, respectively, of the CIDER model. Recall from Section 2.4.3, that the harmonic-domain state vector of a CIDER is built from the state vector of the power hardware and the control software. Hence, the y-axis is partitioned into the states that correspond to the power hardware and the control software, respectively (i.e., dark grey line). Furthermore, note the (sub)partition of the y-axis w.r.t. to the harmonic orders of the states (i.e., the dotted light grey lines). In this respect, recall that the control software of the CIDERs is represented by $h_{max} + 1$ harmonics.

To comprehend the influence of the eigenvalues on the system, and understand their physical meaning, a more detailed interpretation of the eigenvectors is performed. To this end, the entries of the eigenvectors in Fig. 5.3b are grouped by triplets (ABC coordinates) for the part associated with the power hardware and pairs (DQ components) for the part associated with the control software. Then, the triplets transformed to sequence domain are depicted in the figure, as positive (P), negative (N) and homopolar (H) sequences. For the pairs of entries in the part associated to the control software, an equivalent positive sequence (P') is defined by the scenario in which the Q component lags behind the D component by ninety degrees. In contrast, an equivalent negative sequence (N') describes the situation where the Q component leads the D component by ninety degrees [70]. Additionally, the theoretical mapping of harmonic sequence components for a transformation from ABC coordinates (i.e., the power hardware) to DQ(Z) components (i.e., the control software) [70] is illustrated in Fig. 5.3c. Note the different maximum harmonic orders considered for the two coordinate frames (i.e., $h_{max,ABC} = 1$ for the ABC coordinates and $h_{max,DQZ} = h_{max,ABC} + 1 = 2$ for the DQZ components). In the following, the detailed analysis of the eigenvalues is first discussed for the CDV, then for the CDI and finally for the DI eigenvalues.

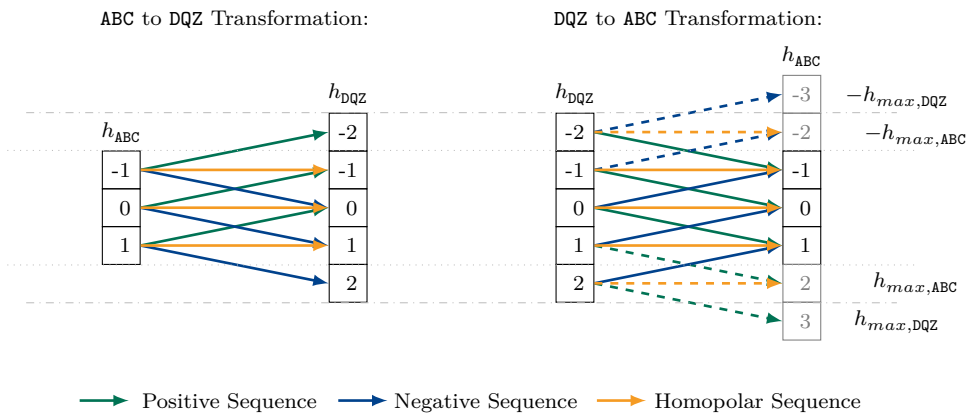
Chapter 5. Harmonic Stability Assessment



(a)



(b)



(c)

Figure 5.3: Classification of the eigenvalues of the grid-forming CIDER. Fig. 5.3a: Eigenvalues on the left-hand side and eigenvector matrix \mathcal{V} on the right-hand side. Fig. 5.3b: Representation of the entries of \mathcal{V} by triplets (ABC) and pairs (DQ) in the sequence domain. Fig. 5.3c: Mapping of the harmonic sequences for a transformation from ABC coordinates to DQZ components and vice versa.

The grid-forming CIDER in Fig. 5.3a possesses four sets of CDV eigenvalues. Each of these sets is composed of three complex conjugate eigenvalues, i.e., one per harmonic order. The corresponding eigenvectors on the right-hand side of Fig. 5.3a have nonzero entries (in green) for both parts of the state vector (i.e., these eigenvalues influence states both in the power hardware and control software). By inspection of the eigenvector in the highlighted area denoted by I in Fig. 5.3b, one observes that the entries in the part associated with the power hardware correspond to ABC-triplets of positive sequence components. Those entries are located at $h = 1$ in the part associated with the power hardware, and at $h = 0$ in the part associated with the control software. Similarly, in the highlighted area denoted with II the entries of the eigenvector associated with the power hardware correspond to ABC-triplets of negative sequence components. Those entries occur at $h = 1$ for the part associated with the power hardware, and at $h = 2$ in the parts associated with the control software. These observations fit with the theoretical mapping of harmonic sequence components for a transformation from ABC coordinates to DQ(Z) components in Fig. 5.3c. The harmonic order is decremented for positive-sequence components and incremented for negative-sequence components.

Only one set of CDI occurs in the eigenvalue graph in Fig. 5.3a. As can be seen from the eigenvector matrix, the corresponding eigenvectors have nonzero entries (in yellow) only in the part of the state vector associated with the power hardware. This is due to the fact that the CDI eigenvalues can not be moved by changing the control parameters (i.e., as by definition). A deeper understanding of this fact can be obtained by inspection of Fig. 5.3b. The nonzero entries of the eigenvectors associated with the CDI eigenvalues exhibit values corresponding to a homopolar sequence component. Recall that for the CIDER models introduced in Section 3.3, the power hardware is modelled in ABC coordinates and the control software in DQ components (i.e., the Z component is not represented in the controller). Thus, a homopolar sequence originating from the power hardware is not mapped to the control software. Hence, the invariance of those eigenvalues w.r.t. the control design.

Finally, one pair of DI eigenvalues is observed in Fig. 5.3a with real part equal to zero. The eigenvectors of the DI eigenvalues are solely nonzero (in blue) in the part of the state vector associated with the control software. In particular, note that these entries correspond to the innermost controller stages (see (3.66)). As illustrated by the right-hand side of Fig. 5.3c, positive sequences at $h = -h_{max}$ and $h = -(h_{max} + 1)$, as well as negative sequences at $h = h_{max}$ and $h = h_{max} + 1$ are cut off during the DQ(Z)-to-ABC transformation. By consequence, such eigenvalues can neither be properly controlled nor analysed if they arise. This explains why the associated eigenvalues are DI.

In line with the remarks regarding spurious eigenvalues in Section 5.3, the above observations underline the fact that the DI eigenvalues are artefacts of the model rather than genuine eigenvalues of the system. Therefore, although the DI eigenvalues possess real parts equal to zero, they do not pose a problem in terms of the HSA. That is, although

they are borderline (un)stable and invariant w.r.t. parameter changes, their origin is clear and their influence is marginal. Naturally, this reasoning is only valid if the maximum harmonic order h_{max} chosen for the HSA is high enough to cover all relevant phenomena. The topic of the choice of h_{max} and its influence on the eigenvalues of the resource is discussed in the next section.

The second CIDER that is analysed in this chapter is the grid-following CIDER considering only the AC-side characteristics (as introduced in Section 3.3.2). The classification of its eigenvalues is shown in Fig. 5.4a. As opposed to the grid-forming CIDER, this grid-following CIDER exhibits an additional set of CDI, CDV and DI eigenvalues due to the additional filter stage (i.e., LCL versus LC filter). The eigenvectors of the DI eigenvalues have entries that are larger than 1E-8 at the states of the two innermost controller stages. Nevertheless, in comparison the values corresponding to the states of the innermost controller stage are by several orders of magnitude higher in absolute value.

Finally, Fig. 5.4b depicts the eigenvalue classification of the third CIDER, i.e., the grid-following CIDER including the DC-side characteristics (as introduced in Section 3.3.3). As compared to the grid-following CIDER in Fig. 5.4a, eigenvalues associated with the additional states corresponding to the filter and controller stages of the DC side are present. At the same time, an additional set of DI eigenvalues occurs due to the controller stage associated with the DC side.

5.4.2 Impact of the Maximum Harmonic Order

Methodology

The impact of the maximum harmonic order on the location of the eigenvalues is assessed. To this end, the eigenvalues of the system matrix are computed for different values of h_{max} .

Additionally, the eigenvalues of the LTP models are compared to the ones of the corresponding LTI model. In general, when modelling CIDERs with LTI models, all parts of the CIDER need to be represented in the same frame of reference (e.g, DQ components). By consequence, the transformation matrices between the power hardware and control software simplify to identity, and the CIDER can be characterised by an LTI model. As to the LTP models, the operating point for deriving the LTI models is taken from the spectra of the TDS in Section 3.4.

To assess how much the eigenvalues move for different maximum harmonic orders, the following metric is introduced. Let $\lambda_{i,LTI}$ be an eigenvalue of the LTI system, where $i = 1 \dots n_{LTI}$, with n_{LTI} being the size of the LTI system matrix. Next, find the n_{LTI} eigenvalues of the LTP system for a given h_{max} , that are located closest to the eigenvalues

5.4 Harmonic Stability Assessment of the Resources

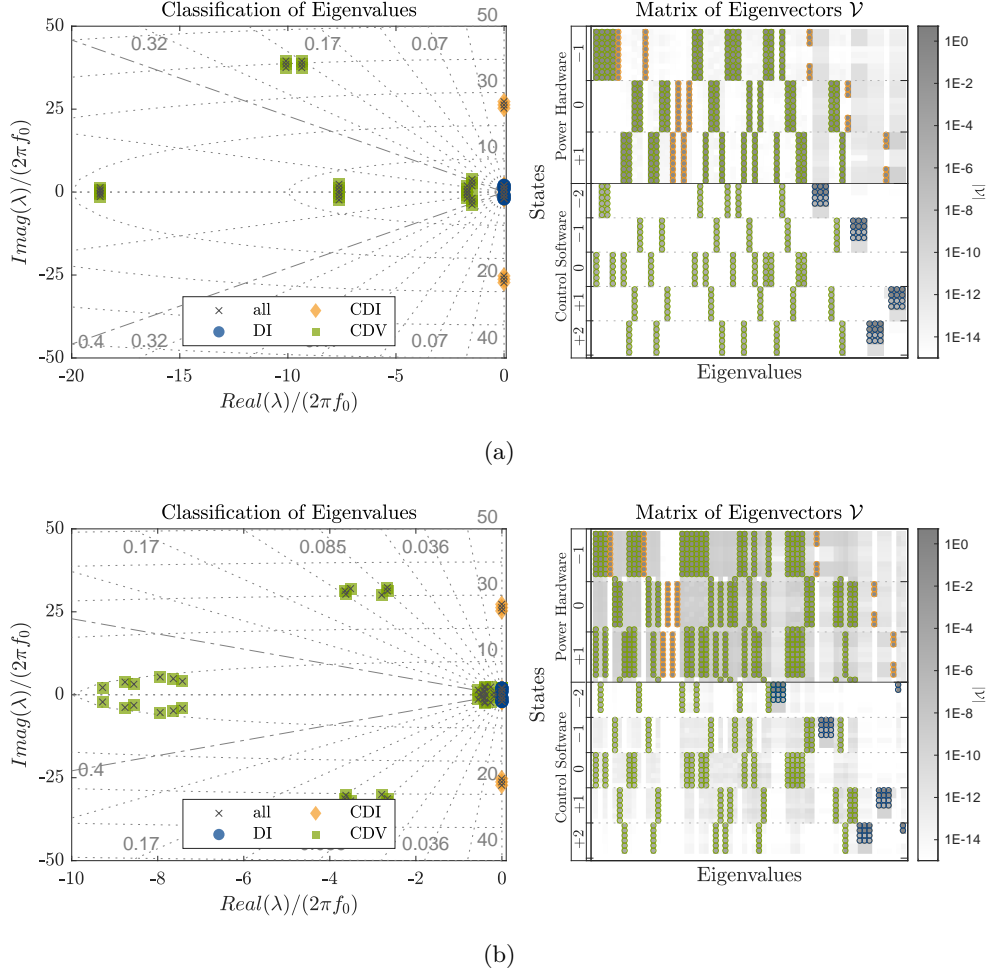


Figure 5.4: Classification of the eigenvalues of the grid-following CIDER considering only AC-side characteristics (Fig. 5.4a) and the grid-following CIDER including the DC-side characteristics (Fig. 5.4b). The eigenvalues are shown on the left-hand side and the matrix of the eigenvectors \mathcal{V} on the right-hand side.

of the LTI system. Denote these n_{LTI} eigenvalues of the LTP model with maximum harmonic order h_{max} by $\lambda_{i,LTP}^{h_{max}}$, where $i = 1 \dots n_{LTI}$. Note that $\lambda_{i,LTP}^{h_{max}}$ is a subset of all eigenvalues of the LTP model, since in general the size of the system matrix $n_{LTP} > n_{LTI}$. Define the distance between $\lambda_{i,LTI}$ and $\lambda_{i,LTP}^{h_{max}}$ as:

$$d_i(h_{max}) = |\lambda_{i,LTI} - \lambda_{i,LTP}^{h_{max}}| \quad (5.77)$$

Finally, the metric for similarity between the LTI system and the LTP system for a given h_{max} , is defined as follows:

$$d(h_{max}) = \max_i(d_i(h_{max})) \quad (5.78)$$

In other words, it is the maximum of the distances between the set of all LTI eigenvalues and the subset of the LTP eigenvalues for a given h_{max} . Notably, $d(h_{max})$ is i) a measure of similarity between the LTP and LTI model and ii) an indicator for the maximum harmonic order required to represent all relevant phenomena of the system. With regard to the latter, one needs to chose h_{max} large enough so that $d(h_{max})$ reaches a stable value.

Results and Discussion

Fig. 5.5 shows the eigenvalues of the three CIDERs for maximum harmonic orders equal to 1, 7, 13 and 25, as well as for the LTI model. One can clearly see that the sets of eigenvalues are clustered in lines with similar real part, one of which is displayed in detail in the zoomed-in excerpts of Fig. 5.5a–Fig. 5.5c. More precisely, each state in time-domain corresponds to one cluster of eigenvalues in the harmonic domain. When increasing the maximum harmonic order, the number of eigenvalues in such a cluster increases too. This is what one would expect, corresponding to the increase in size of the system matrix.

For the CIDERs which only consider AC-side characteristics (i.e., Fig. 5.5a and Fig. 5.5b), increasing the maximum harmonic order does not affect the location of the eigenvalues. Additionally, the locations of the LTI and LTP eigenvalues coincide for both CIDERs. For the grid-following CIDER that models the DC side, shown in Fig. 5.5c, the location of the eigenvalues changes when increasing the maximum harmonic order.

The observations made above are also confirmed by Fig. 5.6, which shows the maximum distance between the LTI and LTP eigenvalues for a given maximum harmonic order $d(h_{max})$ as defined in (5.78). For the two CIDERs which only model the AC-side characteristics $d(h_{max})$ is constant at zero. This indicates that there are no time-varying phenomena present in the LTP model, which would be missed by the LTI model. However, for the grid-following CIDER which includes the DC-side characteristics, $d(h_{max})$ in Fig. 5.6 increases with h_{max} . For a h_{max} up to four, the difference between the LTI and the LTP eigenvalues is close to zero. When increasing h_{max} further the difference increases. The changes in Fig. 5.6 can be explained by the entries of the operating point. In fact, the grid-following CIDER that models the DC side includes a linearization of the internal response w.r.t. a time-periodic operating point. When increasing h_{max} , more and more of the time-periodic entries are considered in the derivation of the system matrix. Hence, whenever a new nonzero entry of the operating point is considered, the location of the eigenvalues changes. For the case of the grid-following CIDER with DC side, $d(h_{max})$ saturates around a maximum harmonic order of $h_{max} = 7$. This indicates that the dominant aspects of the nonlinear CIDER behaviour are effectively captured by these low-order harmonics. This analysis clearly demonstrates the difference in how CIDERs are represented by LTI models compared to LTP models.

5.4 Harmonic Stability Assessment of the Resources

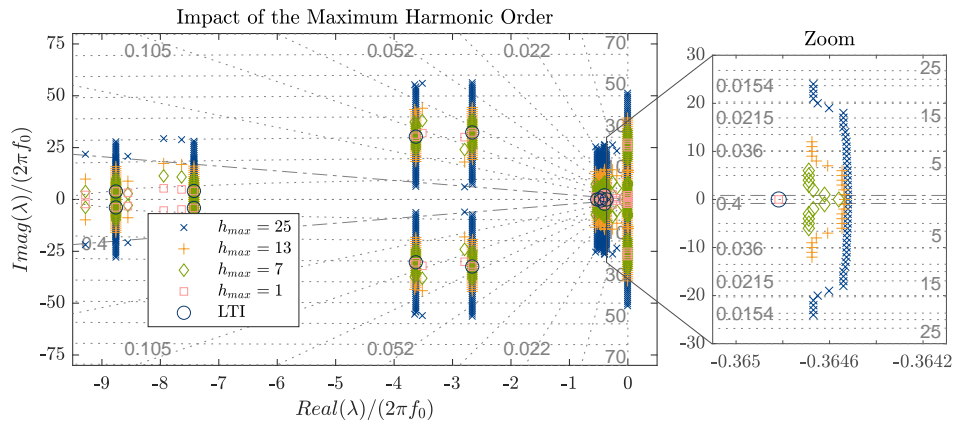
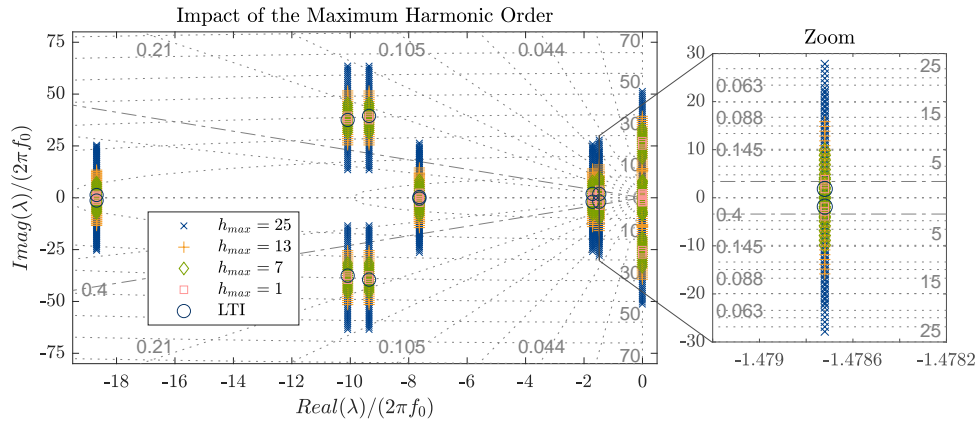
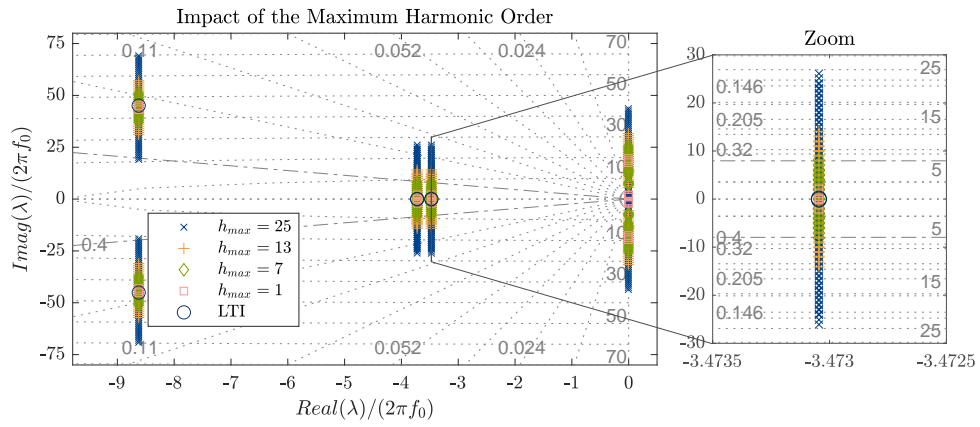


Figure 5.5: Analysis of the impact of the maximum harmonic order on the location of the LTP eigenvalues for the grid-forming CIDER (Fig. 5.5a), the grid-following CIDER (Fig. 5.5b) and the grid-following CIDER that models the DC side (Fig. 5.5c)

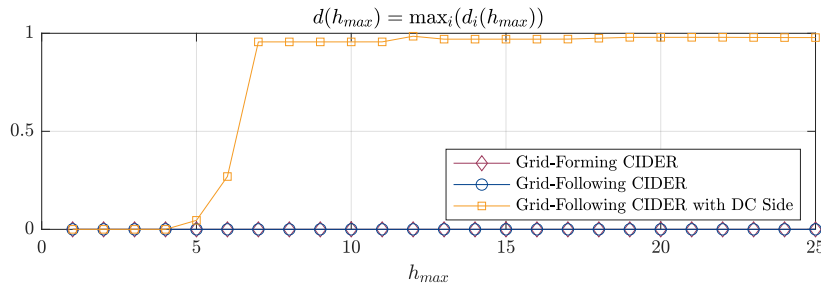


Figure 5.6: Analysis of the impact of h_{max} on the location of the LTP eigenvalues for the three CIDERs. The CIDERs being analysed are the grid-forming and grid-following CIDERs that only model the AC-side characteristics (i.e., Section 3.3.1 and Section 3.3.2, respectively), and the grid-following CIDER that includes the DC-side modelling (i.e., Section 3.3.3). The plot shows the maximum distance between the LTI and the LTP eigenvalues for increasing h_{max} .

5.4.3 Sensitivity Analysis of the Eigenvalues w.r.t. to the Control Parameters

Methodology

In order to determine the sensitivity of the eigenvalues w.r.t. certain controller parameters, it suffices to vary only these parameters individually (i.e., as opposed to the previous analysis where several or all parameters are varied simultaneously). Then, the eigenvalues of the original and modified system are sorted employing the LAP, following the same principles as described in Section 5.4.1. This procedure is repeated for several incremental changes of the control parameter under investigation. In this way, one can trace the eigenvalue loci in the s-plane.

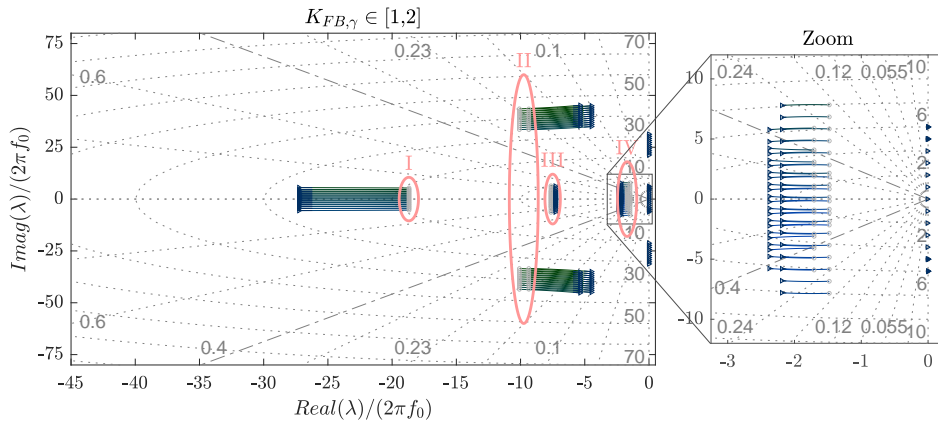
As a trade-off between complexity of the proposed CIDERs and conciseness of the results, the case of the grid-following CIDER, which only models the AC-side characteristics that was introduced in Section 3.3.2, is shown in detail. To this end, the sensitivity of the eigenvalues w.r.t. to the change of the controller feedback gains K_{FB} for the three stages of the CIDER are analysed. The controller gains are incrementally increased by a factor of 0.01 from their initial values given in Table 3.4 for $N = 70$ iterations. For cascaded control schemes, the inner loops usually respond faster than the outer ones (i.e., their time constants T_{FB} are smaller). For this reason, the time constants of the controller stages cannot be tuned independently from each other and therefore not analysed in detail in this case study.

The sensitivities of the eigenvalues w.r.t. control parameters are useful in the context of parameter-tuning problems. More precisely, one can select the optimal locations of the eigenvalues (i.e., w.r.t. a given objective function) while ensuring that the system is stable. In this thesis, it is shown how to obtain the sensitivities and perform a

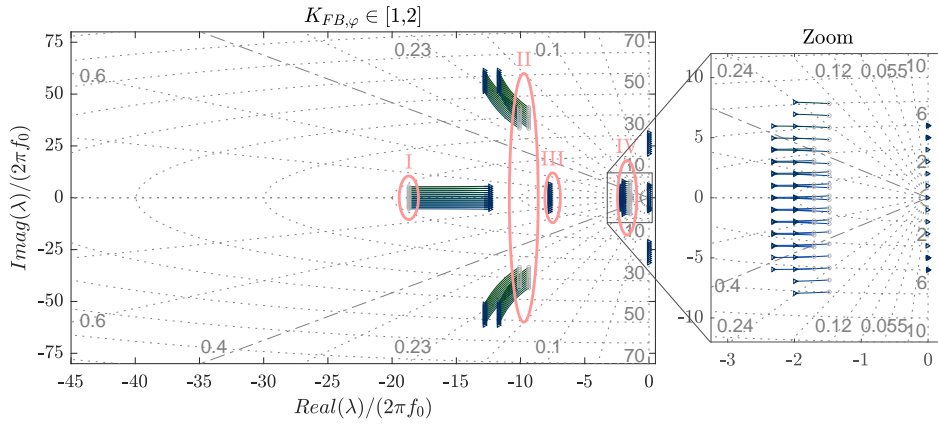
preliminary analysis of the resource and system behaviour w.r.t. to changes of selected control parameters. The optimal tuning of the parameters remains for future work.

Results and Discussion

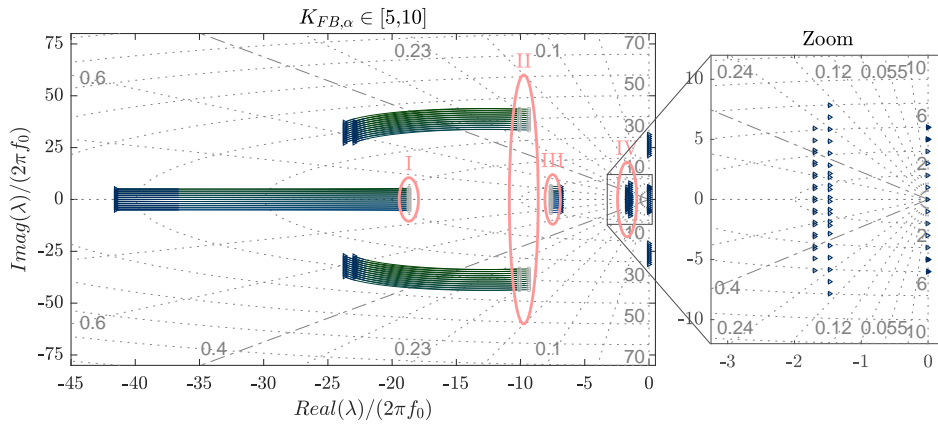
Fig. 5.7 shows the eigenvalue loci of the grid-following CIDER, which models only the AC-side characteristics. To simplify the discussion, the eigenvalues are order into areas I to IV. Fig. 5.7a shows the eigenvalue locus w.r.t. feedback gain of the outer-most controller stage. It becomes obvious that increasing $K_{\text{FB},\gamma}$ leads to a shift of the eigenvalues in area I, away from the imaginary axis (see also the zoomed portion of the figure). On the other hand, increasing $K_{\text{FB},\gamma}$ also moves the eigenvalue pairs in area II and III closer to the imaginary axis, thereby decreasing the stability margin of the resource. Similarly, increasing $K_{\text{FB},\varphi}$ in Fig. 5.7b leads to an analogous shift of the eigenvalues in area I. The eigenvalues in area II move away from the imaginary axis, while keeping a similar damping factor. The change of tuning of $K_{\text{FB},\alpha}$ of the inner-most controller stage leads to a very low sensitivity of the eigenvalues in area I in Fig. 5.7c (i.e., they do almost not change). The eigenvalues in area II-IV on the other hand, are significantly moved in direction of the negative real axis. In conclusion, in order to obtain a better tuning of the CIDER it seems to be most beneficial to increase $K_{\text{FB},\alpha}$ of the inner-most controller stage. As can be seen from Fig. 5.7c, by increasing the gain up to 10, the eigenvalues of area II can be moved into the area of damping factors bigger than 0.4.



(a)



(b)



(c)

Figure 5.7: Sensitivity curves w.r.t. the feedback gain K_{FB} of the controller stage associated with the grid-side inductance (Fig. 5.7a), the controller stage associated with the capacitance (Fig. 5.7b) and the controller stage associated with the actuator-side inductance (Fig. 5.7c) of the grid-following CIDER, which models only the AC-side characteristics. The maximum harmonic order considered for this analysis is $h_{max} = 5$.

5.5 Harmonic Stability Assessment of a Power System

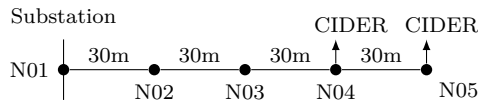


Figure 5.8: Schematic diagram of the test system used for the HSA. Its line lengths and cable parameters are based on the CIGRÉ low-voltage benchmark microgrid [1]. All cables are of type UG1 - for their parameters see Table 4.3.

5.5 Harmonic Stability Assessment of a Power System

This section discusses the HSA of an entire power system. First, the test system is introduced and the considered steady-state operating point is characterized by means of a HPF study. Then, similar to the HSA of the individual CIDERS, the system eigenvalues are classified as CDV, CDI or DI and a brief discussion w.r.t. to the eigenvectors is provided. Next, both a general and a detailed discussion on the system eigenvalues is provided. More precisely, a comparison to the eigenvalues of the open-loop resources and grid, as well as to the LTI eigenvalues is performed. Finally, a case of harmonic instability is identified using the loci of the system eigenvalues and validated through TDS with Simulink.

5.5.1 Test System Setup

The proposed HSA is applied to the test system shown in Fig. 5.8. Notably, for the ease of understanding, i.e., a reasonable number of eigenvalues, a small-scale example system is chosen. The parameters are taken from the CIGRÉ low-voltage benchmark microgrid [1]. The HSS is derived for the complete system model, and used to assess the system's eigenvalues.

The test system is characterized as follows. The substation is located in node N01. Its short-circuit parameters, are listed in Table 3.1. Recall from Section 3.4 that, the TE voltage source injects harmonics, whose levels are given in Table 3.2 and set according to the limits specified in the standard BS-EN-50160:2000 [3]. All lines are built from underground cables of type UG1, whose sequence parameters are given in Table 4.3. Two grid-following CIDERS, of which only the AC-side characteristics are modelled, are connected at nodes N04 and N05. Their parameters are the same as for the resource validation, see Table 3.4. In line with the analysis in Section 5.4.3, the parameters of one of the CIDERS are retuned in order to achieve better overall damping. More precisely, the feedback gain of the inner-most controller stage $K_{FB,\alpha}$ for the CIDER at N04 is increased to 16. The setpoints for both grid-following CIDERS are set to $P_\sigma = -50$ kW and $Q_\sigma = -16.4$ kVar.

In order to derive the HSS of the system, the harmonic operating point of the system is derived through the HPF introduced in Section 4.3. Notably, the operating points

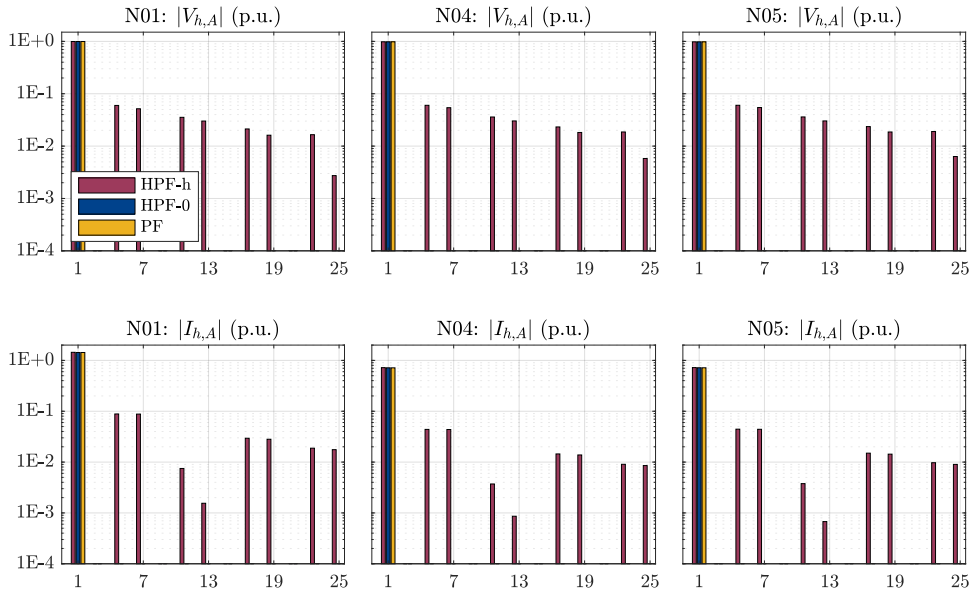


Figure 5.9: Results of the HPF for a system with harmonic distortion (HPF-h), the HPF for a system with zero harmonic distortion (HPF-0) and a conventional power-flow (PF) at the fundamental frequency. The figure shows the magnitudes of the nodal quantities for phase A, at the three nodes, where resources are connected.

needed for the system under consideration are the harmonic phasors of the nodal voltages at the nodes where the grid-following CIDERS are connected. As previously explained in Section 3.2.5, the nodal voltages are used in the linearization of the reference calculation of the grid-following CIDERS. Throughout this section, the eigenvalues obtained from the HSS model will be compared to the ones obtained from a classical LTI state-space model. Analogously to the LTP model, the LTI model requires the nodal voltages at nodes, where the grid-following CIDERS are connected, for the linearization of the reference calculation. In order to derive the nodal voltages for the LTI case, a conventional power-flow at the fundamental frequency is conducted. The operating points which have been obtained for the described cases are displayed in Fig. 5.9. Is it worth noting that the fundamental component of the nodal voltages is close to 1 p.u. in magnitude, which means that the system is only lightly loaded.

5.5.2 Classification of the System Eigenvalues

Methodology

For the classification of the LTP eigenvalues as DI, CDI and CDV, the same analysis as introduced in Section 5.4.1 is performed. Namely, in order to obtain the DI eigenvalues, all parameters of the system are varied simultaneously. The DI eigenvalues are those that

5.5 Harmonic Stability Assessment of a Power System

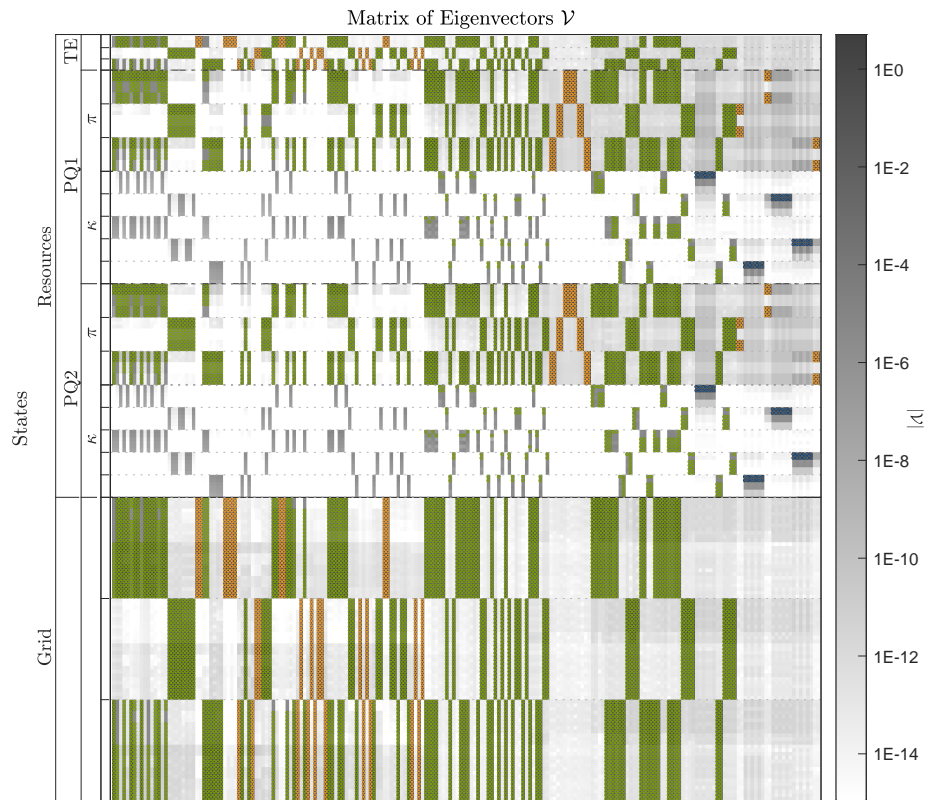
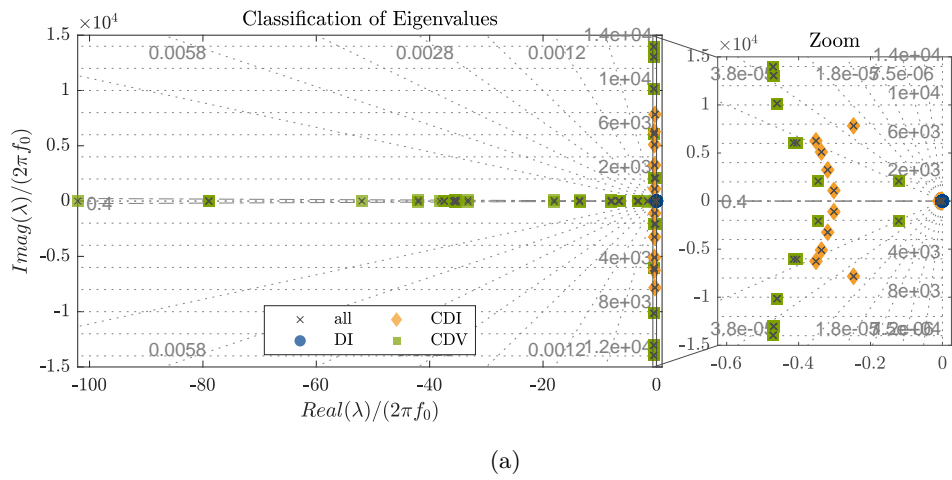


Figure 5.10: Classification of the closed-loop system eigenvalues into DI, CDI and CDV (Fig. 5.10a), and visualization of the eigenvector matrix associated with the eigenvalues (Fig. 5.10b).

remain unchanged upon the variation of the parameters. For the derivation of the CDI eigenvalues, all control parameters (i.e., of the two CIDERS) are varied. Additionally, a brief analysis of the associated eigenvectors is performed. To improve the understanding of the composition of the eigenvector matrix, the composition of the system state vector is recalled. For the ease of understanding, the maximum harmonic order for this analysis is set to $h_{max} = 1$.

This is a preliminary analysis, to understand the characteristics of the system eigenvalues, and which ones are sensitive to the control parameters of the CIDERS. As mentioned in Section 5.3, more detailed studies, such as participation factor or modal analyses can be performed.

Results and Discussion

In Fig. 5.10 the classification of the closed-loop system eigenvalues is given. Fig. 5.10a shows the overview of all system eigenvalues and their classification as DI, CDI and CDV. On the right-hand side, a zoom-in on the eigenvalues which are located close to the imaginary axis is shown. Fig. 5.10b represents the matrix of the eigenvectors obtained from the eigenvalue decomposition of the closed-loop system. As for the classification of the eigenvalues for the individual CIDERS, the magnitude of each entry is shown on a logarithmic scale. Additionally, the entries that exceed a threshold value of 1E-5 are highlighted using the same colour as the associated classification (e.g., if the eigenvalue associated with the eigenvector is CDV, the corresponding entries of \mathbf{V} are also highlighted in green). The matrix of the eigenvectors relates the eigenvalues with the states of the system. Therefore the entries on the horizontal dimension correspond to the eigenvalues and the vertical dimension is associated with the states of the system. The composition of the system state vector is recalled on the y-axis in Fig. 5.10b. Namely, the upper and lower part of the system state consist of the states of the resources (i.e., the TE and the two grid-following CIDERS), and of the grid, respectively.

Similar to the classification of the individual resources in Section 5.4.1, the CDI eigenvalues of the system are associated with the homopolar sequences of the grid and power hardware of the resources. In the eigenvector plots, there is no connection between the homopolar sequences associated with the grid and the states of the CIDERS and vice versa (i.e., either block of the eigenvector is entirely zero). This is due to the circuit configuration of the grid-following CIDERS, which does not allow homopolar sequences to pass from or into the power hardware. The DI eigenvalues are the same as for the classification of the individual CIDER in Fig. 5.4a, namely one set of DI per controller stage of each CIDER.

5.5.3 Detailed Analysis of the System Eigenvalues

Methodology

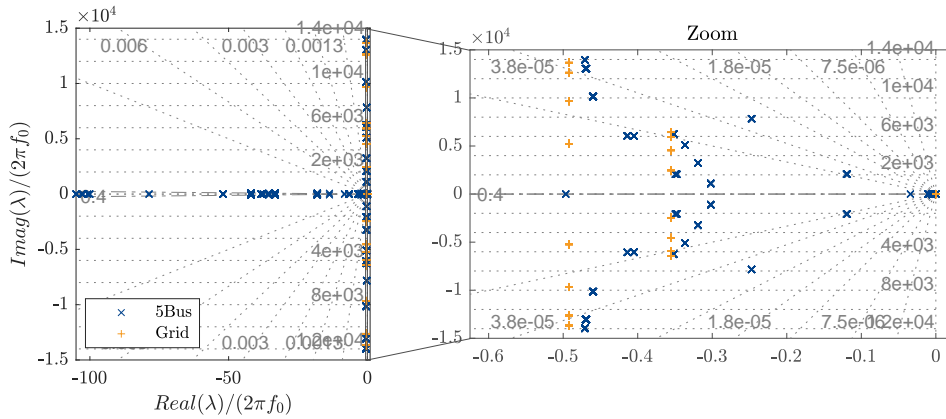
For the detailed analysis of the system eigenvalues, a maximum harmonic order of $h_{max} = 25$ is considered. The aim of this analysis is to give a general understanding of the different groups of eigenvalues being analysed. Due to the large amount of eigenvalues, as well as their wide distribution, a separation into two sets of eigenvalues is introduced, i.e., one each associated with the grid and the resources, respectively. The set of system eigenvalues associated with the grid is briefly discussed in the following. To this end, they are compared to their open-loop equivalents (i.e., the eigenvalues of the open-loop grid model).

Subsequently, a more detailed discussion of the set of eigenvalues associated with the resources is given. First, they are compared to the eigenvalues of the TE and the two CIDERs (i.e., the open-loop resource models). Second, the impact of the harmonics on the system eigenvalues is analysed. To this end, the eigenvalues of a system that includes harmonics as in Table 3.2 is compared to one without harmonic distortion. Notably, for the two analyses different operating points (i.e., computed through the HPF with and without harmonic distortion) need to be considered when deriving the HSS model of the system. Third, the two sets of system eigenvalues are compared to the ones obtained by an LTI system model. Notably, LTI models are entirely represented in DQ components, in order to circumvent the consideration of the time-periodic transformation matrices. Thus, the difference between LTP and LTI is the modelling of the power hardware in ABC coordinates and DQ components, respectively, as well as the specific consideration of the transformation blocks in the LTP model.

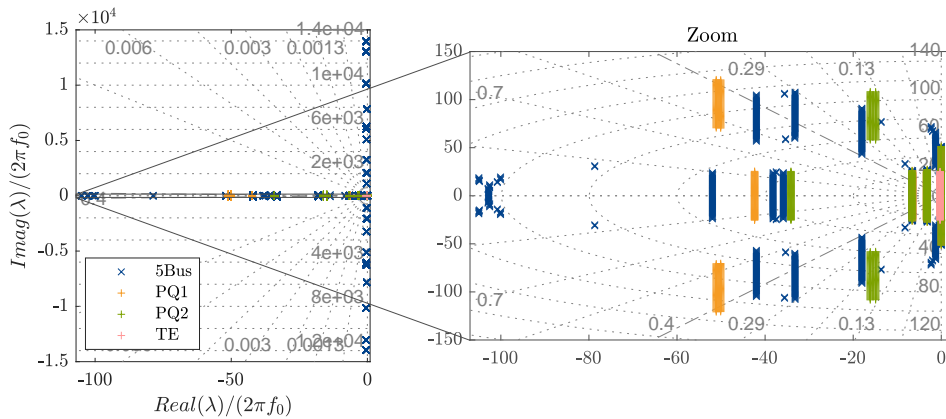
The comparison of the eigenvalues obtained from the system with harmonic distortion, the system without harmonic distortion, and the LTI model, allows to understand whether (i) an observed instability occurs due to harmonic distortion, and whether (ii) it can be detected by the conventional stability criteria (i.e., by the eigenvalues of the LTI system).

Results and Discussion

Fig. 5.11 shows the comparison of the eigenvalues of the closed-loop system with those of the open-loop components. To this end the eigenvalues are divided into two sets. The first set includes the eigenvalues located closer to the imaginary axis (i.e., Fig. 5.11a). The second set comprises the eigenvalues, that are located closer to the real axis (i.e., Fig. 5.11b). As will be shown shortly, the two sets of eigenvalues can be associated with the grid and the resources, respectively. Both subfigures in Fig. 5.11 give the overview of all eigenvalues on the left-hand side and a zoomed portion of interest on the right-hand side.



(a)



(b)

Figure 5.11: Division of the system eigenvalues into the two sets associated with the grid (Fig. 5.11a) and with the resources (Fig. 5.11b), respectively. The left-hand side of both figures show the entire region containing all eigenvalues, while the right-hand side figures show a zoom on the regions of interest. Additionally, the eigenvalues of the open-loop grid and resource models are shown in (Fig. 5.11a) and (Fig. 5.11b), respectively.

Additionally to the closed-loop eigenvalues of the system, Fig. 5.11a displays the eigenvalues of the grid state-space model (i.e., the open-loop model). One can see that the eigenvalues of the system (i.e., the closed-loop model) are slightly shifted w.r.t. those of the grid (i.e., the open-loop model). Notably, most of the eigenvalues in Fig. 5.11a have fairly large imaginary parts (i.e, they occur at high frequencies). These eigenvalues are related to the shunt capacitances of the lines, which are extremely small (see Table 4.3). By consequence, their shunt admittance becomes important only at very high frequencies (i.e., since $Y = j\omega C$). In low-voltage distribution systems, the line capacitances are usually negligible [1], even though they have to be considered in the derivation of the HSS model of the grid. This is due to the fact that the nodal voltages, which are state variables of the system model, are associated with these elements.

5.5 Harmonic Stability Assessment of a Power System

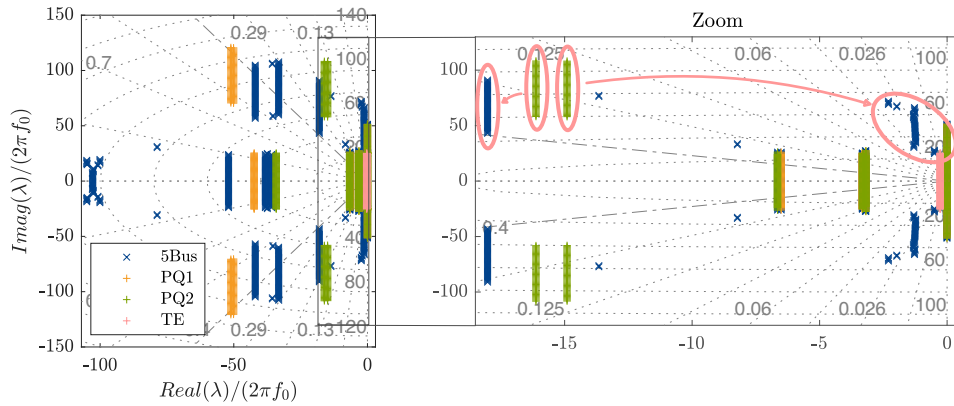


Figure 5.12: Detailed view of the system eigenvalues associated with the resources. Additionally, the eigenvalues of the open-loop resource models are shown (i.e., PQ1/2 and TE). Note the indication showing how this set of eigenvalues of PQ2 change their location for the system model.

Fig. 5.11b shows the portion of the system eigenvalues that are associated with the resources of the system. For this reason, the eigenvalues of the two grid-following resources at node N04 and N05 and the TE at node N01 are depicted too. In order to analyse the characteristics of this set of eigenvalues in detail, further analyses are performed in the following. For the sake of clarity, all subsequent figures directly show the zoom on these eigenvalues.

In Fig. 5.12, the system eigenvalues associated with the resources and the eigenvalues of the open-loop resource models (i.e., the TE and the two grid-following resources) are shown. Notably, the eigenvalues of the closed-loop system significantly change their locations compared to those of the open-loop models. In particular, the sets of eigenvalues related to the CIDER at N05 (see indications in Fig. 5.12), which have low damping, further reduce their damping factors.

Fig. 5.13 illustrates the impact of harmonic distortion in a system on the location of the eigenvalues. The figure compares the eigenvalues of the system with harmonic distortion to the eigenvalues of a system with purely sinusoidal waveforms. One can clearly observe how the set of LTP eigenvalues with low damping factor becomes more dispersed for the system with harmonic distortion. This is due to the nonlinearity of the reference calculation of the CIDER, which causes coupling between different frequencies (i.e., non-zero off-diagonal elements of the system matrix). Since the reference calculation is not part of the internal response of the CIDERs, this effect can only be seen once the closed-loop system is calculated. This is further underlined by the fact that the associated open-loop components in Fig. 5.12 do not show this dispersion.

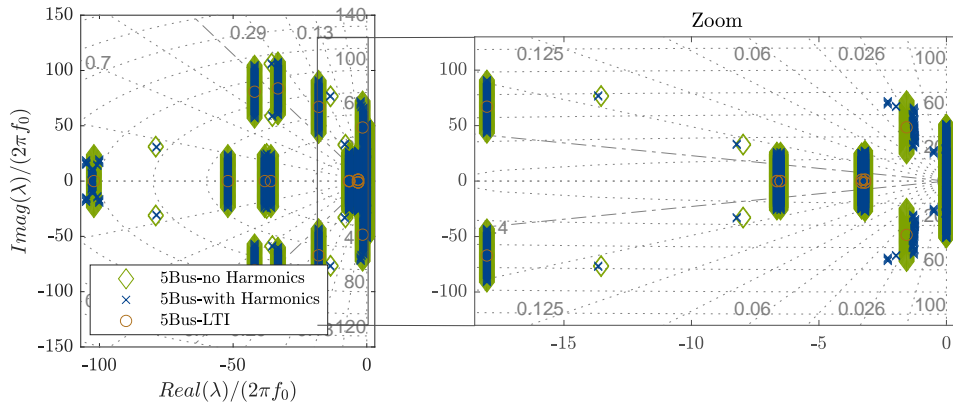


Figure 5.13: Detailed view of the system eigenvalues associated with the resources. Comparison of the system eigenvalues obtained with the HSS model considering a system with zero harmonic distortion to one with harmonic distortion. Additionally, the eigenvalues of the LTI model are shown.

In Fig. 5.13, the real parts of the eigenvalues of the LTP system without harmonics match with those of the LTI system. This is according to expectations, since the LTI and LTP models of the CIDERS are equivalent in the absence of harmonic distortion. For the sake of clarity, the eigenvalues of the LTI system are used subsequently to represent an LTP system without harmonic distortion.

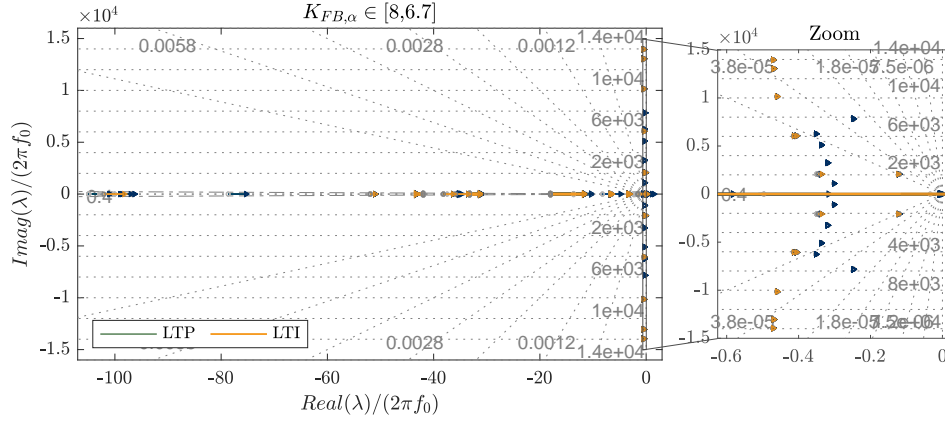
5.5.4 Sensitivity Analysis and Harmonic Instability

Methodology

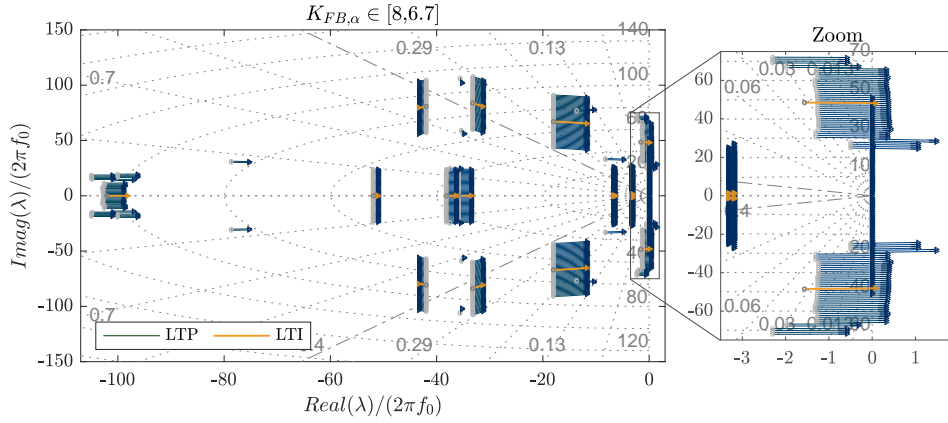
A sensitivity analysis of the system eigenvalues w.r.t. to $K_{FB,\alpha}$ of the CIDER at N05 is performed. The goal of this analysis is to find a case of harmonic instability. Namely, an instability that occurs only if harmonic distortion is present in the system. To this end, the controller gain is incrementally reduced by 1% of its previous value for $N = 18$ iterations. Recall from Fig. 5.7c, that an increase of $K_{FB,\alpha}$ yields better damping of the individual grid-following CIDER. Based on the eigenvalue loci, the stability boundary obtained from the LTP and LTI system eigenvalues are compared.

Finally, the same test is performed through TDS with Simulink. The model components are reused from the Simulink models employed for the validations in Chapter 3 and Chapter 4. More precisely, two simulations are conducted in Simulink. In both simulations, the feedback gain $K_{FB,\alpha}$ of the CIDER at N05 is decreased repeatedly over time. The time between two changes is chosen long enough such that the system reaches a new steady state, before changing the parameter again. The difference between the two simulations are the background harmonics injected at the substation. In the first scenario, the TE does not inject any harmonics, thus the approximate LTI model is expected to yield

5.5 Harmonic Stability Assessment of a Power System



(a)



(b)

Figure 5.14: Sensitivity analysis of the system eigenvalues for the LTP and LTI models w.r.t. the controller gain $K_{\alpha,FB}$ of the grid-following CIDER at N05. Fig. 5.14a and Fig. 5.14b show the system eigenvalues associated with the grid and the resources, respectively. The maximum harmonic order of this analysis is $h_{max} = 25$.

accurate stability boundaries. Conversely, in the second scenario, harmonics are injected as specified in Table 3.2. In this case, the more accurate LTP model should outperform the LTI model in terms of HSA.

Results and Discussion

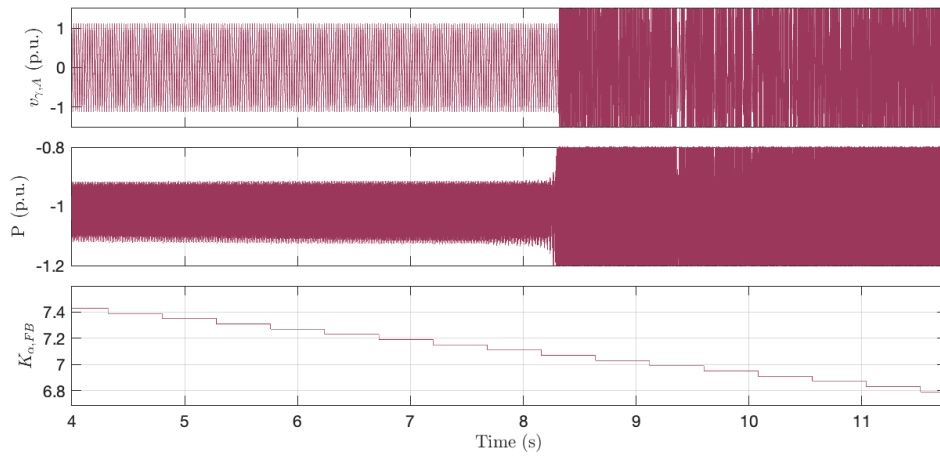
Fig. 5.14 shows the sensitivity of the system eigenvalues w.r.t. the controller gain $K_{\alpha,FB}$ of the grid-following CIDER at N05. Fig. 5.14a depicts a zoom on the eigenvalue loci associated with the grid. As can be seen, the sensitivities of these eigenvalues are virtually negligible (i.e., the eigenvalues do not move significantly when changing the control parameter).

Chapter 5. Harmonic Stability Assessment

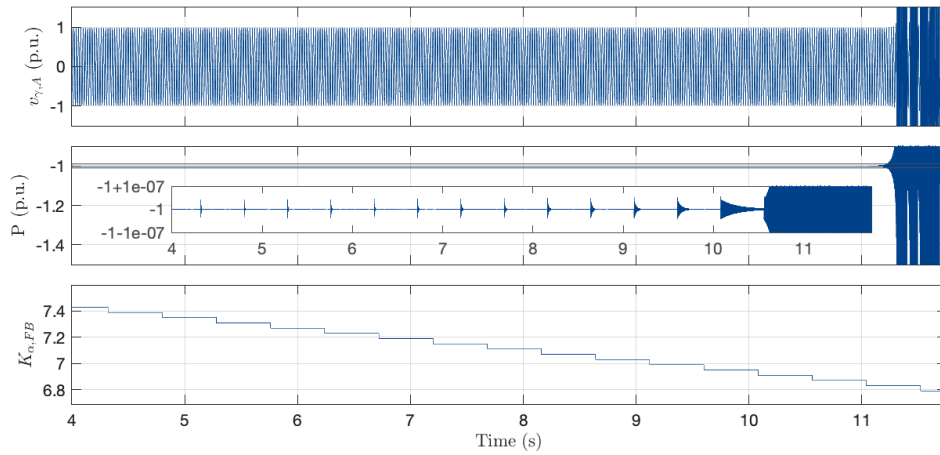
Fig. 5.14b shows the eigenvalue loci associated with the resources. More precisely, the curves obtained from the LTP and LTI analysis are compared. One can observe that the eigenvalues of the LTP model cross the imaginary axis earlier than the ones of the LTI model. Thus, there exists a gain, which only leads to instability in case harmonic distortion is present in the system. Furthermore, it is not possible to observe this instability with conventional stability criteria (i.e., the eigenvalues of the LTI model).

Fig. 5.15 shows the validation of the observed stability boundary in Fig. 5.14b through TDS in Simulink. In Fig. 5.15b, the system is excited with a pure fundamental component at the substations, while in Fig. 5.15a, the usual harmonic distortion is injected at the TE. Both subfigures show the nodal voltage and the injected active power at node N05 of the test system. The last subplot in the subfigures shows how the controller gain $K_{\alpha,FB}$ is decreased gradually until the system becomes unstable. As can be seen in Fig. 5.15a, the system becomes unstable earlier in the presence of harmonics. (i.e., as compared to purely sinusoidal behaviour at the substation as illustrated Fig. 5.15b). This confirms the observations, made in Fig. 5.14, and shows a case of harmonic instability, that can not be observed with conventional stability criteria. That is, an instability of this type can only be detected by the LTP model but not by the LTI model.

5.5 Harmonic Stability Assessment of a Power System



(a)



(b)

Figure 5.15: Validation of the observed instability through TDS in Simulink. Fig. 5.15a gives the stability boundary for the test system if harmonics are present in the system (i.e., a “harmonic instability” in line with the definition in Section 1.2), and Fig. 5.15b shows the case without harmonic injection at the substation (i.e., purely sinusoidal behaviour). Each figure shows the nodal voltage of phase A (i.e., $v_{\gamma,A}$) and the injected power P at node N05, in the first and second plot of the figure, respectively. The last plot in both figures depicts the decrease of the controller gain $K_{\alpha,FB}$ of the grid-following CIDER at N05 as the system becomes unstable.

6 Conclusion

This thesis developed and validated methods for the HA of power systems with a high share of CIDERs. Specifically, a suitable modelling framework was proposed in Chapter 2 (along with a library of component models detailed in Chapter 3), and subsequently employed for HPF studies and for the HSA in Chapter 4 and Chapter 5, respectively. Both methods were demonstrated to be accurate and applicable to typical power systems. In particular, it was shown that the coupling between harmonic frequencies in power systems with numerous CIDERs has a considerable impact on the propagation of harmonics (i.e., Chapter 4), as well as instabilities that occur due to them (i.e., Chapter 5).

An important objective of the presented research was to achieve generality w.r.t. the structure of CIDERs and their control laws, as well as modularity w.r.t. their specific components. To this end, the modelling framework in Chapter 2 was proposed, which is based on LTP systems theory. The component models were first formulated in time domain, and then transformed to harmonic domain by means of the Fourier and Toeplitz theory. Moreover, extensions of the modelling framework which account for nonlinearities within the internal structure of the CIDER, and enable the modelling of hybrid AC/DC power systems were proposed. For the latter, the model of the NICs was introduced as a variation of the CIDER model. This modelling framework presents a powerful foundation for the analysis of power systems, due to the modularity and generality of the underlying models, as well as accuracy w.r.t. to the coupling between harmonic frequencies.

In Chapter 3, the applicability of the proposed modelling framework to typical grid-forming and grid-following CIDERs was demonstrated. The models of common types of CIDERs as well as a library of frequently used CIDER components were presented. More precisely, the models of grid-forming and grid-following CIDERs that only model the AC-side characteristics, as well as, a grid-following CIDER including the modelling of the DC-side characteristics were proposed. It was demonstrated that these models can accurately represent the interaction among harmonics in a single CIDER, as shown by comparing their harmonic domain grid responses with TDS conducted in Simulink.

Chapter 6. Conclusion

In Chapter 4, a HPF method for the analysis of propagation of harmonics within large power systems with numerous CIDERs was proposed. The HPF problem was formulated by combining the hybrid nodal equations of the grid with the HDR of the CIDERs, and solved using the Newton-Raphson method. First, the case of purely AC power systems was considered, and then extended for treating the CIDER model including the DC side, and finally fully generalized for the analysis of hybrid AC/DC power systems. All formulations of HPF method were shown to yield accurate results when analysing benchmark grids, i.e., a modified version of the CIGRÉ low-voltage benchmark microgrid and a typical hybrid AC/DC grid. The extended methods provide improved accuracy at the cost of increase computational burden. By consequence, a compromise has to be made between the benefit of increased accuracy and the drawback of additional computation time. The implementation of the tree types of the HPF method and its validation through example systems are open source and can be found on this [GitHub](#).

In Chapter 5, the HSS model of a generic power system was introduced and employed in the context of HSA through eigenvalue analysis. The HSS model of the power system is obtained by combining the HSS models of the resources and the grid in closed-loop configuration. The applicability of the HSA to both individual CIDERs as well as entire power systems was demonstrated. Based on the sensitivity of the eigenvalues to parameter changes, a classification into control-design variant, control-design invariant and design invariant eigenvalues was proposed. An in-depth analysis of the classification of the eigenvalues, the impact of the maximum harmonic order on the eigenvalue loci, and the sensitivity of the eigenvalues w.r.t. to specific control parameters was performed. Finally, the HSA was demonstrated to accurately detect harmonic instability in a test system, as identified through the system eigenvalues and confirmed with TDS in Simulink.

The proposed research can potentially support grid operators, device manufacturer, and standardization committees in tackling the challenges arising from the prevalence of harmonics in modern power systems. Grid operators can benefit from the strengths of the HPF models and methods for analysing the existing systems and optimizing their future design. Device manufactures can exploit the insights gained from the HSA in order to evaluate the control schemes of CIDERs and tune the associated parameters such that robustness w.r.t. harmonic distortion is achieved. Finally, standardization committees can leverage both of the aforementioned tools in order to revise the metrics and operational boundaries for modern power systems.

Future Work

Building on the research presented in this thesis, the following topics are suggested for further investigation:

- The library of CIDER models could be expanded further. Specifically, additional components of the CIDER that introduce further nonlinearities could be investigated. In collaboration with the Chair of Power Electronics at Kiel University, the impact of grid synchronization on the propagation of harmonics was examined by employing the proposed HPF method [111]. Additional topics to explore include different types of controllers (e.g., PR), controllers that are not following the cascaded structure, more types of actuators including modular multi-level converters, and other types of CIDERs (e.g., grid-forming CIDERs including in-depth models of the DC side and synchronverters).
- The convergence behaviour of the initial version of the HPF algorithm proposed in Section 4.3.2 merits a detailed examination. In a ongoing research collaboration between the Distributed Electrical Systems Laboratory at EPFL and the Electrical Engineering and Information Technology Department at the University of Naples Federico II, a fixed-point formulation of the algorithm has been developed in order to study the convergence behaviour. This formulation is being studied with respect to explicit sufficient conditions that ensure the existence and uniqueness of the solution of the HPF problem.
- The computational performance of the proposed HPF and HSA methods needs to be better investigated for large, complex systems. While both the modelling framework and the solution method are capable to handle large, complex systems, their performance may scale poorly due to the size of the matrices involved. In order to alleviate this issue, different strategies could be employed, such as model-order reductions, use of more efficient programming languages (e.g., C++) and/or numerical libraries (e.g., LAPACK/BLAS), parallelization of the calculation in software and hardware (e.g., multi-core/machine setup).
- In the context of the eigenvector analysis, the subject of participation factors for the HSA based on LTP models has been discussed briefly. Performing a more comprehensive analysis in this regard would be beneficial for gaining a clearer understanding of the significance of individual eigenvalues associated to the different harmonic frequencies.
- Moreover, the sensitivity analysis of the eigenvalues could be employed to perform parameter tuning for individual CIDERs or the entire system (i.e., including a system-level controller). Such a parameter-tuning problem would aim at tuning the controllers robustly w.r.t. to harmonic distortions and instability.

Chapter 6. Conclusion

- Finally, ongoing research efforts aim at including the effect of communication delays into the HA. The primary goal of this work is to investigate the stability of systems where the system-level control is prone to communication delays. In principle, such delays can readily be incorporated in the proposed framework. More precisely, any time delay affecting a particular variable translates to different phase shifts in the harmonic phasors of this quantity. Preliminary analyses of this phenomenon have already been carried out using a testbench that comprises a real-time simulator from OPAL-RT and a communication network emulator from Paket Storm, but further work is required.

A Appendix

A.1 Measurement Accuracy of Instrument Transformers

The accuracy of instrument transformers, is defined by several standards [5, 4, 86]. For the measurements of harmonics, it is referred to commonly used 0.5 class instrument transformers, whose accuracies are given in Table A.1. The values are defined in percentage of the rated voltage magnitude.

Table A.1: Accuracy requirements for instrument transformers for voltage measurements including harmonics [4, 5].

h	$e(V)$	$e(\arg(V))$
1	0.5 %	6 mrad
2-4	5 %	87.3 mrad
5-6	10 %	174.5 mrad
7-9	20 %	349.1 mrad
10-13	20 %	349.1 mrad
above 13	20-100 %	-

A.2 Modelling of Sources of Harmonics other than CIDERS

Naturally, harmonics may originate from sources which are not CIDERS, such as conventional resources or upstream and downstream power grids (i.e., “background” harmonics). Indeed, the proposed approach can accommodate such sources of harmonics which are not converter-interfaced. Namely – much like CIDERS – they can be represented by transfer functions in the harmonic domain. In this respect, the sole prerequisite is that such transfer functions can somehow be obtained – i.e., either from a suitable model or via system identification.

Appendix A. Appendix

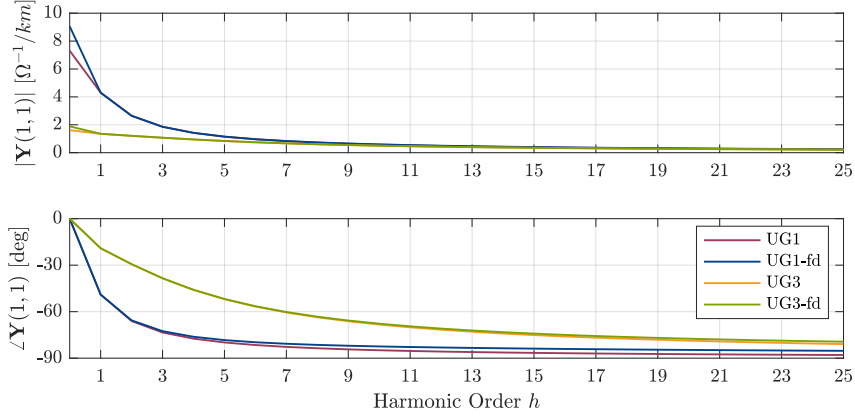


Figure A.1: Comparison of line branch admittances of the π -section equivalents with and without frequency-dependence of the cable parameters. For illustration, the element (1, 1) of the compound admittance matrices of the cable types (i.e., UG1 and UG3) is shown. The curves labelled with the suffix “fd” correspond to the cable models with frequency-dependent parameters.

For instance, a harmonic TE or NE can be used. Let $m \in \mathcal{N}$ be a node at which a non-CIDER source of harmonics is located. If a TE is used, the injected current is given by

$$\hat{\mathbf{I}}_m = \hat{\mathbf{Z}}_{\text{TE},m}^{-1}(\hat{\mathbf{V}}_m - \hat{\mathbf{V}}_{\text{TE},m}) \quad (\text{A.1})$$

where $\hat{\mathbf{V}}_{\text{TE}}$ and $\hat{\mathbf{Z}}_{\text{TE}}$ are the harmonic voltage source and harmonic impedance, respectively, of the TE. If a NE is used instead, the injected current is given by

$$\hat{\mathbf{I}}_m = \hat{\mathbf{I}}_{\text{NE},m} - \hat{\mathbf{Y}}_{\text{NE},m} \hat{\mathbf{V}}_m \quad (\text{A.2})$$

where $\hat{\mathbf{I}}_{\text{NE}}$ and $\hat{\mathbf{Y}}_{\text{TE}}$ are the harmonic current source and harmonic admittance, respectively, of the NE. In these cases, the generation of harmonics is represented by the equivalent voltage or current sources, and the coupling between harmonics by the equivalent impedances or admittances (i.e., by the off-diagonal blocks of these matrices).

A.3 Frequency-Dependent Line Parameters

A.3.1 Impact on the Branch Admittance of the Line Model

The CIGRÉ report [1], in which the benchmark microgrid is specified, does not provide any information on the frequency dependency of the cable parameters. Therefore, the cable parameters were calculated using EMTP-RV based on the available data on cable material and geometry. The behaviour of the branch admittances as function of frequency is shown in Figure A.1. For illustration, the element (1, 1) of the compound admittance matrices are shown. As one can see, whether or not the frequency dependency of the

parameters is considered has virtually no impact on the magnitude of the line admittance. In the phase, there is a slight difference between the two models at higher frequencies.

A.3.2 Impact on the Results of the Harmonic Power-Flow Study

In order to assess the impact on the results of the HPF study, analyses were conducted on the benchmark system using either the line model with frequency-invariant or -dependent parameters. The obtained results are shown in Figure A.2. For illustration, the comparison is done at three nodes throughout the benchmark system. The results are compared at three nodes throughout the system. As one can see, the spectra obtained using the different line models are congruent. This is in line with the previously discussed analyses made in EMTP-RV.

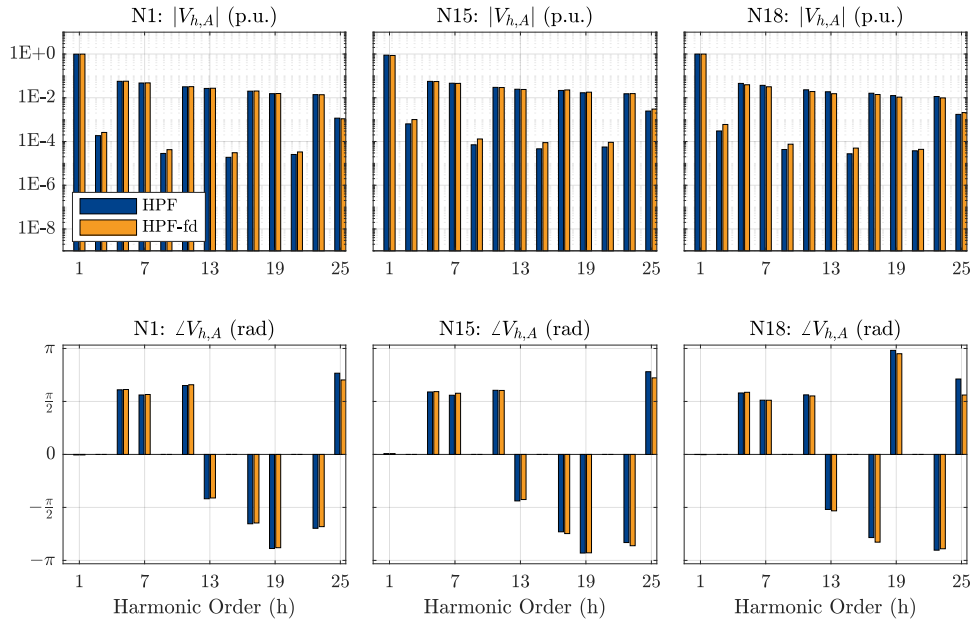
A.4 Decoupled Harmonic Power Flow

In the decoupled HPF, the CIDERS are represented by harmonic current sources. The harmonic content of these current sources is determined a priori through appropriate simulations or measurements. More precisely, the harmonic current phasors are characterized by a complex ratio w.r.t. the fundamental current phasor:

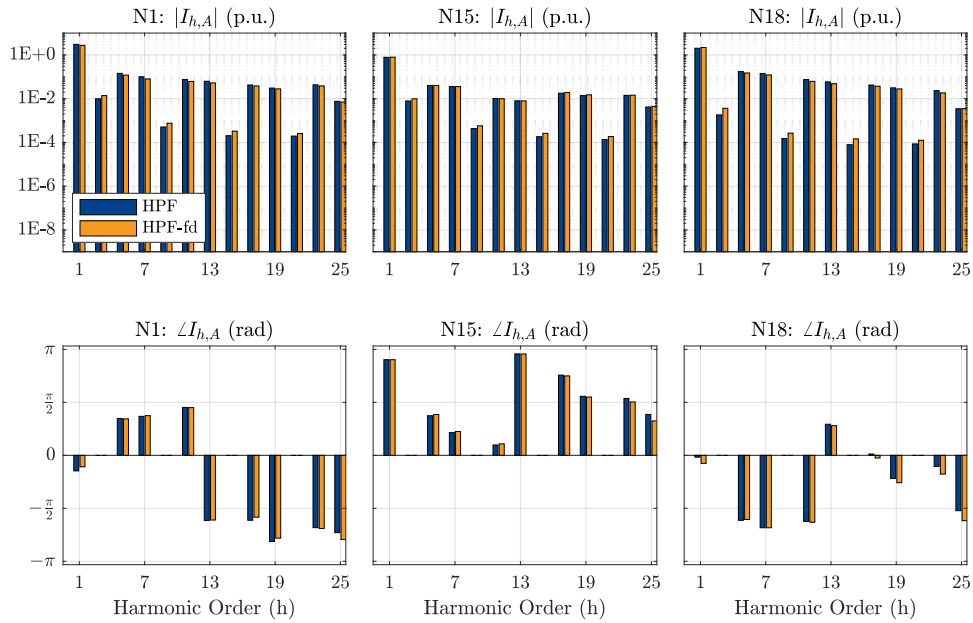
$$\alpha_h = \frac{I_h}{I_1} \in \mathbb{C} \quad (\text{A.3})$$

For the HPF analysis, a power flow study is first performed at the fundamental frequency. Then, the harmonic currents are inferred from the calculated fundamental currents and the available harmonic ratios. The system equations are solved independently at each harmonic frequency using the hybrid parameters of the grid. For further details please refer to [87].

Appendix A. Appendix



(a)



(b)

Figure A.2: Impact of the frequency-dependent parameters on the results of the HPF study. The results are compared at three nodes throughout the benchmark system. The voltages for Phase A are given in A.2a and the currents in A.2b. The results labelled with the suffix “fd” correspond to the line models with frequency-dependent parameters.

Bibliography

- [1] K. Strunz *et al.*, “Benchmark systems for network integration of renewable and distributed energy resources,” CIGRÉ, Paris, IDF, FR, Tech. Rep. 575, 2014.
- [2] S. Papathanassiou, N. Hatziargyriou, K. Strunz *et al.*, “A benchmark low voltage microgrid network,” in *Proceedings of the CIGRE symposium: power systems with dispersed generation*, 2005, pp. 1–8.
- [3] “Voltage characteristics of electricity supplied by public distribution networks,” British Standards Institution, London, UK, Std. BS-EN-50160:2000, 2000.
- [4] “Instrument transformers - part 3: Additional requirements for inductive voltage transformers,” International Electrotechnical Commission, Std. IEC 61869-3:2011, 2011.
- [5] “Instrument transformers - part 6: Additional general requirements for low-power instrument transformers,” International Electrotechnical Commission, Std. IEC 61869-6:2016, 2016.
- [6] F. Blaabjerg, Z. Chen, and S. B. Kjaer, “Power electronics as efficient interface in dispersed power generation systems,” *IEEE Trans. Power Electron.*, vol. 19, no. 5, pp. 1184–1194, 2004.
- [7] F. Milano, Ed., *Advances in Power System Modelling, Control, and Stability Analysis*. Stevenage, ENG, UK: IET, 2016.
- [8] C. D’Adamo *et al.*, “Development and operation of active distribution networks,” CIGRÉ, Tech. Rep. 457, 2011.
- [9] C. A. Cañizares *et al.*, “Microgrid stability definitions, analysis, and modeling,” IEEE PES, Tech. Rep. PES-TR66, 2018.
- [10] N. Hatziargyriou *et al.*, “Stability definitions and characterization of dynamic behavior in systems with high penetration of power electronic interfaced technologies,” IEEE PES, Tech. Rep. PES-TR77, 2020.

Bibliography

- [11] J. H. R. Enslin and P. J. M. Heskes, “Harmonic interaction between a large number of distributed power inverters and the distribution network,” *IEEE Trans. Power Electron.*, vol. 19, no. 6, pp. 1586–1593, 2004.
- [12] J. Arrillaga, B. C. Smith, N. R. Watson, and A. R. Wood, *Power System Harmonic Analysis*. Hoboken, NJ, USA: Wiley, 1997.
- [13] M. Paolone, T. Gaunt, X. Guillaud, M. Liserre, S. Meliopoulos, A. Monti, T. Van Cutsem, V. Vittal, and C. Vournas, “Fundamentals of power systems modelling in the presence of converter-interfaced generation,” *Electric Power Systems Research*, vol. 189, p. 106811, 2020.
- [14] C. A. Canizares, “Calculating optimal system parameters to maximize the distance to saddle-node bifurcations,” *IEEE Trans. on Circuits and Systems I: Fundamental Theory and Applications*, vol. 45, no. 3, pp. 225–237, 1998.
- [15] P. S. Kundur *et al.*, “Definition and classification of power system stability,” *IEEE Trans. Power Syst.*, vol. 19, no. 3, pp. 1387–1401, 2004.
- [16] A. M. Kettner, L. Reyes-Chamorro, J. K. M. Becker, Z. Zou, M. Liserre, and M. Paolone, “Harmonic power-flow study of polyphase grids with converter-interfaced distributed energy resources—part i: Modeling framework and algorithm,” *IEEE Trans. Smart Grid*, vol. 13, no. 1, pp. 458–469, 2021.
- [17] J. K. M. Becker, A. M. Kettner, L. Reyes-Chamorro, Z. Zou, M. Liserre, and M. Paolone, “Harmonic power-flow study of polyphase grids with converter-interfaced distributed energy resources—part ii: Model library and validation,” *IEEE Trans. Smart Grid*, vol. 13, no. 1, pp. 470–481, 2021.
- [18] J. K. M. Becker, A. M. Kettner, Y. Zuo, F. Cecati, S. Pugliese, M. Liserre, and M. Paolone, “Modelling of ac/dc interactions of converter-interfaced resources for harmonic power-flow studies in microgrids,” *IEEE Trans. on Smart Grid*, vol. 14, no. 3, pp. 2096–2110, 2022.
- [19] J. K. M. Becker, Y. Zuo, M. Paolone, and A. M. Kettner, “Harmonic power-flow study of hybrid ac/dc grids with converter-interfaced distributed energy resources,” in *2023 IEEE Belgrade PowerTech*, 2023, pp. 1–6.
- [20] L. O. Chua and P.-M. Lin, *Computer-Aided Analysis of Electronic Circuits*. Upper Saddle River, NJ, USA: Prentice Hall, 1975.
- [21] P. Dimeo, *Nodal Analysis of Power Systems*. Tunbridge Wells, UK: Abacus Press, 1975.
- [22] H. W. Dommel, “Digital computer solution of electromagnetic transients in single- and multiphase networks,” *IEEE Trans. Power App. Syst.*, no. 4, pp. 388–399, 1969.

-
- [23] L. W. Nagel and D. O. Pederson, “SPICE: Simulation program with integrated circuit emphasis,” UC Berkeley, Tech. Rep. UCB M382, 1973.
- [24] C.-W. Ho, A. E. Rühli, and P. A. Brennan, “The modified nodal approach to network analysis,” *IEEE Trans. Circuits Syst.*, vol. 22, no. 6, pp. 504–509, 1975.
- [25] J. Mahseredjian *et al.*, “On a new approach for the simulation of transients in power systems,” *Elect. Power Syst. Research*, vol. 77, no. 11, pp. 1514–1520, 2007.
- [26] R. H. Park, “Two-reaction theory of synchronous machines,” *Trans. AIEE*, vol. 48, no. 3, pp. 716–727, 7 1929.
- [27] X. Wang, F. Blaabjerg, and W. Wu, “Modeling and analysis of harmonic stability in an ac power-electronics-based power system,” *IEEE Trans. on power electronics*, vol. 29, no. 12, pp. 6421–6432, 2014.
- [28] C. Yoon, H. Bai, R. N. Beres, X. Wang, C. L. Bak, and F. Blaabjerg, “Harmonic stability assessment for multiparalleled, grid-connected inverters,” *IEEE Trans. on Sustainable Energy*, vol. 7, no. 4, pp. 1388–1397, 2016.
- [29] J. Arrillaga, A. Medina, M. L. V. Lisboa, M. A. Cavia, and P. Sanchez, “The harmonic domain. a frame of reference for power system harmonic analysis,” *IEEE Trans. Power Syst.*, vol. 10, no. 1, pp. 433–440, 1995.
- [30] M. Madrigal and E. Acha, “Modelling of custom power equipment using harmonic domain techniques,” in *Ninth International Conference on Harmonics and Quality of Power. Proceedings (Cat. No. 00EX441)*, vol. 1. IEEE, 2000, pp. 264–269.
- [31] A. Ramirez, A. Semlyen, and R. Iravani, “Harmonic domain characterization of the resonant interaction between generator and transmission line,” *IEEE Trans. on power delivery*, vol. 20, no. 2, pp. 1753–1762, 2005.
- [32] N. M. Wereley, “Analysis and control of linear periodically time-varying systems,” Ph.D. dissertation, MIT, Cambridge, MA, USA, 1991.
- [33] J. Kwon, X. Wang, F. Blaabjerg, C. L. Bak, V.-S. Sularea, and C. Busca, “Harmonic interaction analysis in a grid-connected converter using harmonic state-space (hss) modeling,” *IEEE Trans. Power Electron.*, vol. 32, no. 9, pp. 6823–6835, 2016.
- [34] H. Yang, M. Eggers, P. Teske, and S. Dieckerhoff, “Comparative stability analysis and improvement of grid-following converters using novel interpretation of linear time-periodic theory,” *IEEE Journal of Emerging and Selected Topics in Power Electronics*, vol. 10, no. 6, pp. 7049–7061, 2022.
- [35] S. Golestan, J. M. Guerrero, A. M. Abusorrah, J. C. Vasquez, and Y. Al-Turki, “Ltp modeling and stability assessment of multiple second-order generalized integrator-based signal processing/synchronization algorithms and their close variants,” *IEEE Trans. on Power Electronics*, vol. 37, no. 5, pp. 5062–5077, 2021.

Bibliography

- [36] J. B. Kwon, X. Wang, F. Blaabjerg, C. L. Bak, A. R. Wood, and N. R. Watson, "Harmonic instability analysis of a single-phase grid-connected converter using a harmonic state-space modeling method," *IEEE Trans. on Industry Applications*, vol. 52, no. 5, pp. 4188–4200, 2016.
- [37] V. Salis, A. Costabeber, P. Zanchetta, and S. Cox, "Stability analysis of single-phase grid-feeding inverters with pll using harmonic linearisation and linear time periodic (ltp) theory," in *2016 IEEE 17th Workshop on Control and Modeling for Power Electronics (COMPEL)*. IEEE, 2016, pp. 1–7.
- [38] J. Sun and H. Liu, "Sequence impedance modeling of modular multilevel converters," *IEEE Journal of Emerging and Selected Topics in Power Electronics*, vol. 5, no. 4, pp. 1427–1443, 2017.
- [39] H. D. Abboud and A. Benigni, "Data-driven modeling of a commercial photovoltaic microinverter," *Modelling Simulation Eng.*, 2018.
- [40] Y. Liu, Y. Li, J. Ren, S. Wang, and L. Li, "A data-driven harmonic modeling method for electric vehicle charging stations," *Proc. Int. Conf. Electricity Distrib. (CIRED), Madrid, Spain*, 2019.
- [41] A. Semlyen and A. Medina, "Computation of the periodic steady-state in systems with nonlinear components using a hybrid time- and frequency-domain methodology," *IEEE Trans. Power Syst.*, vol. 10, no. 3, pp. 1498–1504, 1995.
- [42] W. Wiechowski *et al.*, "Hybrid time/frequency-domain modelling of nonlinear components," in *Proc. Int. Conf. Elect. Power Qual. Util., Barcelona, CAT, ES*, 2007, pp. 1–6.
- [43] J. J. Rico, M. Madrigal, and E. Acha, "Dynamic harmonic evolution using the extended harmonic domain," *IEEE Trans. Power Del.*, vol. 18, no. 2, pp. 587–594, 2003.
- [44] F. Yahyaie and P. W. Lehn, "On dynamic evaluation of harmonics using generalized averaging techniques," *IEEE Trans. on Power Systems*, vol. 30, no. 5, pp. 2216–2224, 2014.
- [45] E. Karami, G. B. Gharehpetian, and M. Madrigal, "A step forward in application of dynamic harmonic domain: Phase shifting property of harmonics," *IEEE Trans. on Power Delivery*, vol. 32, no. 1, pp. 219–225, 2016.
- [46] A. Stankovic, P. Mattavelli, V. Caliskan, and G. Verghese, "Modeling and analysis of facts devices with dynamic phasors," in *2000 IEEE Power Engineering Society Winter Meeting. Conference Proceedings (Cat. No.00CH37077)*, vol. 2, 2000, pp. 1440–1446 vol.2.

-
- [47] T. Demiray, G. Andersson, and L. Busarello, "Evaluation study for the simulation of power system transients using dynamic phasor models," in *2008 IEEE/PES Transmission and Distribution Conference and Exposition: Latin America*, 2008, pp. 1–6.
- [48] P. De Rua, Ö. C. Sakinci, and J. Beerten, "Comparative study of dynamic phasor and harmonic state-space modeling for small-signal stability analysis," *Electric Power Systems Research*, vol. 189, p. 106626, 2020.
- [49] X. Wang and F. Blaabjerg, "Harmonic stability in power electronic-based power systems: Concept, modeling, and analysis," *IEEE Trans. Smart Grid*, vol. 10, no. 3, pp. 2858–2870, 2018.
- [50] A. M. Kettner and M. Paolone, "Performance assessment of kron reduction in the numerical analysis of polyphase power systems," in *2019 IEEE Milan PowerTech*, 2019, pp. 1–6.
- [51] J. Arrillaga and C. P. Arnold, *Computer Analysis of Power Systems*. Chichester, SXW, UK: Wiley, 1990.
- [52] C. L. Fortescue, "Method of symmetrical co-ordinates applied to the solution of polyphase networks," *Trans. AIEE*, vol. 37, no. 2, pp. 1027–1140, 1918.
- [53] J. Das and R. H. Osman, "Grounding of ac and dc low-voltage and medium-voltage drive systems," *IEEE Trans. on Industry Applications*, vol. 34, no. 1, pp. 205–216, 1998.
- [54] T.-H. Chen and W.-C. Yang, "Analysis of multi-grounded four-wire distribution systems considering the neutral grounding," *IEEE Trans. on Power Delivery*, vol. 16, no. 4, pp. 710–717, 2001.
- [55] M. A. Laughton, "Analysis of unbalanced polyphase networks by the method of phase coordinates. Part 1: System representation in phase frame of reference," *Proc. IEE*, vol. 115, no. 8, pp. 1163–1172, 1968.
- [56] Z. Xin *et al.*, "Grid-current-feedback control for *LCL*-filtered grid converters with enhanced stability," *IEEE Trans. Power Electron.*, vol. 32, no. 4, pp. 3216–3228, 2016.
- [57] J. M. Guerrero *et al.*, "Advanced control architectures for intelligent microgrids, part i: Decentralized and hierarchical control," *IEEE Trans. Ind. Electron.*, vol. 60, no. 4, pp. 1254–1262, 2012.
- [58] J. Guerrero *et al.*, "Advanced control architectures for intelligent microgrids, part ii: Power quality, energy storage, and ac/dc microgrids," *IEEE Trans. Ind. Electron.*, vol. 60, no. 4, pp. 1263–1270, 2012.

Bibliography

- [59] G. N. Love and A. R. Wood, "Harmonic state-space model of power electronics," in *Proc. Int. Conf. Harmon. Qual. Power, Wollongong, NSW, AU*, 2008, pp. 1–6.
- [60] W. C. Duesterhoeft, M. W. Schulz, and E. Clarke, "Determination of instantaneous currents and voltages by means of α , β , and 0 components," *Trans. AIEE*, vol. 70, no. 2, pp. 1248–1255, 1951.
- [61] C. D. Meyer, Jr, "Generalized inverses of block triangular matrices," *SIAM Journal on Applied Mathematics*, vol. 19, no. 4, pp. 741–750, 1970.
- [62] M. S.-P. Hwang and A. R. Wood, "A new modelling framework for power supply networks with converter based loads and generators-the harmonic state-space," in *2012 IEEE International Conference on Power System Technology (POWERCON)*. IEEE, 2012, pp. 1–6.
- [63] J. Kwon, X. Wang, F. Blaabjerg, C. L. Bak, A. R. Wood, and N. R. Watson, "Linearized modeling methods of ac–dc converters for an accurate frequency response," *IEEE Journal of Emerging and Selected Topics in Power Electronics*, vol. 5, no. 4, pp. 1526–1541, 2017.
- [64] G. De Carne, G. Lauss, M. H. Syed, A. Monti, A. Benigni, S. Karrari, P. Kotsampopoulos, and M. O. Faruque, "On modeling depths of power electronic circuits for real-time simulation—a comparative analysis for power systems," *IEEE Open Access Journal of Power and Energy*, vol. 9, pp. 76–87, 2022.
- [65] T.-F. Wu, C.-H. Chang, L.-C. Lin, and C.-L. Kuo, "Power loss comparison of single-and two-stage grid-connected photovoltaic systems," *IEEE Trans. Energy Conv.*, vol. 26, no. 2, pp. 707–715, 2011.
- [66] S. B. Kjaer, J. K. Pedersen, and F. Blaabjerg, "A review of single-phase grid-connected inverters for photovoltaic modules," *IEEE Trans. Ind. Appl.*, vol. 41, no. 5, pp. 1292–1306, 2005.
- [67] D. Lu, X. Wang, and F. Blaabjerg, "Impedance-based analysis of dc-link voltage dynamics in voltage-source converters," *IEEE Trans. Power Electron.*, vol. 34, no. 4, pp. 3973–3985, 2018.
- [68] B. Gao, Y. Wang, and W. Xu, "An improved model of voltage source converters for power system harmonic studies," *IEEE Trans. Power Del.*, 2021.
- [69] M. Cespedes and J. Sun, "Impedance modeling and analysis of grid-connected voltage-source converters," *IEEE Trans. Power Electron.*, vol. 29, no. 3, pp. 1254–1261, 2013.
- [70] A. Rygg, M. Molinas, C. Zhang, and X. Cai, "On the equivalence and impact on stability of impedance modeling of power electronic converters in different domains," *IEEE Journal of Emerging and Selected Topics in Power Electronics*, vol. 5, no. 4, pp. 1444–1454, 2017.

-
- [71] N. Pogaku, M. Prodanovic, and T. C. Green, "Modeling, analysis and testing of autonomous operation of an inverter-based microgrid," *IEEE Trans. Power Electron.*, vol. 22, no. 2, pp. 613–625, 2007.
- [72] B. P. McGrath and D. G. Holmes, "A general analytical method for calculating inverter dc-link current harmonics," *IEEE Trans. Ind. Appl.*, vol. 45, no. 5, pp. 1851–1859, 2009.
- [73] Q. Fu, W. Du, and H. Wang, "Analysis of harmonic oscillations caused by grid-connected vscs," *IEEE Trans. Power Del.*, vol. 36, no. 2, pp. 1202–1210, 2020.
- [74] S. Chiniforoosh, J. Jatskevich, A. Yazdani, V. Sood, V. Dinavahi, J. Martinez, and A. Ramirez, "Definitions and applications of dynamic average models for analysis of power systems," *IEEE Trans. Power Del.*, vol. 25, no. 4, pp. 2655–2669, 2010.
- [75] J. Peralta Rodriguez, "Dynamic averaged models of vsc-based hvdc systems for electromagnetic transient programs," Ph.D. dissertation, École Polytechnique de Montréal, 2013.
- [76] F. Blaabjerg, R. Teodorescu, M. Liserre, and A. V. Timbus, "Overview of control and grid synchronization for distributed power generation systems," *IEEE Trans. Ind. Electron.*, vol. 53, no. 5, pp. 1398–1409, 2006.
- [77] J. Wang, N. C. P. Chang, X. Feng, and A. Monti, "Design of a generalized control algorithm for parallel inverters for smooth microgrid transition operation," *IEEE Trans. Ind. Electron.*, vol. 62, no. 8, pp. 4900–4914, 2015.
- [78] J. Rocabert, A. Luna, F. Blaabjerg, and P. Rodriguez, "Control of power converters in AC microgrids," *IEEE Trans. Power Electron.*, vol. 27, no. 11, pp. 4734–4749, 11 2012.
- [79] R. Teodorescu, M. , and P. Rodriguez, *Grid Converters for Photovoltaic and Wind Power Systems*. John Wiley & Sons, 2011, vol. 29.
- [80] S. Golestan, J. M. Guerrero, and J. C. Vasquez, "Three-phase plls: A review of recent advances," *IEEE Trans. on Power Electronics*, vol. 32, no. 3, pp. 1894–1907, 2017.
- [81] A. Edrei and G. Szegö, "A note on the reciprocal of a Fourier series," *Proc. AMS*, vol. 4, no. 2, pp. 323–329, 1953.
- [82] A. Yazdani and R. Iravani, "An accurate model for the dc-side voltage control of the neutral point diode clamped converter," *IEEE Trans. Power Del.*, vol. 21, no. 1, pp. 185–193, 2005.
- [83] G. F. Franklin, J. D. Powell, and A. Emami-Naeini, *Feedback Control of Dynamic Systems*, 5th ed. Upper Saddle River, NJ, USA: Pearson Education Inc., 2006.

Bibliography

- [84] M. Liserre, F. Blaabjerg, and S. Hansen, "Design and control of an LCL-filter-based three-phase active rectifier," *IEEE Trans. Ind. Appl.*, vol. 41, no. 5, pp. 1281–1291, 2005.
- [85] J. W. Umland and M. Safiuddin, "Magnitude and symmetric optimum criterion for the design of linear control systems: what is it and how does it compare with the others?" *IEEE Trans. on Industry Applications*, vol. 26, no. 3, pp. 489–497, 1990.
- [86] "Instrument transformers - part 2: Additional requirements for current transformers," International Electrotechnical Commission, Std. IEC 61869-2:2012, 2012.
- [87] A. Ulinuha, M. Masoum, and S. Islam, "Harmonic power flow calculations for a large power system with multiple nonlinear loads using decoupled approach," in *2007 Australasian Universities Power Engineering Conference*. IEEE, 2007, pp. 1–6.
- [88] S. Herraiz, L. Sainz, and J. Clua, "Review of harmonic load-flow formulations," *IEEE Trans. Power Del.*, vol. 18, no. 3, pp. 1079–1087, 2003.
- [89] J. Arrillaga, N. R. Watson, and G. N. Bathurst, "A multifrequency power flow of general applicability," *IEEE Trans. Power Del.*, vol. 19, no. 1, pp. 342–349, 2004.
- [90] D. Xia and G. T. Heydt, "Harmonic power flow studies. Part I+II," *IEEE Trans. Power App. Syst.*, vol. 101, no. 6, pp. 1257–1270, Jun. 1982.
- [91] W. Xu, J. R. Martí, and H. W. Dommel, "A multiphase harmonic load-flow solution technique," *IEEE Trans. Power Syst.*, vol. 6, no. 1, pp. 174–182, 1991.
- [92] M. Valcárcel and J. Garcia Mayordomo, "Harmonic power flow for unbalanced systems," *IEEE Trans. Power Del.*, vol. 8, no. 4, pp. 2052–2059, Oct. 1993.
- [93] J. Arrillaga and C. Callaghan, "Three-phase AC/DC load and harmonic flows," *IEEE Trans. Power Del.*, vol. 6, no. 1, pp. 238–244, 1991.
- [94] O. S. Nduka and A. R. Ahmadi, "Data-driven robust extended computer-aided harmonic power flow analysis," *IET Gener. Transm. Distrib.*, vol. 14, no. 20, pp. 4398–4409, 2020.
- [95] A. Borghetti, F. Napolitano, C. A. Nucci, and F. Rachidi, "Telegrapher's equations for field-to-transmission-line interaction," in *Advances in Power System Modelling, Control, and Stability Analysis*, F. Milano, Ed. Stevenage, ENG, UK: IET, 2016.
- [96] A. M. Kettner and M. Paolone, "On the properties of the compound nodal admittance matrix of polyphase power systems," *IEEE Trans. on Power Systems*, vol. 34, no. 1, pp. 444–453, 2018.

-
- [97] B. Gustavsen and A. Semlyen, "Enforcing passivity for admittance matrices approximated by rational functions," *IEEE Trans. Power Syst.*, vol. 16, no. 1, pp. 97–104, Feb. 2001.
- [98] F. L. Alvarado, "Formation of Y -node using the primitive Y -node concept," *IEEE Trans. Power App. Syst.*, no. 12, pp. 4563–4571, 1982.
- [99] B. C. Smith, J. Arrillaga, A. R. Wood, and N. R. Watson, "A review of iterative harmonic analysis for AC/DC power systems," *IEEE Trans. Power Del.*, vol. 13, no. 1, pp. 180–185, 1998.
- [100] A. Medina, J. Segundo-Ramirez, P. Ribeiro, W. Xu, K. Lian, G. Chang, V. Dinavahi, and N. R. Watson, "Harmonic analysis in frequency and time domain," *IEEE Trans. Power Del.*, vol. 28, no. 3, pp. 1813–1821, 2013.
- [101] T. Van Cutsem and C. Vournas, *Voltage Stability of Electric Power Systems*. Berlin, BE, DE: Springer, 1998.
- [102] W. Lambrichts and M. Paolone, "Linear recursive state estimation of hybrid and unbalanced ac/dc micro-grids using synchronized measurements," *IEEE Trans. on Smart Grid*, 2022.
- [103] J. Sun, "Impedance-based stability criterion for grid-connected inverters," *IEEE transactions on power electronics*, vol. 26, no. 11, pp. 3075–3078, 2011.
- [104] Y. Peng, Z. Shuai, X. Liu, Z. Li, J. M. Guerrero, and Z. J. Shen, "Modeling and stability analysis of inverter-based microgrid under harmonic conditions," *IEEE Trans. on Smart Grid*, vol. 11, no. 2, pp. 1330–1342, 2019.
- [105] S. R. Hall and N. M. Wereley, "Generalized nyquist stability criterion for linear time periodic systems," in *1990 American Control Conference*. IEEE, 1990, pp. 1518–1525.
- [106] V. Salis, A. Costabeber, S. M. Cox, P. Zanchetta, and A. Formentini, "Stability boundary analysis in single-phase grid-connected inverters with pll by ltp theory," *IEEE Trans. on Power Electronics*, vol. 33, no. 5, pp. 4023–4036, 2017.
- [107] J. Kwon, X. Wang, F. Blaabjerg, and C. L. Bak, "Comparison of lti and ltp models for stability analysis of grid converters," in *2016 IEEE 17th Workshop on Control and Modeling for Power Electronics (COMPEL)*. IEEE, 2016, pp. 1–8.
- [108] P. Kundur, *Power system stability and control*. McGraw-Hill Education, 1994.
- [109] H. Yang, H. Just, M. Eggers, and S. Dieckerhoff, "Linear time-periodic theory-based modeling and stability analysis of voltage-source converters," *IEEE Journal of Emerging and Selected Topics in Power Electronics*, vol. 9, no. 3, pp. 3517–3529, 2020.

Bibliography

- [110] I. S. Duff and J. Koster, “On algorithms for permuting large entries to the diagonal of a sparse matrix,” *SIAM Journal on Matrix Analysis and Applications*, vol. 22, no. 4, pp. 973–996, 2001.
- [111] F. Cecati, J. K. M. Becker, S. Pugliese, Y. Zuo, M. Liserre, and M. Paolone, “Ltp modeling and analysis of frequency coupling in pll-synchronized converters for harmonic power flow studies,” *IEEE Trans. on Smart Grid*, vol. 14, no. 4, pp. 2890–2902, 2023.

JOHANNA KRISTIN MARIA BECKER

EPFL-STI-IEL-DESL, ELL 117, Station 11, CH-1015 Lausanne, Switzerland

(+41) 21 693 63 02 ◊ johanna.becker@epfl.ch ◊ [LinkedIn](#) ◊ [Orcid](#)

Nationality: German ◊ Date of Birth: 18.02.1992

EDUCATION

Ph.D. in Electrical Engineering

07/2019 - 12/2023

Distributed Electrical Systems Laboratory,

École Polytechnique Fédérale de Lausanne (EPFL), Switzerland

Thesis Title: *“Unified Harmonic Power-Flow and Stability Analysis of Power Grids with Converter-Interfaced Distributed Energy Resources”*

Thesis directors: *Prof. Mario Paolone, Dr. Andreas Martin Kettner*

M.Sc. in Electrical Engineering

09/2016 - 02/2019

Smart Grids Science and Technology Orientation,

Final Grade: 5.58/6

École Polytechnique Fédérale de Lausanne, Switzerland

Thesis Title: *“Evaluation of Approximation Methods for Loadability Surfaces in Power Distribution Networks”*

Thesis director: *Prof. Mario Paolone*

B.Sc. in Microsystems Engineering

09/2012 - 09/2015

Freiburg University, Freiburg, Germany

Final Grade: 1.6¹

Thesis Title: *“Modellierung und Regelung eines Flugobjekts mit zwei Freiheitsgraden”*,

English Thesis Title: *“Modelling and Control of a Flying Object with Two Degrees of Freedom”*

Thesis director: *Prof. Moritz Diehl*

EXPERIENCE

Student Research Assistant, Distributed Electrical Systems Laboratory, EPFL, Switzerland

04/2018 - 08/2018

Implementation of PLL techniques and a test signal generator in Labview FPGA for the synchrocheck of a microgrid.

Student Research Assistant, Fraunhofer Institute for Physical Measurement

05/2016 - 07/2016

Techniques IPM, Freiburg, Germany

09/2012 - 10/2015

Characterization of thermoelectrical materials, PCB assembly (SMD soldering), construction, functional analysis and troubleshooting of measuring devices for thermoelectric materials.

Student Research Assistant, Systems Control and Optimization Laboratory

03/2016 - 07/2016

Freiburg University, Germany

Modelling of the dynamics of the so-called Sharpe windmill, a kite promising in the context of airborne wind energy.

¹German grading scale, where 1.0 is the best

Intern, Ampyx Power, The Hague, the Netherlands 11/2015 - 02/2016
PLC programming and control optimization for an airborne wind energy kite.

Intern, Fraunhofer Institute for Physical Measurement Techniques IPM, 05/2012 - 06/2012
Freiburg, Germany
Introduction to the construction and operation of thermoelectrical measuring devices, PCB soldering.

Intern, Central Department Research & Development, 10/2011 - 11/2011
Sick AG, Waldkirch (Breisgau), Germany
Contribution to the development of a technical-scientific text database and participation in projects related to laser analysis, optics studies, and photometric measurements.

PUBLICATIONS

Journal Articles:

- A. M. Kettner, L. Reyes-Chamorro, **J. K. M. Becker**, Z. Zou, M. Liserre, and M. Paolone, “Harmonic power-flow study of polyphase grids with converter-interfaced distributed energy resources—part i: Modeling framework and algorithm,” *IEEE Trans. Smart Grid*, vol. 13, no. 1, pp. 458–469, 2021.
- **J. K. M. Becker**, A. M. Kettner, L. Reyes-Chamorro, Z. Zou, M. Liserre, and M. Paolone, “Harmonic power-flow study of polyphase grids with converter-interfaced distributed energy resources—part ii: Model library and validation,” *IEEE Trans. Smart Grid*, vol. 13, no. 1, pp. 470–481, 2021.
- **J. K. M. Becker**, A. M. Kettner, Y. Zuo, F. Cecati, S. Pugliese, M. Liserre, and M. Paolone, “Modelling of ac/dc interactions of converter-interfaced resources for harmonic power-flow studies in micro-grids,” *IEEE Trans. on Smart Grid*, vol. 14, no. 3, pp. 2096–2110, 2022.
- F. Cecati, **J. K. M. Becker**, S. Pugliese, Y. Zuo, M. Liserre, and M. Paolone, “Ltp modeling and analysis of frequency coupling in pll-synchronized converters for harmonic power flow studies,” *IEEE Trans. on Smart Grid*, vol. 14, no. 4, pp. 2890–2902, 2023.

Conference Articles:

- **J. K. M. Becker**, Y. Zuo, M. Paolone, and A. M. Kettner, “Harmonic power-flow study of hybrid ac/dc grids with converter-interfaced distributed energy resources,” in *2023 IEEE Belgrade PowerTech*, 2023, pp. 1–6.

PRESENTATIONS

- 15th PowerTech Conference, Belgrade, Serbia: “Harmonic Power-Flow Study of Hybrid AC/DC Grids with Converter-Interfaced Distributed Energy Resources”, **J. K. M. Becker**, Y. Zuo, M. Paolone and A. M. Kettner, 2023.
- 15th PowerTech Conference, Belgrade, Serbia: Tutorial on “Stability and harmonic power flow in converter-dominated grids under consideration of converters control nonlinearities”, F. Cecati, **J. K. M. Becker**, M. Liserre, M. Paolone, 2023

TEACHING ACTIVITIES

- Teaching assistant for the “Smart Grids Technologies” course,** *07/2020 - present*
M.Sc. in electrical engineering, EPFL, Switzerland
- Teaching assistant for the “Systemtheorie und Regelungstechnik” course,** *04/2015 - 07/2015*
B.Sc. in Microsystems Engineering, Freiburg University, Germany

SUPERVISED STUDENT PROJECTS

- Developpment of a Simulink Model for the Study of Harmonics in Hybrid AC/DC Grids,** *07/2022 - 09/2022*
Distributed Electrical Systems Laboratory, EPFL, Switzerland
Master Project, Mr. Guillaume Reylandt, EPFL
- Effect of Frequency-Dependent Cable Parameters on Power-System Harmonic Analysis in EMTP-RV,** *02/2022 - 07/2022*
Distributed Electrical Systems Laboratory, EPFL, Switzerland
Bachelor Project, Mrs. Cecilia Männik, EPFL
- Development of a Simulation Model for Power-System Harmonic Analysis in EMTP-RV,** *09/2021 - 01/2022*
Distributed Electrical Systems Laboratory, EPFL, Switzerland
Master Project, Mr. Stevan Jokic, EPFL
- Developpment and Implementation of a Control Scheme for a Balancing Robot,** *01/2017 - 08/2017*
Chair of Discrete Optimization, EPFL, Switzerland
Bachelor Project, Mr. Samuel Sekarski, EPFL

LANGUAGE SKILLS

- German** - Mother tongue.
English - Full professional proficiency.
French - Conversant.
Spanish - Learning.

AWARDS AND SCHOLARSHIPS

- Ferry Porsche Award** for outstanding achievements in Maths and Physics in high school *06/2011*